

# Experimental and Numerical Investigations on the Effectiveness of Protective Barriers against Air Blast

Weifang Xiao

Vollständiger Abdruck der von der Fakultät für Bauingenieurwesen und Umweltwissenschaften der Universität der Bundeswehr München zur Erlangung des akademischen Grades eines

Doktor-Ingenieurs (Dr.-Ing.)

genehmigten Dissertation.

Gutachter:

1. Univ.-Prof. Dr.-Ing. habil. Norbert Gebbeken
2. Univ.-Prof. Hong Hao, Ph.D.

Die Dissertation wurde am 13. September 2018 bei der Universität der Bundeswehr München eingereicht und durch die Fakultät für Bauingenieurwesen und Umweltwissenschaften am 13. Februar 2019 angenommen. Die mündliche Prüfung fand am 26. Februar 2019 statt.



## Abstract

Protective barriers are often proposed in order to protect buildings and their properties against air blast. On the one hand, they act as stand-off barriers, on the other hand as obstacles in the propagation path of the shock wave. If properly designed, they can also act as barriers in order to stop vehicles.

This Dissertation analyses experimentally and numerically the effectiveness of protective barriers in attenuating the shock wave. While the distribution of blast loads from explosions in the free field is well understood, only limited information is available on the blast loads behind non-conventional walls or barriers, especially if the wall or parts of it do not behave rigidly or if the barrier has a surface containing openings. In this context, two different types of protective barriers are investigated, i.e. blast walls with a canopy on top and protective barriers made of steel posts. New experimental results of these protective barriers are provided, i.e. the overpressure-time histories at the gauges both in front of and behind the barriers.

Numerical simulations using the software LS-DYNA are performed to complement and / or to substitute the experiments. Prior to the experiments, numerical models are developed in order to predict the blast loads numerically. The numerical simulations use the approach proposed by Slavik to couple empirical blast loads to Arbitrary-Lagrangian-Eulerian (ALE) air domains. The numerical simulation is subdivided into two stages. In the first stage, the empirical formulae of Kingery and Bulmash are used to calculate the blast loads on a layer of ambient ALE air elements, which is situated at the front face of the air domain facing the charge. The front face of the air domain is located 2m in front of the barrier. In the second stage, the shock wave propagation is simulated by using the ALE formulation with a multi-material option, where the results from the first stage are used as input for the ambient ALE air elements. Applying this coupled approach combines the advantages of both the empirical method and the ALE method.

For blast walls with a canopy, the solid blast wall is considered as a rigid body. The canopy is modelled applying two assumptions: firstly as a rigid structure, secondly as a flexible bending plate. For protective barriers made of steel posts, the steel posts are modelled with two assumptions: firstly as rigid structures, secondly as flexible structures. Using the Fluid-Structure-Interaction (FSI), the shock wave and the barrier are coupled in the numerical analysis. The coupling algorithm of FSI utilizes the ALE air mesh to derive the dynamic forces on the barrier. Meanwhile, the barrier provides a dynamic constraint to the shock wave propagating through the air domain. The influence of the structural flexibility on the blast load distribution behind the barriers is investigated by comparing the numerical results based on the rigid and flexible assumptions. The experimental data is used to validate the developed numerical models. After validation, they are applied to carry out parametric studies in order to explore the influence of further parameters of the barriers on the shock wave attenuation performance. Based on the overpressure-time histories at the gauges, both the peak overpressures and the maximum impulses can be calculated. They are employed to estimate the effectiveness of protective barriers by means of overpressure and impulse reduction factors.

This research contributes to the blast-resistant design of blast walls with a canopy and protective barriers made of steel posts.



## **Kurzfassung**

Um Gebäude und ihre direkte Umgebung gegen Schockwellen zu schützen, werden häufig Schutzbarrieren errichtet. Zum einen vergrößern Barrieren den Abstand zwischen einer Explosion und dem zu schützenden Bereich, zum anderen wirken sie als Hindernisse für die Ausbreitung der Schockwelle. Wenn sie richtig entworfen sind, können Schutzbarrieren auch dazu dienen, Fahrzeuge anzuhalten.

In dieser Dissertation wird, mit experimentellen und numerischen Methoden, die Wirksamkeit von Schutzbarrieren bei der Druck- und Impulsreduzierung untersucht. Während die Verteilung der Explosionslasten im freien Feld gut verstanden wird, stehen nur begrenzte Informationen über die Explosionslasten hinter unkonventionellen Wänden oder Barrieren zur Verfügung. Dies gilt insbesondere, wenn sich die Wand oder Teile davon nicht starr verhalten oder wenn die Barriere eine Oberfläche mit Öffnungen besitzt. In diesem Kontext werden zwei unterschiedliche Arten von Schutzbarrieren untersucht, nämlich auf Schutzwände montierte Leitbleche und Barrieren aus Stahlpfosten. In diesem Rahmen werden neue Versuchsergebnisse zu diesen Schutzbarrieren zur Verfügung gestellt. Dabei handelt es sich um die Überdruck-Zeit-Verläufe an den Messsensoren vor und hinter den Barrieren.

Unter Verwendung der Software LS-DYNA werden numerische Simulationen durchgeführt, um die Versuchsergebnisse zu ergänzen und die Notwendigkeit weiterer Versuche zu verringern. Bereits vor den Versuchen wurden numerische Modelle entwickelt, um die zu erwartenden Explosionslasten vorherzusagen. Die numerischen Simulationen wurden mit dem von Slavik vorgeschlagenen Ansatz durchgeführt, bei dem die Explosionslasten aus einem empirischen Ansatz mit Arbitrary-Lagrangian-Eulerian (ALE)-Luftvolumen gekoppelt werden. Die Durchführung der numerischen Simulationen geschieht hierbei in zwei Schritten. Der erste Schritt erfolgt unter Verwendung der empirischen Formeln von Kingery und Bulmash. Hierbei werden die auf die Außenfläche des ALE-Luftvolumens einwirkenden Explosionslasten berechnet, welche sich an der, der Ladung zugewandten Vorderseite des Luftvolumens befindet. Die Außenfläche des Luftvolumens befindet sich 2m von der Barriere entfernt. In dem zweiten Schritt wird die Druckwellenausbreitung im Luftvolumen unter Verwendung der ALE-Formulierung mit einer Multi-Material-Option simuliert. Die empirisch ermittelten Ergebnisse des ersten Schrittes werden als Eingangswerte für die ALE-Luftelemente verwendet. Die Anwendung dieses gekoppelten Ansatzes kombiniert die Vorteile der empirischen Methode und der ALE-Methode.

Bei der Untersuchung der auf den Schutzwänden montierten Leitbleche werden die Schutzwände (Gabionenwände) als starr angenommen. Die Leitbleche werden mit zwei unterschiedlichen Annahmen modelliert: erstens als unbewegliche, starre Strukturen und zweitens als flexible Biegeplatten. Bei den Barrieren aus Stahlpfosten werden die Stahlpfosten ebenso mit diesen beiden Annahmen modelliert. Mit Hilfe Fluid-Struktur-Interaktion (FSI) werden in der numerischen Analyse die Schockwelle und die Barriere gekoppelt. Der Kopplungsalgorithmus der FSI verwendet das Netz der ALE-Luftelemente für die Berechnung der dynamischen Kräfte auf die Barriere. Gleichzeitig bildet die Barriere eine dynamische Randbedingung für die Schockwelle, welche sich durch das Luftvolumen ausbreitet. Der

Einfluss der Flexibilität der Struktur auf die Verteilung der Explosionslasten hinter den Barrieren wird untersucht, indem die numerischen Ergebnisse auf der Grundlage der starren und flexiblen Annahmen miteinander verglichen werden.

Die Ergebnisse der Versuche werden zur Validierung der entwickelten numerischen Modelle verwendet. Nach der Validierung werden die Modelle zur Durchführung von Parameterstudien eingesetzt, um den Einfluss weiterer Parameter der Barrieren auf die Druck- und Impulsreduzierung zu untersuchen. Basierend auf den Überdruck-Zeit-Verläufen an den Messsensoren können sowohl die Spitzenüberdrücke, als auch die maximalen Impulse berechnet werden. Diese dienen zur Abschätzung der Wirksamkeit von Schutzbarrieren durch die Ermittlung von Überdruck- und Impulsreduktionsfaktoren.

Die durchgeführte Forschung im Bereich des Explosionsschutzes gibt neue Hinweise zur Planung von Schutzwänden mit Leitblechen und Barrieren aus Stahlpfosten.

## **Acknowledgements**

This work was developed during my time as a research associate at the Institute of Engineering Mechanics and Structural Analysis at the University of the Bundeswehr in Munich.

First of all, I want to express my deep gratitude to my supervisor, Univ.-Prof. Dr.-Ing. habil. Norbert Gebbeken, for giving me the opportunity to create the thesis at the institute and for granting me all the scientific freedom during this work. His open-minded and unreserved support led to many valuable and fruitful discussions. Without his support, constructive feedback and time for fruitful conversations, this Dissertation would not have been possible. I would like to thank my second examiner, Univ.-Prof. Hong Hao, Ph.D, for the revision of the thesis and for his valuable advice in the specific areas of expertise. I would also like to thank Univ.-Prof. Dr.-Ing. Michael Brünig for his work as chairman of the Doctoral Degree Committee.

Furthermore, I warmly thank all my colleagues for the open and intensive discussions on plenty of research topics and for providing a good working atmosphere. Among them, I want to mention especially Matthias Andrae, Georgios Michaloudis, Maximilian Garsch and Beatriz Esteban, who inspired my work with numerous discussions and did the proofreading of my thesis.

Moreover, I would like to thank the Federal Office of Civil Protection and Disaster Assistance (BBK), Department II.5 - Structural Protection, Emergency Preparedness (Water) in Germany for their financial support to carry out this research work. I would also like to express my gratitude to the whole team at the Bundeswehr Technical Centre for Protective and Special Technologies (WTD52) in Germany for the good collaboration during the conduction of the experiments. Their expertise was a valuable contribution to the success of the experiments. I hope that the analysis methods of this Dissertation are also useful for their future investigations.

Finally, I would like to thank my family, especially my wife Danyang, for always staying by my side and support me. Their steady encouragement has given me the necessary strength, confidence and optimism.

Munich, February 2019

Weifang Xiao



---

## Table of Contents

<b>1</b>	<b>Introduction .....</b>	<b>1</b>
1.1	Motivation .....	1
1.2	Layout of the thesis .....	2
<b>2</b>	<b>Protective barrier overview .....</b>	<b>4</b>
2.1	Blast walls .....	4
2.1.1	Rigid blast walls .....	4
2.1.2	Flexible blast walls .....	19
2.2	Barriers with openings .....	21
2.2.1	Interaction between the shock wave and the solid obstacles .....	21
2.2.2	Shock wave trapping concept .....	24
2.3	Summary: protective barrier overview .....	24
<b>3</b>	<b>Shock wave propagation .....</b>	<b>25</b>
3.1	Basic parameters of shock waves .....	25
3.2	Overpressure-time history .....	26
3.2.1	Two-parameter form .....	28
3.2.2	Three-parameter form .....	29
3.2.3	Four-parameter form .....	31
3.2.4	Five-parameter form .....	31
3.2.5	Comparison of different forms of overpressure-time histories .....	31
3.3	Scaling laws .....	33
3.3.1	Hopkinson-Cranz scaling law .....	33
3.3.2	Sachs scaling law .....	34
3.4	TNT equivalence .....	35
3.4.1	Theoretical method .....	36
3.4.2	Laboratory tests .....	38
3.4.3	Field tests .....	39
3.4.4	Numerical method .....	41
3.4.5	Discussion on TNT equivalence .....	42
3.5	Diffraction process .....	43
3.6	Drag coefficient .....	45

## Table of Contents

---

3.7	Clearing effect.....	48
3.7.1	Clearing correction method for an observation point .....	48
3.7.2	Clearing correction method averaged over the front face.....	50
3.8	Type of burst .....	52
3.8.1	Free-air burst .....	53
3.8.2	Surface burst .....	53
3.8.3	Height-of-burst detonation.....	53
3.9	Summary: shock wave propagation .....	59
<b>4</b>	<b>Theoretical background of numerical simulations.....</b>	<b>61</b>
4.1	Basic aspects of numerical simulations.....	61
4.1.1	Material models .....	61
4.1.1.1	Air.....	61
4.1.1.2	Explosive material.....	63
4.1.1.3	Structural material (steel) .....	64
4.1.2	Time step control .....	64
4.1.2.1	Critical time step size for solid elements.....	65
4.1.2.2	Critical time step size for shell elements.....	65
4.1.3	Element formulations.....	66
4.1.4	Mapping techniques .....	67
4.1.4.1	Mapping from 1D to 2D and from 1D to 3D .....	67
4.1.4.2	Mapping from 2D to 3D .....	68
4.1.5	Fluid-Structure-Interaction (FSI) algorithm .....	69
4.2	Modelling strategies .....	70
4.2.1	Empirical method (LBE).....	70
4.2.2	Arbitrary-Lagrangian-Eulerian (ALE) method.....	72
4.2.3	Combined method (LBE / ALE).....	73
4.2.4	Comparison of modelling strategies .....	76
4.3	Summary: theoretical background of numerical simulations.....	77
<b>5</b>	<b>Experiments with protective barriers.....</b>	<b>78</b>
5.1	Blast walls with a canopy on top .....	78
5.1.1	Experimental set-up .....	78

---

5.1.2	Blast wall configurations .....	81
5.1.3	Experimental instrumentation.....	82
5.1.4	Experimental data .....	85
5.1.4.1	Overpressure-time history .....	85
5.1.4.2	Data statistics at the gauges in front of the blast wall .....	87
5.1.4.3	Data statistics at the gauges behind the blast wall.....	90
5.1.4.4	Evaluation of overpressure and impulse reduction .....	91
5.1.5	Conclusion: blast walls with a canopy on top.....	93
5.2	Protective barriers made of steel posts.....	94
5.2.1	Experimental set-up .....	94
5.2.2	Steel posts configurations .....	96
5.2.3	Experimental instrumentation.....	97
5.2.4	Experimental data .....	98
5.2.4.1	Overpressure-time history .....	98
5.2.4.2	Data statistics at the gauges in front of the barrier .....	100
5.2.4.3	Data statistics at the gauges behind the barrier .....	102
5.2.4.4	Evaluation of overpressure and impulse reduction .....	104
5.2.5	Conclusion: protective barriers made of steel posts .....	106
<b>6</b>	<b>Numerical investigations on the effectiveness of protective barriers.....</b>	<b>107</b>
6.1	Influence of ambient conditions on the blast loads.....	107
6.1.1	Altitude .....	110
6.1.2	Atmospheric temperature.....	111
6.1.3	Conclusions: influence of ambient conditions on the blast loads .....	113
6.2	Influence of the charge height on the blast loads.....	113
6.3	Blast walls with a canopy on top .....	115
6.3.1	Numerical models of blast walls with a canopy on top .....	115
6.3.2	Mesh convergence study and model verification.....	117
6.3.3	Model validation .....	119
6.3.4	Numerical results .....	120
6.3.4.1	Overpressure-time history .....	120
6.3.4.2	Clearing effect of shock waves around wooden plates .....	123
6.3.4.3	Shock wave propagation .....	125

## Table of Contents

---

6.3.4.4	Overpressure distribution across the facade .....	128
6.3.4.5	Flexibility of the canopy.....	129
6.3.4.6	Blast walls having infinite width.....	130
6.3.5	Parametric studies .....	133
6.3.5.1	Thickness of the canopy .....	134
6.3.5.2	Angle of inclination of the canopy .....	135
6.3.6	Conclusions: blast walls with a canopy on top .....	139
6.4	Protective barriers made of steel posts.....	140
6.4.1	Numerical models of protective barriers made of steel posts .....	140
6.4.2	Mesh convergence study and model verification.....	141
6.4.3	Model validation .....	141
6.4.4	Numerical results .....	143
6.4.4.1	Overpressure reduction by the steel frame and the gabion walls .....	143
6.4.4.2	Overpressure-time history .....	144
6.4.4.3	Clearing effect of shock waves around wooden plates .....	147
6.4.4.4	Shock wave propagation .....	148
6.4.4.5	Structural flexibility .....	150
6.4.4.6	Overpressure and impulse reductions.....	151
6.4.5	Parametric studies .....	152
6.4.5.1	Relative opening fraction (ROF).....	152
6.4.5.2	Cross-sectional shape .....	154
6.4.5.3	Double-layer arrangement.....	157
6.4.6	Conclusions: protective barriers made of steel posts.....	160
6.5	Comparison of protective barriers (blast walls with a canopy on top versus protective barriers made of steel posts).....	161
<b>7</b>	<b>Conclusions and outlook .....</b>	<b>164</b>
	<b>Bibliography .....</b>	<b>168</b>

---

**List of Figures**

Figure 2-1: Empirical method of calculating the blast loads on the building presented by Philip 1942 .....	5
Figure 2-2: Experimental set-up used by Beyer 1986 (a) vertical cantilever blast wall; (b) blast wall having a canopy near the top of the wall facing the charge ..	6
Figure 2-3: Experimental set-up used by Jones et al. 1987 .....	7
Figure 2-4: Overpressure and impulse reduction factors according to Mayor and Flanders 1990 .....	9
Figure 2-5: Experimental set-up used by Rose et al. 1993 and Rose et al. 1995 .....	9
Figure 2-6: Contour plots of the peak side-on overpressures ( $p_{so}$ in kPa) given as the natural logarithm (a) without a wall and (b) with a wall .....	10
Figure 2-7: Typical design charts for peak overpressure (top curve) and scaled maximum impulse (bottom curve), $H/W^{1/3} = 0.5\text{m/kg}^{1/3}$ , $r/W^{1/3} = 0.327\text{m/kg}^{1/3}$ (a) $h/W^{1/3} = 1.0\text{m/kg}^{1/3}$ ; (b) $h/W^{1/3} = 1.5\text{m/kg}^{1/3}$ .....	11
Figure 2-8: Blast wall and revetment configurations (a) plane wall; (b) blast wall having an inclined canopy, angle of inclination $45^\circ$ ; (c) blast wall having a horizontal canopy; (d) mounded revetment .....	12
Figure 2-9: Peak overpressures behind blast walls and revetments (a) at the ground level; (b) at height H .....	12
Figure 2-10: Scaled maximum impulse behind blast walls and revetments (a) at the ground level; (b) at height H .....	13
Figure 2-11: Experimental set-up used by Chapman et al. 1995a .....	14
Figure 2-12: Factored quantities versus modified scaled distance $Z_m$ (a) peak reflected overpressure $p_f$ ; (b) scaled maximum reflected impulse $i_f$ .....	15
Figure 2-13: Air flows around the sides and over the top of the wall .....	16
Figure 2-14: Shadow region provided by a blast wall .....	17
Figure 2-15: Blast wall configuration used by Zhou and Hao 2008 .....	18
Figure 2-16: Peak overpressures on the ground behind different types of blast walls ..	20
Figure 2-17: Effectiveness factors of frangible walls compared to rigid walls .....	20
Figure 3-1: Idealized side-on overpressure-time history generated from a far-field detonation .....	27
Figure 3-2: Dependence of the decay rate $\alpha$ on the scaled distance $Z$ , (data from Kinney and Graham 1985) .....	30
Figure 3-3: Side-on overpressure-time histories generated from a detonation (5kg TNT equivalent) on the ground at different stand-off distances .....	32
Figure 3-4: TNT equivalence factors for overpressure and impulse (a) composition B; (b) composition C4; (c) pentolite; (d) tritonal (data from Swisdak 1975) ..	40
Figure 3-5: TNT equivalence factors for side-on and reflected overpressure and impulse for PETN (data from Shin et al. 2015) .....	42
Figure 3-6: Diffraction of a plane shock wave over a wall having an infinite width in the out-of-plane direction, side view .....	44
Figure 3-7: Diffraction of a plane shock wave over a wall having a finite width, plan view ..	45

## List of Figures

---

Figure 3-8: Typical flow pattern around a thin flat plate, line a-a marks a plane of symmetry .....	47
Figure 3-9: Drag coefficients for various structural shapes ( <i>Kinney and Graham 1985</i> ).....	47
Figure 3-10: Sketch of the clearing effect at the front face of a wall having finite dimensions (a) three-dimensional wall structure; (b) observation point P at distance $S_p$ from the nearest edge, front view.....	48
Figure 3-11: Overpressure-time histories at the front face due to the influence of the clearing effect (a) observation point P at distance $S_p$ from the nearest edge; (b) simplified form.....	49
Figure 3-12: Sonic velocity $c_r$ in the air of the reflected region versus peak side-on overpressure $p_{so}$ (data from <i>UFC 3-340-02</i> ) .....	49
Figure 3-13: Empirical clearing correction method according to <i>UFC 3-340-02</i> .....	51
Figure 3-14: Reflected overpressure-time histories at the front face of walls having infinite and finite dimensions .....	52
Figure 3-15: Configurations of different burst types (a) free-air burst; (b) surface burst; (c) height-of-burst detonation .....	52
Figure 3-16: Blast environment from a height-of-burst detonation .....	54
Figure 3-17: Schematic pressure contours at successive times after a detonation near the ground surface (a) unimpeded shock wave in the atmosphere; (b) regular reflection of the shock wave at angles of incidence $\alpha < \alpha_{min}$ ; (c) generation of the origin of the triple point path at angle of incidence $\alpha = \alpha_{min}$ ; (d) Mach stem formation at angles of incidence $\alpha > \alpha_{min}$ ; (e) surface burst behaviour at distances appreciably larger than the charge height (adapted from <i>Kinney and Graham 1985</i> ).....	55
Figure 3-18: Angle of incidence for transition from regular reflection region to Mach reflection region .....	57
Figure 3-19: Transition from regular reflection region to Mach reflection region and transition from Mach reflection region to surface burst behaviour for the reference nuclear explosion of one kiloton TNT .....	58
Figure 3-20: Dual-solution-domain between regular reflection and Mach reflection regions (data from <i>Ivanov 2001</i> ) .....	59
Figure 4-1: Element formulation (a) Lagrange; (b) Euler ( <i>Larcher 2007</i> ) .....	66
Figure 4-2: Sketch of mapping techniques (a) free air burst detonation; (b) surface burst detonation; (c) height-of-burst detonation.....	68
Figure 4-3: Sketch of a building subjected to air blast (a) without a protective barrier; (b) with a protective barrier.....	70
Figure 4-4: Definition of the angle of incidence $\alpha$ .....	70
Figure 4-5: Cosine distribution of overpressures in dependence on the angle of incidence $\alpha$ ..	71
Figure 4-6: Sketch of the numerical model associated with the combined method LBE / ALE .....	73
Figure 4-7: Shock front at successive times (a) $t = t_0$ ; (b) $t > t_0$ .....	74
Figure 4-8: Flow chart of the combined method LBE / ALE .....	76
Figure 5-1: Experimental set-up of configurations (a) plan view; (b) side view, M1 - GWC back; (b) side view, M2 - GW; (b) side view, M3 - GWC front.....	80

Figure 5-2: Blast wall configurations (a) M1 - GWC back; (b) M2 - GW; (c) M3 - GWC front (photos: WTD52 / UniBwM) .....	81
Figure 5-3: Geometry of the gabion wall and canopy .....	82
Figure 5-4: Experimental instrumentation (a) gauges ps2 - ps4; (b) gauges pr1 - pr4; (c) distance between gabion wall and wooden plate where gauges were mounted; (d) explosive charge with the wooden gallow and the steel plate (photos: WTD52 / UniBwM) .....	84
Figure 5-5: Detonation process (a) initial state; (b) ignition point; (c) accompanying fireball (photos: WTD52 / UniBwM) .....	84
Figure 5-6: Side-on overpressure-time histories measured in experiment V1, M3 - GWC front (a) ps1; (b) ps2; (c) ps3; (d) ps4 .....	85
Figure 5-7: Reflected overpressure-time histories measured in experiment V1, M3 - GWC front (a) pr1; (b) pr2; (c) pr3; (d) pr4 .....	86
Figure 5-8: Slit between cubic gabion boxes (photos: WTD52 / UniBwM).....	87
Figure 5-9: Peak side-on overpressures at gauges ps1 of the experiments .....	88
Figure 5-10: Experimental recordings at gauges ps1 measured in experiment V1 for configurations M1 - GWC back, M2 - GW and M3 - GWC front (a) overpressure-time histories; (b) impulse-time histories .....	89
Figure 5-11: Experimental results (a) peak side-on overpressures; (b) peak reflected overpressures; (c) maximum side-on impulses; (d) maximum reflected impulses.....	92
Figure 5-12: Experiment set-up (a) plan view; (b) side view.....	95
Figure 5-13: Barrier configurations (a) Mref, no posts; (b) M1, $n_{post} = 8$ ; (c) M2, $n_{post} = 5$ ; (d) M3, $n_{post} = 6$ (photos: WTD52 / UniBwM).....	96
Figure 5-14: Configurations of steel posts with a square hollow section, plan view.....	97
Figure 5-15: Experimental instrumentation (a) gauges ps2 - ps4; (b) gauges pr1 - pr4 (photos: WTD52 / UniBwM) .....	98
Figure 5-16: Side-on overpressure-time histories measured in experiment V3, configuration M1, $n_{post} = 8$ (a) ps1; (b) ps2; (c) ps3; (d) ps4.....	99
Figure 5-17: Reflected overpressure-time histories measured in experiment V3, configuration M1, $n_{post} = 8$ (a) pr1; (b) pr2; (c) pr3; (d) pr4.....	100
Figure 5-18: Peak side-on overpressures at gauges ps1 measured in the experiments .....	101
Figure 5-19: Iso-pressure line plots of a plane at an elevation of 0.63m above the ground, configuration M1, $n_{post} = 8$ (a) $t = 5.8\text{ms}$ ; (b) $t = 6.0\text{ms}$ ; (c) $t = 6.4\text{ms}$ ; (d) $t = 7.0\text{ms}$ .....	104
Figure 5-20: Experimental results (a) peak side-on overpressures; (b) peak reflected overpressures; (c) maximum side-on impulses; (d) maximum reflected impulses .....	105
Figure 6-1: Scaling factors for pressure $S_p$ , distance $S_d$ and time $S_t$ at different altitudes ....	108
Figure 6-2: Sketch of the two-dimensional axisymmetric numerical model .....	109
Figure 6-3: Influence of the altitude on the peak overpressures at gauges (a) ps0 - ps4; (b) pr1 - pr4 .....	110
Figure 6-4: Influence of the altitude on the arrival time of the shock wave at gauges (a) ps0 - ps4; (b) pr1 - pr4 .....	111
Figure 6-5: Influence of the atmospheric temperature on the peak overpressures at gauges (a) ps0 - ps4; (b) pr1 - pr4 .....	112

## List of Figures

---

Figure 6-6: Influence of the atmospheric temperature on the arrival time of the shock wave at gauges (a) ps0 - ps4; (b) pr1 - pr4 .....	112
Figure 6-7: Comparison of the peak overpressures at the gauges in the experiments of blast walls with a canopy on top in case of surface burst (SF) and height-of-burst (HOB) detonations (a) gauges ps1 - ps4; (b) gauges pr1 - pr4.....	114
Figure 6-8: Comparison of the peak overpressures at the gauges in the experiments of protective barriers made of steel posts in case of surface burst (SF) and height-of-burst (HOB) detonations (a) gauges ps1 - ps4; (b) gauges pr1 - pr4.....	114
Figure 6-9: Sketch of the numerical model of the blast wall with a canopy on top ( <i>Xiao et al. 2018c</i> ).....	116
Figure 6-10: Mesh convergence study (a) side-on overpressures; (b) reflected overpressures .....	118
Figure 6-11: Configuration M0 (no wall) (a) peak side-on overpressures; (b) peak reflected overpressures .....	119
Figure 6-12: Configuration M3 - GWC front (a) peak side-on overpressures; (b) peak reflected overpressures .....	120
Figure 6-13: Side-on overpressure-time histories, M3 - GWC front (a) ps1; (b) ps2; (c) ps3; (d) ps4.....	121
Figure 6-14: Reflected overpressure-time histories, M3 - GWC front (a) pr1; (b) pr2; (c) pr3; (d) pr4.....	122
Figure 6-15: Sketch of the numerical model including wooden plates, M3 - GWC front.....	124
Figure 6-16: Pressure contour plots of a horizontal plane at an elevation of 1m above the ground, M3 - GWC front, plan view (a) $t = 4.0\text{ms}$ ; (b) $t = 7.6\text{ms}$ ; (c) $t = 8.5\text{ms}$ ; (d) $t = 11.7\text{ms}$ ; (e) $t = 13.3\text{ms}$ ; (f) $t = 15.6\text{ms}$ .....	125
Figure 6-17: Pressure contour plots of a horizontal plane at an elevation of 2m above the ground, M3 - GWC front, plan view (a) $t = 8.8\text{ms}$ ; (b) $t = 10.0\text{ms}$ ; (c) $t = 11.2\text{ms}$ ; (d) $t = 13.3\text{ms}$ .....	126
Figure 6-18: Pressure contour plots of the vertical plane through the centre of the blast wall, M3 - GWC front, side view (a) $t = 4.0\text{ms}$ ; (b) $t = 7.6\text{ms}$ ; (c) $t = 10.0\text{ms}$ ; (d) $t = 11.2\text{ms}$ ; (e) $t = 13.3\text{ms}$ ; (f) $t = 15.6\text{ms}$ .....	127
Figure 6-19: Distribution of peak reflected overpressures across the facade .....	129
Figure 6-20: Displacement-time histories of the canopies.....	130
Figure 6-21: Dependence of the peak reflected overpressure distribution across the facade on the width of gabion walls .....	131
Figure 6-22: Overpressure and impulse reduction for blast walls having infinite width (a) $F_p$ at gauges ps2 - ps4; (b) $F_p$ at gauges pr1 - pr4; (c) $F_i$ at gauges ps2 - ps4; (d) $F_i$ at gauges pr1 - pr4 .....	133
Figure 6-23: Dependence of the peak reflected overpressure distribution across the facade on the thickness of the canopy .....	134
Figure 6-24: Influence of the thickness of the canopy on the displacement of the canopy ...	135
Figure 6-25: Overpressure and impulse reduction factors versus angle of inclination of canopy .....	136
Figure 6-26: Overpressure reduction factors versus effective height of the blast wall (a) pr1; (b) pr2; (c) pr3; (d) pr4 .....	137

Figure 6-27: Impulse reduction factors versus effective height of the blast wall (a) pr1; (b) pr2; (c) pr3; (d) pr4.....	138
Figure 6-28: Numerical model (a) sketch of the total model; (b) FE-mesh of the steel posts and the steel frame ( <i>Xiao et al. 2017a</i> and <i>Xiao et al. 2018d</i> ) .....	140
Figure 6-29: Configuration Mref (no posts) (a) peak side-on overpressures; (b) peak reflected overpressures .....	142
Figure 6-30: Comparison of the peak overpressures at three different numerical models, GW&SF represents the model that consists of a steel frame in the middle and a gabion wall at each side, GW represents the model that only consists of gabion walls, Free field represents a free field scenario (a) gauges ps1 - ps4; (b) gauges pr1 - pr4 .....	144
Figure 6-31: Side-on overpressure-time histories, configuration M1, $n_{post} = 8$ (a) ps1; (b) ps2; (c) ps3; (d) ps4.....	145
Figure 6-32: Reflected overpressure-time histories, configuration M1, $n_{post} = 8$ (a) pr1; (b) pr2; (c) pr3; (d) pr4.....	146
Figure 6-33: Sketch of the numerical model including wooden plates, M1 ( $n_{post} = 8$ ).....	148
Figure 6-34: Pressure contour plots of a horizontal plane at an elevation of 0.63m above the ground, M1 ( $n_{post} = 8$ ), plan view (a) $t = 4.0\text{ms}$ ; (b) $t = 5.6\text{ms}$ ; (c) $t = 6.4\text{ms}$ ; (d) $t = 7.0\text{ms}$ ; (e) $t = 9.4\text{ms}$ ; (f) $t = 11.9\text{ms}$ .....	149
Figure 6-35: Influence of the structural flexibility on the peak reflected overpressures .....	150
Figure 6-36: Overpressure and impulse reduction for the steel post configurations (a) $F_p$ at gauges ps2 - ps4; (b) $F_p$ at gauge pr1 - pr4; (c) $F_i$ at gauges ps2 - ps4; (d) $F_i$ at gauge pr1 - pr4 .....	151
Figure 6-37: Influence of relative opening fraction on the overpressure and impulse reduction, square cross-section (a) $F_p$ at gauges ps2 - ps4; (b) $F_p$ at gauges pr1 - pr4; (c) $F_i$ at gauges ps2 - ps4; (d) $F_i$ at gauges pr1 - pr4 .....	153
Figure 6-38: Cross-sectional shapes of the steel posts (a) square; (b) circular; (c) triangular I, vertex oriented away from the charge; (d) triangular II, vertex facing the charge .....	154
Figure 6-39: Overpressure reductions of different cross-sectional shapes, single-layer arrangement (a) gauge ps4; (b) gauge pr2.....	155
Figure 6-40: Impulse reductions of different cross-sectional shapes, single-layer arrangement (a) gauge ps4; (b) gauge pr2.....	156
Figure 6-41: Details of the arrangements of steel posts.....	158
Figure 6-42: Overpressure reductions of different steel post arrangements at gauges (a) ps2 - ps4; (b) pr1 - pr4.....	159
Figure 6-43: Impulse reductions of different steel post arrangements at gauges (a) ps2 - ps4; (b) pr1 - pr4 .....	160
Figure 6-44: Overpressure and impulse reduction factors across the building envelope for configurations M3 (GWC front) and M1 ( $n_{post} = 8$ ) (a) overpressure reduction $F_p$ ; (b) impulse reduction $F_i$ .....	162

## List of Tables

Table 3-1: TNT equivalence factors for PETN based on heat of detonation.....	36
Table 3-2: TNT equivalence factors for PETN based on velocity of detonation.....	37
Table 3-3: TNT equivalence factors for PETN based on specific energy.....	37
Table 3-4: TNT equivalence factors for PETN based on Berthelot, power index and hydrodynamic work methods .....	38
Table 3-5: TNT equivalence factors for PETN derived from laboratory tests.....	38
Table 3-6: TNT equivalence factors for PETN derived from field tests.....	41
Table 4-1: Material parameters of the strength model for high explosive material PETN and TNT ( <i>Dobratz and Crawford 1985</i> ) .....	63
Table 4-2: Material parameters of the EoS for high explosive material PETN and TNT ( <i>Dobratz and Crawford 1985</i> ) .....	63
Table 4-3: Material parameters of the structural material (steel).....	64
Table 4-4: Comparison of three modelling strategies .....	76
Table 5-1: Overview of the experimental series .....	78
Table 5-2: Statistics of experimental data at gauges ps1 ( $R = 4\text{m}$ , $h = 1\text{m}$ ).....	89
Table 5-3: Statistics of experimental data at gauges ps2 - ps4 and pr1 - pr4, M1 (GWC back) .....	90
Table 5-4: Statistics of experimental data at gauges ps2 - ps4 and pr1 - pr4, M2 (GW).....	90
Table 5-5: Statistics of experimental data at gauges ps2 - ps4 and pr1 - pr4, M3 (GWC front) .....	90
Table 5-6: Statistics of experimental data at gauges ps1 ( $R = 4\text{m}$ , $h = 0.63\text{m}$ ).....	101
Table 5-7: Statistics of experimental data at gauges ps2 - ps4 and pr1 - pr4, Mref (no posts) .....	102
Table 5-8: Statistics of experimental data at gauges ps2 - ps4 and pr1 - pr4, M1 ( $n_{post} = 8$ )	102
Table 5-9: Statistics of experimental data at gauges ps2 - ps4 and pr1 - pr4, M2 ( $n_{post} = 5$ )	103
Table 5-10: Statistics of experimental data at gauges ps2 - ps4 and pr1 - pr4, M3 ( $n_{post} = 6$ ) .....	103
Table 6-1: Comparison of the computational time in the mesh convergence study .....	117
Table 6-2: Barrier combinations .....	157

# 1 Introduction

This Dissertation contributes to the topic of the effectiveness of protective barriers against air blast. Whilst extensive research has been conducted on ordinary protective barriers (e.g. reinforced concrete walls), non-conventional barriers (e.g. blast walls with a canopy on top, protective barriers made of steel posts) have been comparatively seldom investigated in the open literature. Therefore, this Dissertation aims to shed light on this matter.

## 1.1 Motivation

In the past few years, the need for blast-resistant design has been arisen due to the frequent terrorist attacks with explosive devices, e.g. 24<sup>th</sup> July 2016 in Ansbach, 22<sup>nd</sup> May 2017 in Manchester and 15<sup>th</sup> September 2017 in London. Nowadays, the protection of military and civilian buildings from terrorist threats has become one of the most important tasks to structural researchers.

The structural design process of buildings against air blast requires an accurate prediction of the blast loads (overpressure-time histories and impulse-time histories) at the building envelope. In order to protect buildings and their occupants that may be subjected to an explosion, protective barriers are often erected around buildings serving as perimeter protection. If a shock wave hits the protective barrier, firstly, a part of the shock wave is reflected back by the front face of the barrier. Secondly, if a barrier or one of its components is flexible such that it undergoes deformation, a certain amount of blast energy can be absorbed by the barrier. Thirdly, a part of the shock wave is diffracted by the barrier. Fourthly, the shock wave may be partly transmitted through the permeable surface of the barrier or through the openings within the barrier. Consequently, a combination of energy reflection, absorption, diffraction and transmission reduces the blast loads in a certain region behind the barrier. The distribution of blast loads from explosions in a free field is well understood, e.g. by the empirical formulae of *Kingery and Bulmash 1984* and *Kinney and Graham 1985*, by the design charts of *UFC 3-340-01* and *UFC 3-340-02* as well as by the software *ConWep (Hyde 1988)*, *DYNA2D/DYNA3D (Randers-Pehrson and Bannister 1997)* and *EUROPLEXUS (Larcher 2008)*. However, only limited information is available on the blast loads behind non-conventional barriers (e.g. staggered, shaped, open surface), especially if the barrier or parts of it do not behave rigidly or if the barrier has a surface containing openings.

Therefore, it is crucial to understand the process of shock wave propagation when barriers are erected between the conceivable charge and the building to be protected. This Dissertation aims to shed light on how protective barriers should be blast-resistant designed in order to achieve high performance in attenuating the shock wave.

Firstly, experiments were conducted to gain understanding of the complex physical phenomena involved in the process of shock wave propagation and hence to analyse the effectiveness of protective barriers. Secondly, numerical simulations were carried

out in this Dissertation in order to complement the experiments. They were validated against the experimental data and then employed to carry out parametric studies in order to determine the parameters, which play a key role in the effectiveness of protective barriers. Such investigations would be impractical and unrealistic to be done experimentally.

Through the experimental and numerical results, this Dissertation aims to provide contributions to the evaluation of the effectiveness of protective barriers against air blast, which is expressed in terms of overpressure and impulse reduction.

### 1.2 Layout of the thesis

The aim of this Dissertation is to develop a comprehensive method to evaluate the effectiveness of protective barriers against air blast. The following three chapters introduce the background of the experiments and the numerical simulations, whose results are then analysed and discussed in the main part of this Dissertation, Chapter 5 and 6. In the end, Chapter 7 closes this Dissertation with conclusions and outlooks.

Chapter 2 reviews the blast walls and the barriers containing openings. Both rigid and flexible blast walls are discussed. Regarding the barriers containing openings, the interaction between the shock wave and the solid obstacles is discussed. Finally, the shock wave trapping concept is briefly explained.

In Chapter 3, the shock wave propagation phenomenon is described. Firstly, basic parameters of shock waves are introduced and different forms of overpressure-time histories are depicted and compared. Secondly, three fundamental principals in the field of air blast, i.e. Hopkinson-Cranz scaling law, Sachs scaling law and TNT equivalence, are described. Thirdly, the diffraction process is briefly explained. After that, the drag coefficient and the clearing effect are introduced and briefly depicted. Lastly, three different types of burst are discussed.

Chapter 4 provides information regarding the numerical simulations conducted in this Dissertation. On the one hand, the basic aspects of numerical simulations, i.e. material models, time step control, element formulations, mapping techniques and Fluid-Structure-Interaction (FSI) algorithms, are explained. On the other hand, three numerical modelling strategies and their application to the numerical problems of this Dissertation are compared and discussed in the end.

Chapter 5 describes the experimental configurations, instrumentation and data for two experimental series, blast walls with a canopy on top and protective barriers made of steel posts. At first, a plausibility analysis is carried out to assess the quality of the data recorded in the experiments. After that, statistics of the experimental data at the gauges, i.e. mean values, standard deviations and coefficients of variation, are calculated. Lastly, the experimental data is evaluated, regarding the overpressure and impulse reduction.

In Chapter 6, numerical investigations are conducted for both types of protective barriers. At first, the influences of the ambient conditions (altitude and atmospheric temperature) and the charge height above the ground on the blast loads are

investigated. Then, the numerical models are verified by the empirical formulae and validated against the experimental data. After that, numerical results of overpressure-time histories are presented and the shock wave propagation is visualized. In addition, the influences of the clearing effect of shock waves and the structural flexibility on the blast loads are discussed. Furthermore, the effectiveness of protective barriers in terms of overpressure and impulse reduction is evaluated. Moreover, parametric studies are carried out in order to gain more insight into the effectiveness of protective barriers. At the end of this chapter, both barrier types involving in this Dissertation are compared regarding the mechanism of shock wave propagation, the aesthetical attractiveness and the performance in attenuating the shock wave.

Chapter 7 closes this Dissertation by drawing key conclusions from this research and giving recommendations for future work.

## 2 Protective barrier overview

The protection measures can be categorized into active and passive protection measures (*Krauthammer 2017*). In the former, measures, e.g. interception of the ordnance and suppression of the blast effects, are used to reduce the magnitude of blast loads. In the latter, measures are employed either to enhance the resistance of the building to be protected or to reduce the magnitude of the blast loads. In order to enhance the resistance of the building, one can use stronger structural elements, e.g. innovative materials, dimensions and detailing. In order to mitigate the blast loads, one can try to increase the stand-off distance from the charge to the building or to shield the building, e.g. by protective barriers. In this sense, protective barriers belong to a passive protection measure. It is well known that protective barriers are an effective protective structure to reduce blast loads and to mitigate consequences. On the one hand, they increase the stand-off distance between the conceivable explosive source and the building. On the other hand, they act as obstacles to disrupt the shock wave propagation. If properly designed they can also act as barriers in order to stop vehicles. The following sections give a review on the rigid and flexible blast walls (Section 2.1) as well as barriers with openings (Section 2.2).

### 2.1 Blast walls

Research interest in the blast wall effectiveness started as long ago as World War II and has continued ever since. Solid blast walls have shown their performance in resisting blast loads if the stand-off distance between the charge and the wall is relatively small. Solid blast walls are usually made of reinforced concrete (RC), concrete masonry unit (CMU) or steel-concrete-steel (SCS) composite materials. The blast wall could also be a composite wall composed of sand between two reinforced concrete walls connected by shear diaphragms or a solid reinforced concrete wall backed by a massive earth berm (“retaining wall”). In practice, blast walls are often so rigidly designed that their deformations are negligibly small. However, flexible barriers can also perform as well as rigid walls (*Rose et al. 1998, Bogosian and Piepenburg 2002, Gebbeken and Döge 2010a, Gebbeken et al. 2011 and Gebbeken et al. 2012*). Hence, rigid and flexible blast walls will be discussed in the following subsections.

#### 2.1.1 Rigid blast walls

In order to protect a building against terrorist attacks, a perimeter wall surrounding the building or its property is often proposed. The perimeter wall reduces the overpressures and impulses in a certain region behind the wall, and, therefore, if a building is placed behind, it may benefit from this blast load reduction. It should be noted that the perimeter wall effectiveness depends on the relative position of the building with respect to the wall, the relative position of the wall with respect to the charge and the building geometry. It is well-known that a relatively distant and tall building, e.g. a multi-storey building, will hardly benefit from the presence of a

perimeter wall, especially in the upper storeys of the building. Regarding the overpressure and impulse reduction, various parameters of the wall and its distances to the charge and to the building are of interest. Most of the previous works, e.g. *Beyer 1986*, *Rose et al. 1993*, *Chapman et al. 1995a*, *Chapman et al. 1995b*, *Rose et al. 1995*, *Rose et al. 1997*, *Ngô et al. 2004* and *Zhou and Hao 2008*, were concerned with the basic parameters, such as charge mass, charge height above the ground, wall height, distance from the charge to the wall, distance from the wall to the point of observation and gauge elevation.

*Philip 1942* presented a method to calculate the blast loads (overpressure and impulse) behind a wall which were generated from an explosive charge in front of the wall. This method is based on empirical reduction factors, which are related to the sum of two angles describing the geometrical configuration of the wall (Figure 2-1). The first one is the angle  $\alpha$  formed by the line connecting the charge to the top of the wall and the horizontal. The second one is the angle  $\beta$  formed by the line jointing the top of the wall to the observation point on the building and the horizontal. These reduction factors are applied to the blast parameters calculated from the length of the shock wave propagation path, i.e. distance  $L_1$  from the charge to the top of the wall plus distance  $L_2$  from the top of the wall to the observation point on the building.

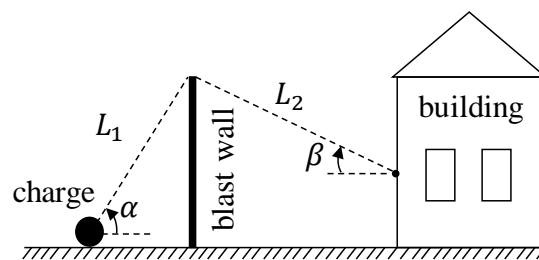


Figure 2-1: Empirical method of calculating the blast loads on the building presented by *Philip 1942*

*Whitham 1957* developed an analytical method to estimate the pulse shape of the shock wave diffracted around external corners. In order to apply this method to blast walls, two assumptions were made. Firstly, the incident shock front at the top of the wall is assumed vertical and plane. Secondly, the reflection of the shock wave from the ground surface has not yet occurred behind the wall. Consequently, this method is applicable for the shock waves that have propagated only a short distance behind the wall.

In the late 1970s, terrorists began to use high explosive devices in the Middle East and Northern Ireland. For this reason, an upsurge of investigation on the blast wall effectiveness was motivated. *Beyer 1986* presented preliminary design criteria for vertical cantilever blast walls (Figure 2-2a) and for blast walls having a canopy near the top of the wall facing the charge (Figure 2-2b). The experiments were carried out at a model scale of one-sixth. The experimental set-up is illustrated in Figure 2-2.

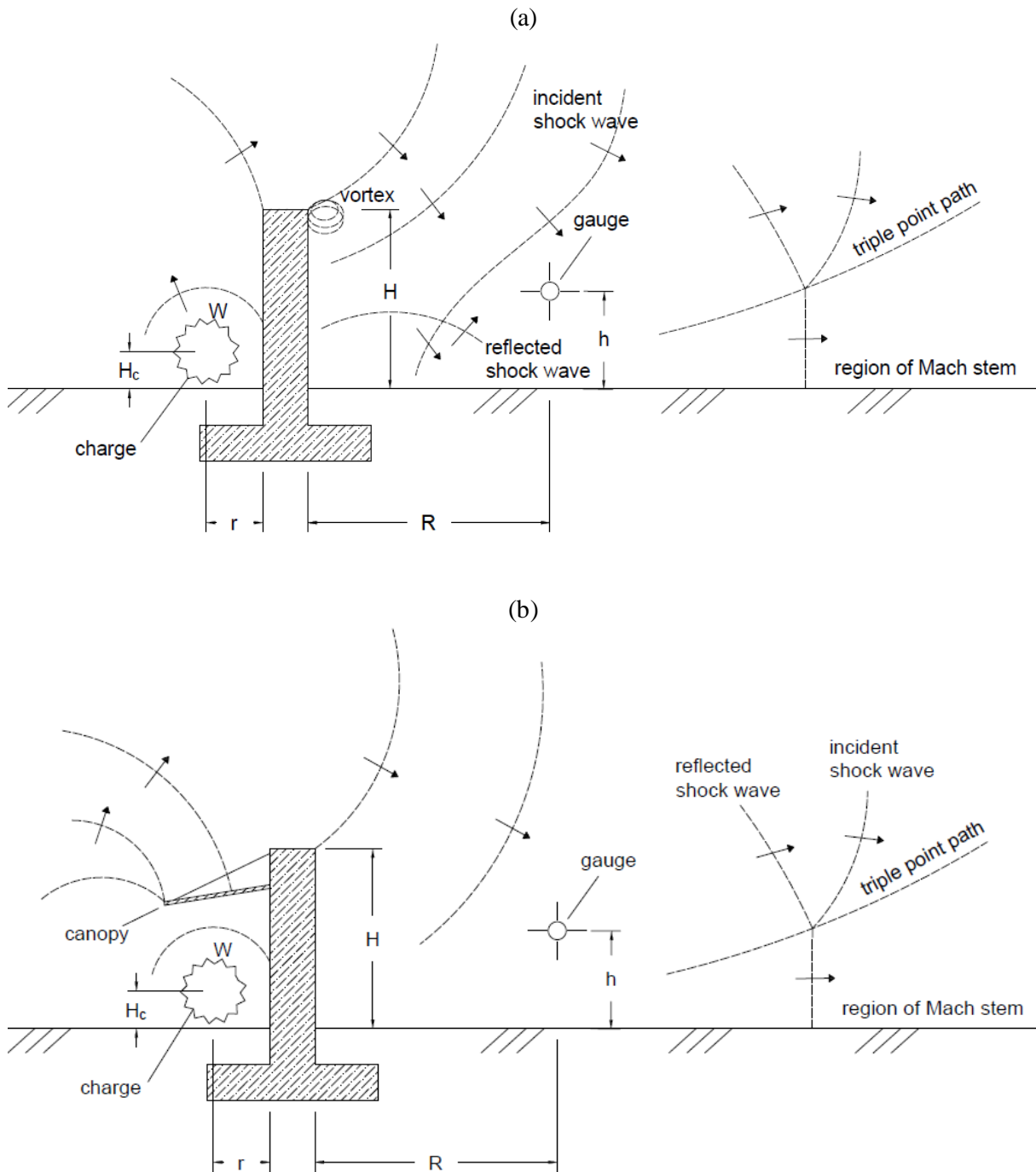


Figure 2-2: Experimental set-up used by *Beyer 1986* (a) vertical cantilever blast wall; (b) blast wall having a canopy near the top of the wall facing the charge

A charge was detonated at a small distance  $r$  in front of the wall to generate a shock wave. After a short time, the shock wave impinged the front face of the vertical wall. The wall was made of rigid reinforced concrete. The canopy was made of a steel sheet. Gauges located at various distances behind the wall were used to capture the side-on overpressure-time histories. Thus, the trajectories of different waves behind the wall can be schematically visualized, i.e. the incident shock wave flowing over the top of the wall, the wave reflected from the ground surface behind the wall as well as the Mach stem formed behind the wall by coalesce of the incident and reflected waves (Section 3.8.3).

The objective of this research was to express the blast parameters, i.e. peak side-on overpressure, maximum side-on impulse and positive phase duration, in terms of the parameters depicted in Figure 2-2, namely, charge mass  $W$ , charge height  $H_c$ , horizontal distance  $r$  from the charge to the wall, horizontal distance  $R$  from the wall to the gauge, gauge elevation  $h$  above the ground, wall height  $H$  and mass  $m$  of the canopy.

Due to the presence of the vertical cantilever wall (Figure 2-2a), the blast loads behind the wall are mitigated. In addition, they may be further mitigated by arranging a canopy (Figure 2-2b) near the top of the wall facing the charge since the canopy can also reflect a part of the shock wave back towards the charge. Although the canopy can shatter and be blown away by the shock wave, it would probably remain in place long enough to attenuate the shock wave. *Beyer 1986* indicated that the additional contribution of the canopy to the shock wave attenuation depended on its mass, surface area and location with respect to the vertical cantilever wall. However, no quantitative statement was made.

*Jones et al. 1987* conducted a series of experiments in order to gain a better understanding of the blast wall effectiveness. The experimental set-up is exemplarily illustrated in Figure 2-3. There were two objectives to these experiments. Firstly, it was to evaluate the benefit from the presence of a perimeter wall in terms of the overpressure and impulse reduction on the building behind the wall. Secondly, it was to inspect diverse perimeter wall designs. The perimeter wall was assumed rigid. A model scale of one-tenth was used. The charge was detonated at various distances from the building. The building envelope was represented by a rigid vertical wall, on which the reflected overpressure-time histories were measured.

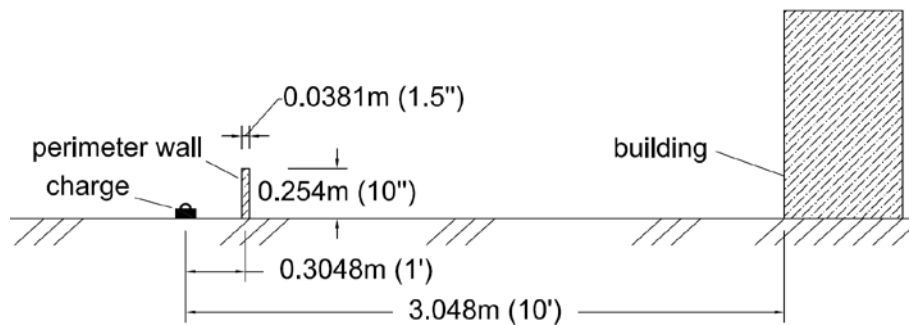


Figure 2-3: Experimental set-up used by *Jones et al. 1987*

*Mayor and Flanders 1990* employed the experimental data of *Jones et al. 1987* to derive empirical equations for overpressure and impulse reduction factors. It should be noted that these equations were not intended to precisely describe the process of the shock wave diffraction around the wall but to provide a guide for structural designers, which have only information about the distance from the charge to the building to be protected. It was assumed that the peak reflected overpressures and the maximum reflected impulses at the ground level were the same as those at height  $H$ . These equations are only valid if the observation point on the building is not in a direct line of sight to the charge. In addition, no information about the distance from the

charge to the wall is given. As a result, the correlation between these equations and the experimental data is poor.

The peak reflected overpressures on a building without a perimeter wall ( $p_{wo}$  in kPa) and with a perimeter wall ( $p_w$  in kPa) can be calculated as

$$p_{wo} = 1603.7 \left( \frac{R}{W^{1/3}} \right)^{-2.21}, \quad (2-1)$$

$$p_w = 177.7 \left( \frac{R}{W^{1/3}} \right)^{-1.57}, \quad (2-2)$$

where  $R$  (in meters) is the distance from the charge to the building.  $W$  is the charge mass in TNT equivalent.

Similarly, the maximum reflected impulse without a perimeter wall ( $i_{wo}$  in kPa·ms) and with a perimeter wall ( $i_w$  in kPa·ms) can be specified as

$$i_{wo} = 19.3 \left( \frac{R}{W^{1/3}} \right)^{-0.977} W^{1/3}, \quad (2-3)$$

$$i_w = 7.4 \left( \frac{R}{W^{1/3}} \right)^{-0.822} W^{1/3}. \quad (2-4)$$

Comparing the two pairs of equations for the overpressure and impulse, the overpressure and impulse reduction factors ( $F_p$  and  $F_i$ ) can be readily expressed as

$$F_p = 1 - \frac{p_w}{p_{wo}} = 1 - 0.1108 \left( \frac{R}{W^{1/3}} \right)^{0.64}, \quad (2-5)$$

$$F_i = 1 - \frac{i_w}{i_{wo}} = 1 - 0.3834 \left( \frac{R}{W^{1/3}} \right)^{0.155}. \quad (2-6)$$

According to *Mayor and Flanders 1990* (Eq. (2-5) and Eq. (2-6)), Figure 2-4 depicts the dependence of the overpressure and impulse reduction factors on the scaled distance  $Z$  (Eq. (3-1)), which is defined as  $Z = R/W^{1/3}$ . It is observed in Figure 2-4 that the erection of a perimeter wall between the charge and the building significantly reduces the blast loads on the building.

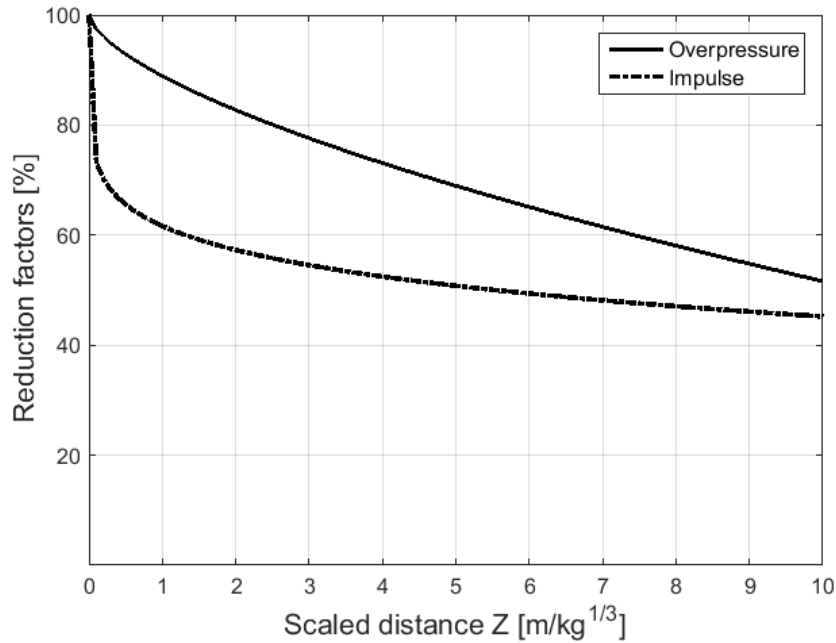


Figure 2-4: Overpressure and impulse reduction factors according to *Mayor and Flanders 1990*

Due to the terrorist attacks on a range of conventional buildings in Northern Ireland, research interest in the blast wall effectiveness was prompted in the United Kingdom. With the project ‘Leakage pressures behind blast walls’, which was sponsored by the United Kingdom Ministry of Defence (MoD), the Defence Academy of the United Kingdom started the research on this field. ‘Leakage’ in the title of the project denotes the shock wave that flows over the top of the wall into the region behind the wall.

*Rose et al. 1993* and *Rose et al. 1995* described a research programme, in which detailed pressure measurements were made behind a one-tenth scaled vertical blast wall (Figure 2-5). The objective of this research was to accurately evaluate the blast loads behind vertical walls. The charges were detonated in front of a rigid blast wall. A specific measurement region was established behind the wall, i.e. six times the wall height horizontally (x-direction) and three times the wall height vertically (y-direction). Regarding a wall height of 3m, this region was considered to be the most important area of interest.

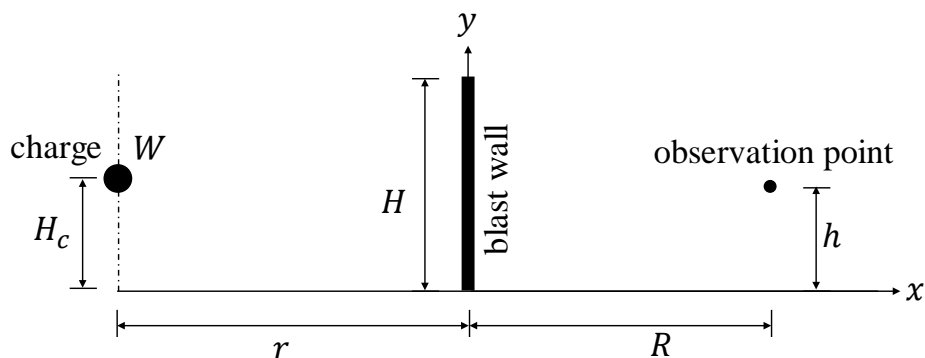


Figure 2-5: Experimental set-up used by *Rose et al. 1993* and *Rose et al. 1995*

**Chapter 2 - Protective barrier overview**

Based on the measured overpressure-time histories, contour plots of the side-on overpressures and impulses were developed. Figure 2-6 shows exemplarily the contour plots of the peak side-on overpressures ( $p_{so}$  in kPa) in the measured region for the experiments without and with a blast wall. The results are given as the natural logarithm and shown on special axes which are marked at intervals of the wall height  $H$ .

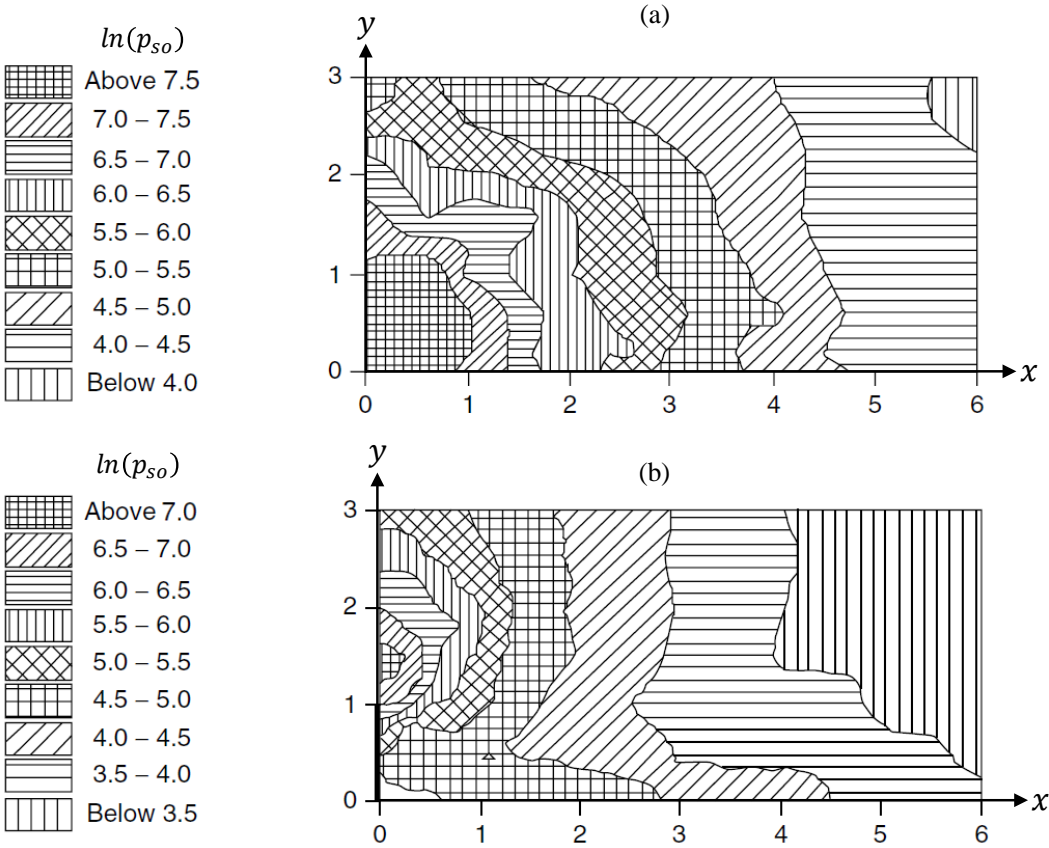


Figure 2-6: Contour plots of the peak side-on overpressures ( $p_{so}$  in kPa) given as the natural logarithm (a) without a wall and (b) with a wall

The benefit from the presence of a blast wall can be evaluated by comparing the contour plots of the overpressures and impulses from two sets of experiments, i.e. with and without a blast wall. In general, the shielding effect of the blast wall against air blast diminishes if the distance from the building to the blast wall increases. The authors concluded that the protected region can be defined to a distance of about three times the wall height behind the wall. However, this still also depends on the distance from the charge to the wall.

*Rose et al. 1997* conducted an extensive research program to the previous work in 1993 and 1995. The influences of the geometrical parameters, i.e. wall height  $H$ , horizontal distance  $r$  from the charge to the wall, horizontal distance  $R$  behind the wall and gauge height  $h$ , as well as charge mass  $W$  on the blast loads behind the wall were investigated. The aim of this research was to develop a series of design charts that were of assistance to the structural engineers in designing blast walls having high performance in blast load mitigation. Figure 2-7 shows an example of these design charts.

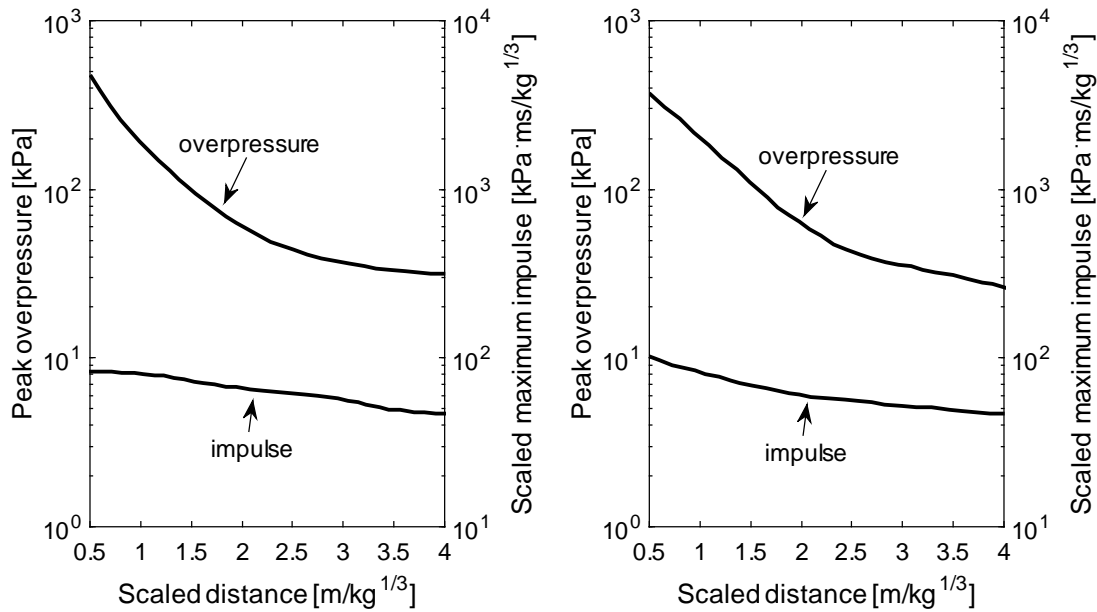


Figure 2-7: Typical design charts for peak overpressure (top curve) and scaled maximum impulse (bottom curve),  $H/W^{1/3} = 0.5\text{m/kg}^{1/3}$ ,  $r/W^{1/3} = 0.327\text{m/kg}^{1/3}$   
 (a)  $h/W^{1/3} = 1.0\text{m/kg}^{1/3}$ ; (b)  $h/W^{1/3} = 1.5\text{m/kg}^{1/3}$

Based on the work of *Rose et al. 1997*, notably the studies to explore the effect of the scaled distance  $r/W^{1/3}$  from the charge to the wall and the scaled wall height  $H/W^{1/3}$  on the blast loads behind the wall, the program DESIGN was complemented. The program DESIGN requires three quantities as input, namely, charge mass  $W$ , wall height  $H$  and horizontal distance  $r$  from the charge to the wall. An output file will be generated, in which the values of peak side-on overpressures and maximum side-on impulses are calculated for different values of the horizontal distance  $R$  behind the wall and the gauge height  $h$  above the ground.

Figure 2-8 shows a plane wall (Figure 2-8a) and a mounded revetment (Figure 2-8d) as well as two walls with different canopy arrangements. The first one (Figure 2-8b) is inclined at  $45^\circ$  with respect to the horizontal and the second one (Figure 2-8c) is horizontal. Both canopies are oriented facing the charge. The overall height of both walls having a canopy is the same as that of the plane wall, denoted as  $H$ . The effect of canopy arrangements on the blast loads behind the wall was examined (*UFC 3-340-01*). It was indicated that the blast wall having an inclined canopy provided some, though relatively small, additional mitigation in the blast loads compared to the plane wall. A marginal improvement was offered by the wall having a horizontal canopy compared to the wall having a canopy inclined at  $45^\circ$  with respect to the horizontal. It should be mentioned that these outcomes were valid for rigid walls. If the wall deflects during the blast load pulse, a part of the blast energy is absorbed by the deflection of the wall. In addition, the connection between the vertical wall and the canopy might further enhance the blast wall effectiveness, since a certain amount of the blast energy is absorbed by the formation of plastic hinges at the connection. In order to enhance the blast wall effectiveness, the wall should be placed at a relatively short distance

from the charge. Thus, the shock wave is intercepted in the early phase of the propagation process.

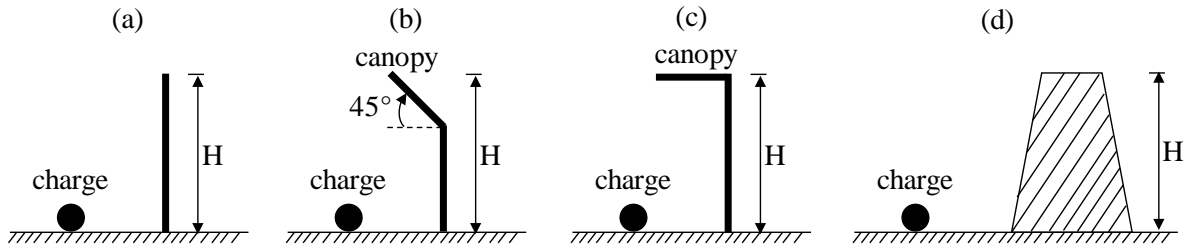


Figure 2-8: Blast wall and revetment configurations (a) plane wall; (b) blast wall having an inclined canopy, angle of inclination 45°; (c) blast wall having a horizontal canopy; (d) mounded revetment

Figure 2-9 and Figure 2-10 illustrate the peak overpressures and the scaled maximum impulses behind blast walls and revetments (*UFC 3-340-01*). Peak overpressure and maximum impulse at height H are somewhat lower than the ones at the ground level. As indicated in Figure 2-9, the peak overpressure behind a wall varies with the blast wall configurations, where mounded means a revetment with sloping front and rear faces (Figure 2-8d). The amount of blast load mitigation depends principally on the scaled height  $H/W^{1/3}$  and the shape of the wall or revetment. Mounded revetments have the minimum mitigation effect on the blast loads. In general, the peak overpressures near the wall on the side opposite the charge are significantly reduced, but they gradually approach the values of a free-field scenario, as the distance behind the wall increases (Figure 2-9).

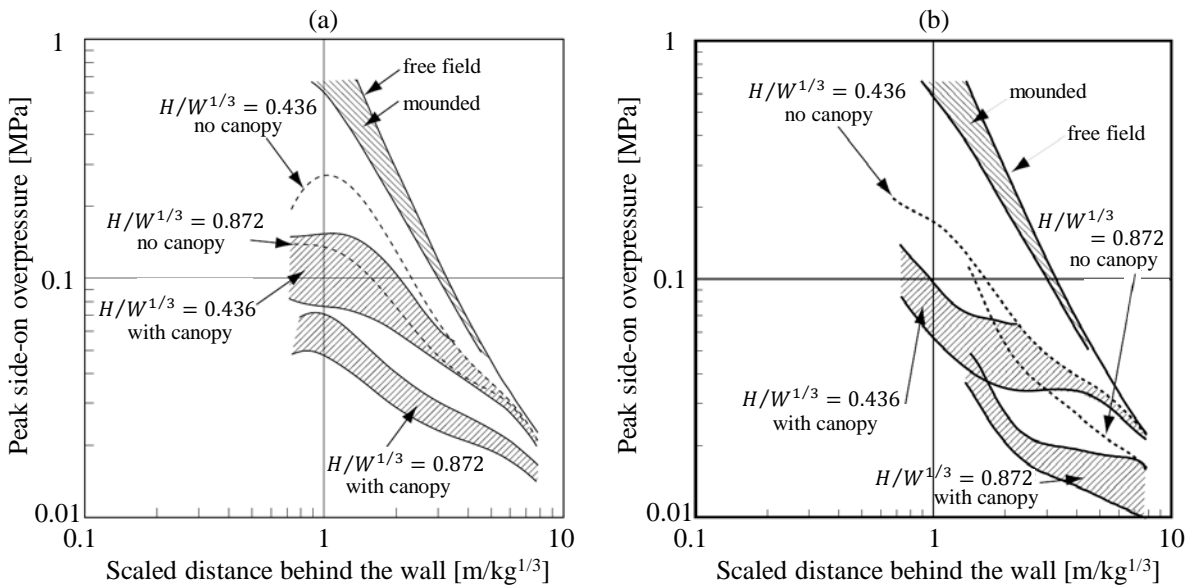


Figure 2-9: Peak overpressures behind blast walls and revetments (a) at the ground level; (b) at height H

Compared to the plane wall configuration, the canopy arrangements further reduce the peak overpressure behind the wall (Figure 2-9). The impulse reduction behind the wall

is similar but less dramatic than the overpressure reduction (Figure 2-10). The maximum impulse at height  $H$  (Figure 2-10b) is reduced to less than half of the free field values near the wall, where the maximum impulse remains essentially constant with the range, then joins the free field value at large distances. The amount of the impulse reduction depends also on the scaled wall height  $H/W^{1/3}$ . The maximum impulse at height  $H$  is reduced more significantly than at the ground level. The arrangement of a canopy further reduces the maximum impulse behind the wall, compared to the plane wall.

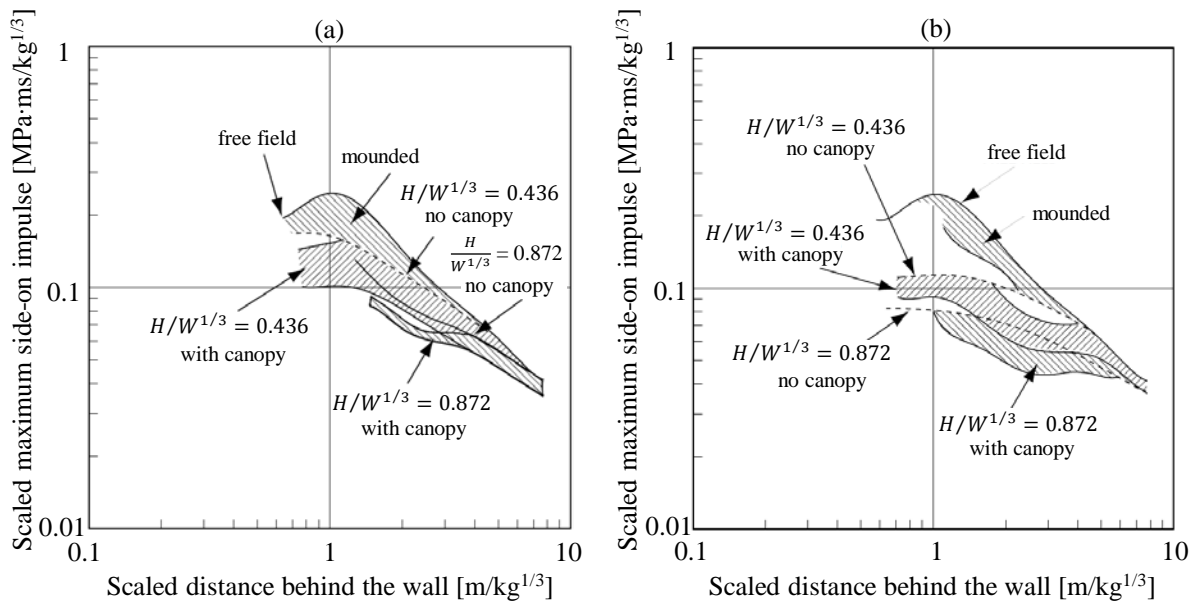


Figure 2-10: Scaled maximum impulse behind blast walls and revetments (a) at the ground level; (b) at height  $H$

*Chapman et al. 1995a* modified the experimental set-up used by *Rose et al. 1993* and *Rose et al. 1995* to take account of a vertical target structure (Figure 2-11). The target structure was located at distance  $R$  behind the blast wall of height  $H$ . This analysis assumed that all reflecting surfaces were perfectly rigid and the thickness of the blast wall was supposed to be negligibly small. A series of small-scale (approximately 1:10) experiments were conducted. To measure the reflected overpressure, four pressure gauges were embedded in a vertical array on the centre line of the target structure at heights (denoted as  $H_t$ ) of 150mm, 300mm, 450mm and 600mm, respectively. A charge mass  $W$  was detonated at height  $H_c$  above the ground and at distance  $r$  from the blast wall. To keep the study as simple as possible, the blast wall height  $H$  ( $H = 300\text{mm}$ ) and the gauge configuration were kept constant during the experiments. The objective of this research was to derive the relationship between the blast loads on the target structure and the important variables that were vital to predict the blast loads, i.e. the charge mass  $W$  and the parameters describing the geometrical configuration of the blast wall and the target structure ( $r$ ,  $R$ ,  $H_c$ ,  $H$  and  $H_t$ )

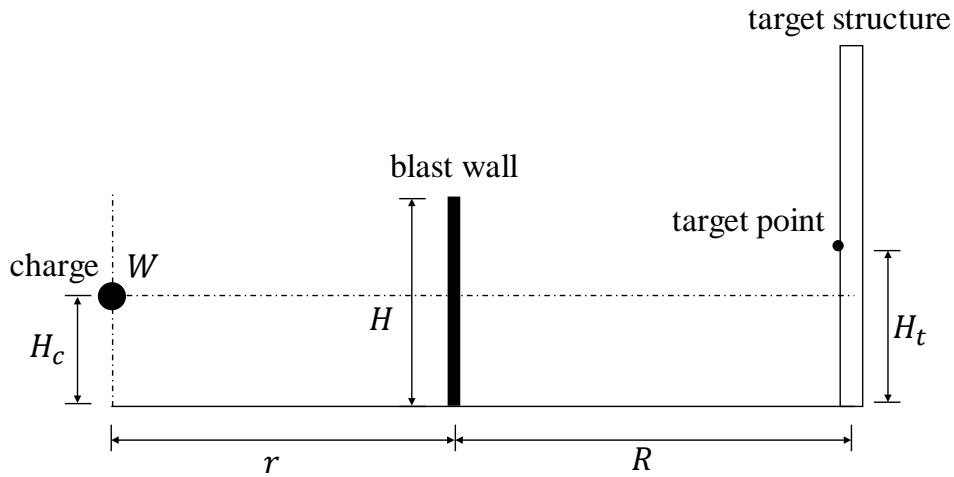


Figure 2-11: Experimental set-up used by *Chapman et al. 1995a*

Based on the measured reflected overpressure-time histories at the gauges on the target structure, peak reflected overpressures and maximum reflected impulses were assessed. *Chapman et al. 1995a* proposed a modified scaled distance  $Z_m$  to account for relevant parameters pertaining to the blast wall and the target structure, given as

$$Z_m = Z_H \frac{H}{H_c + H_t}, \quad (2-7)$$

where  $Z_H$  is the scaled horizontal distance from the charge to the target structure,  $Z_H = (r + R)/W^{1/3}$ .

Thus, the peak reflected overpressure and the maximum reflected impulse can be expressed as a function of  $Z_H$ ,  $H$ ,  $H_c$  and  $H_t$ , leading to

$$p_r = f\left(Z_H, H, \frac{1}{H_c}, \frac{1}{H_t}\right), \quad (2-8)$$

$$i_r = g\left(Z_H, H, \frac{1}{H_c}, \frac{1}{H_t}\right). \quad (2-9)$$

To seek a better correlation to  $Z_m$ , the peak reflected overpressure  $p_r$  is transformed to the quantity  $p_f$ , which has units of kPa/m and is given by

$$p_f = \frac{p_r(H_c + H_t)}{(r + R)H}. \quad (2-10)$$

Figure 2-12a shows a log-log plot of the factored scaled peak reflected overpressure  $p_f$  versus the modified scaled distance  $Z_m$ .

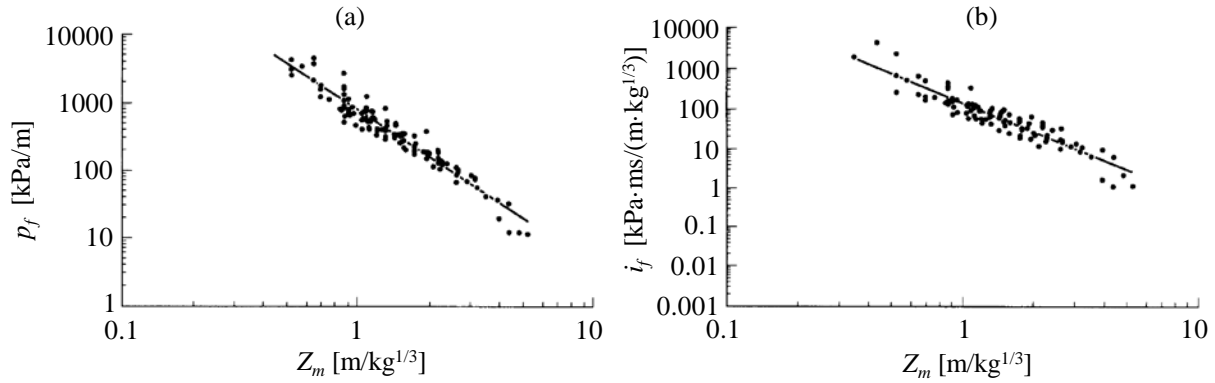


Figure 2-12: Factored quantities versus modified scaled distance  $Z_m$  (a) peak reflected overpressure  $p_f$ ; (b) scaled maximum reflected impulse  $i_f$

Applying the least-squares method of linear regression, the line of best fit was computed. The associated equation is given by

$$p_f = 10^{2.881} Z_m^{-2.363}. \quad (2-11)$$

Similarly, the scaled maximum reflected impulse is transformed to the quantity  $i_f$  which has units of  $\text{kPa}\cdot\text{ms}/(\text{m}\cdot\text{kg}^{1/3})$  and is given by

$$i_f = \frac{i_r(H_c + H_t)}{(r + R)HW^{1/3}}. \quad (2-12)$$

Figure 2-12b shows the factored scaled maximum reflected impulse  $i_f$  plotted against the modified scaled distance  $Z_m$ . Using the least-squares method of linear regression, the line of best fit was derived. The associated equation is given by

$$i_f = 10^{2.155} Z_m^{-2.399}. \quad (2-13)$$

To complement the experimental work by *Chapman et al. 1995a*, *Chapman et al. 1995b* carried out two-dimensional axisymmetric numerical simulations, in which the interaction between the shock wave and the blast wall was modelled. The numerical results showed a good agreement with the experimental results presented in *Chapman et al. 1995a*.

An important question that is often raised in connection with the blast wall effectiveness is how long the wall should be so that no air flows around the sides of the wall. In other words, when can a wall be considered as effectively semi-infinite. A wall is denoted as semi-infinite if it has an effectively infinite dimension in the out-of-plane direction (*Rose 2001*). However, there is no straightforward answer to this question. Figure 2-13 illustrates the horizontal air flow around the sides of the wall and the vertical air flow over the top of the wall. It is assumed that the wall thickness is much smaller than the width and height of the wall. Hence, the wall thickness is negligible in the calculation of the length of the shock wave propagation. A wall is

considered as effectively semi-infinite if the horizontal air flow around the sides of the wall can be neglected. This means that the magnitude of overpressure generated by the horizontal air flow is negligibly small compared to that generated by the vertical air flow.

Regarding a height-of-burst detonation (Section 3.8.3) depicted in Figure 2-13, the magnitude of overpressure at the gauge, which is elevated at a height of  $h$  above the ground, depends on the charge mass  $W$ , charge height  $H_c$  and length  $d$  of the shock wave propagation from the charge centre to the gauge. For the horizontal air flow around the sides of the wall, the length  $d_h$  of the shock wave propagation is given as

$$d_h = d_{h,1} + d_{h,2} = \sqrt{r^2 + \left(\frac{B}{2}\right)^2 + \left(\frac{H_c - h}{2}\right)^2} + \sqrt{R^2 + \left(\frac{B}{2}\right)^2 + \left(\frac{H_c - h}{2}\right)^2}, \quad (2-14)$$

whereas the length  $d_v$  of the shock wave propagation for the vertical air flow over the top of the wall is given as

$$d_v = d_{v,1} + d_{v,2} = \sqrt{r^2 + (H - H_c)^2} + \sqrt{R^2 + (H - h)^2}. \quad (2-15)$$

If the ratio  $p_h/p_v$  of overpressures which are caused by the horizontal and vertical air flow is appreciably smaller than unity, i.e.  $p_h/p_v \ll 1$ , the wall can be regarded as effectively semi-infinite. The overpressures  $p_h$  and  $p_v$  depend on the charge mass  $W$ , the charge height  $H_c$  and the respective length of the shock wave propagation ( $d_h$  and  $d_v$ ). In this sense, whether a wall can be considered as effectively semi-infinite or not, it depends on the charge mass  $W$ , the charge height  $H_c$ , the wall height  $H$ , the distance  $r$  from the charge to the wall, the distance  $R$  from the wall to the observation point and the elevation  $h$  of the observation point above the ground.

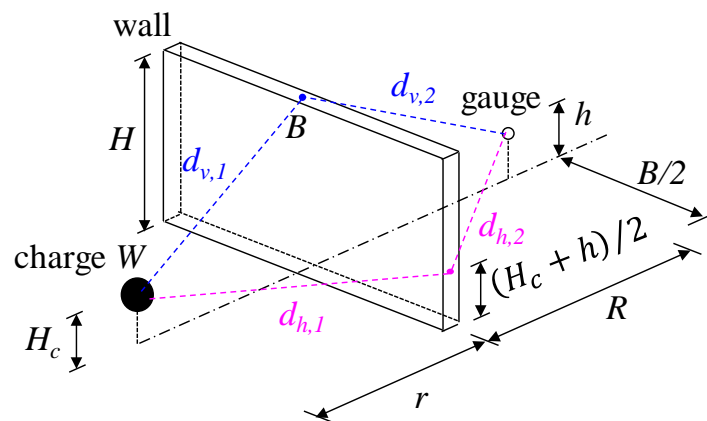


Figure 2-13: Air flows around the sides and over the top of the wall

It is worth mentioning that all the blast walls considered in the studies of Rose et al. and Chapman et al. are assumed as semi-infinite. This means that the shock wave diffracted around the sides of the wall is neglected.

Research on the blast wall effectiveness in attenuating the shock wave is being complemented by both experimental and numerical studies. Due to the availability of powerful computing resources, numerical simulations which account for the interaction between the shock wave and the blast wall become increasingly attractive.

*Ngo et al. 2004* carried out parametric studies to evaluate the blast wall effectiveness. A charge mass of 800kg TNT equivalent was used. The blast wall was composed of a 300mm thick reinforced concrete wall with 1% reinforcement ratio. The influences of the distance from the charge to the wall and the wall height on the blast wall effectiveness were explored. The wall was modelled as either a rigid wall or a flexible wall. The interaction between the shock wave and the blast wall was modelled via the Fluid-Structure-Interaction (FSI) algorithm. The numerical results showed that the blast loads on the flexible wall were approximately 5% less than on the rigid wall. To provide an insight into the complex air flow (e.g. vortex) around the blast walls, visualizations obtained from numerical simulations were analysed. It was found that, if the distance from the charge to the wall was small, the peak overpressures at the front face of the building were significantly reduced. This effect was more pronounced in the lower storeys of the building than in the upper ones. As the distance from the charge to the wall increases, the overpressure reduction on the building diminishes. This is because the region on the building shielded by the blast wall diminishes as the distance from the charge to the wall increases (Figure 2-14).

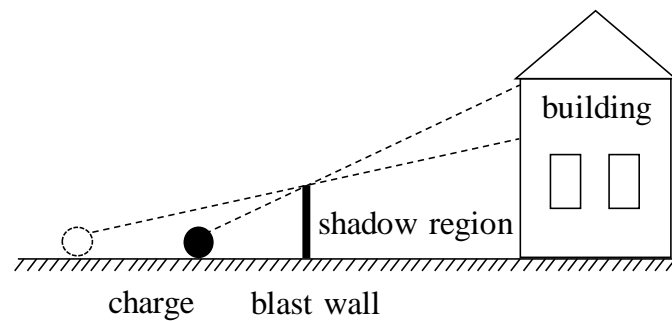


Figure 2-14: Shadow region provided by a blast wall

*Zhou and Hao 2008* conducted three-dimensional numerical simulations to derive pseudo-analytical formulae, by which the reflected overpressure-time history on the building behind a blast wall can be calculated. In order to simplify the evaluation process of the blast loads (overpressure and impulse) on the building, the modification factors for the overpressure and impulse ( $A_p$  and  $A_i$ ) were introduced. They are given as

$$A_p = \frac{p_{with\ barrier}}{p_{no\ barrier}}, \quad (2-16)$$

$$A_i = \frac{i_{with\ barrier}}{i_{no\ barrier}}, \quad (2-17)$$

where  $p_{with\ barrier}$  and  $i_{with\ barrier}$  are the peak overpressure and the maximum impulse on the building when a barrier is present.  $p_{no\ barrier}$  and  $i_{no\ barrier}$  are the peak overpressure and the maximum impulse on the building at the ground level when no barrier is present. The values of  $p_{no\ barrier}$  and  $i_{no\ barrier}$  were calculated by the empirical formulae of *UFC 3-340-02*. Multiplying with the modification factors ( $A_p$  and  $A_i$ ), the peak reflected overpressure and the maximum reflected impulse distributed on the building behind a barrier can then be calculated. The derivation of the formulae for  $A_p$  and  $A_i$  were based on the best-fit curves to the numerical results. These formulae were expressed in terms of the determining parameters that affected the blast loads behind the barrier (Figure 2-15). They are charge mass  $W$ , distance  $r$  from the charge to the wall, distance  $D$  from the charge to the building, blast wall height  $H$ , building height  $H_B$  and gauge height  $h$ .

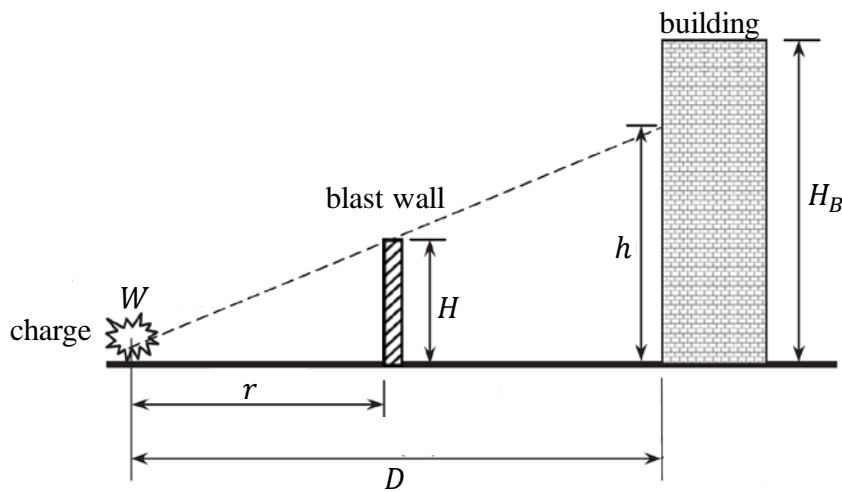


Figure 2-15: Blast wall configuration used by Zhou and Hao 2008

Only hemi-spherical surface bursts were considered in this study. Both the wall and the building were regarded as rigid structures. If the wall was placed very close to the charge, the resulting blast loads may destroy the wall. Under such circumstances, debris of the wall are generated and they may strike the building. This effect was not considered in this study. However, it may become a source of casualties and should be a subject of further studies.

*Gebbeken and Döge 2008* and *Gebbeken and Döge 2010a* presented different possibilities to protect buildings against air blast, in which the influence of the urban environment was taken into account. The authors showed that blast walls performed better than sloped terrains in protecting the buildings. In addition, the authors implied that the construction of hardened buildings does not necessarily mean that the buildings and the structural elements must be extremely massive.

*Smith 2010* reviewed the studies concerning the blast wall performance and the improvements in the blast-resistant design. It was recognized that it was not necessary for a blast wall to remain intact to provide protection, as long as it remained in place during the blast load pulse. But this strategy has to be changed due to the fact that multiple attacks took place at recent attacks.

In total, there are four different empirical procedures to predict the blast loads behind a wall, namely

- preliminary design curves provided by *Beyer 1986*,
- empirical formulae of *Mayor and Flanders 1990* and the associated program DESIGN,
- design charts provided by *Rose et al. 1997*,
- pseudo-analytical formulae of *Zhou and Hao 2008*.

It should be noted that each procedure has its own region of validity, which has already explained afore in this section.

### 2.1.2 Flexible blast walls

Ordinary blast walls are most likely to be rigid, massive and of strong construction. In addition, the construction cost of ordinary rigid blast walls is usually prohibitive. However, flexible blast walls can also perform as well as rigid walls (*Rose et al. 1998* and *Bogosian and Piepenburg 2002*).

Barriers of limited robustness were experimentally investigated by *Rose et al. 1998*. The considered wall were designed to be only so stiff that the wall remained in place during the blast load pulse. Such walls were classified as partially falling. This means that the blast loads inflict a certain level of damage to the wall and the wall remains no longer intact after the passage of the shock wave. In other word, they are partially or completely failed after the passage of the shock wave. It is worth noting that partial or complete failure of the walls should not produce fragments that could inflict damage to the building to be protected and hurt its occupants. The resistance of such blast walls was offered by either mass or strength. Materials, such as plain sand, polymer sheets, wood, water and ice, were involved. Figure 2-16 compares exemplarily the peak overpressures on the ground at different distances behind the steel wall (*Rose et al. 1995*), the water and ice walls (*Rose et al. 1998*). It is found that all these three types of blast walls mitigate the blast loads behind the wall, compared to those of a free field scenario when no wall is present. Finally, the authors concluded that flexible blast walls could provide as high degree of the shock wave attenuation as rigid blast walls. Thus, it was not always necessary to erect a blast wall that remained essentially undeforming during the blast load pulse. The shock wave interacts with the wall and flows over the top of the wall, as long as the wall remains in place during this process, the blast loads in the shadow region (Figure 2-14) behind the wall are reduced.

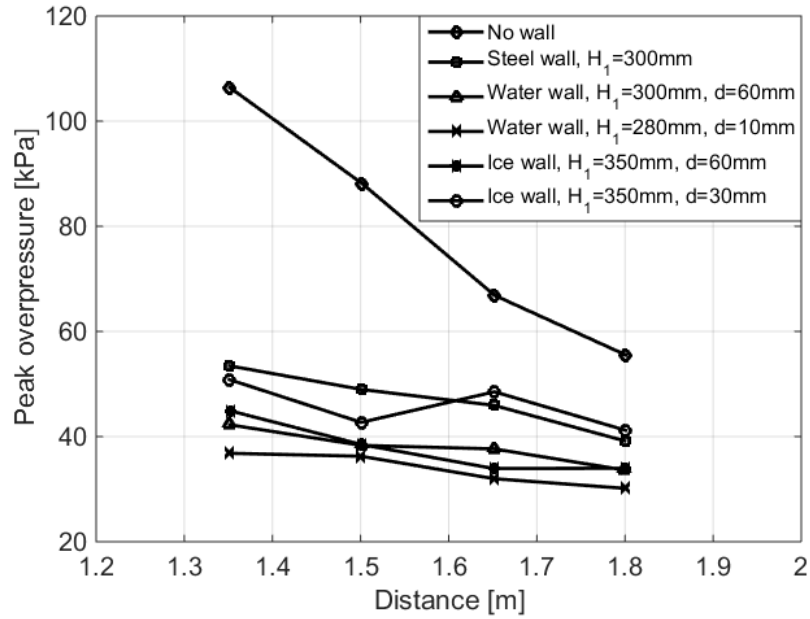


Figure 2-16: Peak overpressures on the ground behind different types of blast walls

*Bogosian and Piepenburg 2002* carried out experiments to evaluate the effectiveness of frangible walls in the shock wave attenuation. Figure 2-17 compares the effectiveness factors of four different types of frangible walls, which are averaged over the height.

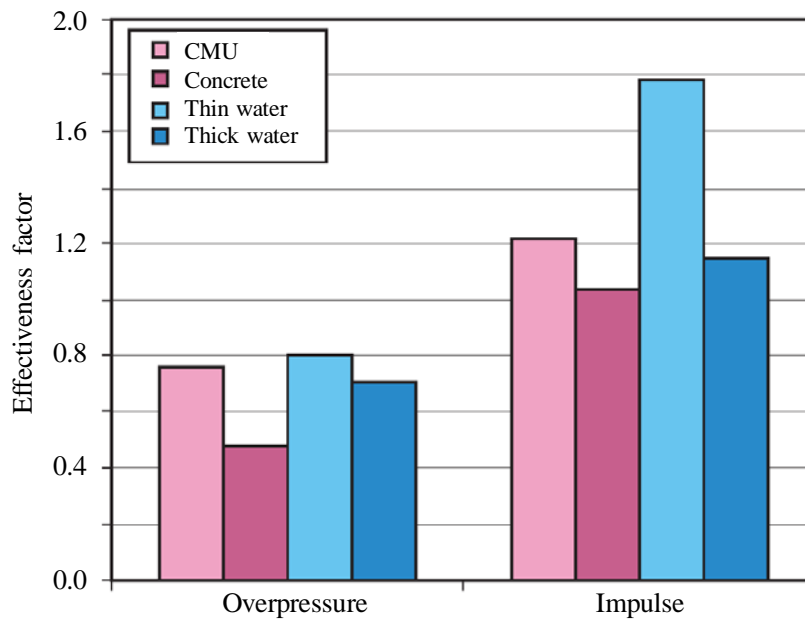


Figure 2-17: Effectiveness factors of frangible walls compared to rigid walls

The effectiveness factor was defined as the ratio of overpressure or impulse behind a frangible wall to the values behind a rigid wall. It was found that lightweight walls (e.g. concrete masonry units (CMUs) and thin pre-cast concrete panels) and water walls were as effective as rigid ones. In addition, the water walls had a special attraction that no hazardous debris would be generated from the failure of the wall.

## 2.2 Barriers with openings

Solid blast walls without openings (Section 2.1) have shown their performance in resisting blast loads if the distance between the charge and the wall is relatively small. In practice, the solid walls are often so rigidly designed that their deformations are negligible, which gives rise to a cumbersome appearance of walls with strong foundations. At the same time, the construction cost is mostly prohibitive. Moreover, ordinary solid walls are not readily accepted by urban society. They are usually aesthetically unattractive since they may give the occupants a prison-like feeling (living behind walls). Recently, the need for innovative solutions has greatly grown. An idea is to arrange the obstacles in such a way that, on the one hand, the protection requirement against blast is reasonably met, and on the other hand, the arrangement of obstacles meets the aesthetic demand to a satisfactory level. Thus, they can be integrated, for example, in an artwork during the city planning process. In addition, they can serve as a non-permanent protection for temporary use. However, there are only relatively few studies dedicated to this research field, e.g. *Löhner and Baum 2010* and *Löhner et al. 2010*. Löhner and co-authors carried out numerical simulations to investigate the shock wave attenuation performance of architecturally appealing alternatives to ordinary blast walls.

### 2.2.1 Interaction between the shock wave and the solid obstacles

In the past, considerable research efforts have been dedicated to the interaction between the shock wave and solid obstacles, e.g. sphere (*Abe and Takayama 2001* and *Shi and Yamamura 2004*), cylinders (*Rogg et al. 1985*, *Takayama 1998*, *Abe and Takayama 2001*, *Suzuki et al. 2000*, *Rice et al. 2003*, *Shi et al. 2007*, *Gebbeken and Döge 2010a*, *Chaudhuri et al. 2013* and *Niollet et al. 2015*), square and rectangular bars (*Rice et al. 2003*, *Shi et al. 2007*, *Gebbeken and Döge 2010a* and *Chaudhuri et al. 2013*) and triangular bars (*Skews et al. 1998* and *Chaudhuri et al. 2013*). Much work so far has focused on the cross-sectional shape study (*Shi et al. 2007*, *Gebbeken and Döge 2010a* and *Chaudhuri et al. 2013*) and on the arrangement of solid obstacles (*Rogg et al. 1985*, *Suzuki et al. 2000*, *Chaudhuri et al. 2013* and *Niollet et al. 2015*). The structural flexibility of obstacles was neglected and a rigid assumption was made. Moreover, most of these previous studies were based on shock tube tests. Hence, it is difficult to provide a direct guidance for the structural protection against blast in urban areas, since most of the experiments were conducted either at a small model scale or in shock tubes.

*Rogg et al. 1985* conducted shock tube tests to explore the flow patterns of the shock waves through an array of staggered cylinders. However, the emphasis was on the heat transfer estimation and on the derivation of the drag coefficients. *Takayama 1998* described in detail the unsteady flow field of the shock waves through a cylinder array. *Suzuki et al. 2000* conducted shock tube tests to investigate the effect of cylinder arrays on the shock wave attenuation. The main focus was the derivation of the drag force generated during the passage of the shock wave through the cylinder array. Several parameters were considered in this study, such as the arrangement type (single-layer

or multi-layer, aligned or staggered) and the cross-sectional diameter. It was found that

- In the upstream region of the cylinder array, the pressure was augmented, due to the wave reflected from the cylinders.
- Significant pressure oscillation occurred in the wake of the cylinder array, due to the formation of vortices.
- In the downstream region of the cylinder array, an attenuation of the transmitted shock wave occurred.
- The extent of the pressure augmentation and attenuation mainly depends on the blockage ratio of cylinders in the tube and the number of cylinder layers. The blockage ratio is defined as the ratio of the non-open area to the overall cross-sectional area of the tube. In the shock tube tests, the pressure augmentation in the upstream region was much more pronounced than the pressure attenuation in the downstream region. The shock wave attenuation performance increased with the number of cylinder layers. However, the influence of changing the arrangement type from aligned to staggered on the shock wave attenuation performance was negligibly small.

*Abe and Takayama 2001* discussed the attenuation effect of the shock waves propagating over complex geometries, i.e. an array of spheres and cylinders. The shock wave attenuation was visualized quantitatively by sequential holographic interferometry (*Abe and Takayama 2001*). It was revealed that, for an identical blockage ratio, the shock wave was attenuated faster over the sphere array than over the cylinder array. *Rice et al. 2003* carried out a numerical study to quantify the effect of the cross-sectional shapes of columns on the blast loads and on the response of columns. Square and circular cross-sectional shapes were involved. Three charge masses were considered, i.e. 100kg TNT representing a car-sized weapon, 200kg TNT and 500kg TNT representing a small truck attack. The stand-off distance from the charge was kept constant ( $R = 3.05\text{m}$ ).

*Shi and Yamamura 2004* investigated experimentally the interaction between the shock waves and the solid spheres. However, this study was mainly focused on the sensitivity of the shock wave attenuation to the Mach number of the incident wave as well as the size, arrangement and separation distance of the spheres. *Shi et al. 2007* carried out numerical simulations to study the shock wave interaction with a standalone column. It was indicated that a circular column resulted in less reflection but more diffraction of the shock wave than a rectangular column. The overpressure at the front face of a circular column was smaller than that of a rectangular column, whereas the contrary result was observed at the rear face.

In recent years, protective barriers have been increasingly important in blast-resistant design. To reduce the blast effects on buildings, *Barakat and Hetherington 1998* and *Barakat and Hetherington 1999* presented several architectural concepts using specific forms and landscape techniques, i.e. changes in the ground profile. To gain more insight, *Gebbeken and Döge 2008* and *Gebbeken and Döge 2010a* extended these studies by taking three shape studies, in which the horizontal, vertical and spatial shape

of the building were discussed. The authors concluded that, from a structural engineering viewpoint, the circular cross-section is the best choice for column design. In addition, *Gebbeken et al. 2011* and *Gebbeken et al. 2012* presented architectural attractive and constructional protective barriers as well as intelligent design in landscaping to protect the buildings in the urban areas. *Chaudhuri et al. 2013* conducted numerical simulations to examine the effect of the shape and the arrangement of solid obstacles on the shock wave attenuation. The authors concluded that reverse triangular obstacles (i.e. the base of the triangle facing the charge) with a staggered arrangement had the best shock wave attenuation performance among all considered obstacle arrangements. *Niollet et al. 2015* presented experimental and numerical results for different cylinder configurations. The cylinders were placed between the charge and the target plate. The aim was to understand how cylinders disrupted the shock wave propagation and to assess their performance on reducing the target plate deflections. The experiments were carried out in a shock tube. The charge mass varied from 20g to 70g. The results showed that not only attenuation effects but also augmentation effects on the target plate deflection may occur, depending on the number of cylinders and the cylinder arrangement. The cylinder arrangement was likely to have a greater influence on the target plate deflection than the number of cylinders. For the considered cylinder arrangements and the charge masses in the experiments, the number of cylinders had insignificant influence on the target plate deflection. *Ehrhardt et al. 2016* presented a research programme (BLASTHOR) on the interaction between the shock wave and the thorax. Two simplified torso surrogates, i.e. cuboid and cylinder, were involved. The authors revealed that the cylinder experiences lower impulses at the front face than the cuboid, since the cylinder has a more aerodynamic profile, whilst the opposite effect was observed at the rear face.

Recently, *Zong et al. 2017* proposed a conceptual design of the fence type blast wall in order to mitigate the blast loads. Numerical simulations were employed to examine the influence of the column geometry, spacing, dimension as well as the number of column layers and the separation distance of the layers on the shock wave attenuation. Two-dimensional axisymmetric models were employed. This meant that the wave flowing over the top of the wall and the influence of the blast load distribution over the column height were neglected in this preliminary study. Since the column deformation was expected to be negligibly small, columns were assumed rigid in the numerical analyses. It was found that, if a single layer arrangement was employed, the square and rectangular cross-sections were most effective in mitigating the blast loads, while the triangular cross-section with the vertex facing the charge was least effective. To further explore this concept, *Hao et al. 2017* extended the numerical investigations by *Zong et al. 2017*. Field experiments were conducted in order to further study the effectiveness of fence type blast walls in reducing the overpressures and impulses. Fence-type blast walls with different cross-sections and arrangements (single-layer or double-layer, aligned or staggered) were taken into consideration. A masonry wall was constructed as a solid barrier to provide a reference for comparison. The authors confirmed the above-mentioned conclusion made by *Zong et al. 2017*. Furthermore, the authors found that, for a double-layer arrangement, the staggered triangular (front

layer) and circular (rear layer) column system performed better than all the other arrangements considered in the study.

### 2.2.2 Shock wave trapping concept

Regarding the blast-resistant design, both the performance and the integrity of individual columns are crucial for ensuring the functionality of protective barriers, particularly if multiple explosions occur. Under such circumstances, a balanced design should be carried out, in which a compromise is made between the effectiveness in attenuating the shock wave and the reduction of the net blast loads on individual columns. Consequently, a shock wave trapping concept was proposed by *Skews et al. 1998* and recommended by *Chaudhuri et al. 2013* and *Hao et al. 2017* for the multi-layer arrangement of obstacles, which provides an easy entrance for the incoming shock wave with a weak reflection from the front layer followed by a strong reflection through the additional layers.

### 2.3 Summary: protective barrier overview

This chapter presents an overview of rigid and flexible blast walls as well as protective barriers containing openings. In the past, considerable efforts have been dedicated to the ordinary protective barriers. However, only limited information is available on the blast loads behind non-conventional barriers (e.g. staggered, shaped, open surface), especially if the barrier or parts of it do not behave rigidly or if the barrier has a surface containing openings. In order to gain an insight into this matter, this Dissertation focuses on these two types of protective barriers, on which experimental and numerical investigations are carried out in Chapters 5 and 6, respectively.

### 3 Shock wave propagation

When a certain amount of high explosive material is detonated, the hot and highly compressed gaseous detonation products force the air surrounding the high explosive material out of its original volume so rapidly that the air is shocked up to generate a shock wave. As the shock wave strikes a structure, the blast effects are resulted on the structure. More details about the description of the shock wave formation and the blast effects on structures can be found in *Smith and Hetherington 1994* and *Gebbeken and Döge 2010b*. This chapter describes briefly some fundamental aspects on the process of shock wave propagation.

#### 3.1 Basic parameters of shock waves

During the process of detonations, a huge amount of explosive energy is abruptly released. Three different types of detonations, i.e.

- contact detonations ( $Z = 0\text{m/kg}^{1/3}$ ),
- near-field detonations ( $Z < 0.5\text{m/kg}^{1/3}$ ) and
- far-field detonations ( $Z > 0.5\text{m/kg}^{1/3}$ ),

can be classified according to *Mayrhofer 2004*. The classification is based on the scaled distance  $Z$  given by

$$Z = \frac{R}{W^{1/3}}, \quad (3-1)$$

where  $R$  is the stand-off distance from the charge to the point of interest.  $W$  is the charge mass. This Dissertation will focus on the third detonation type, namely, the far-field detonations, in which a plane shock wave is assumed to be applied on the structure.

The Mach number  $M$ , which is a dimensionless index of the shock velocity, is often invoked to measure a motion. For a shock wave moving at shock velocity  $U$ , the Mach number  $M$  is defined as

$$M = \frac{U}{c}, \quad (3-2)$$

where  $c$  is the sonic velocity in the air ahead of the shock front. It is given as

$$c = \sqrt{\gamma R_s T}. \quad (3-3)$$

The ratio  $\gamma$  of specific heats is an item of frequent concern. It is defined as

$$\gamma = \frac{c_p}{c_v}, \quad (3-4)$$

where  $c_p$  is the specific heat at constant pressure,  $c_p = \gamma/(\gamma - 1) R_s$ .  $c_v$  is the specific heat at constant volume,  $c_v = 1/(\gamma - 1) R_s$ .

The ratio of specific heats varies with the overpressure and the air density ( $\gamma = 1.176 - 1.402$ , *UFC 3-340-01*). In practice, however, for peak side-on overpressures less than 6894.8kPa (1000psi), a constant value of  $\gamma = 1.4$  can be used (*Swisdak 1975*).  $R_s$  is the specific gas constant,  $R_s = 287\text{J}/(\text{kg}\cdot\text{K})$  for air.  $T$  is the absolute air temperature.

### 3.2 Overpressure-time history

Scaled blast parameters are often used to calculate the overpressure-time history generated from a charge of a specified mass at a given stand-off distance. The most commonly cited source of the scaled blast parameters is *Kingery and Bulmash 1984*, in which a series of fitted curves to air blast experimental data were developed for either free-air bursts (Section 3.8.1) or surface bursts (Section 3.8.2). The charge mass varies from less than 1kg to over 400ton. Three fundamental principals in the field of air blast were used to handle the experimental data, i.e. Hopkinson-Cranz scaling law (Section 3.3.1) for impulse, distance and time with the cube root of the charge mass, Sachs scaling law (Section 3.3.2) considering the influence of ambient conditions (e.g. altitude and atmospheric temperature), and TNT equivalence of different high explosives (Section 3.4).

The empirical formulae associated with the fitted curves are given as a function of the scaled distance  $Z$  for the blast parameters such as peak side-on and reflected overpressure ( $p_{so}$  and  $p_r$ ), maximum side-on and reflected impulse ( $i_s$  and  $i_r$ ), shock velocity  $U$ , time of arrival  $t_a$ , and positive phase duration  $t_d$  etc. These formulae are only valid for stand-off distances great than about three charge radii, which is often quoted as the lower bound of the applicability range for the formulae of *Kingery and Bulmash 1984*. These formulae are automated in the software ConWep (*Hyde 1988*) and DYNA2D/DYNA3D embedded in LS-DYNA (*LSTC 2017*).

Figure 3-1 shows an idealized side-on overpressure-time history, which is generated from a far-field detonation (Section 3.1). The overpressure-time history is characterized by the time of arrival  $t_a$ , peak overpressure  $p_{so}^+$ , minimum suction pressure  $p_{so}^-$ , maximum impulse  $i_s^+$ , positive and negative phase duration ( $t_d^+$  and  $t_d^-$ ). The shock front is the boundary layer between the air in the initial state and that in the shocked state. It arrives at the point of interest at time  $t_a$  and the pressure raises instantaneously from the atmospheric pressure  $p_0$  to the peak side-on pressure  $p_1$ . After then, the side-on pressure decays exponentially and returns to the atmospheric pressure  $p_0$  at time  $t_a + t_d^+$ . This is defined as the positive phase of the overpressure-time history. The positive phase duration  $t_d^+$  is the length of time required for the pressure from the peak side-on pressure  $p_1$  returns to the atmospheric pressure  $p_0$ . Following the positive phase is a negative phase of the duration  $t_d^-$ , in which the pressure drops below the atmospheric pressure  $p_0$ .

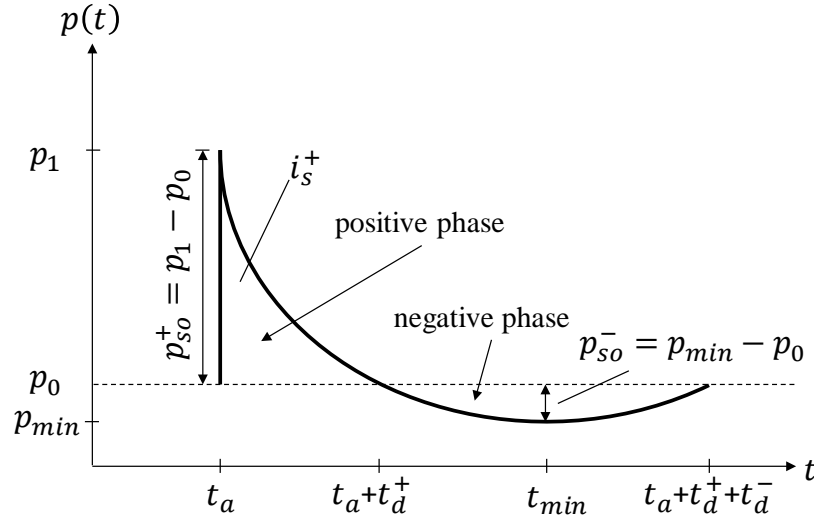


Figure 3-1: Idealized side-on overpressure-time history generated from a far-field detonation

The peak side-on overpressure  $p_{so}^+$  is the difference between the peak side-on pressure  $p_1$  and the atmospheric pressure  $p_0$ , i.e.  $p_{so}^+ = p_1 - p_0$ . The relation between the peak side-on overpressure  $p_{so}^+$  at the shock front and the shock velocity  $U_i$  of the incident wave is expressed by the Rankine-Hugoniot equation (Kinney and Graham 1985), which is given as

$$p_{so}^+ = \frac{2\gamma p_0}{\gamma + 1} \left[ \left( \frac{U_i}{c} \right)^2 - 1 \right], \quad (3-5)$$

where  $p_0$  is the atmospheric pressure,  $p_0 = 101.325\text{kPa}$  at mean sea level and at the standard temperature of  $15^\circ\text{C}$ .

Thus, the shock velocity  $U_i$  of the incident wave can be defined by rewriting Eq. (3-5) as

$$U_i = c \sqrt{\frac{\gamma + 1}{2\gamma} \frac{p_{so}^+}{p_0} + 1}. \quad (3-6)$$

As indicated by this equation, the higher the side-on overpressure  $p_{so}^+$  at the shock front, the greater the shock velocity  $U_i$  of the incident wave.

Inserting Eq. (3-2) into Eq. (3-5), one obtains

$$p_{so}^+ = \frac{2\gamma p_0}{\gamma + 1} (M_i^2 - 1). \quad (3-7)$$

This equation describes the unique relation between the Mach number  $M_i$  of the incident wave and the side-on overpressure  $p_{so}^+$  it develops. For  $\gamma = 1.4$ , it yields that

$$p_{so}^+ = \frac{7}{6} p_0 (M_i^2 - 1). \quad (3-8)$$

Furthermore, the ideal gas law is expressed as

$$p = \rho R_s T \cdot \quad (3-9)$$

Inserting Eq. (3-3) and Eq. (3-9) into Eq. (3-5), one obtains an interesting relation between the side-on overpressure  $p_{so}^+$  and the shock velocity  $U_i$  of the incident wave as

$$p_{so}^+ = \frac{2\rho_0}{\gamma + 1} (U_i^2 - c^2). \quad (3-10)$$

This equation indicates that the shock velocity  $U_i$  of the incident wave is necessarily supersonic ( $U_i > c$ ) in order to develop a positive side-on overpressure ( $p_{so}^+ > 0$ ). As the stand-off distance from the charge increases, the strength of the shock wave diminishes and the side-on overpressure decreases. At the end of the positive phase, the side-on overpressure approaches zero ( $p_{so}^+ \rightarrow 0$ ). This indicates that the shock velocity approaches the sonic velocity in the air, i.e.  $U_i = c$ . In this sense, any shock wave will finally degenerate into an acoustic wave ( $U_i = c$ ).

The maximum impulse  $i_s^+$  is the area of the overpressure-time history in the positive phase, i.e.

$$i_s^+ = \int_{t_a}^{t_a+t_d^+} p_{so}(t) dt. \quad (3-11)$$

In order to depict an idealized overpressure-time history, one should define the characteristics and its shape as a function of time. Based on the curve fitting techniques, several different formulae in terms of the scaled distance are proposed to match the measured blast parameters. *Teich 2012* compared the blast parameters from different sources, e.g. *Brode 1955, Baker 1973, Henrych and Abrahamson 1980, Kingery and Bulmash 1984, Korenev and Rabinovič 1985 and Kinney and Graham 1985* etc. As stated by the author, primary emphasis has been given to fit the blast parameters in the positive phase, i.e. peak overpressure and maximum impulse. More details about this topic can be found in *Teich 2012*. This section will focus on the forms of the overpressure-time histories. The number of parameters required to depict the forms of the overpressure-time histories varies from two to five. The functional forms are based on empirical curve fitting to the measured or theoretically predicted overpressure-time histories. The peak overpressure  $p_{so}^+$ , maximum impulse  $i_s^+$ , time of arrival  $t_a$  and positive phase duration  $t_d^+$  can be obtained from the experimental recordings.

### 3.2.1 Two-parameter form

The simplest form of describing the overpressure-time histories involves two parameters ( $p_{so}^+$  and  $t_d^+$  or  $p_{so}^+$  and  $c$ ). The overpressures decay either linearly (Eq. (3-12)) or exponentially (Eq. (3-13)). The linear decay form is given as

$$p(t) = p_{so}^+ \left( 1 - \frac{t - t_a}{t_d^+} \right) \quad t_a < t < t_a + t_d^+. \quad (3-12)$$

In an attempt to fit the linear decay form to the experimental recordings, the actual value of  $p_{so}^+$  is usually preserved and the positive phase duration  $t_d^+$  is adjusted to get the actual value of the maximum impulse  $i_s^+$ . Another possibility is to adjust the positive phase duration  $t_d^+$  to match the initial decay rate  $\frac{\partial p}{\partial t}|_{t=t_a}$  from the experimental recordings. However, this results in an underestimate of the maximum impulse  $i_s^+$ . This simple form is admittedly oversimplified, but it is often adequate for the structural response calculation using the single degree of freedom (SDOF) method (Biggs 1964, Low and Hao 2001, Low and Hao 2002, Xiao et al. 2015 and Xiao et al. 2016).

Ethridge 1965 proposed an exponential form in order to fit the experimental recordings in the range of the positive phase as closely as possible. The exponential form is given as

$$p(t) = p_{so}^+ e^{-c(t-t_a)} \quad t_a < t < t_a + t_d^+. \quad (3-13)$$

Both options mentioned above can be used to match the experimental recordings, either the values of the peak overpressure  $p_{so}^+$  and the maximum impulse  $i_s^+$  or the values of the peak overpressure  $p_{so}^+$  and the initial decay rate  $\frac{\partial p}{\partial t}|_{t=t_a}$ . This exponential form represents the measured overpressure-time histories better than the linear decay form. It should be noted that even though the side-on overpressure never returns to zero by using this exponential form, the resulting maximum impulse  $i_s^+$  is finite, giving that

$$i_s^+ = \frac{p_{so}^+}{c} (1 - e^{-ct_d^+}). \quad (3-14)$$

### 3.2.2 Three-parameter form

In order to match any three of the four quantities  $p_{so}^+$ ,  $i_s^+$ ,  $t_d^+$  and  $\frac{\partial p}{\partial t}|_{t=t_a}$ , the modified Friedlander equation adds an additional parameter  $\alpha$  to describe the overpressure-time histories, giving that

$$p(t) = p_{so}^+ \left( 1 - \frac{t - t_a}{t_d^+} \right) e^{-\alpha \frac{t-t_a}{t_d^+}} \quad t_a < t < t_a + t_d^+. \quad (3-15)$$

Usually, the decay rate  $\alpha$  is so selected that the measured value of the maximum impulse  $i_s^+$  is retained by the empirical overpressure-time history. The relation between the maximum impulse  $i_s^+$  and the decay rate  $\alpha$  is given as

$$i_s^+ = p_{so}^+ t_d^+ \left[ \frac{1}{\alpha} - \frac{1}{\alpha^2} (1 - e^{-\alpha}) \right]. \quad (3-16)$$

Given the measured maximum impulse  $i_s^+$ , the decay rate  $\alpha$  can be obtained from this equation. However, a direct solution of this equation for the decay rate  $\alpha$  is not feasible. An iterative procedure (e.g. Newton-Raphson method) is required to calculate the decay rate  $\alpha$ . Figure 3-2 illustrates the dependence of the decay rate  $\alpha$  on the scaled distance  $Z$  ranging from  $1\text{m/kg}^{1/3}$  to  $100\text{m/kg}^{1/3}$ . The data originates from *Kinney and Graham 1985*.

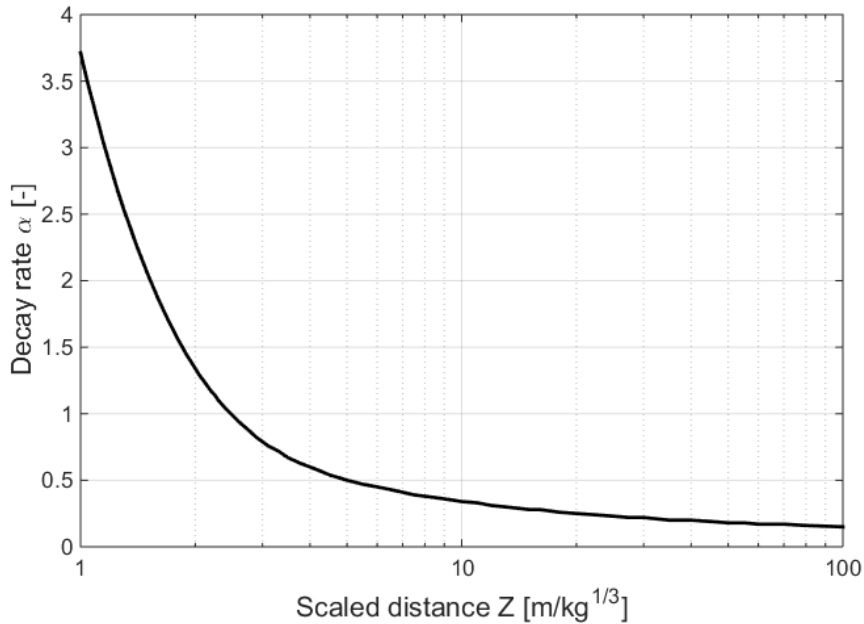


Figure 3-2: Dependence of the decay rate  $\alpha$  on the scaled distance  $Z$ , (data from *Kinney and Graham 1985*)

In addition, the negative phase can also be accommodated by the modified Friedlander equation (Eq. (3-15)). The minimum suction pressure  $p_{so}^-$  is the difference between the minimum pressure  $p_{min}$  and the atmospheric pressure  $p_0$ , i.e.  $p_{so}^- = p_{min} - p_0$ . Setting the time derivative of the modified Friedlander Equation (Eq. (3-15)) to zero, i.e.  $\partial p / \partial t = 0$ , one obtains time  $t_{min}$  (Figure 3-1) when the minimum suction pressure  $p_{so}^-$  occurs, giving that

$$t_{min} = t_a + t_d^+ \left(1 + \frac{1}{\alpha}\right). \quad (3-17)$$

Substituting time  $t_{min}$  back into the modified Friedlander Equation (Eq. (3-15)), one gets the minimum suction pressure  $p_{so}^-$ .

It should be noted that the modified Friedlander equation is only valid for distances larger than about ten charge radii. Since the original equation of Friedlander does not include the decay rate  $\alpha$  in the exponential, Eq. (3-15) is, therefore, often quoted as the modified Friedlander equation.

ConWep provides an alternate form, which can also be used to match any three of the four quantities  $p_{so}^+$ ,  $i_s^+$ ,  $t_d^+$  and  $\frac{\partial p}{\partial t} |_{t=t_a}$ , giving that

$$p(t) = p_{so}^+ \left( 1 - \frac{t - t_a}{t_d^+} \right) e^{-\frac{t-t_a}{a}}. \quad (3-18)$$

The equation of the maximum impulse given as

$$i_s^+ = a^2 \frac{p_{so}^+}{t_d^+} \left( \frac{t_d^+}{a} + e^{-\frac{t_d^+}{a}} - 1 \right), \quad (3-19)$$

can be solved for the decay rate  $a$  via an iterative procedure, e.g. Newton-Raphson method. It is worth mentioning that the decay rates in Eq. (3-15) and Eq. (3-18) are different, i.e.  $a \neq \frac{t_d}{\alpha}$ .

### 3.2.3 Four-parameter form

The initial decay rate  $\frac{\partial p}{\partial t}|_{t=t_a}$  appears to decrease in the experimental recordings, hence, *Ethridge 1965* proposed an alternative form to extend the freedom in matching the experimental recordings, so that all four quantities  $p_{so}^+$ ,  $i_s^+$ ,  $t_d^+$  and  $\frac{\partial p}{\partial t}|_{t=t_a}$  can be matched. This alternative form has four parameters and is expressed as

$$p(t) = p_{so}^+ \left( 1 - \frac{t - t_a}{t_d^+} \right) e^{-b \left( 1 - f \frac{t-t_a}{t_d^+} \right) \frac{t-t_a}{t_d^+}} \quad t_a < t < t_a + t_d^+. \quad (3-20)$$

### 3.2.4 Five-parameter form

*Brode 1956* proposed a five-parameter form given as

$$p(t) = p_{so}^+ \left( 1 - \frac{t - t_a}{t_d^+} \right) \left[ a e^{-\alpha \frac{t-t_a}{t_d^+}} + (1 - a) e^{-\beta \frac{t-t_a}{t_d^+}} \right] \quad t_a < t < t_a + t_d^+. \quad (3-21)$$

This form aims to match the overpressure-time histories in the positive phase, which is predicted by the theoretical calculation of the author for shock waves generated from a point source. *Ethridge 1965* demonstrated that this equation had an excellent performance in fitting the experimental recordings.

### 3.2.5 Comparison of different forms of overpressure-time histories

It is worth noting that all the equations mentioned above are strictly empirical. The two-parameter forms, i.e. the linear decay form (Eq. (3-12)) and the exponential form (Eq. (3-13)), are simple, but both deviate considerably from some of the measured quantities of shock waves. The linear decay form is inaccurate in describing the shape of the overpressure-time histories. The failure of the exponential form to return to the atmospheric pressure is inaccurate. The modified Friedlander equation (Eq. (3-15)) and the ConWep-form (Eq. (3-18)) are still reasonably simple and provide satisfactory accuracy in matching the experimental recordings. The remaining equations (Eq. (3-20) and Eq. (3-21)) are increasingly complicated, but they also offer increasing accuracy in adjusting to the experiment recordings.

In total, the best compromises between the mathematical complexity and the accuracy in describing the forms of the overpressure-time histories are the modified Friedlander equation and the ConWep-form. On the one hand, they allow adjustment to conform to the most relevant properties of shock waves. On the other hand, they are mathematically not too complicated.

If a charge is detonated on or very close to the ground surface, the emerging shock wave propagation can be assumed hemi-spherical. Figure 3-3 depicts the side-on overpressure-time histories generated from a detonation of 5kg TNT equivalent on the ground. Six different stand-off distances are considered, i.e. 4m, 5.5m, 6.5m, 7.5m, 8.5m and 10m. The software ConWep (Hyde 1988) is used to calculate the side-on overpressure-time histories. The peak side-on overpressure  $p_{so}^+$  and the maximum side-on impulse  $i_s^+$  decrease with the stand-off distance  $R$ , whereas the time of arrival  $t_a$  of the incident wave and the positive phase duration  $t_d^+$  increase with the stand-off distance  $R$ .

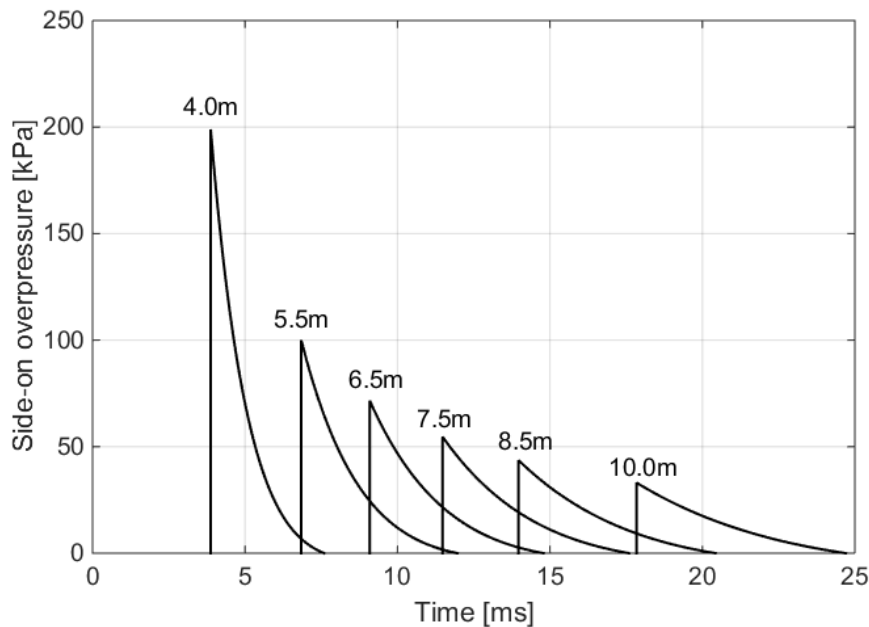


Figure 3-3: Side-on overpressure-time histories generated from a detonation (5kg TNT equivalent) on the ground at different stand-off distances

It should be mentioned that all the equations described in the previous sections are proposed based on the experimental recordings in the positive phase. The information of the negative phase is neglected. However, the negative phase may play a great role in the design of structures, if lightweight structures are concerned or if the structures are possible to fail in a direction opposite to the blast loads (Teich and Gebbeken 2012).

As mentioned in Section 3.2.2, the modified Friedlander equation can also be employed to accommodate the negative phase of the overpressure-time histories. In order to accurately represent the negative phase using the modified Friedlander equation, the decay rate  $\alpha$  should be modified. Based on the published experimental data in the literature and the own experimental data, Borgers and Vantomme 2008 proposed a new formula to calculate the decay rate  $\alpha$ , which is defined as

$$\alpha = 1.5Z^{-0.38} \quad 0.1 < Z < 30. \quad (3-22)$$

The positive phase duration  $t_d^+$  can be solved from Eq. (3-16) as

$$t_d^+ = \frac{i_s^+}{p_{so}} \frac{\alpha^2}{\alpha - 1 + e^{-\alpha}}. \quad (3-23)$$

The reflected wave is often assumed to have a form similar to the incident wave. Thus, the reflected overpressure-time histories can also be represented by the modified Friedlander equation or by the ConWep-form. However, a different decay rate must be used, since the reflected maximum impulse is larger than the side-on maximum impulse.

The peak overpressures, the durations and the maximum impulses appear without superscript plus or minus signs later in this Dissertation, the plus sign indicating the positive phase will be implied.

### 3.3 Scaling laws

Experimental studies of shock wave phenomenology are often rather difficult and expensive, especially when carried out on a large scale. Numerical methods used to derive the shock wave characteristics are often quite involved. From an economic viewpoint, these experimental and numerical investigations are not always possible to be repeated. Therefore, various researchers have attempted to develop scaling laws which would widen the applicability of the experiments and analyses. Hopkinson-Cranz scaling law and Sachs scaling law are by far the most widely used laws in scaling of air blast parameters. They present the experimental data for huge combinations of charge masses and distances in a consistent form. These scaling laws are briefly discussed in the following subsections.

#### 3.3.1 Hopkinson-Cranz scaling law

The most widely used scaling law is that formulated independently by *Hopkinson 1915* and *Cranz 1926*. Hopkinson-Cranz scaling law is often cited as the cube-root scaling law in the literature. It states that two charges of the same explosive type which have similar geometry but different mass and are detonated at the same scaled distance from a target structure under the same ambient conditions will produce the same scaled blast parameters (*Baker 1973*).

This scaling law is based on the geometric scaling, which means that two detonations with different charge masses ( $W_1$  and  $W_2$ ) at different stand-off distances ( $R_1$  and  $R_2$ ) produce the same peak overpressures ( $p_1 = p_2$ ), if the scaled distances of the detonations are the same, i.e.  $Z_1 = Z_2$ . Applying Eq. (3-1), one gets

$$\left(\frac{W_1}{W_2}\right)^{\frac{1}{3}} = \frac{R_1}{R_2}. \quad (3-24)$$

The ratio of other blast parameters (e.g. time of arrival  $t_a$ , positive phase duration  $t_d$  and maximum impulse  $i$ ) between the detonations can then be expressed as

$$\frac{t_{a,1}}{t_{a,2}} = \frac{t_{d,1}}{t_{d,2}} = \frac{i_1}{i_2} = \left(\frac{W_1}{W_2}\right)^{\frac{1}{3}} = \frac{R_1}{R_2}. \quad (3-25)$$

Strictly, this scaling law is only valid under certain conditions, namely, the ambient conditions, charge shape, charge height above the ground and surface roughness are identical. However, in practice, there are used even if only similar conditions are valid.

### 3.3.2 Sachs scaling law

*Sachs 1944* proposed a scaling law in order to account for the effect of ambient conditions (e.g. altitude and atmospheric temperature) on the blast parameters of the shock waves generated from detonations. Considering an atmospheric pressure  $p_a$  and an atmospheric temperature  $T_a$ , the scaling factors for pressure  $S_p$ , distance  $S_d$ , time  $S_t$  and impulse  $S_i$  are defined as (*Glasstone 1980* and *Kingery and Bulmash 1984*)

$$S_p = \frac{p_a}{p_0}, \quad (3-26)$$

$$S_d = \left(\frac{p_0}{p_a}\right)^{\frac{1}{3}}, \quad (3-27)$$

$$S_t = \left(\frac{p_0}{p_a}\right)^{\frac{1}{3}} \left(\frac{T_0}{T_a}\right)^{\frac{1}{2}}, \quad (3-28)$$

$$S_i = \left(\frac{p_a}{p_0}\right)^{\frac{2}{3}} \left(\frac{T_0}{T_a}\right)^{\frac{1}{2}}, \quad (3-29)$$

where  $p_0$  and  $T_0$  are the atmospheric pressure at mean sea level and the standard temperature, i.e.  $p_0 = 101.325\text{kPa}$  and  $T_0 = 15^\circ\text{C}$ .

Normally, a shock wave generated from a given charge mass is less damaging at high altitudes than at low altitudes. This means that smaller overpressure and impulse are exhibited at high altitudes than at low altitudes since the atmospheric pressure  $p_a$  is smaller at high altitudes.

It should be noted that two assumptions are made in order to apply Sachs scaling law. Firstly, it is assumed that changes in the ambient conditions lead only to changes of the scale of pressure, distance, time and impulse. Secondly, the released blast energy does not depend on the ambient conditions but solely on the charge mass, nature of the explosive material and location of the explosive charge with respect to the ground surface.

### 3.4 TNT equivalence

During the process of blast effect evaluation on various target structures, difficulties appear when high explosives other than TNT are used. The empirical formulae, e.g. *Kingery and Bulmash 1984*, are only applicable for the standard explosive TNT. Under such circumstances, the concept of TNT equivalence is often invoked to predict the blast parameters from detonations of high explosives other than TNT. TNT is relatively safe to handle and for specimens of known density and crystalline nature, which gives quite reproducible blast effects (*Kinney and Graham 1985*). Hence, it is often selected as the standard explosive for comparison. It is assumed that the explosive charge is an uncased or bare, centrally initiated sphere. Furthermore, the manner of the explosive energy release is of a similar form to that of TNT.

TNT equivalence factor ( $Eq_{TNT}$ ) is defined as the ratio of the charge mass of TNT ( $W_{TNT}$ ) which produces the same blast effects as the actual high explosive, to the charge mass of the actual high explosive ( $W_{HE}$ ), giving that

$$Eq_{TNT} = \frac{W_{TNT}}{W_{HE}}. \quad (3-30)$$

Thus, multiplying the charge mass of the actual high explosive by the associated TNT equivalence factor, one obtains the equivalent charge mass in TNT. TNT equivalence factors depend on several parameters, e.g. nature of the explosive material, confinement of the explosive (casing, container etc.), charge shape, location of ignition, scaled distance, and selected parameter for comparison (e.g. peak overpressure, scaled maximum impulse, heat of detonation etc.).

The concept of TNT equivalence provides an identification of a given shock wave in terms of the standard explosive TNT whose blast effects have been extensively documented. However, the use of TNT equivalence concept has some drawbacks:

- There are no definitive methods or documents available, which provide accurate and consistent values of TNT equivalence. The variability of TNT equivalence factors obtained from the literature is found to be so significant that errors can be as large as 50%, with 20% to 30% being typical (*Locking 2011*). Furthermore, the values of TNT equivalence provided in the literature give no hints on the uncertainty underlying. Therefore, the accuracy and validity of the published values of TNT equivalence are questionable.
- TNT equivalence factors may differ whether based on overpressure or impulse. They may also differ whether the blast parameters are the incident or reflected ones (*Shin et al. 2015*).
- TNT equivalence factors may vary with the scaled distance (*Swisdak 1975, McKnown et al. 1978, De Yong and Campanella 1989, Formby 1995, Formby and Wharton 1996, Wharton et al. 2000, Jeremic and Bajic 2006, Cheesman 2010, Locking 2011, Pachman 2014 and Shin et al. 2015*). In addition, most high explosives have not been tested sufficiently or at all at small scaled distances to determine a reliable TNT equivalence factor. TNT equivalence factors at small scaled distances, especially inside the fireball,

are different from those at larger scaled distances due to the effect of the expanding detonation products and a ratio of specific heats different from 1.4.

Thus, it is of great importance to derive an appropriate TNT equivalence factor for the high explosive to be examined. Special care must be taken to understand how the TNT equivalence factors are derived. In essence, four different methods can be used to derive TNT equivalence factors. They are based on theoretical considerations (Section 3.4.1), laboratory tests (Section 3.4.2), field tests (Section 3.4.3) and numerical investigations (Section 3.4.4). These methods will be briefly discussed in the following subsections. The values of TNT equivalence of the explosive PETN which was used in the experiments (Chapter 5) are given in the respective subsections, according to the respective methods.

### 3.4.1 Theoretical method

The theoretical method is the simplest method to derive TNT equivalence factors among the four methods described in Section 3.4. The derivation of TNT equivalence factors is based on the ratio of the properties of the actual high explosive to the ones of TNT, e.g. heat of detonation  $H_D$  (Eq. (3-31), *UFC 03-340-02*), velocity of detonation  $D$  (Eq. (3-32), *Copper 1996*) and specific energy  $Q$  (Eq. (3-33), *Smith and Hetherington 1994* and *Mays and Smith 1995*). The pertinent equations are given as

$$Eq_{TNT} = \frac{H_{D,HE}}{H_{D,TNT}}, \quad (3-31)$$

$$Eq_{TNT} = \left( \frac{D_{HE}}{D_{TNT}} \right)^2, \quad (3-32)$$

$$Eq_{TNT} = \frac{Q_{HE}}{Q_{TNT}}, \quad (3-33)$$

where the subscripts TNT and HE represent the standard explosive TNT and the actual high explosive.

Using Eq. (3-31) - Eq. (3-33), TNT equivalent factors for the high explosive PETN are given in Table 3-1 - Table 3-3.

Table 3-1: TNT equivalence factors for PETN based on heat of detonation

Sources	Heat of detonation					
	<i>Dobratz and Crawford 1985</i>		<i>UFC 3-340-02</i>		<i>Krauthammer 2008</i>	
Explosive	$\rho_0$ [kg/m <sup>3</sup> ]	$H_{D,HE}$ [kJ/kg]	$\rho_0$ [kg/m <sup>3</sup> ]	$H_{D,HE}$ [kJ/kg]	$\rho_0$ [kg/m <sup>3</sup> ]	$H_{D,HE}$ [kJ/kg]
TNT	1540	4270-4560 <sup>a</sup>	-	5890	1640	4100-4550 <sup>a</sup>
PENT	1730	5730-6230 <sup>a</sup>	-	6907	1770	6120-6320 <sup>a</sup>
$Eq_{TNT}$	1.34-1.37 <sup>a</sup>		1.17		1.39-1.49 <sup>a</sup>	

<sup>a</sup>The range of parameters is specified between minimum and maximum values.

Table 3-2: TNT equivalence factors for PETN based on velocity of detonation

Sources	Velocity of detonation					
	<i>AMCP 706-177</i>		<i>Dobratz and Crawford 1985</i>		<i>Krauthammer 2008</i>	
Explosive	$\rho_0$ [kg/m <sup>3</sup> ]	$D$ [m/s]	$\rho_0$ [kg/m <sup>3</sup> ]	$D$ [m/s]	$\rho_0$ [kg/m <sup>3</sup> ]	$D$ [m/s]
TNT	1560	6825	1630	6930	1640	6950
PENT	-	-	1500	7450	-	-
	1770	8300	1770	8300	1770	7980-8260 <sup>a</sup>
$Eq_{TNT}$	1.48		1.16 <sup>b</sup> / 1.43 <sup>c</sup>		1.32-1.41 <sup>a</sup>	

<sup>a</sup> The range of parameters is specified between minimum and maximum values.

<sup>b</sup> TNT equivalence factor is valid for the density of 1500kg/m<sup>3</sup>.

<sup>c</sup> TNT equivalence factor is valid for the density of 1770kg/m<sup>3</sup>.

Table 3-3: TNT equivalence factors for PETN based on specific energy

Sources	Specific energy			
	<i>Smith and Hetherington 1994</i>		<i>Gefand 2004</i>	
Explosive	$\rho_0$ [kg/m <sup>3</sup> ]	$Q$ [kJ/kg]	$\rho_0$ [kg/m <sup>3</sup> ]	$Q$ [kJ/kg]
TNT	-	4520	1590	4517
PETN	-	5800	1770	5800
$Eq_{TNT}$	1.28		1.28	

The equations presented so far for determining TNT equivalence factors are based on a single explosive material parameter, which is available in the literature or easily obtainable. The more advanced theoretical methods, e.g. Berthelot method, power index method and hydrodynamic work method, require more calculations to be conducted, which are based on more than one explosive material parameters.

The Berthelot calculation can be done either at the detonation condition or at the fireball condition, whichever better describes the specific application (*Cooper 1996*). The pertinent equation is defined as

$$Eq_{TNT} = 8.4 \frac{\Delta n(-\Delta H_R^0)}{m_{HE}}, \quad (3-34)$$

where  $\Delta n$  is the number of moles of gases produced per mol of explosive.  $\Delta H_R^0$  is the molar heat of detonation in kJ/mol.  $m_{HE}$  is the molecular mass of the actual high explosive in g/mol.

TNT equivalence factors, which are derived by the power index method (Eq. (3-35), *Locking 2011*) and the hydrodynamic work method (Eq. (3-36), *Locking 2013* and *Locking 2014*), are given as

$$Eq_{TNT} = \frac{H_{D,HE} V_{HE}}{H_{D,TNT} V_{TNT}}, \quad (3-35)$$

$$Eq_{TNT} = \frac{p_{CJ,HE}}{p_{CJ,TNT}} \left( \frac{\rho_{0,TNT}}{\rho_{0,HE}} \right)^{0.96}, \quad (3-36)$$

where  $V_{HE}$  and  $V_{TNT}$  are the volume of gases at the standard temperature and pressure per mass of actual high explosive and TNT. Table 3-4 specifies TNT equivalence factors for the high explosive PETN by using Eq. (3-34) - Eq. (3-36).

Table 3-4: TNT equivalence factors for PETN based on Berthelot, power index and hydrodynamic work methods

Methods	Sources	$Eq_{TNT}$
Berthelot	<i>Kinney and Graham 1985</i>	1.73
Power index	<i>Dobratz and Crawford 1985</i>	1.19
	<i>Krauthammer 2008</i>	1.29-1.38 <sup>a</sup>
Hydrodynamic work	<i>Dobratz and Crawford 1985</i>	1.13 <sup>b</sup> / 1.47 <sup>c</sup>

<sup>a</sup> The range of parameters are specified between minimum and maximum values.

<sup>b</sup> TNT equivalence factor is valid for the density of 1500kg/m<sup>3</sup>.

<sup>c</sup> TNT equivalence factor is valid for the density of 1770kg/m<sup>3</sup>.

It should be noted that all the above equations are aiming to assess TNT equivalence factor of a given explosive, regardless of which blast parameter is concerned (overpressure or impulse). However, several researchers, e.g. *Esparza 1986*, *Formby and Wharton 1996* and *Locking 2013*, recommended two different TNT equivalence factors, one for overpressure and another for impulse, in order to evaluate the blast effects.

### 3.4.2 Laboratory tests

TNT equivalence factors can be determined from laboratory tests, e.g. sand crush test, trauzl lead block test, ballistic mortar test and plate dent test. Further details can be found in *Cooper 1994* and *Cheesman 2010*, in which laboratory tests used to derive TNT equivalence factors are well described. Table 3-5 specifies TNT equivalence factors for the high explosive PETN, which are derived from different laboratory tests. The data originates from *AMCP 706-177* and *Kinney and Graham 1985*.

Table 3-5: TNT equivalence factors for PETN derived from laboratory tests

Sources	Sand crush	Trauzl lead block	Ballistic mortar	Plate dent
<i>AMCP 706-177</i>	1.31	1.73	1.45	1.29
<i>Kinney and Graham 1985</i>	-	1.8	1.45	1.29

It should be pointed out that these laboratory tests are not equivalent in determining TNT equivalence factors since different quantities are measured in the different laboratory tests. Therefore, they may give somewhat inconsistent results of TNT equivalence factors (Table 3-5). In addition, such laboratory tests are subjected to uncertainty.

### 3.4.3 Field tests

Explosive charges are detonated in the free field, blast parameters of the emerging shock waves, e.g. incident overpressures and impulses, are measured at various distances. The experimental data is used to derive TNT equivalence factors for overpressure and impulse by using Eq. (3-37) and Eq. (3-38), respectively (*Held 1983, Esparza 1986, Formby 1995, Formby and Wharton 1996 and Wharton et al. 2000*), giving that

$$Eq_{TNT,p} = \frac{W_{TNT}}{W_{HE}} \Big|_{p_{so,HE}=p_{so,TNT}} = \left( \frac{Z_{HE}}{Z_{TNT}} \right)^3 \Big|_{p_{so,HE}=p_{so,TNT}}, \quad (3-37)$$

$$Eq_{TNT,i} = \frac{W_{TNT}}{W_{HE}} \Big|_{i_{so,HE}=i_{so,TNT}} = \left( \frac{Z_{HE}}{Z_{TNT}} \right)^3 \Big|_{i_{so,HE}=i_{so,TNT}}, \quad (3-38)$$

where  $Eq_{TNT,p}$  and  $Eq_{TNT,i}$  are the TNT equivalence factors for overpressure and impulse, respectively.  $Z_{HE}$  is the scaled distance of the high explosive to be examined.  $Z_{TNT}$  is the scaled distance of the standard explosive TNT, which produces the same overpressure or impulse as the actual high explosive.

Field tests are a slightly more detailed method than the theoretical one. Separate values of TNT equivalence are proposed for overpressure and impulse, respectively. The choice of which factor to use depends on whether the peak overpressure or the maximum impulse is to be matched between the actual high explosive and TNT. It is assumed that the experimental configurations are the same or at least similar between the tests using the actual high explosive and the standard explosive TNT.

It is worth mentioning that for different selected blast parameter (overpressure or impulse), TNT equivalence factors may be different. Furthermore, TNT equivalence factors may vary with the distances from the charge and hence vary with the peak side-on overpressures. *Swisdak 1975* described a nonlinear relationship between TNT equivalence factors for overpressure and impulse versus the side-on overpressures. Figure 3-4 illustrates the dependence of TNT equivalence factors of four different explosives, i.e. composition B, composition C4, pentolite and tritonal, on the side-on overpressures. TNT equivalence factors based on both overpressure and impulse are compared. As observed in Figure 3-4, the distribution of TNT equivalence factors for impulse over the overpressure range differs significantly from the one for overpressure.

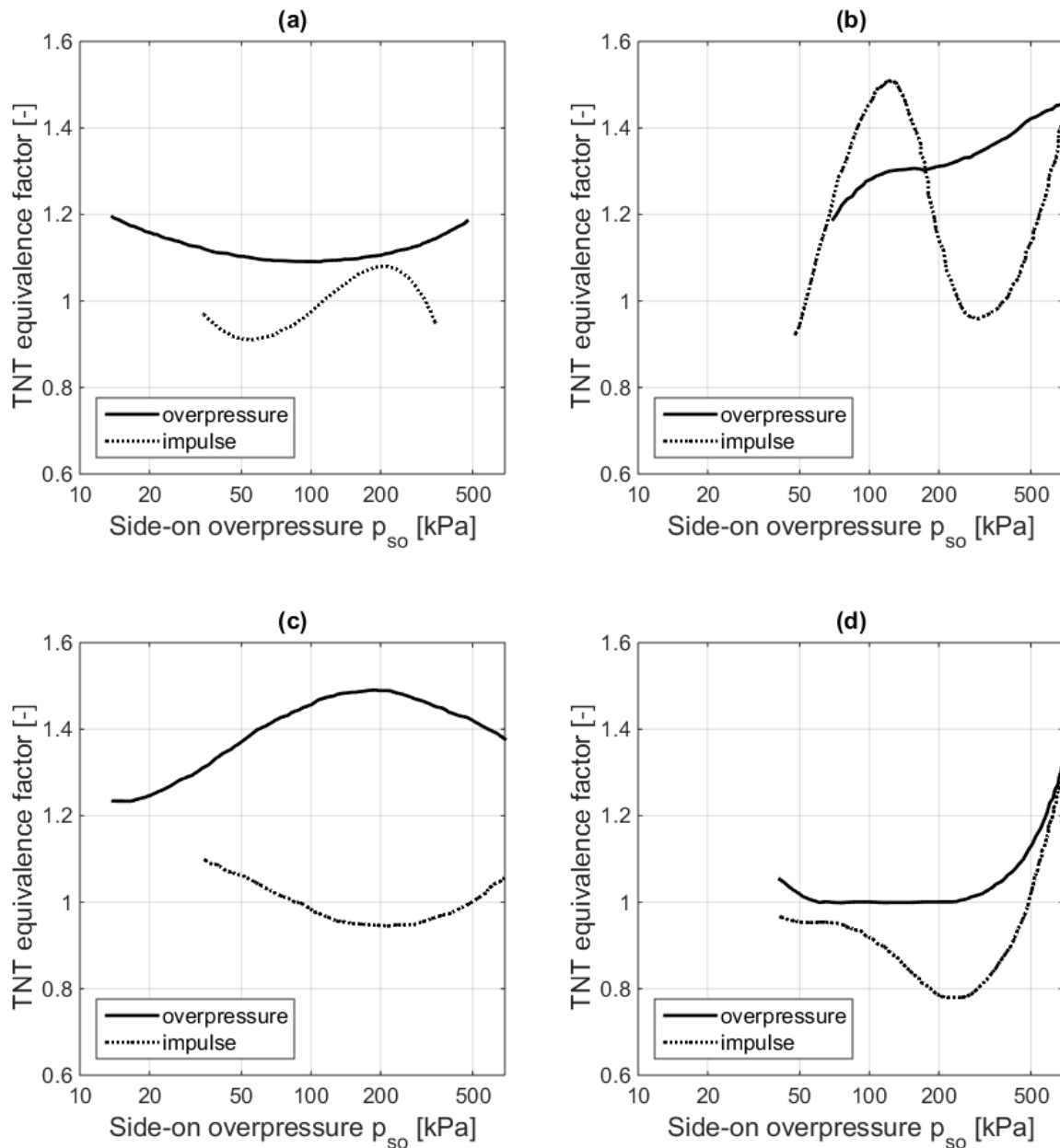


Figure 3-4: TNT equivalence factors for overpressure and impulse (a) composition B; (b) composition C4; (c) pentolite; (d) tritonal (data from *Swisdak 1975*)

For practical reasons, it is often to apply only a single value of TNT equivalence, i.e. the average TNT equivalence factor over a certain overpressure range. Therefore, the overpressure range, at which the average TNT equivalence factor is derived, should be specified. Moreover, for safety reason, it is recommended by *Locking 2011* that the larger one of TNT equivalent factors for overpressure and impulse should be used. Table 3-6 summaries TNT equivalence factors for PETN, which are based on overpressure and impulse, respectively.

Table 3-6: TNT equivalence factors for PETN derived from field tests

Sources	Density [kg/m <sup>3</sup> ]	$Eq_{TNT,p}$ [-]	$Eq_{TNT,i}$ [-]	Pressure range [kPa]
<i>TM5-855-1 /UFC 3-340-01</i> <i>Dusenberry 2010</i>	1770	1.27	1.27	30-690
<i>Swisdak 1975</i>				
<i>Smith and Hetherington 1994</i> <i>Krauthammer 2008</i>	-	1.27	-	34-689
<i>Karlos and Solomos 2013</i> <i>IATG 01.80</i>	1780	1.27	1.11	35-700

It is indicated (e.g. in *Cooper 1994*, *Wharton et al. 2000*, *Dewey 2005*, *Locking 2011* and *Bogosian et al. 2015*) that a single value of TNT equivalence (for either overpressure or impulse) is insufficient for the entire scaled distance range. Different values depending on the scaled distance are required. *Rigby and Sielicki 2014* found that TNT equivalence factors predicted by Eq. (3-31) are in a good agreement with their experimental results. In contrary to other studies mentioned above, the authors showed that, if far-field detonations are concerned, there is no variation of TNT equivalence factors with the scaled distances. The authors concluded, therefore, that a single value of TNT equivalence factor can be used in the far-field detonations for either overpressure or impulse. Similar observation was found by *Grisaro and Edri 2017*.

#### 3.4.4 Numerical method

The numerical method to derive TNT equivalence factor is based on choosing the charge mass of TNT in such a way (by trial and error approach) that the overpressure and impulse values at a specified distance are equal to those of the actual high explosive. Eq. (3-37) and Eq. (3-38) are employed for the calculation of TNT equivalence factors for overpressure and impulse, respectively. *Shin et al. 2015* conducted numerical studies to derive TNT equivalence factors for four high explosives (PETN, Composition B, Pentolite and Tetryl), they are valid for the side-on and reflected overpressure and impulse for a wide range of scaled distance  $Z$  between  $0.06\text{m/kg}^{1/3}$  and  $40\text{m/kg}^{1/3}$  (e.g. Figure 3-5 for PETN).

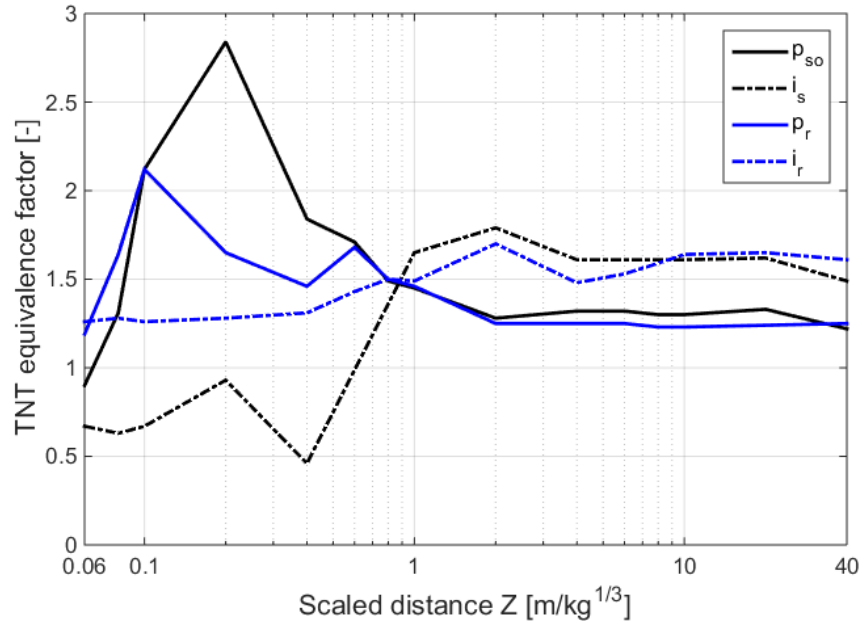


Figure 3-5: TNT equivalence factors for side-on and reflected overpressure and impulse for PETN (data from *Shin et al. 2015*)

*Grisaro and Edri 2017* used one-dimensional numerical simulations to study TNT equivalence factors. It was found that TNT equivalence factors were not equal for overpressure and impulse. However, their variation of TNT equivalence factors is minor over the scaled distance range between  $3\text{m/kg}^{1/3}$  and  $40\text{m/kg}^{1/3}$ . For practical purposes, a single value of TNT equivalence for overpressure, and another one for impulse are appropriate for the blast load calculation in the scaled distance range between  $3\text{m/kg}^{1/3}$  and  $40\text{m/kg}^{1/3}$ . TNT equivalence factors for impulse from the numerical simulations are in a good agreement with the Eq. (3-31), whereas TNT equivalence factors for overpressure agree well with the updated equation by *Locking 2011*, given as

$$Eq_{TNT} = \frac{H_{D,HE}}{0.23138H_{D,TNT} + 0.7341H_{D,HE}} \quad (3-39)$$

However, Eq. (3-39) is not valid for the standard explosive TNT, since for TNT  $Eq_{TNT} = 1.036 \neq 1$ . To overcome this deficiency, *Grisaro and Edri 2017* proposed a new formula to derive TNT equivalence factors for overpressure as

$$Eq_{TNT} = \left( \frac{H_{D,HE}}{H_{D,TNT}} \right)^{0.3254} \quad (3-40)$$

### 3.4.5 Discussion on TNT equivalence

In Section 3.4, four different methods to derive TNT equivalence factors were discussed, i.e. theoretical method, laboratory tests, field tests and numerical method. It is worth mentioning that the applicable overpressure range for TNT equivalence of PETN listed in Table 3-6 is all less than 1MPa. For close-in detonations, e.g. a terrorist bombing, the peak overpressures are

normally higher than 1MPa. Based on the numerical study conducted by *Shin et al. 2015*, TNT equivalence factors of PETN vary relatively slightly in the scaled distance range from  $1\text{m/kg}^{1/3}$  to  $40\text{m/kg}^{1/3}$  (Figure 3-5). This means that the concept of TNT equivalence can be employed in this scaled distance range to predict the blast loads generated from detonations, in which a high explosive other than TNT is used. However, the equivalence factors vary significantly in the scaled distance range less than  $1\text{m/kg}^{1/3}$ , which results in peak side-on overpressures larger than 1.36MPa. For instance, the TNT equivalence factor varies from 0.90 to 2.84, if it is derived based on the side-on overpressure. Under such circumstances, the concept of TNT equivalence is no longer applicable for the blast load calculations.

Actually, the overpressure-time histories (Section 3.2) can be used to estimate both the peak overpressure and the maximum impulse. A TNT equivalence factor of 1.27 (Table 3-6), which is derived from field tests and is based on overpressure, is used to convert the explosive PETN used in the experiments (Chapter 5) to the reference explosive TNT. It should be pointed out that this TNT equivalent factor (1.27) is not based on impulse but on overpressure. However, the same value of 1.27 is estimated in *UFC 3-340-01* for the TNT equivalence factor for impulse. In addition, for the protective barrier configurations involved in this Dissertation, the peak overpressures are regarded as more important than the maximum impulse since the damage capability of a blast wave is conventionally predicted by the peak overpressure in its shock front (*Kinney and Graham 1985*). Therefore, this TNT equivalence factor (1.27) is used to calculate the charge mass in TNT equivalent, which is employed in the numerical simulations (Chapter 6) in order to estimate the peak overpressures and maximum impulses. Compared to the values of the peak overpressures and maximum impulses in a free field scenario, the effectiveness of protective barriers can be evaluated.

### 3.5 Diffraction process

Considering a shock wave hits a structure, e.g. a wall, the diffraction phenomenon plays a great role in the blast load distribution behind the structure. If the wall width is so large that an infinite assumption can be made, the diffraction process can be simplified into a two-dimensional case. Otherwise, a three-dimensional diffraction process should be considered. This section will briefly explain the diffraction process.

Figure 3-6 shows the diffraction process of a plane shock wave over a wall having an infinite width at successive stages. In Figure 3-6a, the incident plane shock wave I travels at shock velocity  $U_I$  along the rigid ground surface. At a certain time, as illustrated in Figure 3-6b, the shock wave encounters the wall protruding from the ground surface. The shock wave hits the front face of the wall at the normal incidence. Thus, the incident wave I is reflected and a reflected wave R is generated, which moves at shock velocity  $U_R$  in the opposite direction of  $U_I$ . Immediately after the impingement, the side-on overpressure at the front face is magnified to the reflected overpressure. As the reflected wave R moves back from the front face of the wall, a rarefaction wave emanating from the upper left corner moves down along the front face. Meanwhile, a vortex is shed from the upper left corner of the wall. The lower portion of the front face still experiences the reflected overpressure, whereas the upper portion experiences a lower overpressure quite near the side-on value. At the top surface of the wall, the incident

wave I continues on relatively undisturbed. The portion of the top surface immediately behind the incident wave I is subjected to the side-on overpressure, whereas the portion in the vicinity of the vortex is subjected to an overpressure of somewhat reduced value due to the influence of the vortex. In Figure 3-6c, the incident wave I has passed beyond the right end of the top surface. It flows around the upper right corner of the wall. A second vortex is formed at the upper right corner of the wall. The wave reflected from the front face has been completely attenuated by the rarefaction wave and the overpressure at the front face is reduced to the stagnation pressure (the sum of the side-on overpressure and the dynamic drag pressure). At the top surface of the wall, the overpressure is still nearly equal to the side-on value. Behind the diffracted wave at the rear face, the value of overpressure is somewhat less than the side-on value due to the influence of the vortex. The peak overpressure at the rear face develops slowly as a result of the vortex formation and the long time required for the rear face to be enveloped by the shock wave. In Figure 3-6d, the incident wave has finally passed beyond the wall. This means that the diffraction process is over and the wall is immersed in the flow field behind the shock front.

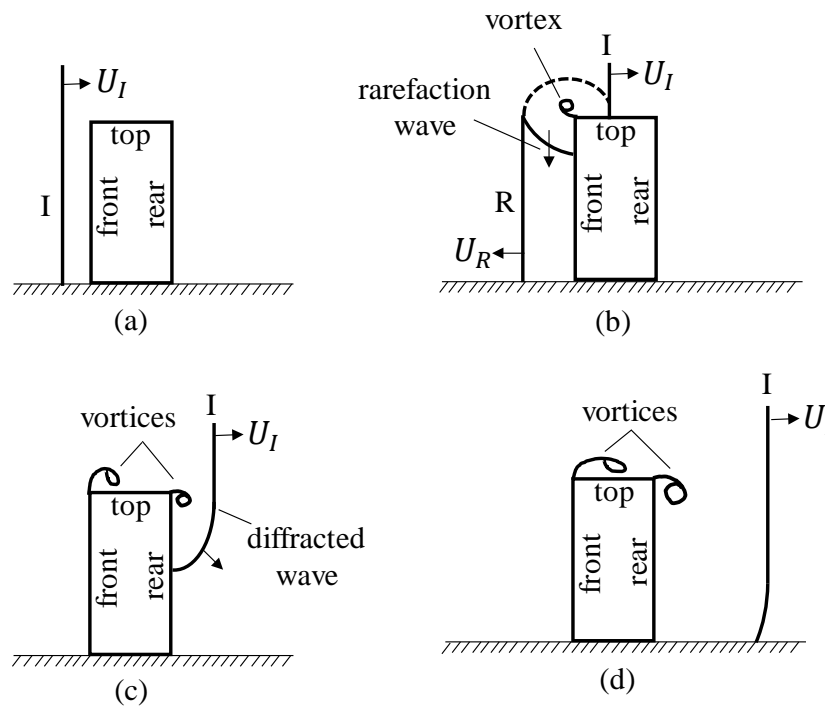


Figure 3-6: Diffraction of a plane shock wave over a wall having an infinite width in the out-of-plane direction, side view

Figure 3-7 illustrates the diffraction process of a plane shock wave over a wall having a finite width at successive stages. In Figure 3-7a, the incident shock wave I moves at shock velocity  $U_I$  towards the front face of the wall. Since the wall width is relatively small, the diffraction phenomenon occurs not only over the top surface of the wall (as already shown in Figure 3-6b) but also around the sides of the wall (Figure 3-7b). The overpressure-time history at the front face of the wall is affected by both the rarefaction wave emanating from the top surface of the wall (Figure 3-6b) and the ones from the sides of the wall (Figure 3-7b). As a result, they reduce the reflected overpressure at the front face of the wall to a somewhat larger extent compared to the wall having an infinite width. For a wall having a finite width, the shock wave flows not

only over the top surface (Figure 3-6c) but also around the sides of the wall (Figure 3-7c). At a later time, these parts of the shock wave merge again behind the rear face of the wall, which may give rise to an overpressure increase. Lastly, the wall is engulfed by the shock wave and the diffraction process is regarded as complete (Figure 3-7d).

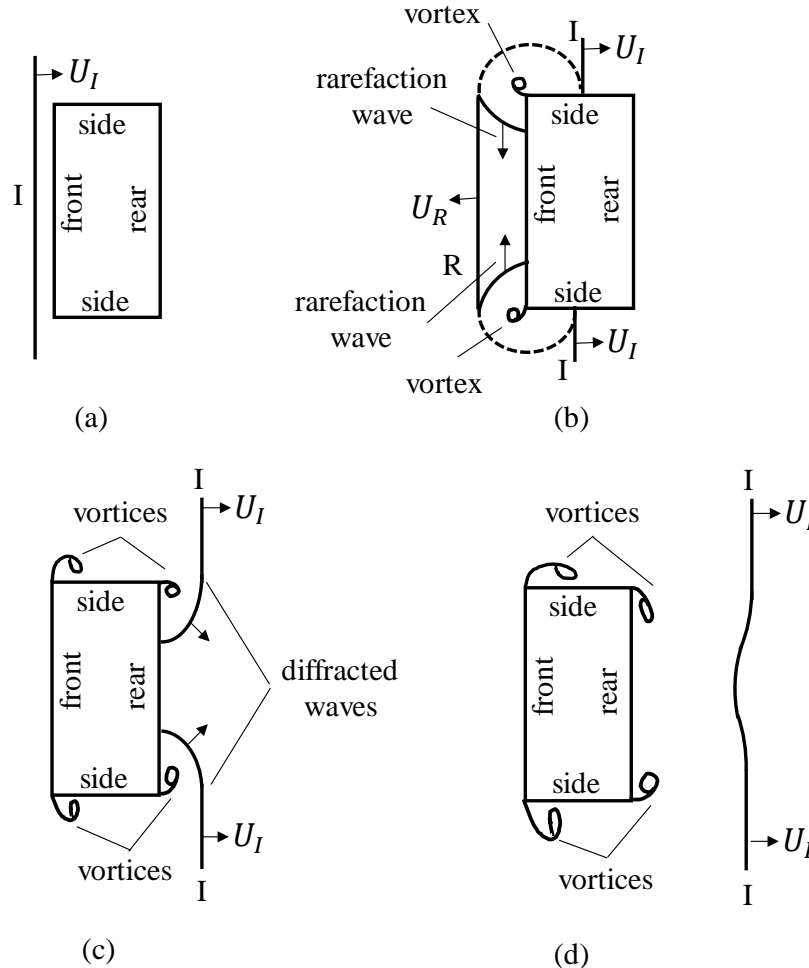


Figure 3-7: Diffraction of a plane shock wave over a wall having a finite width, plan view

In most studies of shock waves travelling around a structure, it is often expedient to assume that the exterior surfaces of the structure are rigid. However, if the structure or parts of it do not behave rigidly, a certain amount of blast energy is absorbed by the structure through the structural deformations. In addition, it is also assumed that the flow is inviscid and non-heat conducting. Actually, some energy exchange occurs between the shock wave and the structure due to heat transfer, cavitation and so forth. Hence, a certain amount of the blast energy is lost during the reflection and diffraction processes.

### 3.6 Drag coefficient

The blast loads (overpressures and impulses) on a structure (e.g. a column) primarily depend on the stand-off distance from the charge to the column, the angle of incidence of the shock wave and the flow resistance of the cross-sectional shapes. In order to

quantify the resistance of the cross-sectional shapes, the drag coefficient  $C_d$  is introduced. It is a dimensionless ratio between two energy items, giving that

$$C_d = \frac{\frac{p_d}{\rho}}{\frac{1}{2}u^2} = \frac{2p_d}{\rho u^2}. \quad (3-41)$$

The first one ( $p_d/\rho$ ) corresponds to the energy required to overcome the drag force.  $p_d$  is the pressure drop which represents the drag force per unit projected area.  $\rho$  is the air density. The second one ( $\frac{1}{2}u^2$ ) is the kinetic energy pertinent to the air velocity  $u$ . If the air is regarded as an ideal gas, the air density can be expressed as

$$\rho = \frac{p}{R_s T}, \quad (3-42)$$

where  $R_s$  is the specific gas constant for air.  $p$  and  $T$  are the air pressure and temperature. Assuming the air density is not affected by the structure on which the drag forces are exerted, the drag coefficient is obtained by substituting Eq. (3-42) into Eq. (3-41)

$$C_d = \frac{2p_d R_s T}{p u^2}. \quad (3-43)$$

Inserting Eq. (3-2) and Eq. (3-3) into Eq. (3-43), one yields

$$C_d = \frac{2p_d}{\gamma M^2 p}, \quad (3-44)$$

where  $M$  is the Mach number of the air flow.

Thus, the pressure drop  $p_d$  can be determined by rewritten Eq. (3-44) as

$$p_d = \frac{1}{2} C_d \gamma M^2 p. \quad (3-45)$$

Experiments showed that the drag coefficient  $C_d$  depends on the geometry of structures and the associated flow pattern passing through the structures. Figure 3-8 illustrates the flow pattern passing through a thin flat plate. If the plate has an infinite width (in the out-of-plane direction), the drag coefficient approaches two ( $C_d \rightarrow 2$ , Figure 3-9). For a plate with a finite width, the air flows from the high-pressure region (upstream,  $p_{up}$ ) around the free edges into the low-pressure region (downstream,  $p_{down}$ ). It reduces the pressure drop  $p_d$  across the plate and hence reduces the associated drag coefficient  $C_d$ . If the air flows around rounded structures, less turbulence occurs in the downstream compared to other structural shapes. Therefore, rounded structures exhibit a smaller drag coefficient than the other shapes.

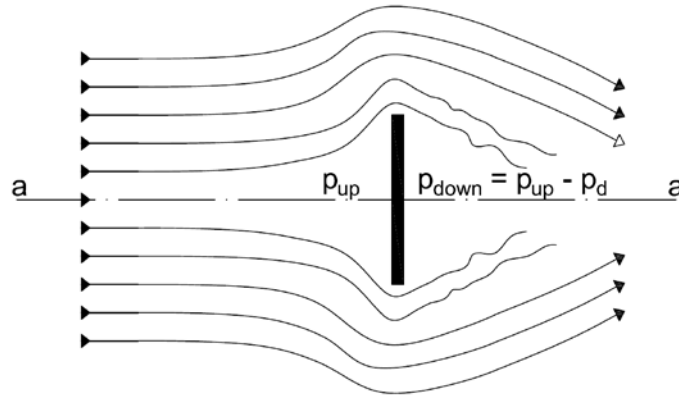


Figure 3-8: Typical flow pattern around a thin flat plate, line a-a marks a plane of symmetry

Figure 3-9 shows exemplarily the drag coefficients  $C_d$  for various structural shapes (Kinney and Graham 1985). The flow direction is from left to right. It should be noted that the values for the structural shapes and the protuberances are only valid for relatively long members such that the flow around the end edges is not a major issue.

Bodies of revolution					
		$C_d$		$C_d$	
sphere		0.10	circular plate		1.17
half sphere		0.42	60° cone		0.50
half sphere		1.42			

Structural shapes (long members without end effects)					
	$C_d$		$C_d$		$C_d$
	2.00		1.80		1.55
	2.00		1.45		2.00
	1.65		2.20		2.00
	2.05		1.20		1.55
	2.00		2.30		1.05
			1.20		1.54

Protuberances (without end effects)			
	$C_d$		$C_d$
	0.80		1.03
	1.20		1.00
	1.25		1.28

Figure 3-9: Drag coefficients for various structural shapes (Kinney and Graham 1985)

It should be noted that the blast winds generated from an explosion exert forces on a structure in quite a similar way to the natural winds. However, the forces developed by the blast winds are of considerably greater magnitude than the ones developed by the ordinary winds. In addition, the drag coefficient is not a constant but varies with the velocity and direction of the flow, the position and shape of the obstacles, the density and viscosity of the fluid.

### 3.7 Clearing effect

As a shock wave generated from a surface burst hits the front face of a structure having finite dimensions (e.g. a wall, Figure 3-10) at the normal incidence, normal reflection of the shock wave occurs. The incident wave is reflected from the front face immediately after the impingement. Thus, a reflected wave is generated and the side-on overpressure is instantly magnified to the reflected overpressure. Since the reflected overpressure is significantly larger than the overpressure in the surrounding air, the air flows from high-pressure region to low-pressure region. This air flow proceeds as a rarefaction wave propagating inwards from the free edges of the front face and moving at the sonic velocity in the air of the reflected region, as already shown in the previous section. This pressure relief phenomenon is referred to as the clearing effect.

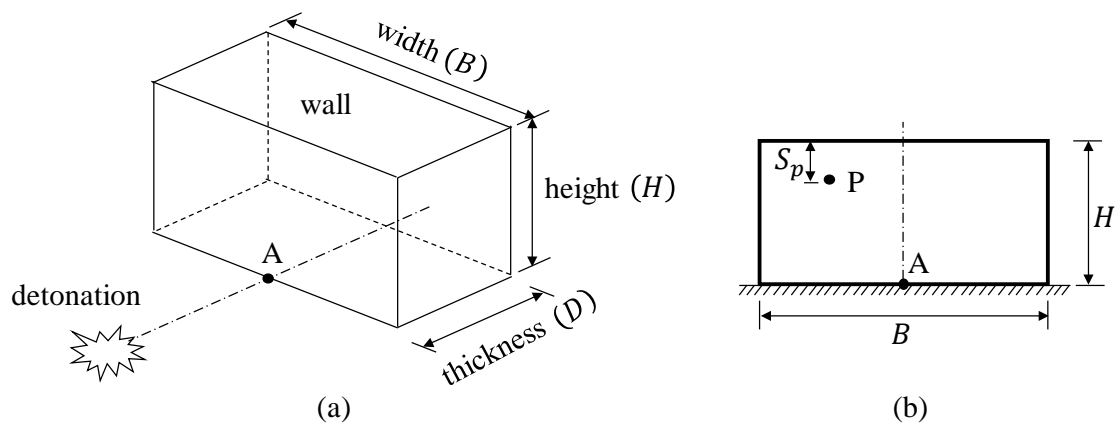


Figure 3-10: Sketch of the clearing effect at the front face of a wall having finite dimensions (a) three-dimensional wall structure; (b) observation point  $P$  at distance  $S_p$  from the nearest edge, front view

In the following subsections, the clearing correction methods are presented either for an observation point on the front face of a structure (Subsection 3.7.1) or averaged over the entire front face (Subsection 3.7.2).

#### 3.7.1 Clearing correction method for an observation point

Consider a point  $P$  (Figure 3-10b), which is located on the front face at distance  $S_p$  from the nearest edge, this point initially experiences the peak reflected overpressure until the rarefaction wave arrives at it. From this moment, the rarefaction wave starts to relieve the overpressure at point  $P$ . The arrival of the rarefaction wave at point  $P$

occurs at time  $t_1$  after the arrival time  $t_a$  of the shock wave (Figure 3-11a). The time  $t_1$  is given as

$$t_1 = \frac{S_p}{c_r}, \tag{3-46}$$

where  $c_r$  is the sonic velocity in the air of the reflected region. Figure 3-12 depicts the dependence of the sonic velocity  $c_r$  on the peak side-on overpressure  $p_{so}$ .

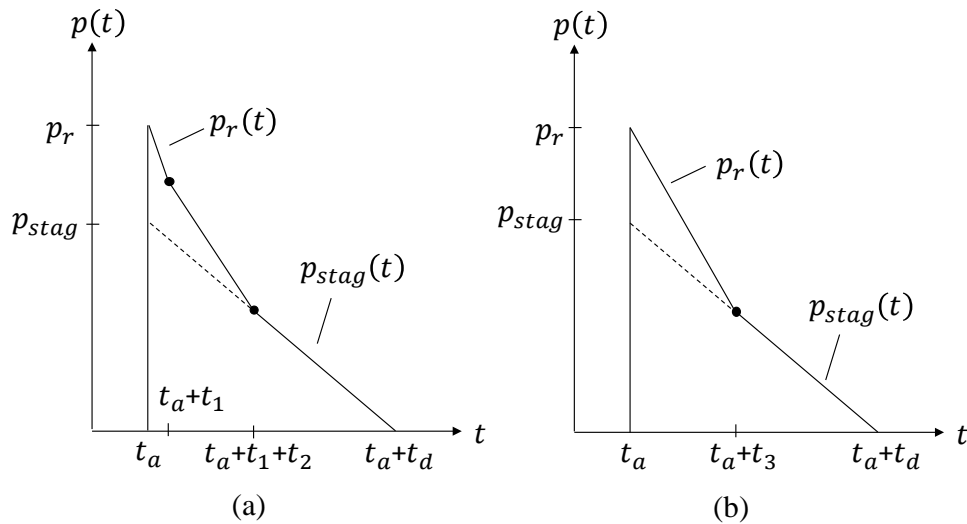


Figure 3-11: Overpressure-time histories at the front face due to the influence of the clearing effect (a) observation point P at distance  $S_p$  from the nearest edge; (b) simplified form

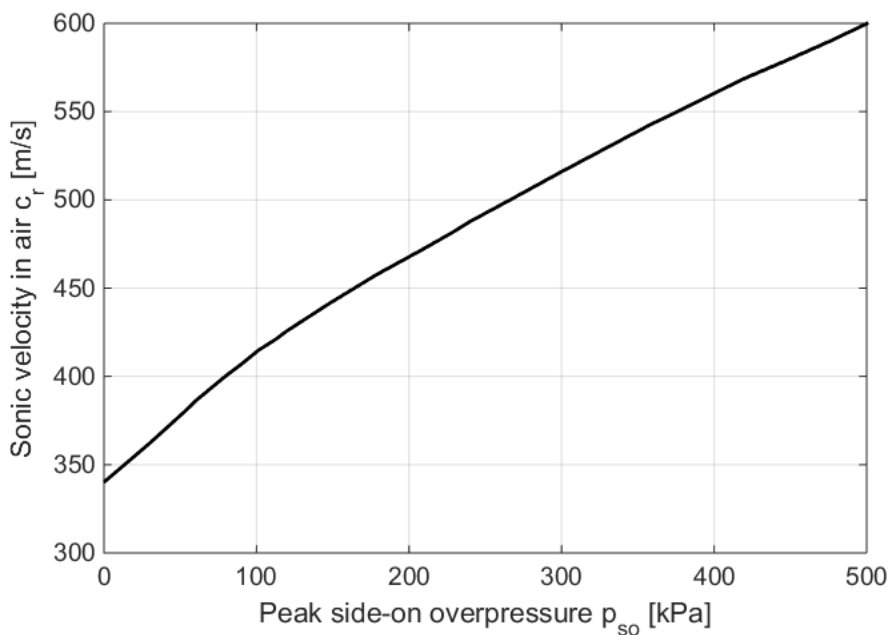


Figure 3-12: Sonic velocity  $c_r$  in the air of the reflected region versus peak side-on overpressure  $p_{so}$  (data from *UFC 3-340-02*)

It is found that the time  $t_2$  required to complete the pressure relief process is about twice as large as time  $t_1$ . It yields

$$t_2 = 2t_1 = \frac{2S_p}{c_r}. \quad (3-47)$$

After time  $t_a + t_2$ , point P experiences the stagnation pressure, i.e. the sum of the side-on overpressure and the dynamic drag pressure. The stagnation pressure  $p_{stag}$  is given as

$$p_{stag}(t) = p_{so}(t) + c_d q(t), \quad (3-48)$$

where  $c_d$  is the drag coefficient (Section 3.6), which varies with the Mach number of the incident wave and the geometry of the structure. A value of  $c_d = 1$  at the front face is usually adequate for the pressure ranges of interest.  $q$  is the dynamic pressure. Between times  $t_a + t_1$  and  $t_a + t_2$ , the overpressure is intermediate between the reflected overpressure  $p_r$  and the stagnation pressure  $p_{stag}$  (Figure 3-11a).

It is worth mentioning that, on the one hand, earliest pressure relief effect occurs for points at the free edge of the front face. On the other hand, the reflection effect is experienced longest at the point furthest from the free edge. Accounting for these both effects, the overpressure-time history at observation point P can be simplified by a line intermediate between the reflected overpressure  $p_r$  at arrival time  $t_a$  of the shock wave to the stagnation pressure  $p_{stag}$  at time  $t_3$  later (Figure 3-11b), which is defined as

$$t_3 = t_1 + t_2 = \frac{3S_p}{c_r}. \quad (3-49)$$

Usually, the time  $t_3$  is referred to as the clearing time  $t_c$  in the literature, which is the time required for the pressure relief to be completed after the arrival of the shock wave. The clearing time  $t_c$  depends on the dimensions of the front face and the sonic velocity  $c_r$  in the air of the reflected region.

### 3.7.2 Clearing correction method averaged over the front face

*UFC 3-340-02* proposed an empirical clearing correction method (Figure 3-13), which does not seek to correct the spatial distribution of the relieved overpressure but to correct the maximum impulse exerted to the structure. Some assumptions are made for this empirical clearing correction method:

- The pressure relief acts uniformly over the entire front face.
- The pressure relief begins immediately after the arrival of the shock wave at the front face.
- The relieved overpressure-time history decays linearly from the peak reflected overpressure  $p_r$  to the stagnation pressure  $p_{stag}$  over the clearing time  $t_c$ . After time  $t_a + t_c$ , the front face experiences the stagnation pressure.

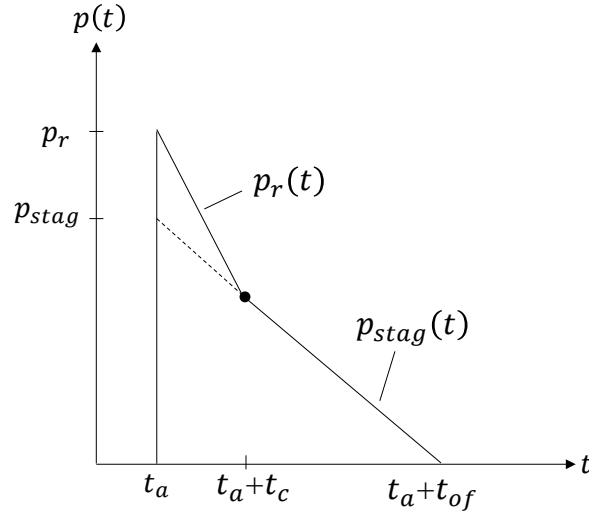


Figure 3-13: Empirical clearing correction method according to *UFC 3-340-02*

According to *UFC 3-340-02*, the average clearing time  $t_c$  needed to completely relieve the reflected overpressure at the front face is given as

$$t_c = \frac{4S}{(1 + R)c_r} = \frac{4BH}{(B + 2H)c_r}, \quad (3-50)$$

where  $S$  is the smaller of the wall height  $H$  and the half wall width  $B/2$  (Figure 3-10).  $G$  is larger one.  $R$  is the ratio of  $S$  to  $G$ .

The positive phase duration  $t_{of}$  is so selected that the triangular form of the side-on overpressure-time history has the same maximum impulse  $i_s$  as the experimental recording. This yields

$$t_{of} = \frac{2i_s}{p_{so}}. \quad (3-51)$$

However, this method has two inherent drawbacks. Firstly, the reflected overpressure-time history is approximated by using a linearly decay form rather than an exponentially decay form. Secondly, it is assumed that the rarefaction wave begins to relieve the overpressure immediately after the arrival of the shock wave. Therefore, the calculation of the clearing time  $t_c$  is somewhat in doubt. As proposed by *Rickman and Murrell 2007*, the arrival time  $t_{rare}$  of the rarefaction wave at the observation point P should be defined as

$$t_{rare} = t_i + \Delta t + \frac{S_p}{c_r}, \quad (3-52)$$

where  $t_i$  is the arrival time of the incident wave at the observation point P.  $\Delta t$  is the difference in the arrival time of the shock wave between the observation point P and the nearest free edge.

Theoretically, no pressure relief occurs if the dimension of the front face hit by the shock wave is so large that an infinite assumption can be made. Figure 3-14 compares

the overpressure-time history at the front face of a wall having infinite dimensions to that of a wall having finite dimensions.

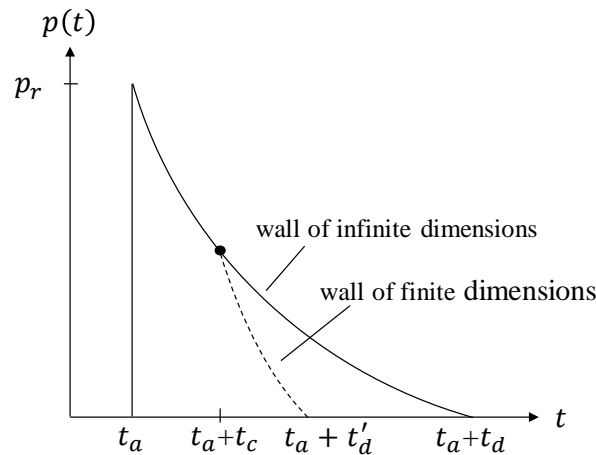


Figure 3-14: Reflected overpressure-time histories at the front face of walls having infinite and finite dimensions

The clearing effect of the shock wave is apparent from the overpressure-time histories illustrated in Figure 3-14. The overpressure-time history of the wall having finite dimensions exhibits a sharp overpressure drop since time  $t_c$  after the arrival time  $t_a$  of the shock wave. It should be noted that the peak reflected overpressure  $p_r$  remains unchanged, since the incident overpressure is instantly magnified to the reflected overpressure immediately after the impingement of the shock wave on the front face. However, the rarefaction wave reduces the reflected overpressure in the late-time portion of the positive phase and therefore reduces the maximum impulse of the positive phase. In addition, the impulse reduction due to the clearing effect is more pronounced for small-size structures than for larger-size structures (Rigby *et al.* 2014). This is attributed to the earlier onset of the pressure relief phenomenon, since the distance over which the rarefaction wave needed to travel from the free edge to the observation point is shorter at a small-size structure than at a large-size structure.

### 3.8 Type of burst

Depending on the location of the charge with respect to the ground surface, the detonations can be classified into three different burst types, i.e. free-air burst (Figure 3-15a), surface burst (Figure 3-15b) and height-of-burst detonation (Figure 3-15c).

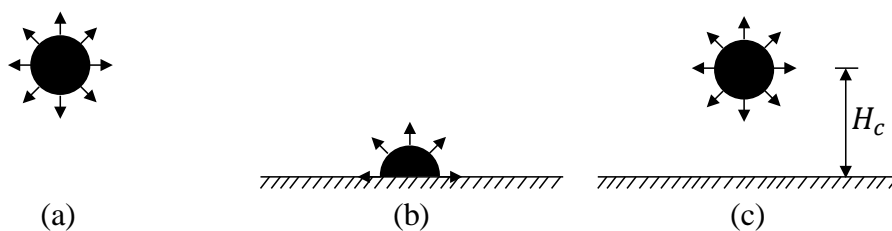


Figure 3-15: Configurations of different burst types (a) free-air burst; (b) surface burst; (c) height-of-burst detonation

The different burst types will be briefly described in the following subsections.

### 3.8.1 Free-air burst

The charge is detonated so high above the ground and so distant from the target structure that the incident wave does not impinge the ground surface before it impinges the target structure. Since the released explosive energy is distributed over a sphere, it is assumed that the shock wave generated from free-air bursts propagates spherically.

### 3.8.2 Surface burst

The charge is detonated on or very near to the ground. Since the released explosive energy is spread over a hemi-sphere, it is assumed that the shock wave generated from surface bursts propagates hemi-spherically. Furthermore, it is assumed that the incident wave and the wave reflected from the ground surface are so rapidly merged after reflection that a single, reinforced wave is formed immediately after reflection. This wave has similar characteristics as that in a free-air burst, but it has greater blast energy. The portion of the energy  $E'$  reflected from the ground surface depends on how perfect a reflector or how perfect an absorber the ground surface is. In other words, how little energy is imparted to the ground in the crater formation and ground shock generation. For a perfect reflector, it holds that  $E' = 2E$  ( $E$  is the released energy in the free-air burst using the same charge mass as the surface burst), whereas for a perfect absorber, it holds that  $E' = E$ . Actually, the energy  $E'$  lies between these limits, i.e.  $E < E' < 2E$ . If the ground surface is considered as a perfectly rigid surface, no energy is lost in the crater formation and ground shock generation, a surface burst would be equivalent to a free-air burst using twice the charge mass as the surface burst. As observed by *Smith and Hetherington 1994*, the free-air burst and the surface burst are closely related. Some energy (about 20%) is lost in the crater formation and ground shock generation, which means that a surface burst would be equivalent to a free-air burst using a 1.8 times the charge mass as the surface burst.

### 3.8.3 Height-of-burst detonation

The charge is detonated at a certain height above the ground. On the one hand, the charge height is too small to be considered as a free-air burst, since the reflection from the ground surface cannot be neglected. On the other hand, the charge height is too large to be considered as a surface burst, because the wave reflected from the ground surface does not merge with the incident wave immediately after the reflection. Hence, this detonation is neither a free-air burst nor a surface burst. The resulting shock wave propagation is neither spherical nor hemi-spherical.

The blast environment from a height-of-burst detonation is illustrated in Figure 3-16. Point A depicts a point of observation on the ground at a horizontal distance  $R$  from ground zero (GZ). The angle of incidence  $\alpha$  is defined as the angle between the vertical line through the charge centre and the line connecting the charge centre to the observation point A. For locations away from ground zero (GZ), the angle of incidence  $\alpha$  grows from  $0^\circ$  to  $90^\circ$ . The region where the incident and reflected waves have not merged to form a Mach stem is referred to as the region of regular reflection (RR); the region where they have merged is referred to as the region of

Mach reflection (MR). The minimum angle of incidence for the Mach stem formation is denoted as  $\alpha_{min}$ , which will be further discussed later in this section. The point at which the Mach stem begins to form is denoted as the origin of the triple point path (OTP). The intersection point of the incident wave (I), the reflected wave (R) and the Mach stem (M) is referred to as the triple point (T). An overview of the available models to describe the triple point path is given in *Xiao et al. 2018a*. As the Mach stem travels along the ground surface (x-direction), the triple point rises in y-direction and the height of the triple point  $H_T$  increases. The characteristics of the Mach stem depend on the charge height  $H_c$ , charge mass  $W$  and properties of the reflecting surface (roughness and hardness).

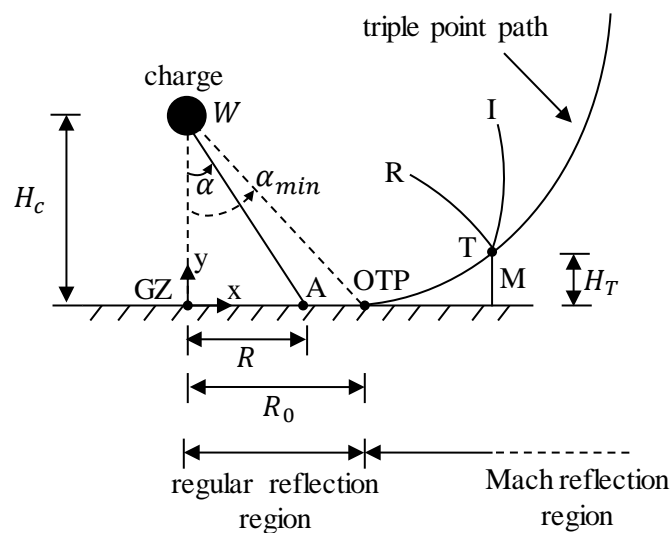


Figure 3-16: Blast environment from a height-of-burst detonation

The spherical shock waves interacting with the ground surface (considered as a rigid reflecting surface) is demonstrated in Figure 3-17, in which the pressure contours at successive times after a detonation near the ground surface are shown. Before the shock front impinges on the ground surface, the incident wave (I) is unimpeded, as shown in Figure 3-17a. At a short time later, soon after impingement on the ground surface, the strength of the incident wave (I) is augmented by the reflection effects, as demonstrated in Figure 3-17b. The reflected wave (R) travels through a region that is heated by the incident wave (I) as it passes. Hence, the air in this region is hotter and denser than the ambient atmosphere. Since the angle of incidence  $\alpha$  is less than  $\alpha_{min}$  (Figure 3-16), regular reflection occurs. Due to the greater shock velocity in heated air, a portion of the reflected wave (R) can, under appropriate conditions, overtake and merge with the incident wave (I, Figure 3-17c). The angle of incidence  $\alpha$  is equal to  $\alpha_{min}$  (Figure 3-16), the Mach stem starts to form at the ground surface. As the shock wave further propagates, the angle of incidence  $\alpha$  becomes greater than  $\alpha_{min}$  (Figure 3-17d). The incident wave (I) and the reflected wave (R) merge and form a single wave called the Mach stem (M), which produces a higher peak overpressure at and near the ground surface than would be produced at the same distance in a free-air burst scenario. The triple point (T) at which the incident wave (I), the reflected wave (R) and the Mach stem (M) meet marks the top of the Mach stem. It should be pointed out that at any instant the triple point is actually not a point, but a horizontal circle with its centre on the vertical line through the charge centre, so it appears as a point on a sectional

drawing. The configuration of the three shock fronts is usually denoted as “Mach-Y”. At a much later time, since the distance travelled by the shock wave is appreciably greater than the charge height, the incident and reflected shock wave are merged into a single wave, as shown in Figure 3-17e. Therefore, the shock wave propagation can be considered as hemi-spherical.

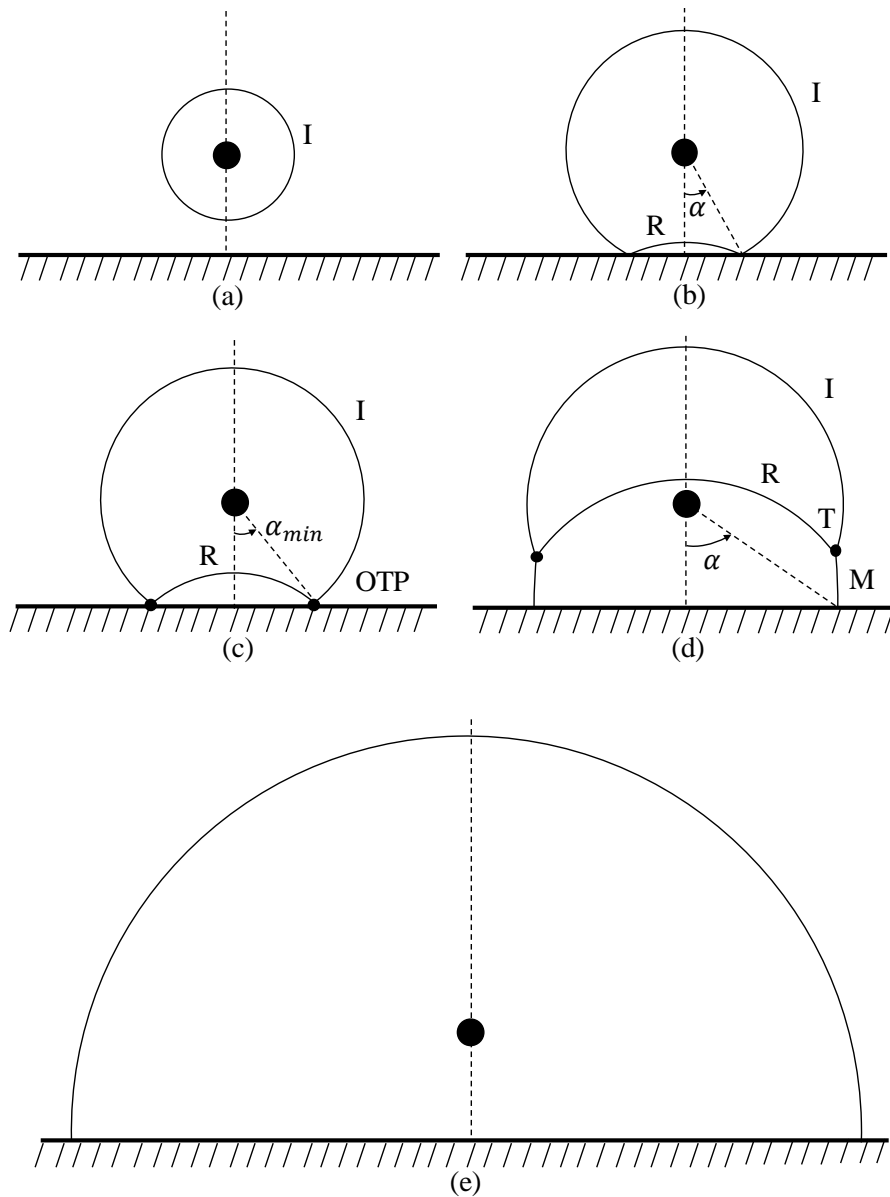


Figure 3-17: Schematic pressure contours at successive times after a detonation near the ground surface (a) unimpeded shock wave in the atmosphere; (b) regular reflection of the shock wave at angles of incidence  $\alpha < \alpha_{min}$ ; (c) generation of the origin of the triple point path at angle of incidence  $\alpha = \alpha_{min}$ ; (d) Mach stem formation at angles of incidence  $\alpha > \alpha_{min}$ ; (e) surface burst behaviour at distances appreciably larger than the charge height (adapted from Kinney and Graham 1985)

As aforementioned, the Mach stem forms when an incident wave impinges on the ground surface at an angle of incidence that is too large to allow regular reflection, i.e.  $\alpha > \alpha_{min}$ . The minimum angle of incidence  $\alpha_{min}$  for a given inverse shock strength  $\xi$  (Eq. (3-56)) at which Mach reflection occurs is analytically expressed by Eichinger 1985 as

$$[2x(\eta^2 x^2 + 1)]^2 - 4 \left\{ \begin{array}{l} [\gamma(\eta(1 + x^2(\eta - 1)) - 1) + \eta(1 + x^2)]^2 \\ -[\eta^2 x^2 + 1]^2 \end{array} \right\} = 0, \quad (3-53)$$

where

$$x = \tan\left(\frac{\pi}{2} - \alpha_{min}\right), \quad (3-54)$$

$$\eta = \frac{\rho_1}{\rho_2} = \frac{\frac{\gamma + 1}{\xi} + \gamma - 1}{\frac{\gamma - 1}{\xi} + \gamma + 1}, \quad (3-55)$$

$\rho_1$  and  $\rho_2$  are the air densities of the incident and reflected wave. The inverse shock strength  $\xi$  is defined as the ratio of the atmospheric pressure  $p_0$  ahead of the shock front to the pressure  $p_1$  at the shock front as

$$\xi = \frac{p_0}{p_1} = \frac{p_0}{p_{so} + p_0}. \quad (3-56)$$

Thus, the inverse shock strength  $\xi$  is always less than 1. The stronger the shock wave, the lower the inverse shock strength.

Using Eq. (3-56) and Eq. (3-8), one can get the relation between the Mach number  $M_i$  and the inverse shock strength  $\xi$  of the incident wave as

$$M_i = \sqrt{\frac{6(1 - \xi)}{7\xi} + 1}. \quad (3-57)$$

Figure 3-18 (pink line) shows the minimum angle of incidence  $\alpha_{min}$  versus the Mach number  $M_i$  of the incident wave using the analytical formulae of *Eichinger 1985* (Eq. (3-53)), which matches very well to the experimental data from *Baker 1973*.

In addition, *Kinney and Graham 1985* proposed an empirical hyperbolic equation to portray the data derived from a series of computational results for the minimum angle of incidence  $\alpha_{min}$  as

$$\alpha_{min} = \frac{1.75}{M_i - 1} + 39. \quad (3-58)$$

As shown in Figure 3-18 (black line), the minimum angle of incidence  $\alpha_{min}$  for the Mach stem formation derived from Eq. (3-58) is only slightly different to the other two sources (*Baker 1973* and *Eichinger 1985*). If  $M_i$  approaches unity ( $M_i \rightarrow 1$ ), i.e. a very weak shock wave, the regular reflection occurs at all angles of incidence between  $0^\circ$  and  $90^\circ$ . In general, regular reflection occurs when the angle of incidence  $\alpha$  is sufficiently small or when the shock wave is sufficiently weak, i.e.  $M_i \rightarrow 1$  or  $\xi \rightarrow 1$ . As  $M_i$  increases, the minimum angle of incidence

$\alpha_{min}$  decreases rapidly. For instance, it reaches approximately  $\alpha_{min} = 52^\circ$  at a Mach number  $M_i$  of 1.1.

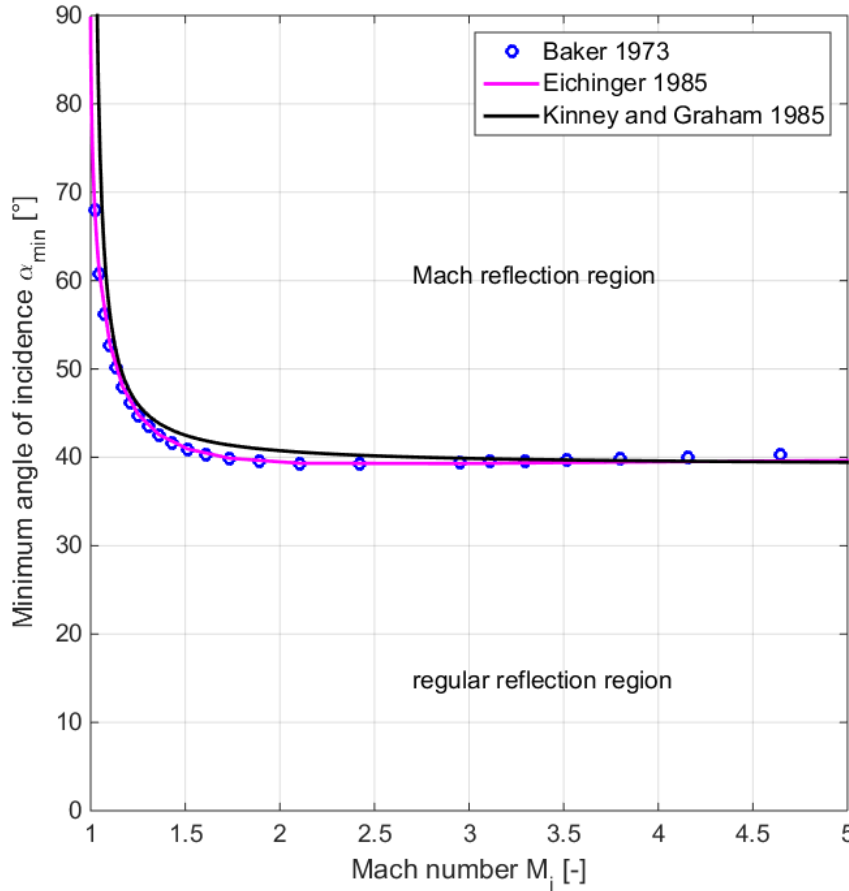


Figure 3-18: Angle of incidence for transition from regular reflection region to Mach reflection region

Given the minimum angle of incidence  $\alpha_{min}$ , the distance  $R_0$  (Figure 3-16) between the ground zero (GZ) and the origin of the triple point path (OTP) can then be calculated as

$$R_0 = H_c \tan \alpha_{min} . \quad (3-59)$$

In order to calculate the distance  $R_0$  without information of the minimum angle of incidence  $\alpha_{min}$ , *Needham 2010* proposed an empirical formula for nuclear explosions as

$$R_0 = \begin{cases} 0.825H_c & \text{if } H_c < 0.9925\text{m/kg}^{1/3} \\ \frac{170H_c}{1 + 25.505H_c^{0.25} + 1.7176 \cdot 10^{-7}H_c^{2.5}} & \text{if } H_c > 0.9925\text{m/kg}^{1/3} \end{cases} , \quad (3-60)$$

where  $H_c$  is the charge height. Although this formula is obtained from nuclear explosions, they can also be used for conventional high explosive tests (*Needham 2010* and *Boutillier et al.*

### Chapter 3 - Shock wave propagation

2018). According to Eq. (3-60), the minimum angle of incidence  $\alpha_{min}$  is  $39.52^\circ$  if  $H_c < 0.9925m/kg^{1/3}$ .

*Kinney and Graham 1985* also proposed a hyperbolic formula for the distance  $R_0$  as

$$R_0 = W^{\frac{1}{3}} \left( \frac{45.4}{7.4 - \frac{H_c}{W^{\frac{1}{3}}}} - 6.3 \right). \quad (3-61)$$

This formula is derived for reference nuclear explosions of one kiloton TNT and is valid for scaled charge heights  $H_c/W^{1/3}$  between  $2m/kg^{1/3}$  and  $6m/kg^{1/3}$ . In addition, the authors proposed also a hyperbolic formula as

$$R_1 = W^{\frac{1}{3}} \left( \frac{2.6}{1.8 - \frac{H_c}{W^{\frac{1}{3}}}} - 1.5 \right), \quad (3-62)$$

to describe the horizontal distance  $R_1$  between the ground zero (GZ) and the transition point from Mach reflection region to surface burst behaviour. It is assumed that the energy loss in the crater formation and ground shock generation is negligible.

Figure 3-19 shows two curves, which represent the transition from regular reflection region to Mach reflection region and the transition from Mach reflection region to surface burst behaviour, respectively.

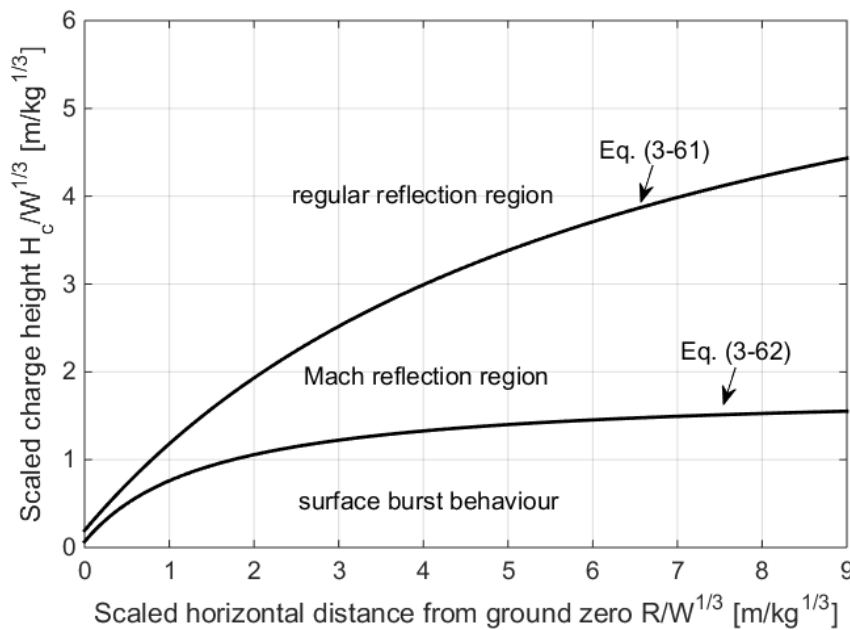


Figure 3-19: Transition from regular reflection region to Mach reflection region and transition from Mach reflection region to surface burst behaviour for the reference nuclear explosion of one kiloton TNT

As described in Eq. (3-61) and Eq. (3-62), the critical scaled charge heights  $H_c/W^{1/3}$  for both transitions depend on the scaled horizontal distance  $R/W^{1/3}$  from the ground zero to the observation point. In practice, however, a transition occurs over a zone rather than at a well-defined point. It is worth mentioning that due to the dust cloud near the ground, the actual origin of the triple point path (OTP) is usually not accurately known. Therefore, much of the experimental data in the literature gives conflicting results of the origin of the triple point path (OTP).

In Figure 3-18, it is assumed that the minimum angle of incidence for the Mach reflection is equal to the maximum angle of incidence for the regular reflection. However, for strong shock waves, there is a domain of the angle of incidence where both regular reflection and Mach reflection are possible. *Von Neumann 1943* analysed the shock wave configurations in his classical work, in which two principal criteria for strong shock waves ( $M_i > 2.2$ ) were derived, i.e. von Neumann or mechanical equilibrium criterion  $\alpha_N$  and detachment criterion  $\alpha_D$ . Based on these criteria, the transition from regular reflection to Mach reflection can be predicted (Figure 3-20).

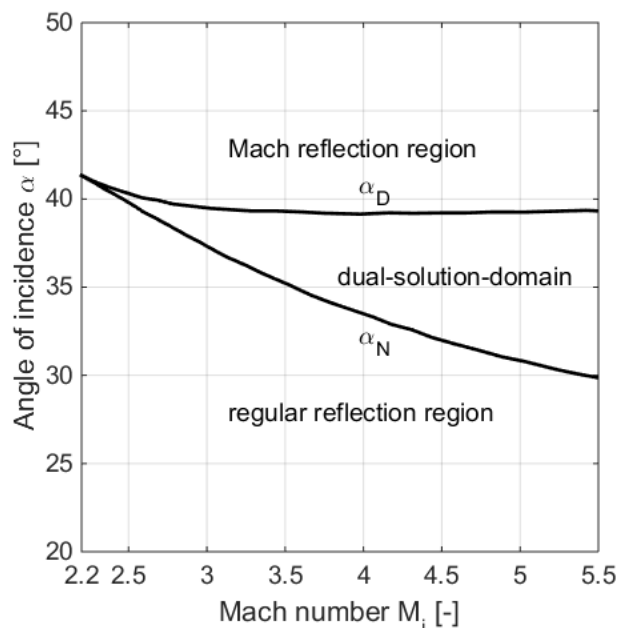


Figure 3-20: Dual-solution-domain between regular reflection and Mach reflection regions (data from *Ivanov 2001*)

As shown in Figure 3-20, only regular reflection occurs if  $\alpha < \alpha_N$ . If  $\alpha > \alpha_D$ , only Mach reflection is possible. In the range  $\alpha_N < \alpha < \alpha_D$ , both reflection types are theoretically possible. This region is referred to as the dual-solution-domain (DSD).

### 3.9 Summary: shock wave propagation

This chapter describes the shock wave propagation phenomenon. Firstly, basic parameters of shock waves are introduced and different forms of overpressure-time histories are depicted and compared. Secondly, three fundamental principals in the field of air blast, i.e. Hopkinson-Cranz scaling law, Sachs scaling law and TNT

### **Chapter 3 - Shock wave propagation**

---

equivalence, are described. Thirdly, the diffraction process is briefly explained. After that, the drag coefficient and the clearing effect are introduced and briefly depicted. Lastly, three different types of burst are discussed. This chapter provides a theoretical background to describe the process of shock wave propagation, which is crucial for the experimental and numerical investigations on the effectiveness of protective barriers (Chapters 5 and 6).

## 4 Theoretical background of numerical simulations

This chapter provides a theoretical background of the numerical simulations in this Dissertation. In order to gain understanding of the complex phenomena occurring in the high dynamic events, both experiments and numerical simulations are usually conducted. The experiment data can be used to validate the developed numerical models. However, experiments often require many resources and their cost could be prohibitive. Nowadays, numerical simulations have been used to represent the physical problem underlying the high dynamic events, mainly due to the continuous advancements in the computational capacity. Therefore, numerical simulations are regarded as a feasible complement to experiments. As long as a numerical model is verified and validated, it can be employed to investigate numerous blast scenarios, which may be impractical to be realized by experiments. Furthermore, it enables the user to obtain a deeper insight and a better understanding of the material behaviours and the underlying physical processes.

### 4.1 Basic aspects of numerical simulations

Numerical methods have been successfully used to model high dynamic events (e.g. *Hiermaier 2008, Teich 2012, Döge 2012* and *Esteban 2017*). Some basic aspects of numerical simulations, i.e. material models (Section 4.1.1), time step control (Section 4.1.2), element formulations (Section 4.1.3), mapping techniques (Section 4.1.4) and Fluid-Structure-Interaction (FSI) algorithm (Section 4.1.5), will be briefly explained in the following subsections.

#### 4.1.1 Material models

For a specific material, the constitutive relation is defined by the material model. Generally, the material model is composed of two parts, i.e. a deviatoric part and a hydrostatic part (*Hiermaier 2008, Esteban and Gebbeken 2016* and *Esteban and Gebbeken 2017*). The former is represented by the strength model, in which the deviatoric stresses are related to strain, strain rate, pressure and material damage. The latter is described by the Equation of State (EoS), in which the hydrostatic pressure of the material is related to the density and the specific internal energy of the material. In order to identify the parameters of the strength model and the EoS, a variety of material tests must be carried out.

This Dissertation involves three different material models needed to be specified (Chapter 6). These are air, high explosive material (PETN and TNT) and structural material (steel). The material models of these three materials will be described in the following subsections.

##### 4.1.1.1 Air

The air is regarded as an ideal gas. The ideal gas law is expressed as

$$pV = nRT, \quad (4-1)$$

where  $p$  and  $T$  are the absolute pressure and temperature, respectively.  $V$  is the volume of the ideal gas.  $R$  is the ideal gas constant,  $R = 8.314\text{J}/(\text{K}\cdot\text{mol})$  for air.  $n$  is the amount

## Chapter 4 - Theoretical background of numerical simulations

---

of substance of the ideal gas, which is the ratio of the mass  $m$  to the molar mass  $M$  of the ideal gas, given as

$$n = \frac{m}{M}. \quad (4-2)$$

Inserting Eq. (4-2) into Eq. (4-1), the ideal gas law is rewritten as

$$p \frac{V}{m} = \frac{R}{M} T. \quad (4-3)$$

Using the definition of density  $\rho = m/V$  and specific gas constant  $R_s = R/M$  ( $R_s = 287\text{J}/(\text{kg}\cdot\text{K})$  for air), the ideal gas law is further simplified as

$$p = \rho R_s T. \quad (4-4)$$

The software LS-DYNA (*LSTC 2017*) is used to carry out the numerical simulations in this Dissertation. The air is modelled via \*MAT\_NULL (*LSTC 2017*) and regarded as an ideal gas with a linear polynomial Equation of State (EoS), in which the pressure is given as

$$p = C_0 + C_1\mu + C_2\mu^2 + C_3\mu^3 + (C_4 + C_5\mu + C_6\mu^2)e, \quad (4-5)$$

$$\mu = \frac{\rho}{\rho_0} - 1, \quad (4-6)$$

where  $\rho$  and  $\rho_0$  are the current and the initial air density, respectively.  $e$  is the specific internal energy, i.e. internal energy per unit volume.  $C_0, C_1, C_2, C_3, C_4, C_5$  and  $C_6$  are constants. Setting  $C_0 = C_1 = C_2 = C_3 = C_6 = 0$  and  $C_4 = C_5 = \gamma - 1$ , the linear polynomial EoS can be used to model the ideal gas ( $\gamma = 1.4$  for air). Eq. (4-5) is then simplified as

$$p = (\gamma - 1)(1 + \mu)e. \quad (4-7)$$

Inserting Eq. (4-6) into Eq. (4-7), one gets the pressure for an ideal gas as

$$p = (\gamma - 1) \frac{\rho}{\rho_0} e. \quad (4-8)$$

The specific internal energy  $e$  is a convenient measure of energy in gases per unit volume and is defined as (*Kinney and Graham 1985*)

$$e = \frac{1}{\gamma - 1} \rho_0 R_s T. \quad (4-9)$$

Solving Eq. (4-9) for  $R_s T$  and inserting into Eq. (4-4), it leads to the same relationship described in Eq. (4-8). This means that the Eq. (4-4) and Eq. (4-8) are equivalent in describing the ideal gas law.

In the studies of shock waves, two assumptions are often made. One is the ideal gas assumption for air. The other is that the ratio  $\gamma$  of specific heats of the air is assumed constant. As mentioned in Section 3.1, it is appropriate to assume a constant value of 1.4 for air.

#### 4.1.1.2 Explosive material

The high explosive material is modelled via \*MAT\_HIGH\_EXPLOSIVE\_BURN (LSTC 2017) with the Jones-Wilkins-Lee (JWL) EoS. The pressure  $p$  is given as

$$p = A \left(1 - \frac{\omega}{R_1 V}\right) e^{-R_1 V} + B \left(1 - \frac{\omega}{R_2 V}\right) e^{-R_2 V} + \frac{\omega e}{V}, \quad (4-10)$$

where  $V$  is the relative volume of the explosive material,  $V = \rho_e / \rho_d$ .  $\rho_e$  and  $\rho_d$  are the density of the explosive material and of the detonation products, respectively.  $A$ ,  $B$ ,  $R_1$ ,  $R_2$  and  $\omega$  are material constants. Typical material parameters of TNT and PETN are listed in Table 4-1 and Table 4-2 for the strength model and for the EoS. As the detonation is ignited, a shock wave propagates away from the point of ignition to the atmosphere surrounding the charge with the velocity of detonation  $D$ . During this process, the explosive material is converted into high-pressure detonation products.  $p_{CJ}$  is the Chapman-Jouguet pressure. The data stems from LLNL explosive handbook (Dobratz and Crawford 1985).

Chapman et al. 1995b stated that if the high explosive material is expanded to more than ten times of its original volume, an ideal gas EoS can be employed for the detonation products. Before that, a special EoS for the explosive material, e.g. Jones-Wilkins-Lee (JWL), is needed in order to describe the complex phenomena during the conversion of the explosive material into detonation products.

Table 4-1: Material parameters of the strength model for high explosive material PETN and TNT (Dobratz and Crawford 1985)

	<u>*MAT_HIGH_EXPLOSIVE_BURN</u>		
	$\rho_e$	$D$	$p_{CJ}$
	[kg/m <sup>3</sup> ]	[m/s]	[Pa]
TNT	1630	6930	2.10E+10
PETN	1500	7450	2.20E+10

Table 4-2: Material parameters of the EoS for high explosive material PETN and TNT (Dobratz and Crawford 1985)

	<u>*EOS_JWL</u>					
	$A$	$B$	$R_1$	$R_2$	$\omega$	$e_0$
	[Pa]	[Pa]	[-]	[-]	[-]	[Pa]
TNT	3.712E+11	3.231E+09	4.15	0.95	0.30	7.00E+09
PETN	6.253E+11	2.329E+10	5.25	1.60	0.28	8.56E+09

A special modelling technique for the explosive charge and the surrounding air is employed for the numerical simulations in Sections 6.1 and 6.2. Initially, the entire computational domain is occupied solely by air. By appropriately initializing the volume fractions of the elements enclosed by the specified charge shape (e.g. spherical), the explosive material is filled to specified elements at the start of the calculation. The distribution of the air and the explosive material is realized by the keyword `*INITIAL_VOLUME_FRACTION_GEOMETRY` (*LSTC 2017*), by which the shape and location of the charge are defined. The detonation is ignited using the keyword `*INITIAL_DETONATION` (*LSTC 2017*).

### 4.1.1.3 Structural material (steel)

The structures involved in this Dissertation, which consist of the canopies (Section 6.3) as well as the posts and the frame construction (Section 6.4). They can be explicitly modelled in the numerical simulations in order to investigate the influence of the flexibility of structures. They are made of steel and have a relatively small thickness. Therefore, they are discretized by Lagrangian shell elements, which use the element formulation of Belytschko-Tsay (*Belytschko et al. 1984*) and two integration points through thickness. The strength model is represented via `*MAT_PLASTIC_KINEMATIC` (*LSTC 2017*), which is a rate-sensitive, elastic-plastic bilinear material with von Mises yield criterion. Strain rate effects are taken into consideration based on the Cowper-Symonds model (*Jones 1983*). Table 4-3 summarizes the pertinent parameters of the structural material (steel).

Table 4-3: Material parameters of the structural material (steel)

Density	Young's modulus	Poisson's ratio	Yield stress	Tangent modulus	Hardening parameter	Strain rate parameter	
$\rho_s$ [kg/m <sup>3</sup> ]	$E_s$ [MPa]	$\mu_s$ [-]	$\sigma_y$ [MPa]	$E_T$ [MPa]	$\beta$ [-]	$C$ [1/s]	$P$ [-]
7850	200000	0.3	500	4200	1	40	5

### 4.1.2 Time step control

This Dissertation uses an explicit time integration scheme, which is only conditional stable. In order to ensure the stability of the scheme, the time step  $\Delta t$  should be equal to or smaller than the one  $\Delta t_{CFL}$  defined by the Courant-Friedrichs-Levy (CFL) condition (*Courant et al. 1928*), which is given as

$$\Delta t \leq \Delta t_{CFL} = CFL \frac{\Delta x_{min}}{c_{max}}, \quad (4-11)$$

where  $\Delta x_{min}$  is the smallest element size and  $c_{max}$  is the maximum wave velocity.  $CFL$  is the safety factor to ensure the stability of the scheme. It is typically set to 0.9. However, if high explosives are used, a smaller value of 0.67 should be used.

During the solution process in LS-DYNA, the time step  $\Delta t$  is determined by taking the minimum value of the time steps over all elements, i.e.

$$\Delta t = CFL \cdot \Delta t_c = CFL \cdot \min\{\Delta t_1, \Delta t_2, \dots, \Delta t_N\}, \quad (4-12)$$

where  $N$  is the total number of elements. Roughly speaking, the critical time step size  $\Delta t_c$  corresponds to the length of time needed for a wave to propagate through the shortest characteristic length of the elements, which will be explained for solid and shell elements, respectively.

#### 4.1.2.1 Critical time step size for solid elements

For solid elements, the critical time step size  $\Delta t_c$  is calculated by

$$\Delta t_c = \frac{L_{e,solid}}{Q + (Q^2 + c^2)^{0.5}}, \quad (4-13)$$

where  $L_{e,solid}$  is the characteristic length of the solid elements. For eight-node solid elements, it is given as

$$L_{e,solid} = \frac{v_e}{A_{e,max}}, \quad (4-14)$$

where  $v_e$  is the element volume.  $A_{e,max}$  is the largest surface area of the element.  $Q$  is a function of the bulk viscosity coefficients  $\eta_0$  and  $\eta_1$ , giving

$$Q = \begin{cases} \eta_1 c + \eta_0 L_{e,solid} |\dot{\epsilon}| & \dot{\epsilon} < 0 \\ 0 & \dot{\epsilon} \geq 0 \end{cases} \quad (4-15)$$

$c$  is the wave velocity in the medium.  $\dot{\epsilon}$  is the strain rate. Considering elastic materials with constant Young's modulus  $E$  and Poisson's ratio  $\nu$ , the wave velocity  $c$  in the medium is determined by

$$c = \sqrt{\frac{E(1-\nu)}{(1+\nu)(1-2\nu)\rho}}, \quad (4-16)$$

where  $\rho$  is the material density.

#### 4.1.2.2 Critical time step size for shell elements

For each shell element, the critical time step size  $\Delta t_c$  is determined by

$$\Delta t_c = \frac{L_{e,shell}}{c}, \quad (4-17)$$

where  $L_{e,shell}$  is the characteristic length of the shell elements. It is given for quadrilateral shell elements as

$$L_{e,shell} = \frac{A_e}{\min\{\max[L_1, L_2, L_3, L_4], \max[D_1, D_2]\}}, \quad (4-18)$$

where  $A_e$  is the area of the shell element.  $L_i$  ( $i = 1 - 4$ ) is the length of the sides defining the shell element.  $D_1$  and  $D_2$  are the length of the diagonals of the shell element.

### 4.1.3 Element formulations

In general, there are two different element formulations, i.e. Lagrange and Euler. In the former (Figure 4-1a), the material moves directly along with the mesh, i.e. the material and the mesh translate, rotate and deform together. The material does not cross the element boundaries. This means that the mass of the material within each element never changes. In the latter (Figure 4-1b), the mesh remains fixed in space and the material can cross the element boundaries, i.e. a certain amount of material flows or advects from one element to adjacent elements. Thus, an Eulerian element may contain a mixture of different materials. This option is referred to as the “multi-material” option.

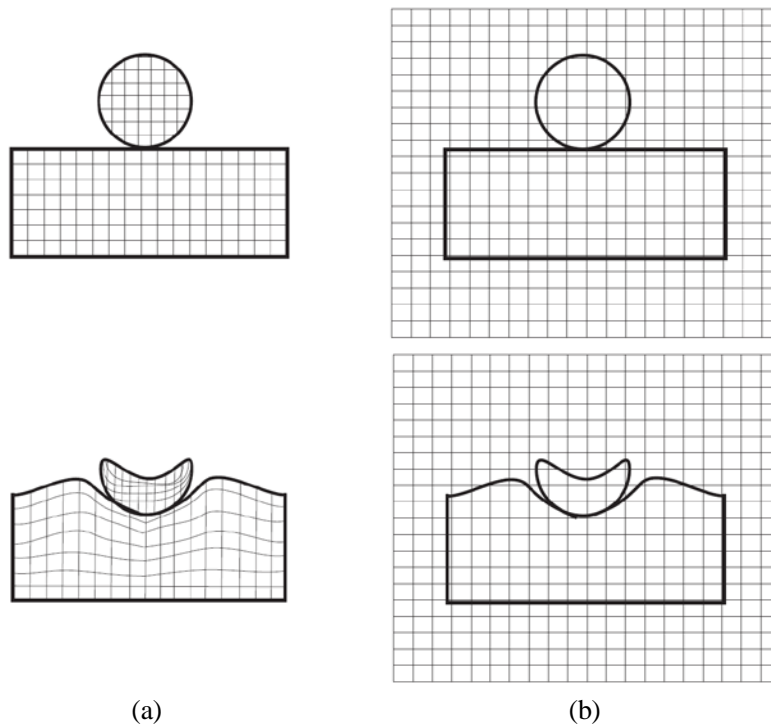


Figure 4-1: Element formulation (a) Lagrange; (b) Euler (*Larcher 2007*)

The Arbitrary-Lagrangian-Eulerian (ALE) formulation is a combination of the two above-mentioned formulations. This is accomplished by splitting a computation cycle into a Lagrangian phase and an advection phase (*Hughes et al. 1981* and *Benson 1992*). In the Lagrangian phase, the material moves with the mesh. The physical problem on the mesh, i.e. equations of mass, momentum and energy conservation, is solved based on the Lagrangian formulation. The Lagrangian phase is followed by the advection phase. In this phase, the behaviour of the mesh with respect to the deformation of the

material can be selected. If the mesh is not advected, a purely Lagrangian formulation is applied. If the mesh is chosen to be advected to the initial shape, a purely Eulerian formulation is used. Finally, if the mesh is advected to a prescribed shape, an ALE formulation is applied.

The main characteristic of the ALE formulation is that the material flow velocity ( $v_F$ ) and mesh velocity ( $v_M$ ) are independent. If the mesh velocity is selected to be equal to the material flow velocity, i.e.  $v_M = v_F$ , the Lagrangian formulation is represented. If the mesh remains fixed in space, i.e.  $v_M = 0$ , then the Eulerian formulation is represented. In this sense, the Lagrangian and Eulerian formulations are two special cases of the ALE formulation wherein the prescribed mesh velocity is either equal to the material flow velocity or equal to zero.

For this Dissertation, the ALE formulation with a multi-material option is adopted, in which the material is able to flow through the mesh and each element may contain more than one materials. Due to the presence of detonation products, the second order accurate Van Leer with Half-Index-Shift advection method (*Van Leer 1977*) is employed.

It should be noted that the ALE mesh and the material (e.g. air) do not move exactly together ( $v_M \neq v_F$ ). The material advection across the element boundaries is still required, but the amount of material advected at each time step is generally less than that of the Eulerian formulation since the mesh is also moving, i.e.  $v_M \neq 0$ . In general, the less material (e.g. air) that is advected per time step, the more accurate the simulation is.

### 4.1.4 Mapping techniques

Mapping techniques are developed in order to avoid the time waste of computing the shock wave propagation in the high dimensional model, which is known a priori. They enable highly refined meshes in the low dimensional geometry and comparatively coarse meshes in the high dimensional geometry. In general, they can be categorized into three different types, i.e. mapping from one-dimensional (1D) to two-dimensional (2D), mapping from one-dimensional (1D) to three-dimensional (3D) and mapping from two-dimensional (2D) to three-dimensional (3D). They will be briefly explained in the following subsections.

It should be noted that if needed, the mapping techniques can also be applied to the models having the same dimensional geometry, i.e. mapping from a small 2D model with a fine mesh to a large 2D model with a coarse mesh or mapping from a small 3D model with a fine mesh to a large 3D model with a coarse mesh. Further details on the mapping techniques can be found in *Aquelet and Souli 2008*, *Lapoujade et al. 2010*, *Kalra et al. 2014* and *Rebelo and Cismasiu 2017*.

#### 4.1.4.1 Mapping from 1D to 2D and from 1D to 3D

A 1D spherically symmetric model can be used to generate the ignition of the explosive material and the expansion of detonation products (Figure 4-2a and c). This simulation

is terminated just before the shock wave reaches the nearest boundary, e.g. the ground surface (Figure 4-2c).

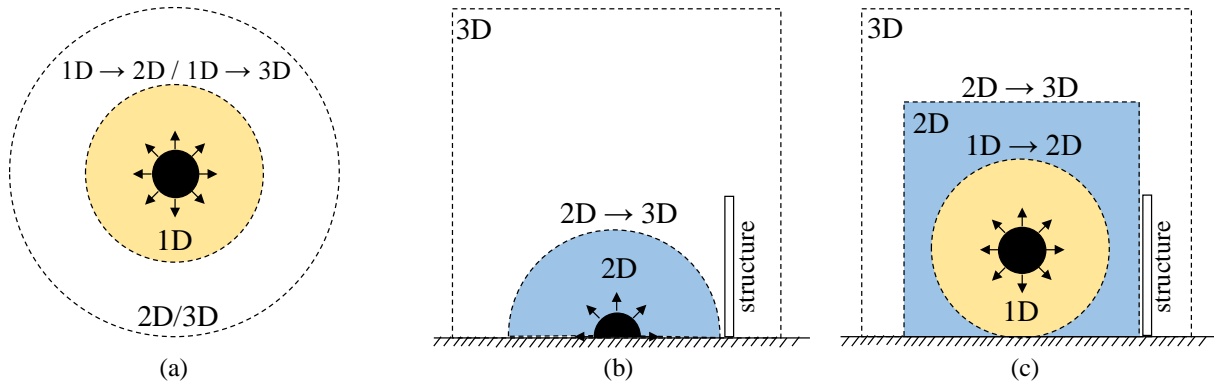


Figure 4-2: Sketch of mapping techniques (a) free air burst detonation; (b) surface burst detonation; (c) height-of-burst detonation

At the last cycle, a binary map file is written. The file contains the results (e.g. pressure) of the 1D domain and is used to fill the 2D or 3D domain. Subsequently, this file is mapped onto an axisymmetric 2D mesh (mapping from 1D to 2D, Figure 4-2a and c) or onto a 3D mesh (mapping from 1D to 3D, Figure 4-2a). After the data initialization, the 2D or 3D model continues to calculate the solution until the termination time is reached.

#### 4.1.4.2 Mapping from 2D to 3D

The idea of the mapping technique from 2D to 3D is to use a 2D axisymmetric model to replace the 3D model. The 2D axisymmetric model calculates the solution as long as the symmetry is preserved (Figure 4-2b and c). At the last cycle, a binary map file is written. The file contains the results (e.g. pressure) of the 2D domain and is used to fill the 3D domain. Subsequently, the data from the last cycle of the 2D model is mapped onto the 3D model. After the data initialization, the 3D model continues to calculate the solution until the termination time is reached. In order to efficiently reduce the computational time, a sufficiently large volumetric expansion (more than 10 times the original volume) must have been occurred so that only an ideal gas EoS is required (Section 4.1.1.1). Therefore, the mapping technique should be used after the complete burn of the explosive material. Furthermore, no constraints should be imposed on the 2D boundary nodes, except along the symmetry axis.

The mapping techniques enable the decomposition of a numerical simulation into several steps. At the end of a fine 2D ALE simulation, pressure data from the last cycle is mapped onto a coarse 3D model. As a compromise between the computational cost and the accuracy of results, the mapping techniques offer a possibility to handle larger-size models. *Lapoujade et al. 2010* demonstrated that using the mapping technique by a fine mesh for the 2D simulation followed by a coarse mesh for the subsequent 3D simulation, the accuracy is improved compared to a single 3D simulation with the same coarse mesh. The pressure data associated with the elements in the 2D model is mapped onto the appropriate element in the 3D model. Due to the fact that the 2D mesh is finer

than the 3D mesh, the values assigned to a specified element in the 3D mesh are the averaged values derived from more than one element in the 2D mesh.

Due to the fine 2D mesh resolution, the ignition and the expansion phases of the explosive material are well modelled. This saves computational time. However, a certain loss in accuracy of the numerical results occurs. Therefore, a reasonable element size ratio during the mapping process needs to be decided. There is little guidance on the reasonable element size ratio during the mapping process in the literature. Firstly, it is problem dependent, e.g. shock wave propagation in water or in air. Secondly, the acceptable loss in accuracy due to the mapping process is application dependent. *Lapoujade 2010* performed a study to evaluate the effect of the element size ratio during the mapping process on the peak overpressures and on the maximum impulses for free air bursts. The element size ratio is defined as the element size after mapping (3D model) to the element size before mapping (2D model). It was concluded that, if peak overpressure is concerned, an element size ratio less than 10 is recommended, and if maximum impulse is concerned, an element size ratio less than 20 is recommended.

### 4.1.5 Fluid-Structure-Interaction (FSI) algorithm

Using the Fluid-Structure-Interaction (FSI) algorithm, the shock wave and the structure can be coupled in the numerical analysis. The coupling algorithm \*CONSTRAINED\_LAGRANGE\_-IN\_SOLID (*LSTC 2017*) utilizes the ALE air mesh to derive the dynamic forces on the structure. Meanwhile, the structure provides a dynamic constraint to the shock wave propagating through the air domain. The interaction between the ALE air elements and the Lagrangian elements of the structure is accomplished by a penalty based method. The coupling algorithm serves to generate forces that resist penetration of the ALE material through the Lagrangian elements. Hence, the Lagrangian mesh must spatially overlap a portion of the ALE mesh.

The number of coupling points (NQUAD) distributed over each Lagrangian element plays a great role in the computational cost of the coupling algorithm. The larger the value of NQUAD, the more expensive the coupling algorithm and the more likely the coupling forces will be excessive such that numerical instability occurs. If the Lagrangian element size is approximately the same as the ALE air element size, the value of NQUAD is to set as 2 or 3. If the Lagrangian mesh is coarser than the ALE mesh, e.g. one Lagrangian element spans two or three ALE air elements, NQUAD should be raised to 4 or 6 in order to provide proper coupling. If the Lagrangian mesh is finer than the ALE mesh, e.g. two or three Lagrangian elements span one ALE air element, NQUAD = 1 would be adequate. In summary, the appropriate NQUAD values must be determined based on the element size ratio between the Lagrangian and ALE meshes. On the one hand, too many coupling points may give rise to numerical instability. On the other hand, not enough coupling points can result in pressure leakage.

## 4.2 Modelling strategies

Considering a building subjected to air blast (Figure 4-3), three modelling strategies are available to simulate the shock wave propagation, i.e. empirical method, Arbitrary-Lagrangian-Eulerian (ALE) method, and combined method.

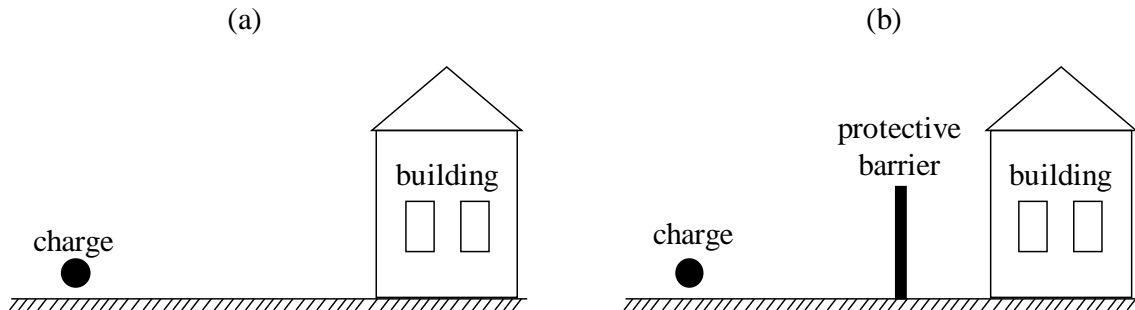


Figure 4-3: Sketch of a building subjected to air blast (a) without a protective barrier; (b) with a protective barrier

These modelling strategies will be explained in the following subsections.

### 4.2.1 Empirical method (LBE)

The empirical method is based on the empirical formulae of *Kingery and Bulmash 1984*, which are derived from a vast amount of experimental data. It has been applied successfully for decades to predict the blast loads in various analyses. The empirical blast loads are generated through the keyword `*LOAD_BLAST_ENHANCED`, which is denoted as LBE. This keyword (LBE) is based on the report of *Randers-Pehrson and Bannister 1997*. The objective of this keyword (LBE) is to generate the overpressure-time histories on the target structure.

The overpressure distribution depends on the angle of incidence  $\alpha$  (Figure 4-4). The angle of incidence  $\alpha_1$  (or  $\alpha_2$ ) is formed by the line from charge centre C to observation points P1 (or P2) on the target structure and the normal vector  $n_1$  (or  $n_2$ ) of the surface at that point.

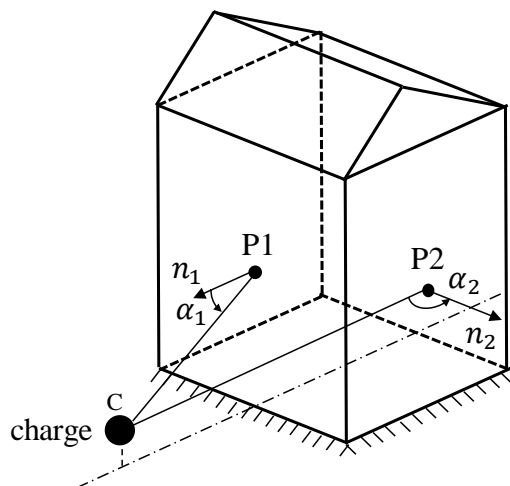


Figure 4-4: Definition of the angle of incidence  $\alpha$

This overpressure distribution is referred to as the cosine distribution and is given as

$$p(t) = \begin{cases} p_{so}(t)(1 + \cos \alpha - 2 \cos^2 \alpha) + p_r(t) \cos^2 \alpha & 0^\circ \leq \alpha < 90 \\ p_{so}(t) & \alpha \geq 90^\circ \end{cases} \quad (4-19)$$

Figure 4-5 displays the cosine distribution of the overpressures in dependence on the angle of incidence  $\alpha$ . If the angle of incidence  $\alpha$  is equal to  $0^\circ$ , the reflected overpressure  $p_r(t)$  is applied on the structure. If the angle of incidence  $\alpha$  is larger than or equal to  $90^\circ$  (e.g. P2 in Figure 4-4), the overpressure  $p(t)$  corresponds to the side-on overpressure  $p_{so}$ . For the angles of incidence  $\alpha$  between  $0^\circ$  and  $90^\circ$  (e.g. P1 in Figure 4-4), the overpressure is comprised of incident and reflected overpressure components.

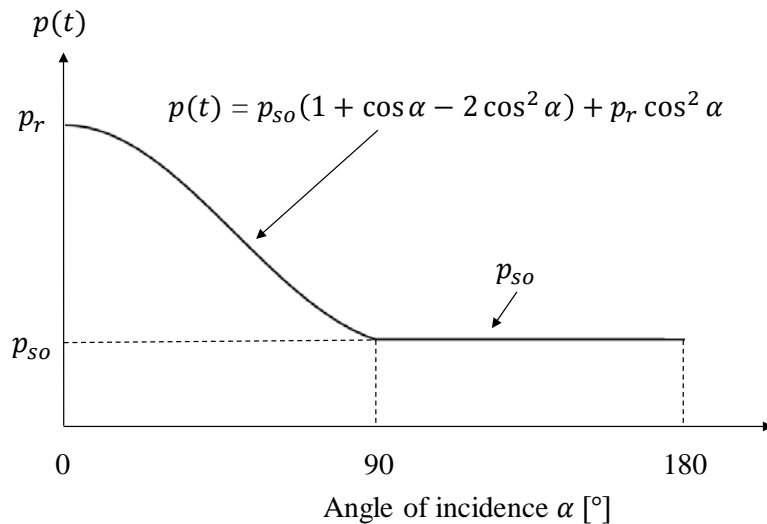


Figure 4-5: Cosine distribution of overpressures in dependence on the angle of incidence  $\alpha$

The inputs required for the keyword LBE are the charge mass in TNT equivalent, the charge location, the ignition time, and the type of burst (free air burst, surface burst and height-of-burst, Section 3.8). To predict the time of arrival at a given range, the equation of shock velocity  $U$  (Eq. (3-6)) can be used. LBE is regarded as the air blast portion of ConWep implemented in LS-DYNA. However, there are two differences between LBE and ConWep:

- LBE has the option to include or to neglect the negative phase of the overpressure-time history, whereas ConWep neglects the negative phase.
- LBE updates the overpressure-time history with respect to changes in the geometry, e.g. deformations, whereas ConWep assumes that the structure is rigid and fixed in space.

Further details on the empirical method (LBE) in LS-DYNA can be found in the report of *Randers-Pehrson and Bannister 1997*.

Using the empirical method (LBE), the blast loads are calculated by empirical formulae of *Kingery and Bulmash 1984*. They are directly applied to the building, which is discretized by Lagrangian elements. Since these empirical formulae only require the charge mass, the

charge location, the ignition time and the type of burst as inputs, it is not necessary to model the explosive and the air between the charge and the building. As a result, it reduces significantly the computational time, especially when large distances from the charge to the building are involved. The computational effort is typically much less than the equivalent simulation using the ALE method (Section 4.2.2). However, this modelling strategy is only valid if a clear line of sight exists between the charge and the building (free field scenario e.g. in Figure 4-3a). If an additional structure (e.g. the protective barrier in Figure 4-3b) intervenes between the charge and the building, a shielding effect of the shock wave is caused by the intervening structure. In addition, a focusing effect may occur, when the shock waves merge again after diffraction around the sides and over the top of the intervening structure. These phenomena cannot be modelled by this empirical method (LBE). Furthermore, since the empirical method (LBE) is only valid for distances greater than three charge radii from the charge, which corresponds to the lower bound of the application range for the formulae of *Kingery and Bulmash 1984*, it is applicable for neither contact detonations nor near-field detonations.

### 4.2.2 Arbitrary-Lagrangian-Eulerian (ALE) method

The Arbitrary-Lagrangian-Eulerian (ALE) method is the straightforward modelling strategy in modelling the shock wave propagation. The explosive and the air are separately modelled using the ALE formulation with a multi-material option (Section 4.1.3). Appropriate Equations of State (EoS) are assigned to the materials (explosive and air). A burn model governs the detonation process of the high explosive material. The shock wave travels through the ALE air domain and then impinges the target structure. The target structure is discretized by Lagrangian elements. The Fluid-Structure-Interaction (FSI) algorithm (Section 4.1.5) is used to handle the communication between the ALE air elements (fluid) and the Lagrangian elements (structure). This method is applicable not only for the free field scenario (e.g. in Figure 4-3a) but also for the scenario when an additional structure intervenes between the charge and the building (e.g. in Figure 4-3b).

In air blast simulations, the boundaries of the ALE air mesh need to be sufficiently far away from the area of interest in order to mitigate the boundary effects. Hence, a large air domain typically needs to be modelled in the numerical simulation. In order to capture the nearly discontinuous shock front, the size of the ALE elements must be sufficiently small. A quite fine mesh is required to adequately resolve the shock wave propagation, especially in the vicinity of the charge. Therefore, the computational burden using the ALE method is further aggravated. Roughly, the rule of thumb for discretization in the region of explosive charge is a minimum of 10 elements across the charge radius. However, *Schwer et al. 2015* recommended 20 elements across the charge radius as a reasonable value. This results in a very small critical time step (Section 4.1.2). If a large distance from the charge is concerned, the air volume is often enormous. Consequently, the ALE method requires extensive input and substantial computational resources.

It should be noted that there are an energy loss mechanisms inherent in the ALE formulation since the dissipation due to the advection phase and the necessary application of artificial bulk viscosity consumes energy and smears the shock front.

Consequently, a certain amount of pressure leakage at the FSI interface is unavoidable and some reduction in the momentum transferred to the structure should be taken into consideration.

#### 4.2.3 Combined method (LBE / ALE)

If an additional structure (e.g. the protective barrier in Figure 4-3b) intervenes between the charge and the building, the shock wave encounters the intervening structure before it strikes the building. Due to the presence of the intervening structure, the phenomena such as reflection, diffraction, absorption and transmission may occur. As already mentioned in Section 4.2.1, the empirical method (LBE) is only valid for the free field scenario. Hence, it is not capable of describing the shock wave propagation in this case. The ALE method (Section 4.2.2) is straightforward to implement. However, the required large computational time cannot be accepted in practice since a small element size and a large air domain are needed in order to ensure the computational accuracy. To overcome these difficulties, *Slavik 2009* presented a combined method to couple empirical blast loads to Arbitrary-Lagrangian-Eulerian (ALE) air domain, which extends the capabilities in the field of air blast simulations. Figure 4-6 illustrates a sketch of the numerical model associated with the combined method (LBE / ALE). The numerical simulation is subdivided into two stages. In the first stage, the empirical method (LBE) is used to calculate the blast loads on a layer of ambient ALE air elements, which is situated at the front face of the air domain facing the charge. Given the charge mass and the distances from the charge to the observation points on the layer of ambient ALE air elements, the overpressure distribution on the layer can be calculated using the formulae of *Kingery and Bulmash 1984*. The overpressure-time histories are described by the modified Friedlander equation (Eq. (3-15)). In the second stage, the shock wave propagation is simulated by using the ALE formulation with a multi-material option (Section 4.1.3), where the results from the first stage are used as input for the ambient ALE air elements.

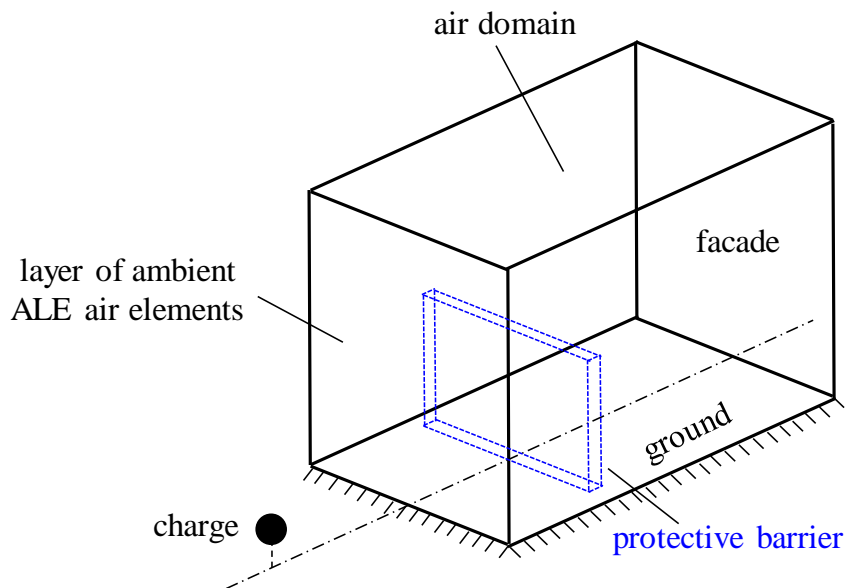


Figure 4-6: Sketch of the numerical model associated with the combined method LBE / ALE

Central to the combined method (LBE / ALE) is the special ALE element formulation referred to as ambient ALE air elements (Figure 4-6). The function of this layer of ambient ALE air elements is to receive the information of blast loads (side-on overpressures) derived from the empirical formulae of *Kingery and Bulmash 1984*. This pressure information is then converted to the thermodynamic state data (temperature and density), which is subsequently used as input for the ambient ALE air elements.

As shown in Figure 4-7, a shock front arrives at  $t = t_0$  at location  $x = x_0$ , the state variables  $p_1$ ,  $\rho_1$  and  $T_1$  are the side-on pressure, density and temperature at the shock front, respectively. The corresponding state variables ahead of the shock front in the undisturbed air are  $p_0$ ,  $\rho_0$  and  $T_0$ , respectively. At a time of  $t > t_0$ , the shock front arrives at location  $x = x_0 + \Delta x$ , the state variables at location  $x = x_0$  are  $p(t)$ ,  $\rho(t)$  and  $T(t)$ .

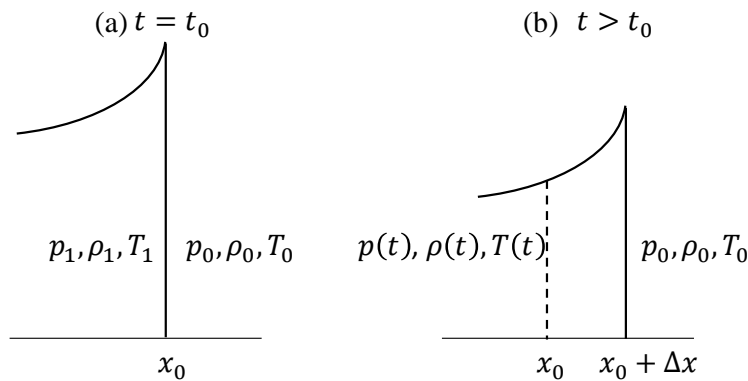


Figure 4-7: Shock front at successive times (a)  $t = t_0$ ; (b)  $t > t_0$

If the air is regarded as an ideal gas, it is valid that (*Kinney and Graham 1985*)

$$\frac{T_1}{T_0} = \frac{p_1}{p_0} \left( \frac{\frac{p_1}{p_0} + 6}{6 \frac{p_1}{p_0} + 1} \right). \quad (4-20)$$

Applying Eq. (4-4), one can get that

$$\frac{\rho_1}{\rho_0} = \frac{p_1 T_0}{p_0 T_1}. \quad (4-21)$$

Inserting Eq. (4-20) into Eq. (4-21), it yields the air density  $\rho_1$  at the shock front

$$\rho_1 = \rho_0 \frac{6p_1 + p_0}{p_1 + 6p_0}. \quad (4-22)$$

This means that the pressure and density suffice to describe the thermodynamic state of the air if the air is regarded as an ideal gas. The side-on pressure is prescribed at the quadrature point situated at the centre of the ambient element. The air density is estimated at the quadrature point of the ambient element in a specific manner described below.

For an ideal gas, the air density  $\rho(t)$  after passage of the shock front obeys the isentropic relation (*Kinney and Graham 1985*), giving that

$$\rho(t) = \rho_1 \left( \frac{p(t)}{p_1} \right)^{\frac{1}{\gamma}}. \quad (4-23)$$

Applying again Eq. (4-4), one can obtain  $T(t)$

$$T(t) = \frac{p(t)}{R_s \rho(t)}. \quad (4-24)$$

In order to completely describe the flow conditions of the shock wave, what remains to be determined is the particle velocity  $u$  in the blast wind. The blast wind is the result of gross violent movement of the particles immediately following the shock wave. Using the Rankine-Hugoniot relation (*Kinney and Graham 1985*), the particle velocity  $u_p$  at the shock front is given as

$$u_p = c \sqrt{\frac{25 \left( \frac{p_1}{p_0} - 1 \right)^2}{42 \frac{p_1}{p_0} + 7}}, \quad (4-25)$$

where  $c$  is the sonic velocity in the air ahead of the shock front. Both Eq. (4-22) and Eq. (4-25) are valid for an ideal gas with a ratio of specific heats  $\gamma = 1.4$ .

The dynamic pressure  $q_s$  at the shock front is defined as

$$q_s = \frac{1}{2} \rho_1 u_p^2, \quad (4-26)$$

and the dynamic pressure-time history is expressed as

$$q(t) = q_s \left( 1 - \frac{t}{t_d} \right) e^{-\varphi \frac{t}{t_d}}, \quad (4-27)$$

where  $\varphi$  is the decay rate of the dynamic pressure. Finally, combining Eq. (4-23), Eq. (4-26) and Eq. (4-27), one yields the particle velocity  $u(t)$  in the blast wind

$$u(t) = \sqrt{\frac{2q(t)}{\rho(t)}}. \quad (4-28)$$

The particle velocity  $u(t)$  calculated by Eq. (4-28) is valid for the particles at the centre of the ambient element. Subsequently, it is distributed to the nodes of the element in an area-weighted manner.

Figure 4-8 depicts the flow chart of the combined method LBE / ALE.

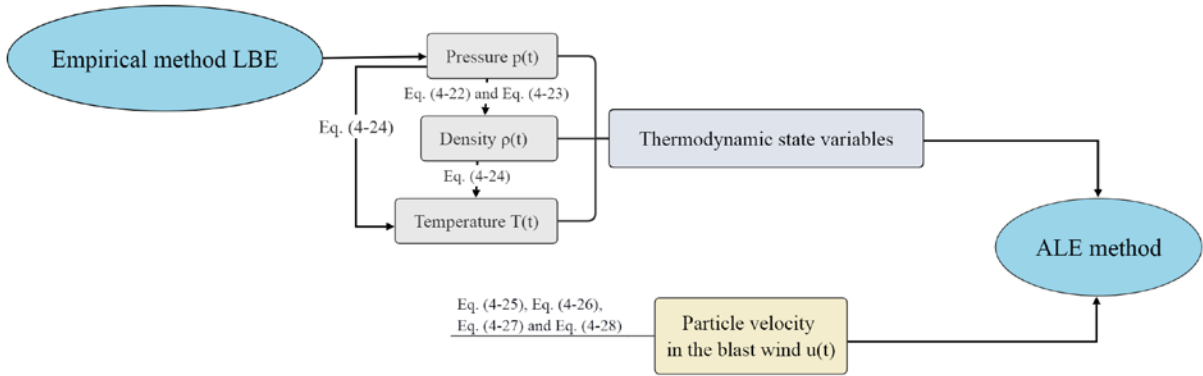


Figure 4-8: Flow chart of the combined method LBE / ALE

Using the combined method (LBE / ALE), only the air domain immediately surrounding the building is required to be modelled if the building is located in a direct line of sight of the charge at a large distance (Figure 4-3a). If an additional structure (e.g. the protective barrier in Figure 4-3b) is located between the charge and the building, the air domain is extended to sufficiently enclose the intervening structure. On the one hand, it is possible to accommodate the processes of diffraction, reflection, absorption and transmission due to the presence of the intervening structure. On the other hand, it avoids to model copious air volumes especially for large distances from the charge to the intervening structure and hence reduces the computational cost.

Since the blast loads are calculated by the empirical method (LBE) and then applied to the layer of ambient ALE air elements, the explosive is not needed to be modelled. In order to assure that the shock wave immediately impinges the layer of ambient ALE air elements at the start of the calculation, a negative offset of the ignition time can be used. Thus, it provides a saving in the computational time, since the calculation is not necessary to wait for the arrival of the shock front whose character is known a priori, i.e.  $p(t) = 0$ . Applying this method combines the advantages of both the empirical method (LBE) and the ALE method. This combined method LBE / ALE has been already verified by several researchers (e.g. *Slavik 2009, Schwer et al. 2015 and Rebelo and Cismasiu 2017*).

4.2.4 Comparison of modelling strategies

In summary, the three modelling strategies of the shock wave propagation presented in the previous sections are compared in Table 4-4.

Table 4-4: Comparison of three modelling strategies

Modelling strategies	Computational time	Intervening structure	FSI
Empirical method LBE	shortest	no	no
ALE method	longest	yes	yes
Combined method LBE/ALE	intermediate	yes	yes

The empirical method (LBE) requires minimal input and minimal computational cost. However, it is only valid for free field scenarios (e.g. Figure 4-3a). If the building is not located

in a direct line of sight of the charge (e.g. Figure 4-3b), the empirical method (LBE) cannot be used. If an interaction between the shock wave and the intervening structure is concerned, it cannot be treated by this empirical method (LBE). Under such circumstances, a different modelling strategy is required to simulate this complex shock wave propagation. The straightforward modelling strategy is the ALE method. However, a large ALE air domain is usually needed in order to avoid the boundary effect. In addition, the element size, especially in the vicinity of the charge, should be sufficiently small to assure the numerical accuracy. As a result, the ALE method requires the longest computational time among the three modelling strategies. The combined method LBE / ALE combines the advantages of the empirical method (LBE) and the ALE method. The computation time is intermediate between the empirical method (LBE) and the ALE method. Therefore, the combined method LBE / ALE will be used in this Dissertation to simulate the shock wave propagation in the numerical models (Chapter 6).

### 4.3 Summary: theoretical background of numerical simulations

This chapter provides a theoretical background of numerical simulations conducted in this Dissertation. Firstly, the basic aspects of numerical simulations, i.e. material models, time step control, element formulations, mapping techniques and Fluid-Structure-Interaction (FSI) algorithms are explained. Secondly, three numerical modelling strategies and their application to the numerical problems of this Dissertation are compared and discussed. The combined method LBE / ALE combines the advantages of the empirical method (LBE) and the ALE method. Therefore, it will be employed to carry out the numerical simulations (Chapter 6).

## 5 Experiments with protective barriers

This chapter describes the experimental configurations, which are employed in Chapter 6 to evaluate the effectiveness of protective barriers in attenuating the shock wave. During the planning phase of the experiments, numerical models were developed in order to predict the main blast and response parameters. Moreover, the experimental data is used to validate the numerical models. Table 5-1 describes two experimental series involved in this Dissertation, i.e. blast walls with a canopy on top (Section 5.1) and protective barriers made of steel posts (Section 5.2).

Table 5-1: Overview of the experimental series

Experimental series	Configurations	Configuration set-ups
Blast walls with a canopy on top	M1 (GWC back)	oriented away from the charge, 45° with respect to the horizontal
	M2 (GW)	no canopy
	M3 (GWC front)	facing the charge, 135° with respect to the horizontal
	Mref (no posts)	no steel posts
Protective barriers made of steel posts	M1 ( $n_{\text{post}} = 8$ )	8 steel posts, square hollow cross-section, spacing 100mm
	M2 ( $n_{\text{post}} = 5$ )	5 steel posts, square hollow cross-section, spacing 200mm
	M3 ( $n_{\text{post}} = 6$ )	6 steel posts, square hollow cross-section, spacing 150mm

In the experimental series of blast walls with a canopy on top, the effect of the canopy is investigated in three different configurations. In the experimental series of protective barriers made of steel posts, the influence of the number of steel posts is investigated in four different configurations.

### 5.1 Blast walls with a canopy on top

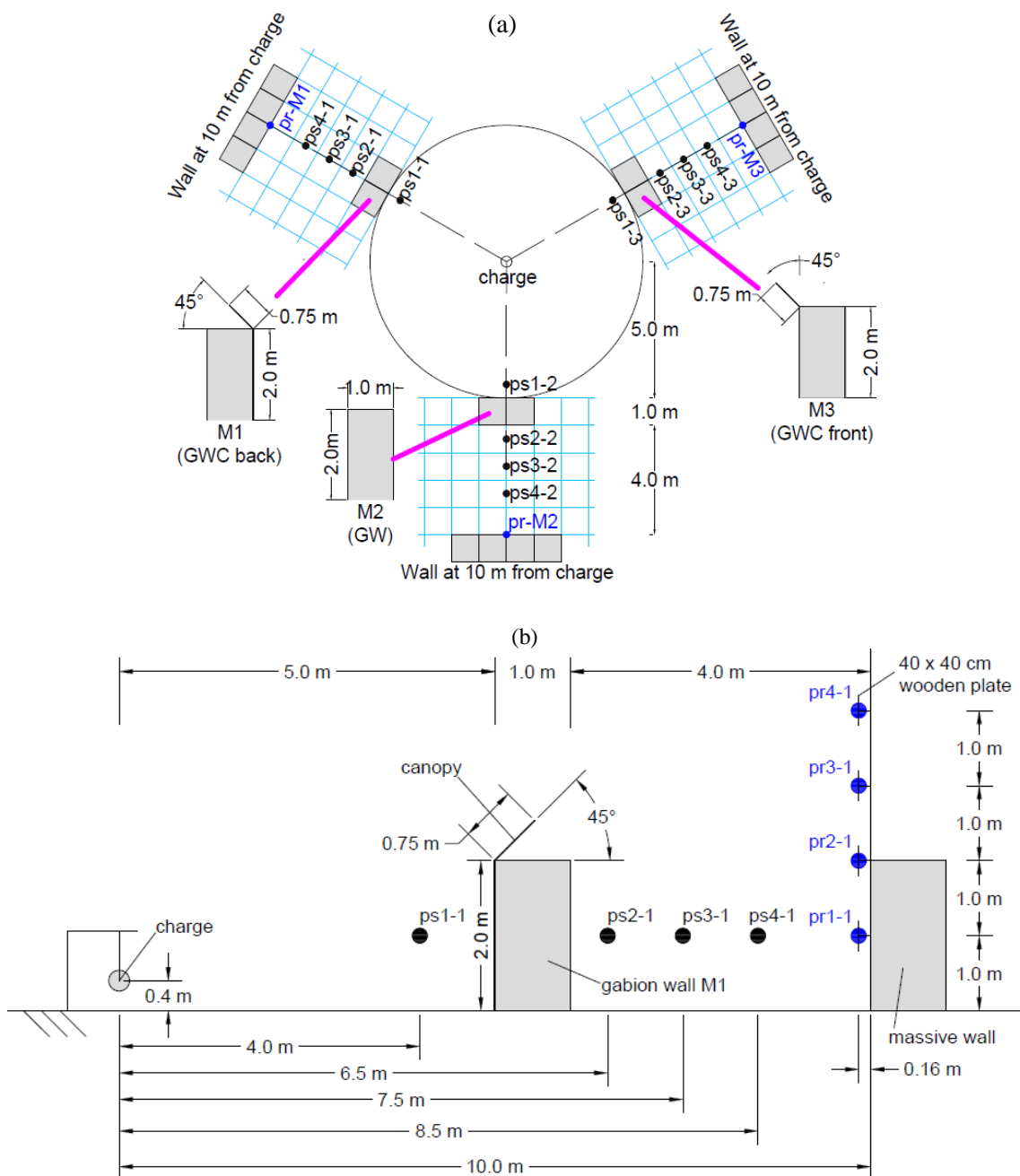
The experiments were conducted on 17<sup>th</sup> August 2016 at the test site of the Bundeswehr Technical Center for Protective and Special Technologies (WTD52) in Germany, which is located at an altitude of 1585 meters above mean sea level. The highest and lowest temperature on 17<sup>th</sup> August 2016 were 23°C and 15°C (day and night time, *Time and Date AS 2018a*). The average temperature on 17<sup>th</sup> August 2016 between 9 and 15 o'clock was 20.2°C.

To evaluate the effectiveness of blast walls, three full-scale experiments for each configuration were carried out. On the one hand, they are used to investigate the influence of the canopy on the blast load distribution behind the wall. On the other hand, they are also used to validate the numerical models presented in Section 6.3.

#### 5.1.1 Experimental set-up

The experimental set-up is illustrated in Figure 5-1. Three protective barriers with different canopy configurations were circularly arranged around the charge (Figure 5-1a). Figure 5-1b, c and d illustrate the set-up of configurations M1, M2 and M3 (designated “GWC back”, “GW” and “GWC front”, respectively) employed in the experiments. The design of the measurement system was linked to the aim of measuring the blast loads in a specific region, 4m horizontally

and 4m vertically behind the wall (Figure 5-1b, c and d). To capture the side-on overpressures behind the blast wall, three gauges (e.g. ps2-1, ps3-1 and ps4-1 in Figure 5-1b) were located between the gabion wall and the massive wall, which represents the envelope of the building to be protected. To record the overpressure-time history in a free field scenario and the subsequent overpressure-time history reflected at the blast wall, an additional gauge (e.g. ps1-1 in Figure 5-1b) was placed 1m in front of the blast wall. Another four gauges (e.g. pr1-1, pr2-1, pr3-1 and pr4-1 in Figure 5-1b) were positioned to measure the reflected overpressures. Side-on overpressure measurements (denoted as ps1-*i*, ps2-*i*, ps3-*i* and ps4-*i* in Figure 5-1a) were made at an elevation of 1m above the ground, where *i* refers to the number of wall configuration and *i* = 1, 2, 3. Reflected overpressures (denoted as pr1-*i*, pr2-*i*, pr3-*i* and pr4-*i*, Figure 5-1a) were measured at heights of 1m, 2m, 3m and 4m, respectively.



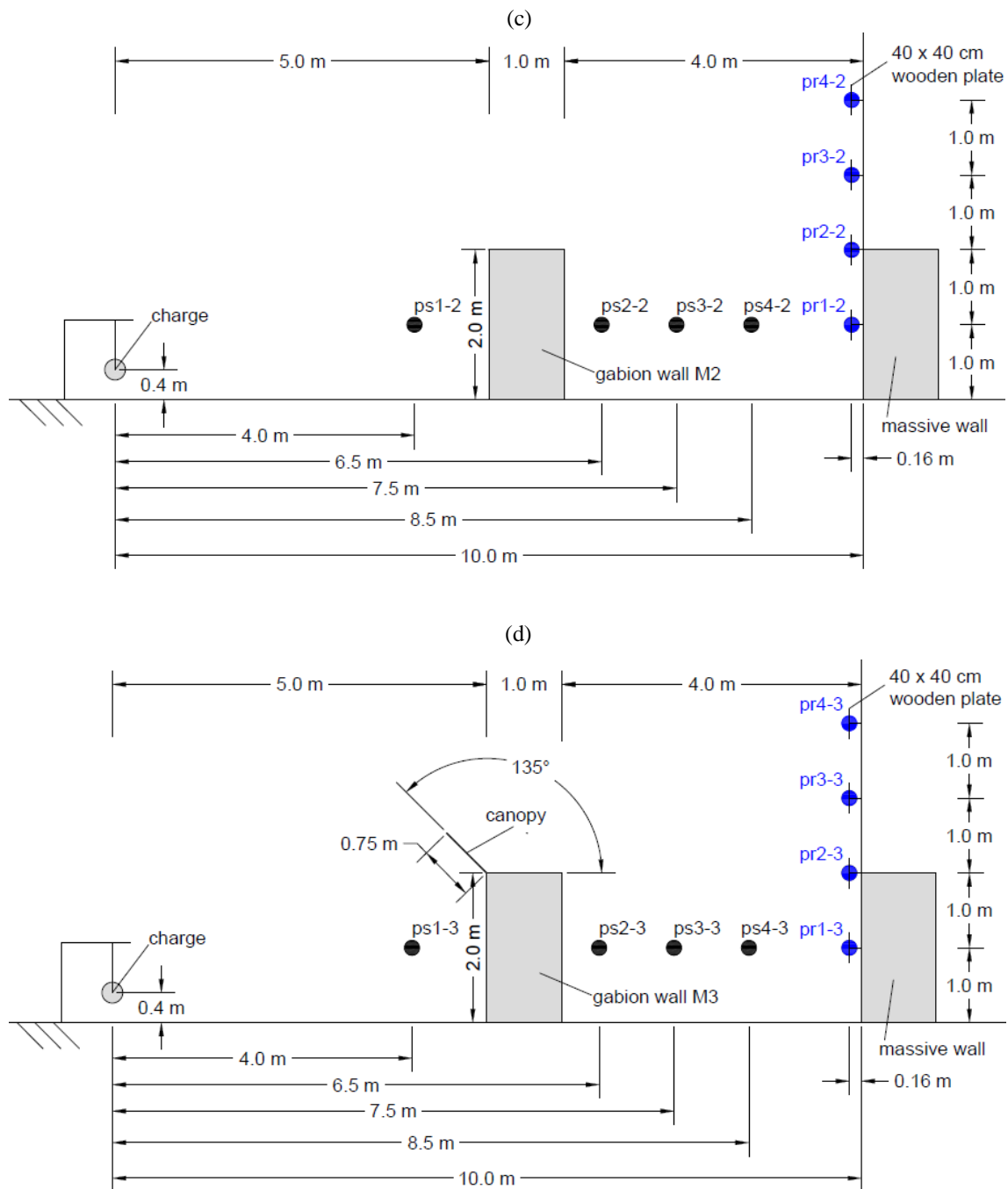


Figure 5-1: Experimental set-up of configurations (a) plan view; (b) side view, M1 - GWC back; (b) side view, M2 - GW; (b) side view, M3 - GWC front

In the experiments, the blast walls were placed 5m in front of the building to be protected. If a shock wave hits the blast wall, firstly, a part of the shock wave is reflected back by the front face of the wall. Secondly, if a blast wall or one of its components is flexible such that it undergoes deformation, a certain amount of explosive energy can be absorbed by the wall. Thirdly, another part of the shock wave is diffracted by the wall. Consequently, a combination of energy reflection, absorption and diffraction reduces the blast loads in a certain region behind the wall.

### 5.1.2 Blast wall configurations

Three different wall configurations were employed in the experiments (Figure 5-2). They are designated as follows:

- M1: GWC back - Gabion Wall Canopy back;
- M2: GW - Gabion Wall (without canopy);
- M3: GWC front - Gabion Wall Canopy front.

Configuration M2 (GW, Figure 5-2b) was composed of a vertical gabion wall measuring 2m x 2m x 1m (width x height x thickness, Figure 5-3) without a canopy. It was composed of four cube gabions with an edge length of 1m, which were filled with coarse-grained gravel. In configuration M1 (GWC back, Figure 5-2a) and M3 (GWC front, Figure 5-2c), two different canopies were mounted to the gabion wall on top. The canopies measuring 2m x 0.75m were made of 8mm thick, plane steel sheets (2m x 1.5m), which were bent on-site and suitably fixed to the front face of the gabion wall using two tension belts (Figure 5-2a and c).

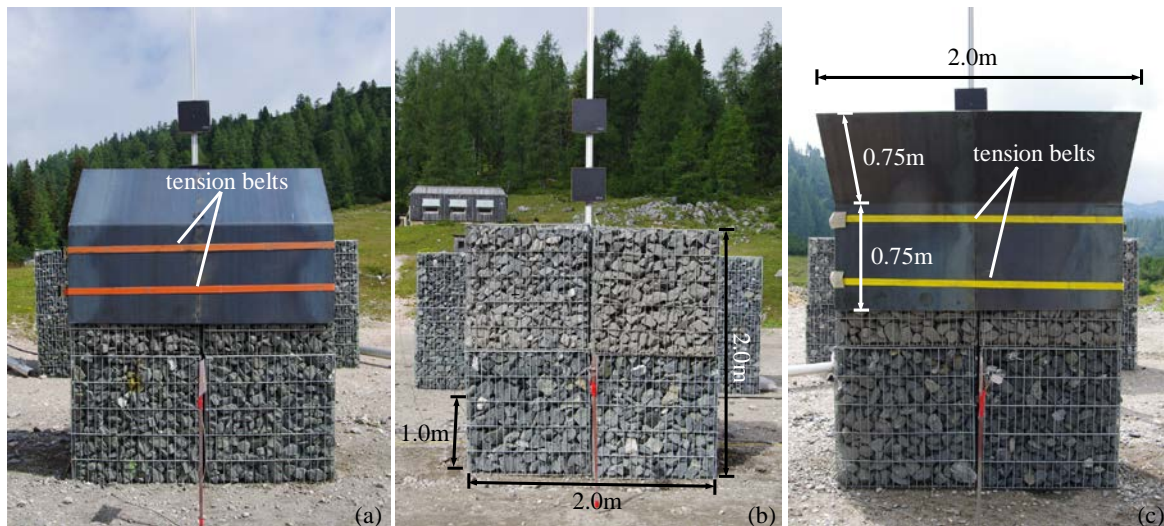


Figure 5-2: Blast wall configurations (a) M1 - GWC back; (b) M2 - GW; (c) M3 - GWC front (photos: WTD52 / UniBwM)

Recently, gabion walls have become very popular in the horticulture and landscape planning. Gabion walls were used in the experiments to provide a base structure for the attachment of the canopies. Permanent blast walls, e.g. reinforced concrete walls, are usually considered as a customary solution. However, the construction of the foundation of reinforced concrete walls takes much more time than the construction of the foundation of gabion walls. Nevertheless, the foundation of gabion walls need to be sufficiently load-bearing, frost-proof and resistant against erosion. The surface of the foundation must be plane in the longitudinal and transverse directions. In addition, gabion walls can be temporarily employed to protect the buildings, if a permanent solution is not necessary. It is worth mentioning that the reflection phenomenon can be affected by the open porous surfaces, e.g. holes between the coarse-grained gravel in the gabion walls (Figure 5-2). The blast energy is partly absorbed by the holes between the coarse-grained gravel in the gabion walls. This leads to a certain decrease in the blast loads behind the

wall. However, the shock wave is multiply reflected by the sharp edges of the coarse-grained gravel, which renders an increase in the blast loads behind the wall. Therefore, the influence of this open porous surface on the blast loads is difficult to specify. Further investigations are required in order to gain a better understanding of the behaviour of the open porous surface. Since the influence of the open porous surfaces of the gabion wall is out of the scope of this Dissertation, it is neglected in the numerical simulations, but it will be analysed in the upcoming experiments as well as in the numerical models.

The angle of inclination  $\alpha$ , the thickness  $t_c$  and the length  $l_c$  of the canopy are defined as illustrated in Figure 5-3.

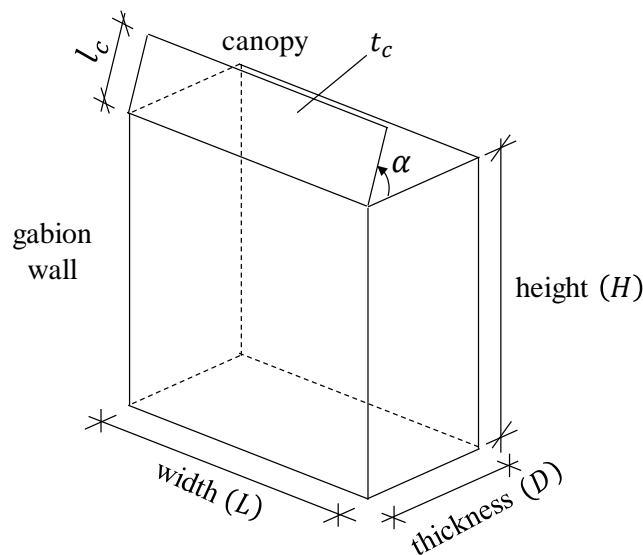


Figure 5-3: Geometry of the gabion wall and canopy

The canopy of M1 (GWC back) was oriented away from the charge at an angle of inclination of  $45^\circ$  with respect to the horizontal, whereas the canopy of M3 (GWC front) was oriented facing the charge at an angle of inclination of  $135^\circ$  with respect to the horizontal.

### 5.1.3 Experimental instrumentation

Figure 5-4 shows the instrumentation of the experiments. Gauges ps2 - ps4 were mounted in small steel plates, which were anchored at the top of steel rods with hollow cross-sections. The normal of the steel plates was oriented parallel to the gabion wall (Figure 5-4a). The facade was composed of a rigid gabion wall and was placed at a distance of 10m from the charge. A post (taller than 4m) was fixed to the facade at the centreline (Figure 5-4b). In addition, four wooden plates measuring 0.4m x 0.4m were attached to the post at elevations of 1m, 2m, 3m and 4m, respectively (Figure 5-4b). The wooden plates to measure the reflected overpressures at the facade were so large and rigid that an ideal rigid reflection assumption can be made. The distance between the gabion wall and the wooden plates, where gauges were mounted, was 0.16m (Figure 5-4c). For the pressure measurement, the gauge type Kulite XT-190 (M) with different pressure categories were used, i.e. 1.7bar for gauges ps1 - ps4 and 0.35bar for gauges pr1 - pr4. If the measured values exceed the burst pressure (three times the pressure category), it may lead to gauge damage. The typical and maximum sensitivity ranges of gauges are  $\pm 0.1\%$

and  $\pm 0.5\%$  based on an air temperature of  $15^{\circ}\text{C}$ . However, these sensitivity ranges of gauges depend also on the air temperature and the temperature gradient. The data was provided with a sampling rate of 500kHz.

As shown in Figure 5-4a, gauges ps2 - ps4 were placed on a small steel plate. Regarding the free field scenario, the shock wave propagates along the line connecting the charge centre and gauges ps1 - ps4. Under such circumstances, the side-on overpressures are measured at the gauges, since the shock wave impinges the gauges at an angle of incidence of  $\alpha = 90^{\circ}$ . In fact, the shock wave propagation is altered due to the presence of the blast wall. The shock wave is partly reflected from the front face of the wall, partly flows around the sides of the wall and partly flows over the top of the wall. As the shock wave arrives at gauges ps2 - ps4, it impinges the gauges at an angle of incidence  $\alpha$  which is near to but different than  $90^{\circ}$ . This means that this pressure gauge arrangement would result in the measured overpressures neither side-on overpressures, nor reflected overpressures. The values of the peak overpressure can be estimated based on the cosine distribution (Eq. (4-19)). Given a deviation of  $5^{\circ}$  in the angle of incidence, i.e.  $\alpha = 85^{\circ}$ , they are expected to be about 10% higher than the side-on values for a free field hemi-spherical scenario.

When measuring the reflected overpressures at the massive wall, the actual reflecting surface areas are the same for gauges pr1 - pr4, i.e. the area of wooden plates (0.4m x 0.4m). As the shock wave impinges the wooden plate, the incident shock wave is reflected and rarefaction waves flow from the free edges of wooden plate towards the plate centre. After a certain time, these rarefaction waves reach the plate centre and the overpressure is relieved. This phenomenon is referred to as the clearing effect (Section 3.7). It is worth noticing that, on the one hand, the clearing effect occurs at a certain time (in literature referred to as the clearing time, e.g. in *UFC 3-340-01*) after the shock wave is reflected from the wooden plate. On the other hand, the side-on overpressure is instantaneously increased to the reflected overpressure at the time of impingement. Therefore, the clearing effect does not reduce the peak overpressures but the maximum impulses measured at gauges pr1 - pr4 to a certain extent. Regarding the peak overpressures, the experimental results seem to be consistent among gauges pr1 - pr4.

A spherical bare charge of 3.9kg PETN was detonated at a distance of 5m in front of the blast wall at an elevation of 0.4m above the ground. This distance (5m) is selected based on two considerations. Firstly, a far-field scenario is represented. As the shock wave hits the walls, a plane wave assumption can be made. Secondly, the three blast wall configurations arranged according to the arena set-up of experiments should not affect each other in the time region of interest. A TNT equivalence factor of 1.27 is used to convert the explosive PETN used in the experiments to the reference explosive TNT (Section 3.4). It results in a charge mass of 5kg TNT equivalent. The charge was hung at a wooden gallow in the air (Figure 5-4d). The charge shape was almost spherical. Thus, it is modelled spherically in the numerical analysis. It is worth mentioning that the charge shape can affect the generated blast loads to a certain extent. To reduce the influence of ground surface roughness on the shock wave reflection and the energy loss due to the crater formation, a square steel plate was placed directly below the charge. The ground at the test site consists of a mixture of rocky materials and gravel. However, the ground surface is assumed to be a flat, even and rigid surface in the numerical simulations.



Figure 5-4: Experimental instrumentation (a) gauges ps2 - ps4; (b) gauges pr1 - pr4; (c) distance between gabion wall and wooden plate where gauges were mounted; (d) explosive charge with the wooden gallow and the steel plate (photos: WTD52 / UniBwM)

The influence of the Mach stem formation (Section 3.8.3) was not measured in the experiments. Hence, it is neglected in the numerical models described in Section 6.3. However, it can be considered in a purely ALE numerical model, which will be discussed in Section 6.2. In addition to pressure measurements, two high-speed cameras were used. Each experiment was recorded at 25000frames/second. The videos revealed what was expected that the deflection of the canopy in configuration M3 (GWC front) was significantly larger than that in M1 (GWC back). No plastic deformation was observed in the canopies throughout the experiments. When replayed in slow motion, it was possible to observe the ignition of the detonation (Figure 5-5b) and the accompanying fireball (Figure 5-5c).



Figure 5-5: Detonation process (a) initial state; (b) ignition point; (c) accompanying fireball (photos: WTD52 / UniBwM)

### 5.1.4 Experimental data

Eight simultaneous pressure measurements for each wall configuration were made corresponding to five different values of the horizontal distance  $R$  from the charge to the gauge and four different values of the gauge elevation  $h$  above the ground. In total, 24 pressure recordings were made in each experiment. To assess the quality of the experimental results in a statistically valid manner, the experiment with the same set-up was repeated three times (V1, V2 and V3 in Table 5-2 - Table 5-5).

#### 5.1.4.1 Overpressure-time history

The overpressure recordings in experiment V1 are shown in Figure 5-6 (side-on overpressures at gauges ps1 - ps4) and Figure 5-7 (reflected overpressures at gauges pr1 - pr4) for configuration M3 (GWC front).

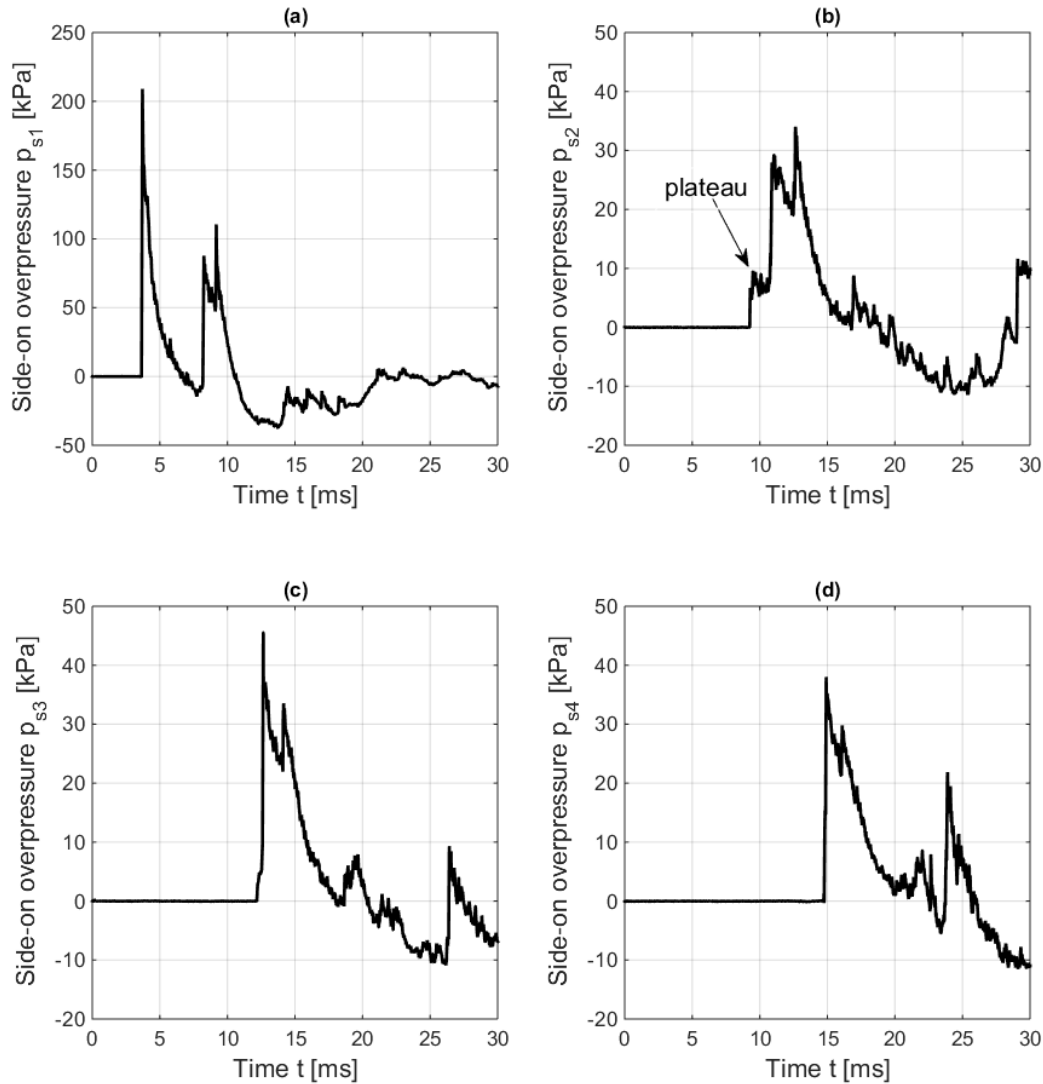


Figure 5-6: Side-on overpressure-time histories measured in experiment V1, M3 - GWC front  
(a) ps1; (b) ps2; (c) ps3; (d) ps4

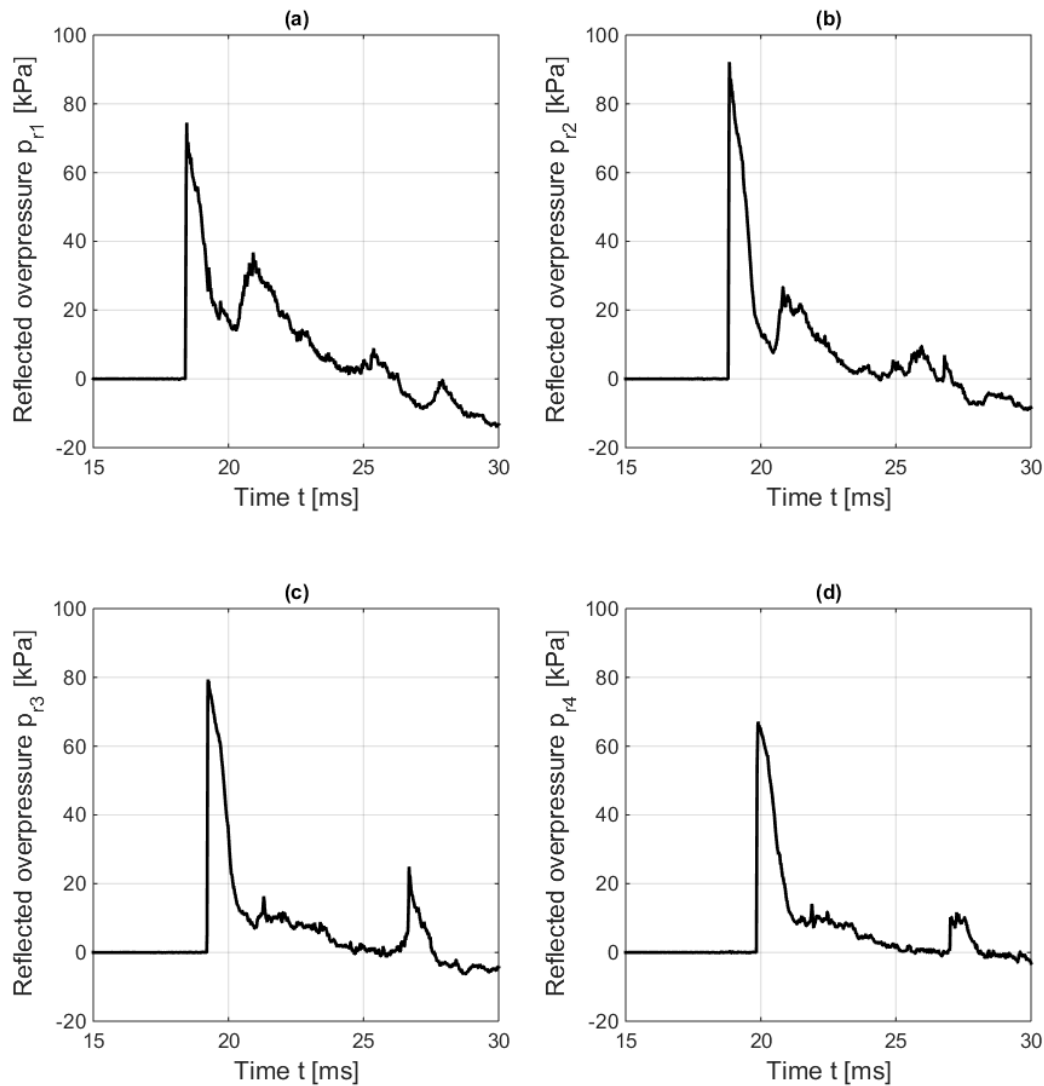


Figure 5-7: Reflected overpressure-time histories measured in experiment V1, M3 - GWC front (a) pr1; (b) pr2; (c) pr3; (d) pr4

The first peak at gauge ps1 (Figure 5-6a) is caused by the arrival of the shock wave at that gauge, whereas the second and third peaks are related to the reflection of the shock wave from the gabion wall and from the canopy. A remarkable plateau is observed in the experimental recording at gauge ps2 (Figure 5-6b). Its magnitude is only about one third of the corresponding peak overpressure, which appears at about 1.6ms later. The reason for this plateau is most likely attributed to the presence of the small openings (slits) between the cubic gabion boxes (Figure 5-8). A small amount of the shock wave propagates directly through this slit to gauge ps2. The arrival time of 9.27ms obtained from the experimental recording conforms well to the value predicted by ConWep (9.09ms), which confirms the presumption mentioned above. The plateau is much less pronounced at gauge ps3 (Figure 5-6c) and is not discernible at gauges ps4 (Figure 5-6d) and pr1 - pr4 (Figure 5-7). At gauge ps2, the peak at  $t = 11.0\text{ms}$  (Figure 5-6b) is associated with the arrival of the shock front, which partly flows around the sides of the wall. Subsequently, these parts of the waves merge with the part flowing over the top of the wall. This gives rise to the peak at  $t = 12.6\text{ms}$ .

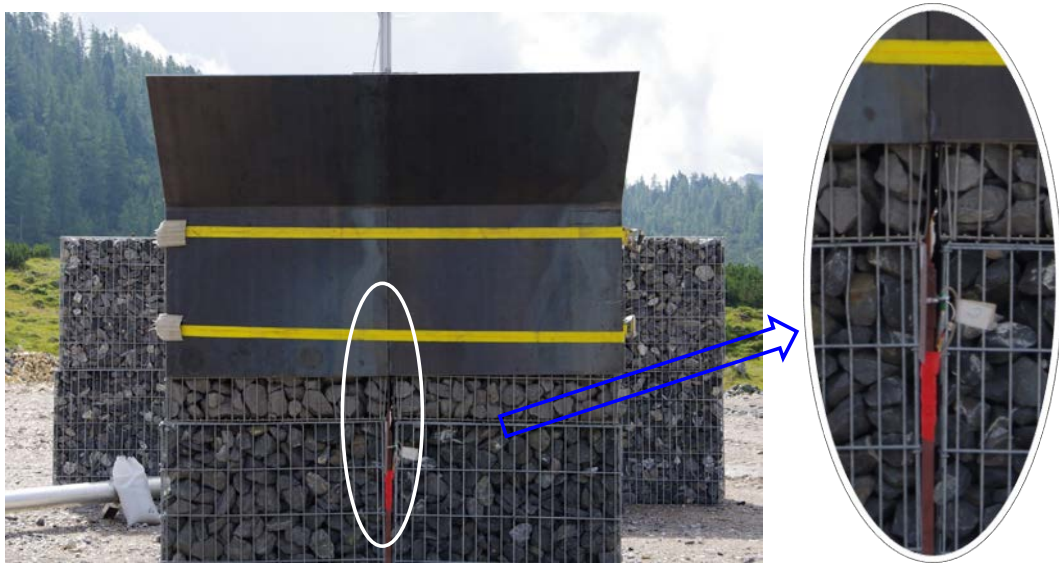


Figure 5-8: Slit between cubic gabion boxes (photos: WTD52 / UniBwM)

In order to visualize the entire relevant reflected overpressure-time histories, the time axes in Figure 5-7 start at 15ms and extend to 30ms, which are different to the ones in Figure 5-6. As the shock wave impinges on the front face of the wooden plate to mount gauge pr1, the incident shock wave is partly reflected and partly diffracted around the free edges of the wooden plate. Due to the small distance (0.16m) between the wooden plates and the massive wall (Figure 5-4c), the diffracted wave is re-reflected from the massive wall and then impinges gauge pr1 once again. This phenomenon leads to the peak overpressures of about 40kPa at  $t = 20.9\text{ms}$  in the experimental recordings (Figure 5-7a). The same phenomenon as occurred at gauge pr1 can also be observed at gauge pr2 (Figure 5-7b). Due to the low height of the massive wall (2m, Figure 5-4b), the reflecting surface area behind the wooden plate to mount gauge pr2 is approximately 50% of that behind the wooden plate to mount gauge pr1. Therefore, the magnitude of the peak overpressures for gauge pr2 (due to the re-reflection from the massive wall) is less than that for gauge pr1. For gauges pr3 and pr4, the diffracted waves will not be re-reflected again, i.e. they will propagate undisturbed away from the rear face of the wooden plates. Hence, the aforementioned phenomenon does not occur at gauges pr3 and pr4.

#### 5.1.4.2 Data statistics at the gauges in front of the blast wall

Since the pressure gauges ps1 are located 1m in front of the wall, the overpressure-time history is not affected by the interaction with any obstacle until the shock wave strikes the wall. Therefore, the first peak overpressures measured in all experiments with three different configurations of blast walls (M1 - GWC back, M2 - GW and M3 - GWC front), in total 9 values, can be considered together to calculate the mean value of the peak overpressures at gauges ps1 (Figure 5-9).

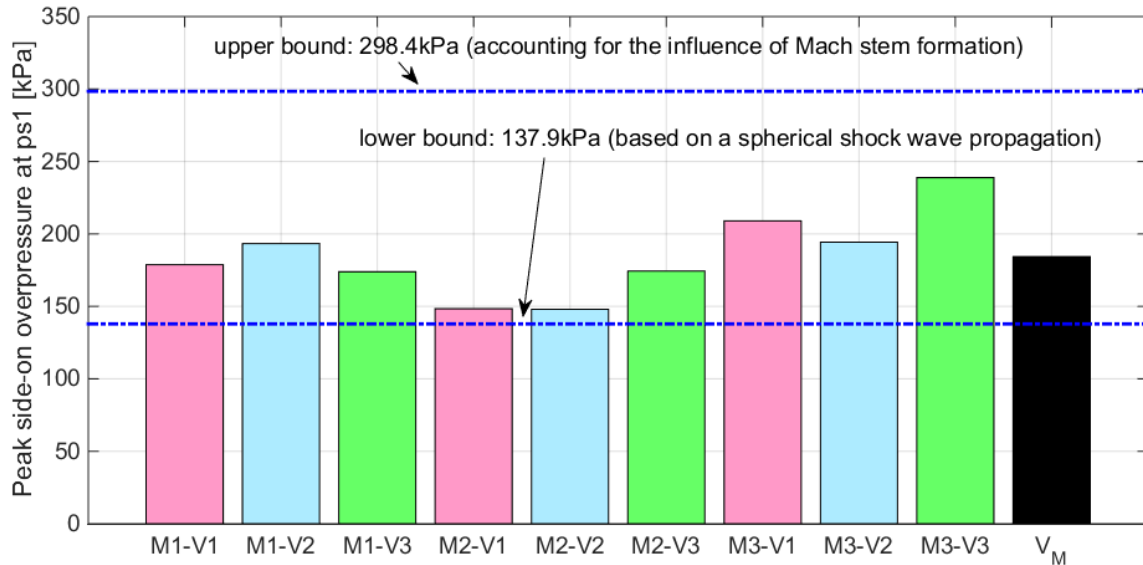


Figure 5-9: Peak side-on overpressures at gauges ps1 of the experiments

If the charge is detonated at a small elevation above the ground, e.g. 0.4m in the experiments, the shock wave propagation is neither spherical nor hemi-spherical. The incident shock wave propagates spherically from the charge centre until it impinges on the ground surface, from which the wave is reflected. At certain distances, the incident and reflected waves are merged and a third wave, the so-called Mach stem, is generated (Section 3.8.3). As observed by *Gebbeken 2017*, the peak overpressures at the gauges in front of the protective barrier may be greatly influenced by the formation of the Mach stem. To assess the quality of the data recorded in the experiments (V1, V2 and V3), a plausibility analysis was carried out, according to the method described by *Gebbeken 2017*. Owing to the same charge mass ( $W = 5\text{kg}$  TNT equivalent) and the same distance from the charge to gauge ps1 ( $R = 4\text{m}$ ), the lower and upper bounds of the theoretically possible overpressures used in *Gebbeken 2017* are directly adopted to verify the peak side-on overpressures measured in the experiments. The lower bound (137.9kPa, Figure 5-9) is based on a spherical shock wave propagation, whilst the influence of the Mach stem formation is accounted for in the upper bound (298.4kPa, Figure 5-9).

As outlined in Figure 5-9, all values measured at gauge ps1 in the experiments (M1-V1, M1-V2, M1-V3 etc.) are within these limit bounds. Therefore, it is justified to use them to calculate the statistical quantities at gauges ps1, i.e. the mean value  $\mu$ , the standard deviation  $\sigma$  and the coefficient of variation  $\vartheta$  (Table 5-2). The mean value of 184.30kPa is somewhat less than the predicted value (193.90kPa) calculated by the formulae of *Kingery and Bulmash 1984*, if the charge is considered to be so close to the ground that a surface burst is assumed. It is observed that the values measured at gauges ps1 (4m from the charge) vary widely. Its standard deviation  $\sigma = 28.76\text{kPa}$  and coefficient of variation  $\vartheta = 0.156$  are the biggest ones among all gauges (Table 5-2 - Table 5-5), which indicates that the scattering at this gauge is considerably large. This is most likely attributed to the so-called cauliflower effect, which arises from the incomplete burning process of detonation products. In addition, the charge shape was not exactly spherical (Figure 5-4d).

Table 5-2: Statistics of experimental data at gauges ps1 ( $R = 4\text{m}$ ,  $h = 1\text{m}$ )

Type	Configuration	Experiment	$t_a$ [ms]	ps1 [kPa]	$\mu$ [kPa]	ps1 $\sigma$ [kPa]	$\vartheta$ [-]
side-on	M1	V1	3.67	178.73	184.30	28.76	0.156
		V2	3.52	193.37			
		V3	3.78	173.86			
	M2	V1	3.91	148.35			
		V2	3.71	147.96			
		V3	3.94	174.36			
	M3	V1	3.71	208.97			
		V2	3.82	194.28			
		V3	3.70	238.86			

The canopy arranged at the top of the wall is used to further reduce the blast loads behind the wall, however, the reflected blast energy would also likely increase the blast loads on the blast wall and become potentially more damaging to the blast wall, which could induce the secondary fragment hazards. Figure 5-10 compares the overpressure- and impulse-time histories recorded at gauges ps1 in front of the blast wall in experiment V1 for configurations M1 (GWC back), M2 (GW) and M3 (GWC front).

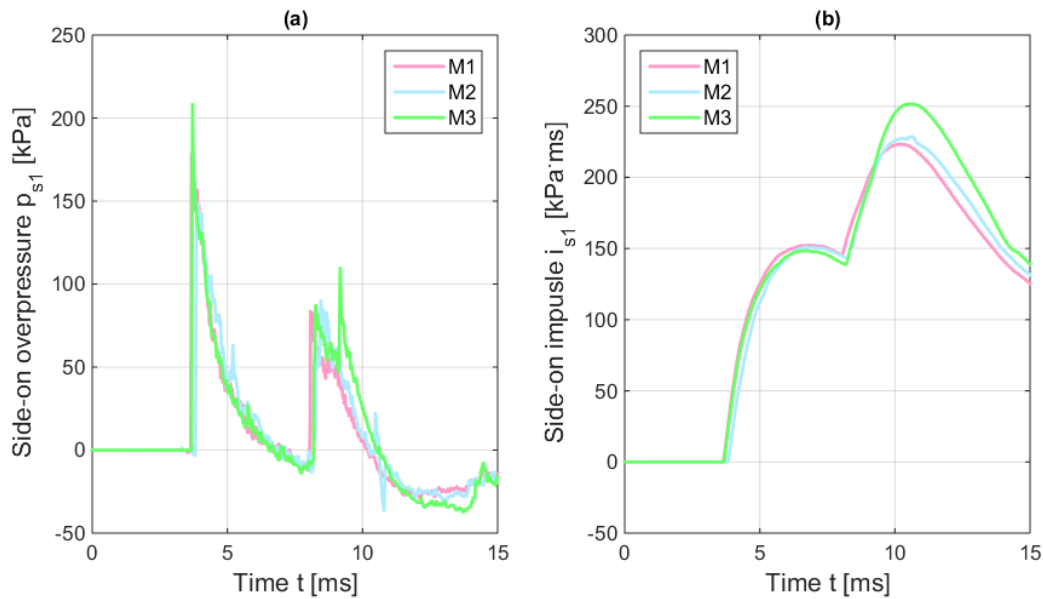


Figure 5-10: Experimental recordings at gauges ps1 measured in experiment V1 for configurations M1 - GWC back, M2 - GW and M3 - GWC front (a) overpressure-time histories; (b) impulse-time histories

As already mentioned in Section 5.1.4.1, the first peak at gauge ps1 (Figure 5-10a) is caused by the arrival of the shock wave at that gauge, whereas the second peak is related to the reflection of the shock wave from the gabion wall. It is noticeable that a third peak (at 9.2ms) is evident in configuration M3 (GWC front). This is attributed to the reflection of the shock wave from the canopy, which is arranged facing the charge. Unlike configuration M3 (GWC front), the canopy oriented away from the charge does not cause a third peak in the overpressure-time

history for configuration M1 (GWC back). Comparing the maximum impulse with and without a canopy (Figure 5-10b), the amount of the blast energy that is reflected by the blast wall (gabion wall and canopy) can be assessed. Configuration M1 (GWC back) reflects only slightly less blast energy (approximately 5%) than configuration M2 (GW) through the arrangement of a canopy oriented away from the charge, whereas the canopy oriented facing the charge causes an increase of about 27% in the blast energy that is reflected from the blast wall.

5.1.4.3 Data statistics at the gauges behind the blast wall

Similarly, the mean values  $\mu$ , the standard deviations  $\sigma$  and the coefficients of variation  $\vartheta$  of the results measured at other gauges are calculated and summarized in Table 5-3, Table 5-4 and Table 5-5 for configurations M1 (GWC back), M2 (GW) and M3 (GWC front).

Table 5-3: Statistics of experimental data at gauges ps2 - ps4 and pr1 - pr4, M1 (GWC back)

Gauges		V1		V2		V3		Statistics				
Type	Label	R [m]	h [m]	t <sub>a</sub> [ms]	p [kPa]	t <sub>a</sub> [ms]	p [kPa]	t <sub>a</sub> [ms]	p [kPa]	P		
										$\mu$ [kPa]	$\sigma$ [kPa]	$\vartheta$ [-]
side-on	ps2-1	6.5	1	12.44	32.00	12.25	34.24	12.55	32.49	32.91	1.18	0.036
	ps3-1	7.5	1	12.53	55.13	12.30	43.78	13.95	48.61	49.17	5.70	0.116
	ps4-1	8.5	1	14.87	43.82	15.60	37.97	15.11	45.28	42.36	3.87	0.091
reflected	pr1-1	9.84	1	18.29	74.60	18.65	64.94	18.51	74.92	71.49	5.67	0.079
	pr2-1	9.84	2	18.49	89.74	18.41	82.99	18.68	87.59	86.77	3.45	0.040
	pr3-1	9.84	3	18.77	74.79	18.70	71.11	18.95	72.37	72.76	1.87	0.026
	pr4-1	9.84	4	19.27	50.77	19.37	44.31	19.39	46.15	47.07	3.33	0.071

Table 5-4: Statistics of experimental data at gauges ps2 - ps4 and pr1 - pr4, M2 (GW)

Gauges		V1		V2		V3		Statistics				
Type	Label	R [m]	h [m]	t <sub>a</sub> [ms]	p [kPa]	t <sub>a</sub> [ms]	p [kPa]	t <sub>a</sub> [ms]	p [kPa]	P		
										$\mu$ [kPa]	$\sigma$ [kPa]	$\vartheta$ [-]
side-on	ps2-2	6.5	1	11.58	34.39	11.35	36.61	12.23	32.70	34.57	1.96	0.057
	ps3-2	7.5	1	12.67	47.33	12.56	45.55	13.24	43.32	45.40	2.01	0.044
	ps4-2	8.5	1	15.10	41.32	14.89	42.28	15.16	44.17	42.59	1.45	0.034
reflected	pr1-2	9.84	1	18.68	76.98	18.53	74.56	18.88	89.76	80.43	8.17	0.102
	pr2-2	9.84	2	18.83	80.30	18.62	74.66	19.02	79.35	78.11	3.02	0.039
	pr3-2	9.84	3	19.30	66.74	19.01	61.99	19.40	62.57	63.77	2.59	0.041
	pr4-2	9.84	4	19.90	53.71	19.65	50.69	20.01	51.51	51.97	1.56	0.030

Table 5-5: Statistics of experimental data at gauges ps2 - ps4 and pr1 - pr4, M3 (GWC front)

Gauges		V1		V2		V3		Statistics				
Type	Label	R [m]	h [m]	t <sub>a</sub> [ms]	p [kPa]	t <sub>a</sub> [ms]	p [kPa]	t <sub>a</sub> [ms]	p [kPa]	P		
										$\mu$ [kPa]	$\sigma$ [kPa]	$\vartheta$ [-]
side-on	ps2-3	6.5	1	12.63	34.02	12.80	33.64	12.59	34.04	33.90	0.23	0.007
	ps3-3	7.5	1	12.65	45.56	12.84	40.90	12.53	34.09	40.18	5.77	0.144
	ps4-3	8.5	1	14.91	38.02	15.13	35.70	14.87	35.83	36.51	1.30	0.036
reflected	pr1-3	9.84	1	18.46	74.50	18.74	71.79	18.41	75.02	73.77	1.73	0.024
	pr2-3	9.84	2	18.84	92.18	19.14	87.02	18.80	88.17	89.12	2.71	0.030
	pr3-3	9.84	3	19.25	79.38	19.57	74.81	19.19	79.15	77.78	2.58	0.033
	pr4-3	9.84	4	19.90	67.14	20.26	64.33	19.85	65.94	65.81	1.41	0.021

An appreciable variance in the peak side-on overpressures is observed at gauges ps3 for configurations with a canopy. The coefficients of variation for configurations M1 (GWC back,  $\vartheta = 0.116$ , Table 5-3) and M3 (GWC front,  $\vartheta = 0.144$ , Table 5-5) are much larger than that for configuration M2 (GW,  $\vartheta = 0.044$ , Table 5-4). This discrepancy at gauges ps3 is most likely related to the complicated pressure field behind the canopy. Due to the presence of the canopy arranged at the top of the gabion wall, a part of the shock wave travels upwards along the gabion wall and the canopy in order to flow over the top of the canopy. This results in vortices at the top of the canopy. After the wave flows over the top of the canopy, the flow pattern behind the canopy becomes very complicated because the wave is reflected not only by the top surface of the gabion wall but also by the rear face of the canopy. In addition, multiple reflections may occur in this region between the top surface of the gabion wall and the rear face of the canopy. Furthermore, the coefficient of variation at gauges pr1 for configuration M2 (GW,  $\vartheta = 0.102$ , Table 5-4) is also relatively large. This is most likely because the parts of the wave flowing around the sides and over the top surface of the gabion wall merge near gauges pr1.

The relatively low standard deviations and coefficients of variation at other gauges indicate that the data is reproducible. It is important to mention that three or less than three data points only provide a tendency for the actual mean value of the results. Hence, the mean values obtained from the experiments only give an approximation, and further experiments are necessary for a statistically reliable statement, especially for gauges ps1, ps3 and pr1. Therefore, it is recommended to conduct at least four experiments for each configuration.

#### 5.1.4.4 Evaluation of overpressure and impulse reduction

To evaluate the effectiveness of blast walls, the mean values of the peak overpressures and maximum impulses recorded at the gauges behind the walls are shown in Figure 5-11 (mean values of ps2 - ps4 in Figure 5-11a and c, mean values of pr1 - pr4 in Figure 5-11b and d). The maximum impulses are derived by numerical integration of the overpressure-time histories. The reference quantities (*Kingery and Bulmash 1984*, denoted as K&B) for the peak overpressures and maximum impulses are also included in Figure 5-11, which are derived by the empirical approach for the scenario where no blast wall is present. Comparing the experimental overpressures to the reference overpressures obtained in a free field scenario, a reduction in the side-on overpressure is clear (Figure 5-11a). The reduction in the side-on overpressures decreases with the distance from the charge to the gauge.

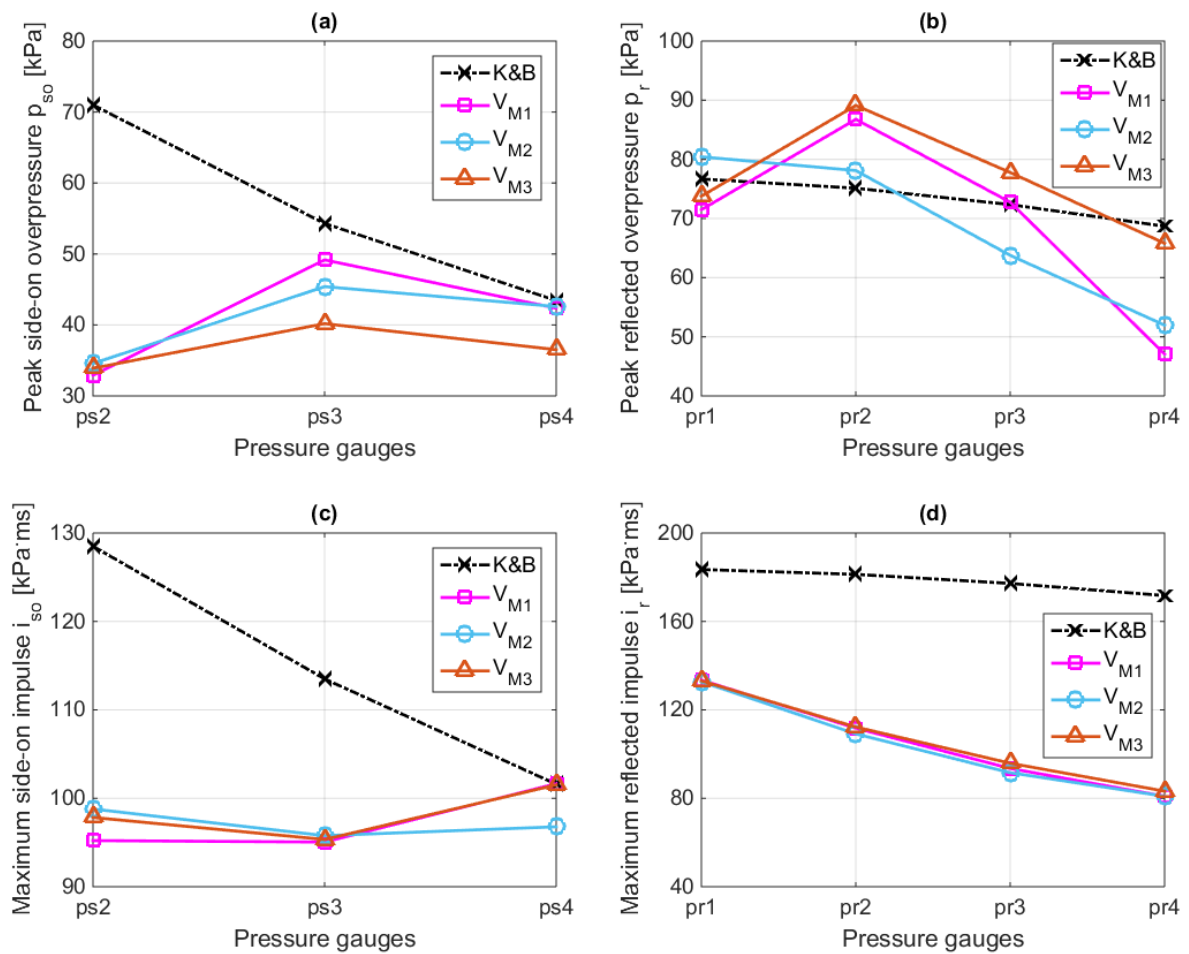


Figure 5-11: Experimental results (a) peak side-on overpressures; (b) peak reflected overpressures; (c) maximum side-on impulses; (d) maximum reflected impulses

The analysed data shows that regarding the results at gauges ps2 (6.5m from the charge), similar values of peak overpressures are measured in configurations M1 (GWC back), M2 (GW) and M3 (GWC front). The overpressures are reduced by approximately 50% compared to the results from K&B. This implies that the arrangement of a canopy at the top of the gabion wall does not provide additional overpressure reduction at this gauge, which is only 0.5m behind the gabion wall. The overpressure reduction is dictated by the shielding effect provided by the gabion wall. In other words, the canopy does not offer any further contribution to reduce the overpressure at this gauge closely behind the wall. At gauges ps3 (7.5m from the charge), configuration M3 (GWC front) shows the highest overpressure reduction and a lower overpressure is measured in configuration M2 (GW) than in M1 (GWC back). The overpressures at gauges ps3 are reduced by 9.4% in M1 (GWC back), 16.4% in M2 (GW) and 26.0% in M3 (GWC front), compared to the results of the shock wave propagation in the free field. From this observation, it is concluded that a canopy oriented away from the charge may have an adverse effect on the overpressure reduction behaviour of the blast wall. At gauges ps4 (8.5m from the charge), M1 (GWC back) and M2 (GW) show a very slight reduction (2% - 3%) in the peak overpressure, whereas M3 (GWC front) reduces the peak overpressure by 15.9%. As expected, configuration M3 (GWC front) shows the best performance in overpressure reduction. Unlike the overpressure, nearly identical reduction in the maximum impulse is achieved by all three

configurations except at gauges ps4. Similarly, the side-on impulse reduction also decreases with the distance from the charge to the observed gauge (Figure 5-11c). At gauges ps4 (8.50m from the charge), M1 (GWC back) and M3 (GWC front) do not provide any impulse reduction, whereas M2 (GW) slightly reduces the maximum impulse by 4.7%. Therefore, it is concluded that a canopy arranged at the top of the gabion wall may have an adverse effect on the impulse reduction behaviour of the blast wall. Regarding the reflected overpressures at the facade, the values of peak reflected overpressures may exceed the expected K&B-values when the blast wall is not present at all, e.g. at an elevation of 2m (pr2) above the ground (Figure 5-11b). This effect is also observed in the numerical simulations in Section 6.3.4. Details will be discussed in Section 6.3.4.4. However, the reflected impulses are reduced from 27.3% at gauges pr1 to 52.9% at gauges pr4 (Figure 5-11d).

### 5.1.5 Conclusion: blast walls with a canopy on top

In summary, the experiments show that configuration M3 (GWC front), in which the canopy is oriented facing the charge (angle of inclination  $\alpha = 135^\circ$ ), achieves the best performance in overpressure and impulse reduction at gauges ps2 - ps4. The overpressure reduction at gauges ps2 - ps4 varies from 15.9% to 52.3% and the impulse reduction varies from 0.1% to 23.9%.

According to the experimental set-up, the blast walls have a width of only 2m and a total height varying from 2m to 2.53m. Given that the charge was detonated 0.4m above the ground, the horizontal air flow around the both sides of the wall is more significant than the vertical air flow over the top of the wall. Furthermore, the waves flowing around the two sides interact with the one over the top of the wall, which causes a superposition effect on the blast loads. This affects significantly the shock wave behind the wall. This effect is indicated in Figure 5-11b by the overpressure increase at gauges pr1 and pr2 in configuration M2 (GW) as well as at gauges pr2 and pr3 in configurations M1 (GWC back) and M3 (GWC front). In practice, however, the blast walls are erected around the buildings to be protected (perimeter walls). Thus, the aforementioned limitation in the wall width (2m) should not be an issue to affect the shielding effect of the blast wall. Based on this consideration, blast walls having a significantly larger width, in which no horizontal air flow occurs, should be used in the forthcoming experiments. Further investigations, e.g. the influence of the wall width on the blast loads and the derivation of the infinite wall width, will be carried out by using numerical simulations in Section 6.3.4.

The arrangement of canopy at the top of the wall would further reduce the blast loads behind the wall. In addition, the canopy is easy to establish at the top of the wall, not only as a part of a new blast wall design but also as a retrofitting measure of an existing blast wall. It can be easily constructed as a fast solution. The mass of the canopy is comparatively low, so that, usually, no reinforcement for the existing foundation of the blast wall is required. However, besides damage to the canopy, the trapped blast energy would also likely increase the blast loads on the wall and become potentially more damaging to the wall, which could induce the secondary fragment hazards.



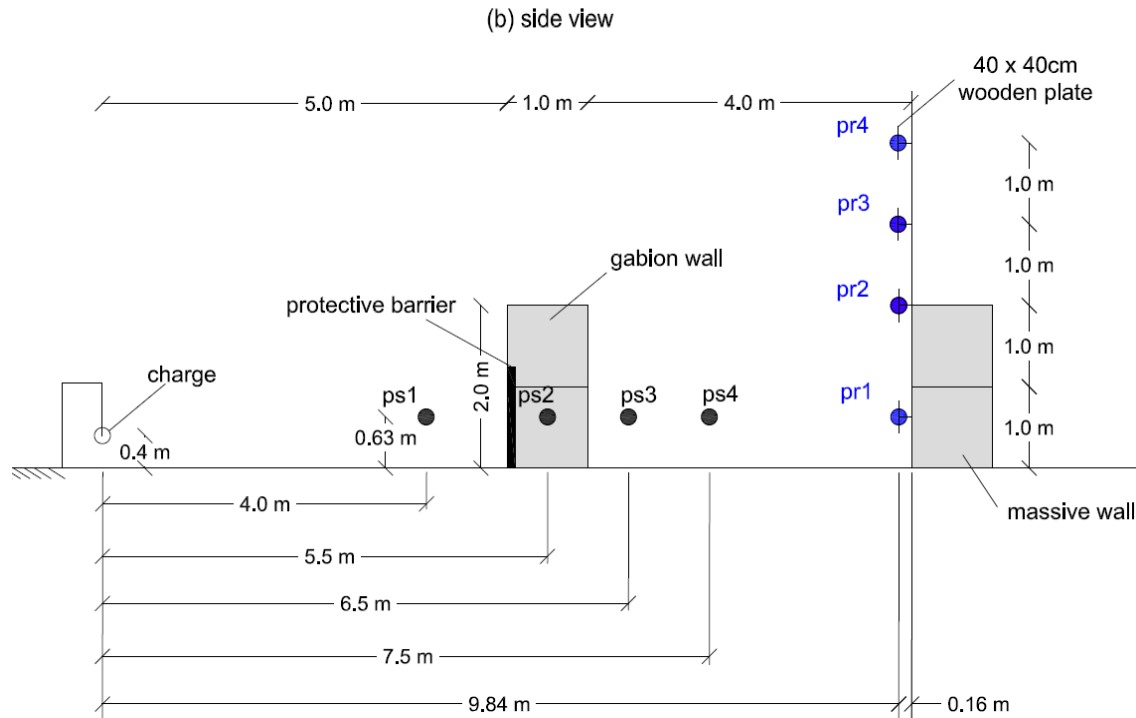


Figure 5-12: Experiment set-up (a) plan view; (b) side view

Two gabion walls measuring 4m x 2m x 1m (width x height x thickness, Figure 5-13a) were placed adjacent to the barrier (steel posts and frame) in order to prevent direct air flow around the sides of the barrier of interest. To evaluate the effectiveness of protective barriers made of three different steel post configurations (M1, M2 and M3, Figure 5-13b, c and d), three experiments (V1, V2 and V3) were carried out. The steel posts were framed by a steel construction. An additional experiment (V0) with the configuration without steel posts (Mref, Figure 5-13a) was carried out in order to provide a reference for comparison. The measured values are also used to validate the numerical models.

In the experiments, the steel posts were placed 5m in front of the building to be protected and framed by a steel construction. As the shock wave strikes the barrier, it is partly transmitted through the openings between the posts and partly reflected from the front faces of the posts towards the charge. Meanwhile, the posts sustain deformations and thus a portion of the blast wave energy is transformed into internal energy (absorption), although as observed throughout the experiments, the deformations of the posts and the frame are negligibly small. Furthermore, the shock wave flows around the sides of the posts and over the top of the barrier (diffraction). Consequently, a combination of energy transmission, reflection, absorption and diffraction mitigates the blast loads on the building.

In order to record the overpressure-time history in a free field scenario and the subsequent overpressure-time history reflected from the barrier, a gauge (ps1, Figure 5-12b) was placed 1m in front of the barrier at a height of 0.63m above the ground. To capture the side-on overpressures behind the barrier, three gauges (ps2, ps3 and ps4, Figure 5-12b) were located at a height of 0.63m between the barrier and the massive wall, which represents the envelope of a building to be protected. Here, at a distance of 9.84m from the charge, another four gauges

(pr1 - pr4, Figure 5-12b) were placed to measure the reflected overpressures. Reflected overpressures were measured at heights of 0.63m, 2m, 3m and 4m, respectively.

### 5.2.2 Steel posts configurations

Figure 5-13 gives an overview of the protective barriers employed in the experiments. A reference configuration without posts (Figure 5-13a) and three different configurations of steel posts (Figure 5-13b, c, d) were examined during the experiments. The basic bearing construction for the steel posts was a rectangular steel frame (Figure 5-13), on which the steel posts were mounted.

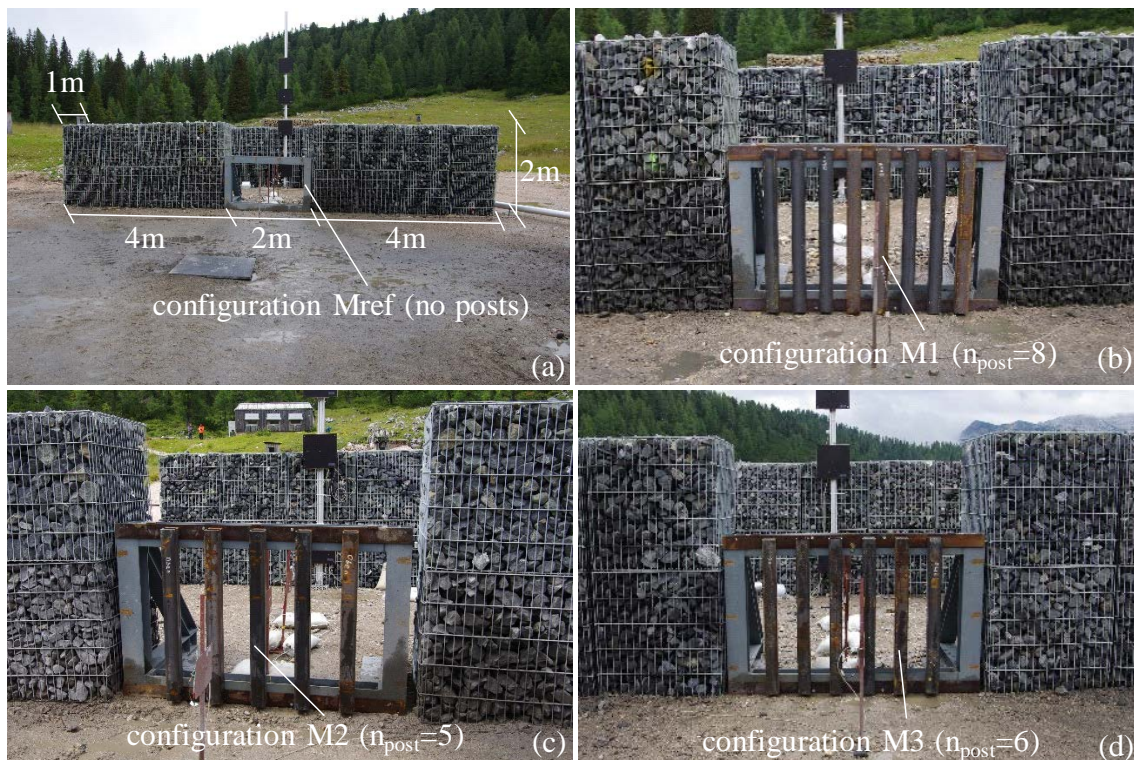


Figure 5-13: Barrier configurations (a) Mref, no posts; (b) M1,  $n_{post} = 8$ ; (c) M2,  $n_{post} = 5$ ; (d) M3,  $n_{post} = 6$  (photos: WTD52 / UniBwM)

A plan view of the configurations (M1, M2 and M3) is shown in Figure 5-14. The number of posts  $n_{post}$  in configurations M1, M2 and M3 is 8, 5 and 6, respectively. Each steel post has a length of 1.25m and has a square hollow section (QRO 100mm x 100mm x 8mm). The posts are arranged with a spacing ranging from 100mm to 200mm. It results in different relative opening fractions (ROF), which are defined as the ratio of opening area to front face area of the barrier, i.e. for configurations Mref (no posts), M1 ( $n_{post} = 8$ ), M2 ( $n_{post} = 5$ ) and M3 ( $n_{post} = 6$ ), the ROFs are 100%, 52.4%, 70.2% and 64.3%, respectively. The centreline of the barrier is also plotted as a dashed line in Figure 5-14. It should be noted that there is a post placed at the centreline of the barrier for configuration M2 ( $n_{post} = 5$ ), whereas no posts are placed at the centreline of the barrier in configurations M1 ( $n_{post} = 8$ ) and M3 ( $n_{post} = 6$ ).

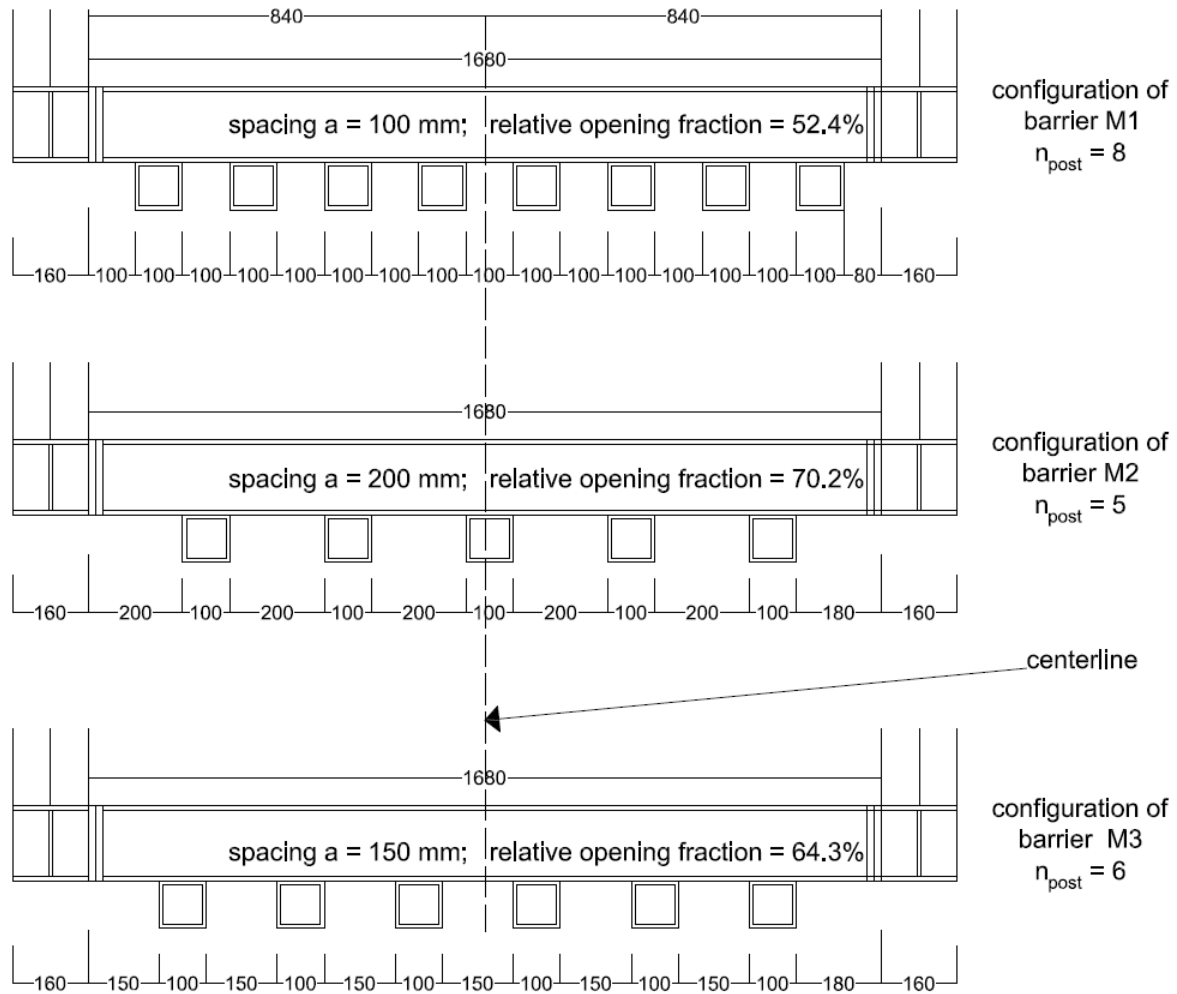


Figure 5-14: Configurations of steel posts with a square hollow section, plan view

As already mentioned in Section 5.1.2, the reflection phenomenon can be affected by the open porous surfaces, e.g. holes between the coarse-grained gravel in the gabion walls (Figure 5-13). This effect was not considered in this study, but it will be analysed in the upcoming experiments as well as in the numerical models.

### 5.2.3 Experimental instrumentation

The instrumentation employed in the experiments of protective barriers made of steel posts is shown in Figure 5-15. They are only two differences compared to the instrumentation employed in the experiments of blast walls with a canopy on top (Figure 5-4). Firstly, gauges ps1 - ps4 and gauge pr1 were located at an elevation of 0.63m above the ground (Figure 5-15). Secondly, gauge ps2, ps3 and ps4 were located at a horizontal distance of 5.5m, 6.5m and 7.5m from the charge, respectively (Figure 5-12b and Figure 5-15a). The remaining instrumentation, e.g. the wooden plates to mount gauges pr1 - pr4, the explosive charge (PETN) and the steel plate below the charge, are the same as in the experiments of blast walls with a canopy on top (Figure 5-4c and d).



Figure 5-15: Experimental instrumentation (a) gauges ps2 - ps4; (b) gauges pr1 - pr4 (photos: WTD52 / UniBwM)

#### 5.2.4 Experimental data

In each experiment, 24 pressure recordings were made. To statistically assess the quality of the experimental results, three experiments with the same set-up (V1, V2 and V3, Table 5-6, Table 5-8 - Table 5-10) and an additional experiment (V0, Table 5-6 - Table 5-7) with the reference configuration Mref (no posts) were conducted. In experiment V0, a similar set-up as shown in Figure 5-12a was used, however, all three configurations were replaced by the reference configurations Mref (no posts). Three pressure recordings (V0-1, V0-2 and V0-3) were captured at each gauge during experiment V0. In total, 96 pressure recordings were obtained during the experiments.

##### 5.2.4.1 Overpressure-time history

The overpressure recordings measured in experiment V3 are shown in Figure 5-16 (side-on overpressures at gauges ps1 - ps4) and Figure 5-17 (reflected overpressures at gauges pr1 - pr4) for configuration M1 ( $n_{post} = 8$ ).

The first peak at gauge ps1 (Figure 5-16a) is caused by the arrival of the shock front at that gauge, whereas the following peaks are related to the reflection of the shock wave from different posts in front of the steel frame construction. The experimental recording exhibits a rather oscillatory behaviour in the reflection from posts, i.e. multiple peaks between  $t = 8.1\text{ms}$  and  $t = 8.9\text{ms}$ . For gauge ps2 (Figure 5-16b), the first peak at  $t = 6.8\text{ms}$  is associated with the arrival of the shock front at that gauge, which is transmitted through the opening in the middle of the barrier (Figure 5-14). Subsequently, the transmitted wave merges with the wave flowing around the sides of the posts and over the top of the barrier. This gives rise to the succeeding peaks.

It is noticed that the experimental recordings at gauges ps2 - ps4 (Figure 5-16b, c and d) are much more oscillatory than the ones at gauges ps1 (Figure 5-16a). It is most likely due to the complicated flow pattern of the shock waves passing through the barrier consisting of posts (Figure 5-19). As the shock wave impinges the posts, the shock wave is partly reflected towards the charge, partly flows around the sides of posts and over the top of the barrier and the

remaining part is transmitted directly through the openings between the posts. Behind the barrier, there are multiple diffracted waves around the sides of posts and multiple transmitted waves through the openings between posts, which interact with each other. It results in a rather complicated flow pattern behind the barrier.

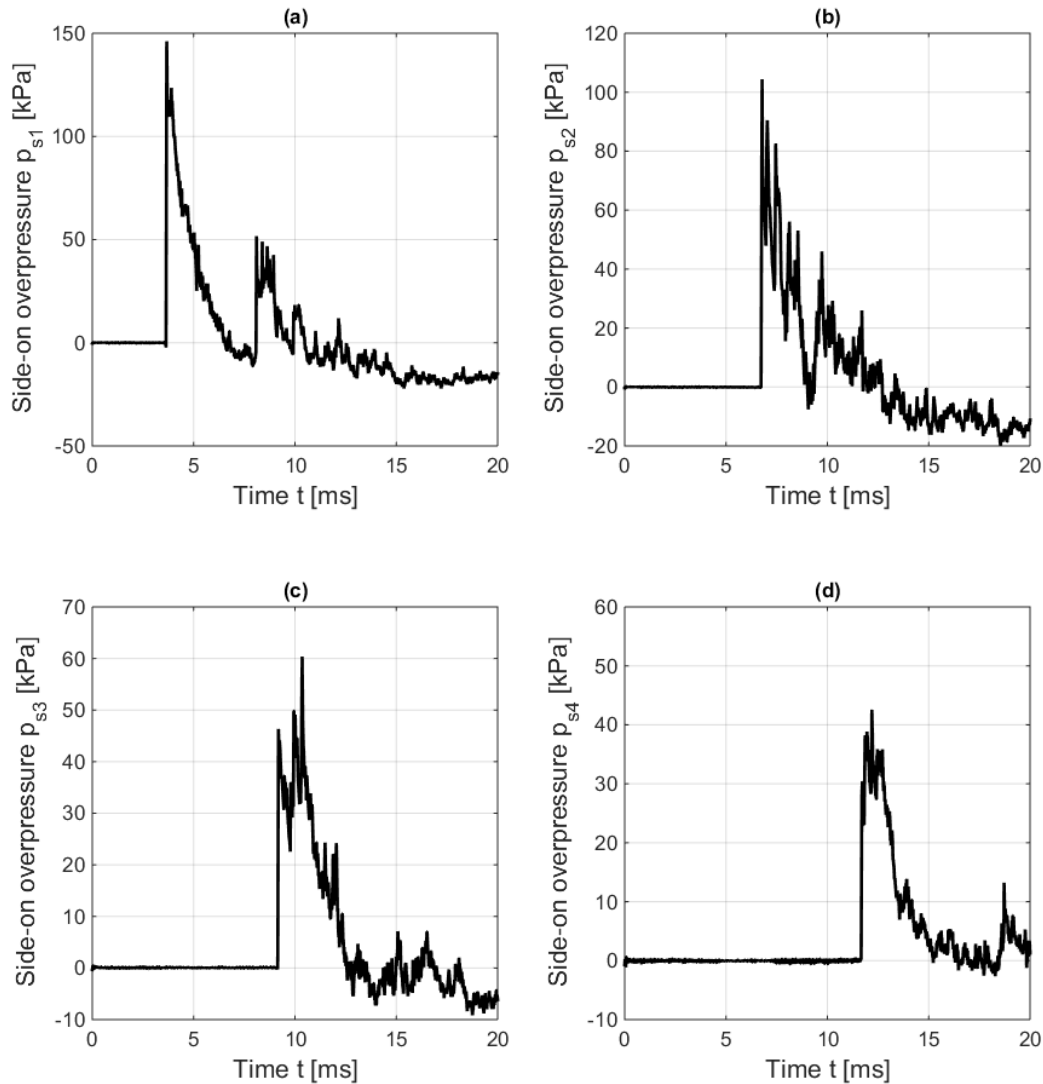


Figure 5-16: Side-on overpressure-time histories measured in experiment V3, configuration M1,  $n_{post} = 8$  (a) ps1; (b) ps2; (c) ps3; (d) ps4

In order to visualize the entire relevant reflected overpressure-time histories, the time axes in Figure 5-17 start at 15ms and extend to 30ms, which are different to the ones in Figure 5-16. As the shock wave impinges on the front face of the wooden plate to mount gauge pr1, the incident shock wave is partly reflected and partly diffracted around the free edges of the wooden plate. Due to the small distance (0.16m) between the wooden plates and the massive wall (Figure 5-4c), the diffracted wave is re-reflected from the massive wall and then impinges gauge pr1 once again. This phenomenon leads to the peak overpressures of about 20kPa between  $t = 19.9\text{ms}$  and  $t = 21.0\text{ms}$  in the experimental recordings (Figure 5-17a). The same phenomenon as occurred at gauge pr1 can also be observed at gauge pr2 by the peak overpressures between  $t = 20.0\text{ms}$  and  $t = 21.5\text{ms}$  (Figure 5-17b). Due to the low height of the

massive wall (2m, Figure 5-15b), the reflecting surface area behind the wooden plate to mount gauge pr2 is approximately 50% of that behind the wooden plate to mount gauge pr1. Therefore, the magnitude of the peak overpressures for gauge pr2 (due to the re-reflection from the massive wall) is somewhat less than that for gauge pr1. For gauges pr3 and pr4, the diffracted waves will not be re-reflected again, i.e. they will propagate undisturbed away from the rear face of the wooden plates. Hence, the aforementioned phenomenon does not occur at gauges pr3 and pr4.

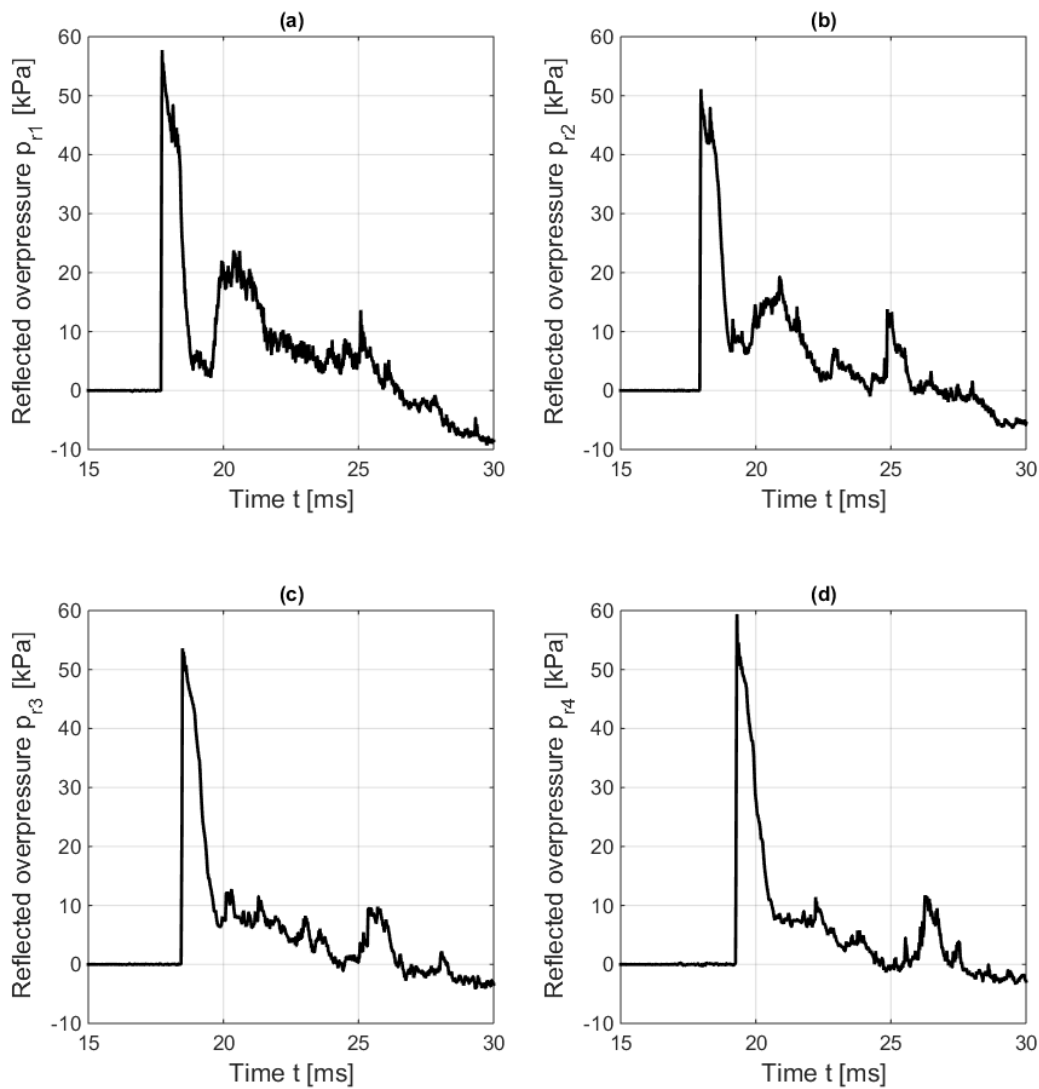


Figure 5-17: Reflected overpressure-time histories measured in experiment V3, configuration M1,  $n_{post} = 8$  (a) pr1; (b) pr2; (c) pr3; (d) pr4

#### 5.2.4.2 Data statistics at the gauges in front of the barrier

Since the pressure gauges ps1 are located 1m in front of the barriers, the overpressure-time history is not affected by the interaction with any obstacle until the shock wave strikes the barrier. Therefore, the first peak overpressures measured in all experiments with four different configurations of barriers (Mref, M1, M2 and M3), in total 12 values, can be considered together to calculate the mean value of the peak overpressures at gauge ps1 (Figure 5-18).

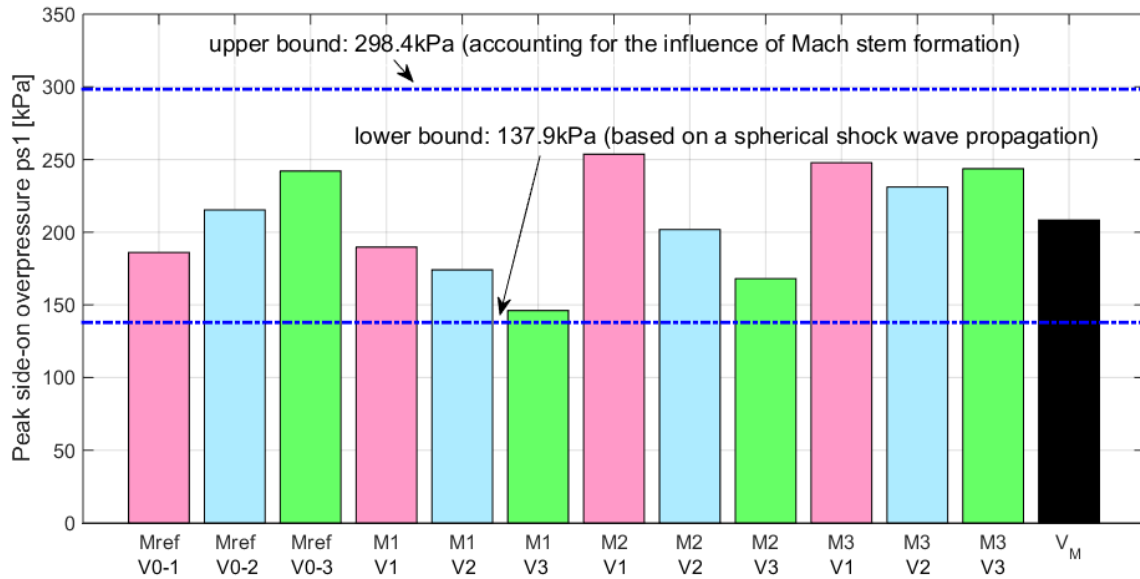


Figure 5-18: Peak side-on overpressures at gauges ps1 measured in the experiments

To assess the quality of the data recorded in the experiments (V0, V1, V2 and V3), a plausibility analysis was carried out, according to the method described by *Gebbeken 2017*, which has already been applied to verify the data at gauges ps1 in the experiments of blast walls with a canopy on top (Section 5.1.4.2). The lower bound (137.9kPa, Figure 5-18) is based on a spherical shock wave propagation, whilst the influence of the Mach stem formation is accounted for in the upper bound (298.4kPa, Figure 5-18). As outlined in Figure 5-18, all values measured at gauges ps1 in the experiments are within these limit bounds. Therefore, it is justified to use them to calculate the statistical quantities at gauges ps1, i.e. the mean value  $\mu$ , the standard deviation  $\sigma$  and the coefficient of variation  $\vartheta$  (Table 5-6).

Table 5-6: Statistics of experimental data at gauges ps1 ( $R = 4\text{m}$ ,  $h = 0.63\text{m}$ )

Type	Configuration	Experiment	$t_a$ [ms]	ps1 [kPa]	$\mu$ [kPa]	ps1 $\sigma$ [kPa]	$\vartheta$ [-]
side-on	M <sub>ref</sub>	V0-1	3.49	186.02	208.28	35.83	0.172
		V0-2	3.63	215.35			
		V0-3	3.71	242.06			
	M1	V1	3.40	189.75 <sup>a</sup>			
		V2	3.73	174.10 <sup>a</sup>			
		V3	3.67	146.11			
	M2	V1	3.56	253.65			
		V2	4.08	201.80			
		V3	3.53	168.00			
	M3	V1	3.60	247.78			
		V2	3.27	231.10			
		V3	3.68	243.67			

<sup>a</sup>Gauges were destroyed at  $t = 4.8\text{ms}$  (V1) and  $t = 9.0\text{ms}$  (V2) during the experiments.

It is observed that the values measured at gauges ps1, i.e. at a distance of 4m from the charge, vary widely. Its standard deviation  $\sigma = 35.83\text{kPa}$  and coefficient of variation  $\vartheta = 0.172$  (Table 5-6) indicate that the scattering at this gauge is considerably large. This is most likely attributed

to the so-called cauliflower effect, which arises from the incomplete burning process of detonation products. In addition, the charge shape was not exactly spherical (Figure 5-4d). The mean value of 208.28kPa is somewhat larger than the predicted value (198.10kPa) derived from the formulae of *Kingery and Bulmash 1984* if the charge is considered to be so close to the ground that a hemi-spherical shock wave propagation occurs.

5.2.4.3 Data statistics at the gauges behind the barrier

Similarly, the mean values  $\mu$ , the standard deviations  $\sigma$  and the coefficients of variation  $\vartheta$  of the results measured at other gauges are calculated and summarized in Table 5-7 - Table 5-10 for configurations Mref (no posts), M1 ( $n_{post} = 8$ ), M2 ( $n_{post} = 5$ ) and M3 ( $n_{post} = 6$ ). Some anomalies appeared in the pressure recordings (Table 5-6, Table 5-7 and Table 5-9). Signal noises were present in configuration M1 ( $n_{post} = 8$ ) at gauges ps1 from  $t = 4.8$ ms in experiment V1 and from  $t = 9.0$ ms in experiment V2 (Table 5-6). One gauge pr2-ref was destroyed during experiment V0-2 (Table 5-7). There was no valid data captured at gauges pr2-2 and pr3-2 for configuration M2 ( $n_{post} = 5$ ) during experiments V1 - V3 since these gauges were damaged by the blast in all three experiments (Table 5-9).

Table 5-7: Statistics of experimental data at gauges ps2 - ps4 and pr1 - pr4, Mref (no posts)

Gauges		V0-1		V0-2		V0-3		Statistics				
Type	Label	R [m]	h [m]	$t_a$ [ms]	p [kPa]	$t_a$ [ms]	p [kPa]	$t_a$ [ms]	p [kPa]	P		
										$\mu$ [kPa]	$\sigma$ [kPa]	$\vartheta$ [-]
side-on	ps2-ref	5.5	0.63	6.30	117.88	6.46	86.20	6.90	102.57	102.22	15.84	0.155
	ps3-ref	6.5	0.63	9.90	56.66	9.40	67.34	9.05	60.92	61.64	5.38	0.087
	ps4-ref	7.5	0.63	11.30	47.42	11.27	47.76	11.59	47.65	47.61	0.17	0.004
reflected	pr1-ref	9.84	1	17.08	63.86	17.39	63.51	17.73	60.58	62.65	1.80	0.029
	pr2-ref	9.84	2	17.61	59.01	-	- <sup>b</sup>	18.27	52.93	55.97	4.30	0.077
	pr3-ref	9.84	3	17.95	55.48	18.42	56.76	18.74	51.02	54.42	3.02	0.055
	pr4-ref	9.84	4	18.84	59.39	19.36	58.08	19.66	52.93	56.80	3.41	0.060

<sup>b</sup>Gauge pr2-ref was destroyed during the experiment.

Table 5-8: Statistics of experimental data at gauges ps2 - ps4 and pr1 - pr4, M1 ( $n_{post} = 8$ )

Gauges		V1		V2		V3		Statistics				
Type	Label	R [m]	h [m]	$t_a$ [ms]	p [kPa]	$t_a$ [ms]	p [kPa]	$t_a$ [ms]	p [kPa]	P		
										$\mu$ [kPa]	$\sigma$ [kPa]	$\vartheta$ [-]
side-on	ps2-1	5.5	0.63	6.38	90.66	6.84	132.71	6.78	104.42	109.26	21.44	0.196
	ps3-1	6.5	0.63	10.03	57.28	9.10	54.56	10.36	60.37	57.40	2.91	0.051
	ps4-1	7.5	0.63	11.88	42.37	11.73	46.16	12.20	42.57	43.70	2.13	0.049
reflected	pr1-1	9.84	1	17.41	57.61	17.61	62.00	17.73	57.75	59.12	2.49	0.042
	pr2-1	9.84	2	17.64	50.19	17.81	52.45	17.97	51.11	51.25	1.14	0.022
	pr3-1	9.84	3	18.21	50.28	18.32	54.88	18.49	53.59	52.91	2.37	0.045
	pr4-1	9.84	4	19.03	55.11	19.15	58.35	19.31	59.41	57.62	2.24	0.039

Table 5-9: Statistics of experimental data at gauges ps2 - ps4 and pr1 - pr4, M2 ( $n_{post} = 5$ )

Gauges		V1		V2		V3		Statistics				
Type	Label	R [m]	h [m]	$t_a$ [ms]	p [kPa]	$t_a$ [ms]	p [kPa]	$t_a$ [ms]	p [kPa]	p		
										$\mu$ [kPa]	$\sigma$ [kPa]	$\vartheta$ [-]
side-on	ps2-2	5.5	0.63	7.01	99.26	7.12	93.33	6.66	90.53	94.37	4.46	0.047
	ps3-2	6.5	0.63	8.78	63.43	9.21	58.06	8.76	58.49	59.99	2.99	0.050
	ps4-2	7.5	0.63	12.08	48.16	12.64	41.93	11.75	44.52	44.87	3.13	0.070
reflected	pr1-2	9.84	1	17.48	63.31	18.15	61.03	17.69	61.93	62.09	1.15	0.018
	pr2-2 <sup>c</sup>	9.84	2	-	-	-	-	-	-	-	-	-
	pr3-2 <sup>c</sup>	9.84	3	-	-	-	-	-	-	-	-	-
	pr4-2	9.84	4	19.42	56.51	20.09	55.42	19.66	57.12	56.35	0.86	0.015

<sup>c</sup>Gauges pr2-2 and pr3-2 were destroyed during the experiments.

Table 5-10: Statistics of experimental data at gauges ps2 - ps4 and pr1 - pr4, M3 ( $n_{post} = 6$ )

Gauges		V1		V2		V3		Statistics				
Type	Label	R [m]	h [m]	$t_a$ [ms]	p [kPa]	$t_a$ [ms]	p [kPa]	$t_a$ [ms]	p [kPa]	p		
										$\mu$ [kPa]	$\sigma$ [kPa]	$\vartheta$ [-]
side-on	ps2-3	5.5	0.63	6.77	102.70	6.59	118.12	6.85	126.81	115.88	12.21	0.105
	ps3-3	6.5	0.63	8.92	60.62	8.69	61.66	8.93	61.38	61.22	0.54	0.009
	ps4-3	7.5	0.63	11.50	45.93	11.27	45.73	11.51	45.98	45.88	0.13	0.003
reflected	pr1-3	9.84	1	17.60	65.25	17.34	66.08	17.57	65.49	65.61	0.43	0.007
	pr2-3	9.84	2	18.19	53.05	17.68	52.90	17.88	52.27	52.74	0.42	0.008
	pr3-3	9.84	3	18.51	52.36	18.26	53.71	18.45	52.73	52.93	0.70	0.013
	pr4-3	9.84	4	19.41	52.31	19.15	54.17	19.35	52.77	53.08	0.97	0.018

It is noticeable in Table 5-7, Table 5-8 and Table 5-10 that the coefficients of variation  $\vartheta$  at gauges ps2 (5.5m from the charge) are also rather large, i.e. 0.155, 0.196 and 0.105 for configurations Mref (no posts), M1 ( $n_{post} = 8$ ) and M3 ( $n_{post} = 6$ ). It is most likely related to the complex flow pattern behind the barriers. Figure 5-19 shows the shock wave propagation in the region of the barrier and the gabion walls, i.e. from 0.3m in front of the gabion walls to 0.1m behind gauge ps2. The shock wave propagation in this region is highlighted by means of iso-pressure line plots. These iso-pressure plots are extracted from a simplified numerical analysis, in which the posts and the frame are not explicitly modelled. They are considered by applying appropriate boundary conditions to their exterior surfaces, i.e. the motion in the normal direction is constrained. Furthermore, only the front part of the steel frame is taken into account in this analysis. Due to the sudden contraction and diffusion of the flow, vortices are generated at the corners of the posts (Figure 5-19a and b). At a later time, e.g. at  $t = 6.4$ ms (Figure 5-19c), the diffracted and transmitted waves interact with each other, which renders a rather complicated flow pattern behind the barrier. Finally, at  $t = 7.0$ ms (Figure 5-19d), the shock wave arrives at gauge ps2. Due to the complicated flow pattern behind the barrier, the recordings measured at gauges ps2 are much more oscillatory than the ones measured at gauges ps1 (Figure 6-31a and b). This indicates that the experimental results at gauges ps2 are susceptible even to a very small change in the experimental set-up, e.g. gauge position and arrangement of steel posts.

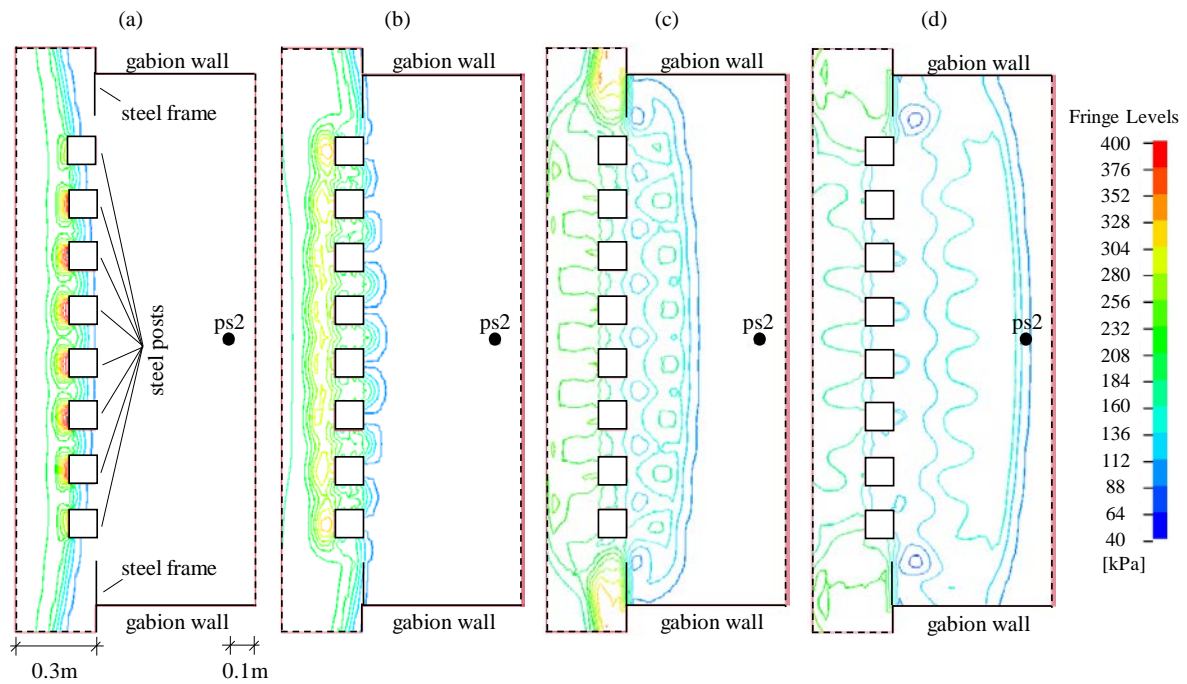


Figure 5-19: Iso-pressure line plots of a plane at an elevation of 0.63m above the ground, configuration M1,  $n_{post} = 8$  (a)  $t = 5.8\text{ms}$ ; (b)  $t = 6.0\text{ms}$ ; (c)  $t = 6.4\text{ms}$ ; (d)  $t = 7.0\text{ms}$

In addition, gauge ps2 is located within the space between the gabion walls at the sides of the barriers (Figure 5-15a). During the diffraction process around the gabion walls, the shock wave is disturbed to a certain extent. Furthermore, as observed in Figure 5-14, there are no posts present in the line of sight between the charge and that gauge for configurations Mref (no posts), M1 ( $n_{post} = 8$ ) and M3 ( $n_{post} = 6$ ). For configuration M2 ( $n_{post} = 5$ ), a coefficient of variation  $\vartheta = 0.047$  (Table 5-9) indicates that no appreciable scattering is observed at gauges ps2. It is due to the shielding effect provided by the steel post in the middle (Figure 5-14), which is located in the line of sight between the charge and that gauge.

The relatively small standard deviations and coefficients of variation at other gauges indicate that the data is reproducible. It is important to mention that three or less than three data points only provide a tendency for the actual mean value of the results. Hence, the mean values obtained from the experiments only give an approximation, and further experiments are necessary for a statistically reliable statement, especially for gauges ps1 and ps2. Therefore, it is recommended to conduct at least four experiments for each configuration.

#### 5.2.4.4 Evaluation of overpressure and impulse reduction

To evaluate the effectiveness of barriers, the mean values of the peak overpressures and the maximum impulses recorded at the gauges behind the barriers are shown in Figure 5-20 (mean values of ps2 - ps4 in Figure 5-20a and c, mean values of pr1 - pr4 in Figure 5-20b and d). The associated impulses are derived by the numerical integration of the overpressure-time histories. Configuration Mref (no posts) is used as the reference configuration for comparison, due to the fact that no data was measured for the free field scenario at the test site.

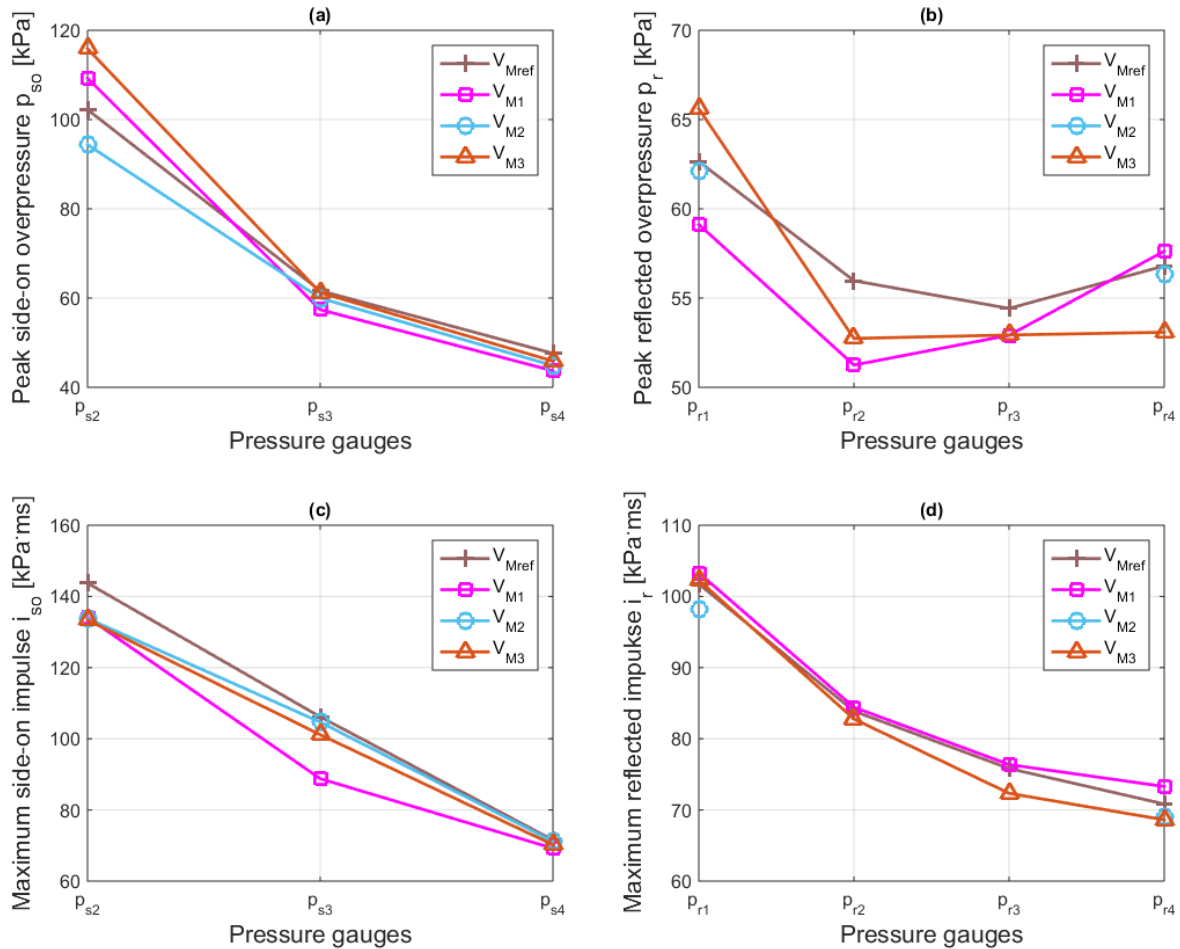


Figure 5-20: Experimental results (a) peak side-on overpressures; (b) peak reflected overpressures; (c) maximum side-on impulses; (d) maximum reflected impulses

Comparing the peak side-on overpressures in configurations M1 ( $n_{post} = 8$ ), M2 ( $n_{post} = 5$ ) and M3 ( $n_{post} = 6$ ) to the ones obtained in configuration Mref (no posts), slight reductions can be observed except at gauge  $p_{s2}$  (Figure 5-20a). At gauge  $p_{s2}$ , an overpressure reduction is only found in configuration M2 ( $n_{post} = 5$ ), whilst an increase in overpressure is observed in configurations M1 ( $n_{post} = 8$ ) and M3 ( $n_{post} = 6$ ), i.e. by 6.9% and 13.4%, respectively. This discrepancy of the results at gauge  $p_{s2}$  is attributed to the contribution of the steel post placed in the line of sight between the charge and that gauge in configuration M2 ( $n_{post} = 5$ , Figure 5-14). This is not the case in configurations M1 ( $n_{post} = 8$ ) and M3 ( $n_{post} = 6$ ). In general, two different effects influence the overpressures behind the barriers. Firstly, the arrangement of the steel posts in front of the steel frame results in a rather complicated flow pattern behind the barriers. The wave behind the barriers cannot be viewed as a single wave but rather as a superposition of multiple waves, i.e. the waves transmitted through openings between the posts and the waves flowing around the sides of the posts. This superposition effect gives rise to an overpressure increase behind the barriers. Secondly, the steel posts provide a shielding effect which causes an overpressure reduction behind the barriers. At gauges  $p_{s2}$ , the superposition effect is dominant in configurations M1 ( $n_{post} = 8$ ) and M3 ( $n_{post} = 6$ ), which causes an overpressure increase. The overpressure reduction achieved in configuration M2 ( $n_{post} = 5$ ) is

related to the shielding effect provided by the steel post placed in the line of sight between the charge and gauge ps2. As the distance between the gauge and the barrier increases, the influence of the superposition effect diminishes, whilst the influence of the shielding effect becomes dominant. This leads to an overpressure reduction at gauges ps3 and ps4 for all configurations. Configuration M1 ( $n_{post} = 8$ ) achieves the largest overpressure reduction at gauges ps3 and ps4, i.e. 6.9% and 8.2%, since it has the largest number of posts among the experimental configurations.

As observed in Figure 5-20c, similar values of the maximum side-on impulses at gauge ps2 are measured in configurations M1 ( $n_{post} = 8$ ), M2 ( $n_{post} = 5$ ) and M3 ( $n_{post} = 6$ ). The maximum side-on impulses are reduced by approximately 7% compared to the results in configuration Mref (no posts). At gauges ps3 and ps4, the maximum impulses are reduced by 0.6% to 16.4% in configurations M1 ( $n_{post} = 8$ ), M2 ( $n_{post} = 5$ ) and M3 ( $n_{post} = 6$ ). This indicates that the influence of the shielding effect provided by the steel posts on the impulse at gauges ps2 - ps4 is more pronounced than the superposition effect. Furthermore, as expected, the impulse reduction increases with an increase in the number of posts. This means that configuration M1 ( $n_{post} = 8$ ) achieves the largest impulse reduction at gauges ps3 and ps4, i.e. 16.4% and 3.3%.

As observed in Figure 5-20b, the peak reflected overpressures are slightly reduced except for gauge pr1 in configuration M3 ( $n_{post} = 6$ ) and for gauge pr4 in configuration M1 ( $n_{post} = 8$ ). No statements on these exceptions can be made, since the scatter in the experimental data of the reflected overpressures within each configuration (e.g. the coefficients of variation vary from 2.9% to 7.7%, Table 5-7) has the same order of magnitude as the calculated overpressure reduction or increase at these gauges. In addition, no valid data was measured at gauges pr2 and pr3 in configuration M2 ( $n_{post} = 5$ ), due to the fact that the gauges were destroyed by the blast during the experiments. Configuration M1 ( $n_{post} = 8$ ) achieves the largest overpressure reduction at gauges pr1, pr2 and pr3 (5.6%, 8.4% and 2.8%). Actually, only very slight impulse reduction can be observed at gauges pr1 - pr4. In configuration M1 ( $n_{post} = 8$ ), even a slight increase in the maximum impulse occurs. Due to the aforementioned reasons, no further valid statement can be made based on the experiments.

### 5.2.5 Conclusion: protective barriers made of steel posts

In summary, the more posts the better shielding. Due to the gabion walls placed adjacent to the barrier (steel posts and frame), there is no direct air flow around the sides of the barrier of interest. Roughly speaking, configuration M1 ( $n_{post} = 8$ ) shows the best performance in overpressure reduction (except at gauges ps2 and pr4) among the configurations tested in the experiments. In addition, it achieves largest impulse reduction at gauges ps2 - ps4. Due to the fact that the scatter in the experimental data at gauges pr1-pr4 has the same order of magnitude as the impulse reduction or increase, no further valid statement can be made at those gauges based on the experiments.

## 6 Numerical investigations on the effectiveness of protective barriers

This chapter describes the numerical investigations on the effectiveness of protective barriers in terms of overpressure and impulse reduction. Firstly, the influence of ambient conditions, e.g. altitude or atmospheric temperature, on the blast loads is investigated in Section 6.1. Secondly, the influence of the charge height on the blast loads is explored in Section 6.2. Thirdly, numerical simulations of blast walls with a canopy on top and protective barriers made of steel posts are presented in Sections 6.3 and 6.4, respectively. On the one hand, these numerical simulations provide a tool to evaluate the effectiveness of protective barriers, which were tested in the experiments (Chapter 5). The validation of numerical models is achieved by comparing the numerical results to the experimental ones, which have been presented in the previous chapter. On the other hand, after validation of numerical models against the experiments, the validated numerical models can be employed to carry out parametric studies, in which several key properties of the barriers (e.g. angle of inclination of a canopy, number of steel posts, arrangement of steel posts etc.) are studied in detail. These parametric studies are crucial for the analyses of blast-resistant protective barriers. Lastly, a comparison is made between these two types of protective barriers involved in this Dissertation.

### 6.1 Influence of ambient conditions on the blast loads

All blast parameters calculated by the formulae of *Kingery and Bulmash 1984* were scaled to standard atmospheric conditions at mean sea level and at the standard temperature (15°C). To account for the effects of changes in ambient conditions, e.g. altitude or atmospheric temperature, on shock waves, Sachs scaling law (Section 3.3.2) must be applied with appropriate scaling factors ( $S_p$ ,  $S_d$  and  $S_t$ ; Eq. (3-26), Eq. (3-27) and Eq. (3-28)) to multiply the blast parameters using the formulae of *Kingery and Bulmash 1984*. However, if the altitude considered is below about 1524m (5000ft), the scaling factors  $S_p$ ,  $S_d$  and  $S_t$  do not differ greatly from unity (Figure 6-1,  $S_p = 0.832$ ,  $S_d = 1.063$  and  $S_t = 1.082$ ). Thus, the approximation of a homogenous atmosphere at mean sea level is not greatly in error (*Glasstone 1980*).

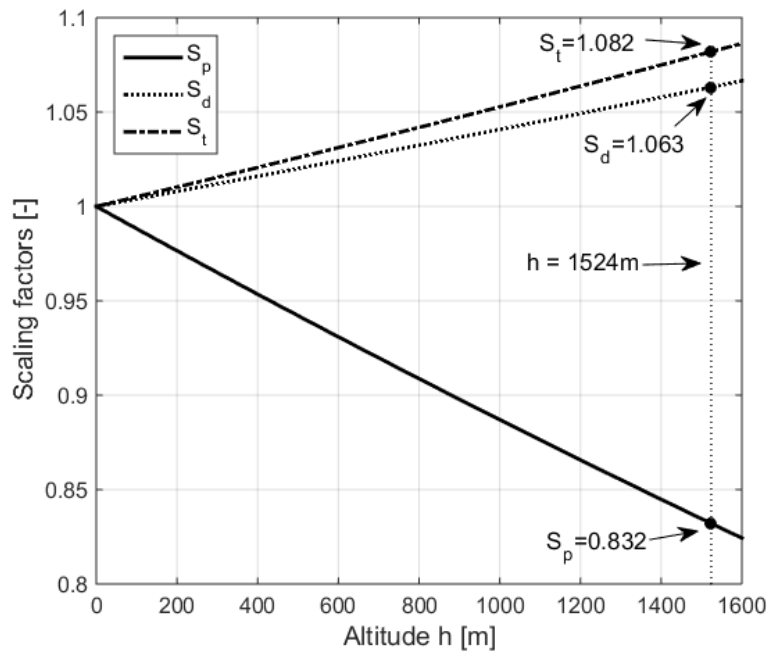


Figure 6-1: Scaling factors for pressure  $S_p$ , distance  $S_d$  and time  $S_t$  at different altitudes

Both pressure and density of ambient air decrease with an increase in altitude. According to the *U.S. Standard Atmosphere 1976*, the atmospheric pressure  $p_a$  at altitude  $h$  (in meters) above mean sea level is given by

$$p_a = p_0 \left( 1 - \frac{0.0065h}{288.15} \right)^{5.255}, \quad (6-1)$$

where  $p_0 = 101.325\text{kPa}$ . This equation assumes that the temperature at altitude  $h$  above mean sea level decreases linearly with altitude, which means that as the altitude is increased by 100m, the temperature will decrease by  $0.65^\circ\text{C}$ .

The ambient air density  $\rho_a$  can be calculated using the ideal gas law, which is expressed as a function of atmospheric pressure  $p_a$  and temperature  $T_a$  (*U.S. Standard Atmosphere 1976*):

$$\rho_a = \frac{p_a}{R_s T_a}, \quad (6-2)$$

where  $R_s = 287.058\text{J}/(\text{kg}\cdot\text{K})$  is the specific gas constant for air.

The experiments of blast walls with a canopy on top (Section 5.1) and protective barriers made of steel posts (Section 5.2) were conducted on 17<sup>th</sup> and 11<sup>th</sup> August 2016 at the test site of the Bundeswehr Technical Center for Protective and Special Technologies (WTD52) in Germany, which is located at an altitude of 1585m above mean sea level. The highest and lowest temperature on 17<sup>th</sup> August 2016 were  $23^\circ\text{C}$  and  $15^\circ\text{C}$  (day and night time, *Time and Date AS 2018a*). The average temperature on 17<sup>th</sup> August 2016 between 9 and 15 o'clock was  $20.2^\circ\text{C}$ . The highest and lowest temperature on 11<sup>th</sup> August 2016 were  $16^\circ\text{C}$  and  $10^\circ\text{C}$  (day and night

time, *Time and Date AS 2018b*). The average temperature on 17<sup>th</sup> August 2016 between 9 and 15 o'clock was 12.1°C. Using Eq. (6-1), an atmospheric pressure of 83.68kPa is calculated at the test site. Using Eq. (6-2), an ambient air density of 0.994kg/m<sup>3</sup> and 1.022 kg/m<sup>3</sup> are calculated for numerical models of the blast walls with a canopy on top and for numerical models of protective barriers made of steel posts, respectively. They represent the ambient conditions at the test site on 17<sup>th</sup> and 11<sup>th</sup> August 2016, respectively.

In order to investigate the effect of the changes in the ambient conditions, e.g. altitude and atmospheric temperature, on the shock wave propagation, two parametric studies based on a free field scenario are made using the two-dimensional purely ALE formulation with a multi-material option (*LSTC 2017*). These studies are based on the set-up of blast wall experiments (Section 5.1). Figure 6-2 shows the two-dimensional axisymmetric numerical model. Both the explosive charge and air are separately modelled. The air is modelled via \*MAT\_NULL (*LSTC 2017*) and regarded as an ideal gas with a linear polynomial EoS (Section 4.1.1.1). The explosive charge (5kg TNT equivalent) is modelled via \*MAT\_HIGH\_EXPLOSIVE\_BURN (*LSTC 2017*) with the Jones-Wilkins-Lee (JWL) EoS (Section 4.1.1.2). The left bound of the air domain represents the symmetry axis. The lower and right bounds of the air domain are used to represent the ground and the building envelope, respectively. Their nodes are constrained in the normal direction. Non-reflecting boundary conditions are applied to the upper bound of the air domain. Gauges ps1 - ps4 and pr1 - pr4 in the blast wall experiments (Section 5.1) are employed here to capture the overpressure-time histories. Moreover, an additional gauge ps0 is placed 3m away from the charge in order to justify the K&B-blast loads used in the numerical models described in Sections 6.3 and 6.4. This distance (3m) coincides with the distance of the ambient layer of ALE air elements from the charge (Figure 6-9). The elevation is the same as gauges ps1 - ps4, namely 1m above the ground.

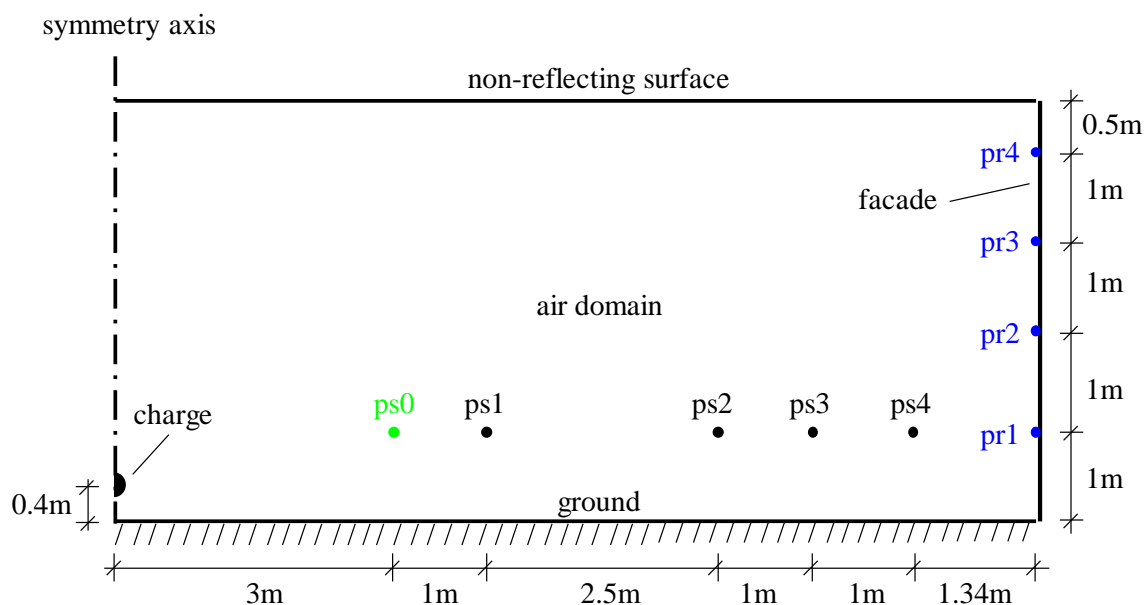


Figure 6-2: Sketch of the two-dimensional axisymmetric numerical model

For the parametric study on altitude, the same temperature as the average temperature (20.2°C) on the experimental date (17<sup>th</sup> August 2016) is used and the altitude ranges from 0m to 1600m

(Subsection 6.1.1) with an interval of 200m. For the parametric study on atmospheric temperature, the altitude at the test site (1585m) is used and the atmospheric temperature varies from 0°C to 24°C (Subsection 6.1.2) with an interval of 2°C. Using Eq. (6-1) and Eq. (6-2), the atmospheric pressure and the ambient air density are calculated according to the respective altitude  $h$  and atmospheric temperature  $T_a$  combinations. These values are further employed for the numerical simulations.

### 6.1.1 Altitude

Figure 6-3 demonstrates the effect of the variation in altitude  $h$  on the peak overpressures  $p_h$  at the respective gauges, which are scaled with the peak overpressures  $p_{h=0}$  at mean sea level. As indicated by the Sachs scaling law, the peak overpressures decrease with increasing altitude. At an altitude of 1600m, the peak overpressures are reduced by 7.1% - 8.5% for gauges ps2 - ps4 and pr1 - pr4. It is noticeable to recognize that the peak overpressures at gauges ps0 and ps1 are only slightly reduced by 1.7% and 2.1%, respectively, which are somewhat less than the ones for gauges ps2 - ps4 and pr1 - pr4. This difference in the peak overpressure reduction at the gauges is most likely attributed to the homogenous atmosphere assumption. Regarding a homogenous atmosphere, the decrease in atmospheric pressure seems to affect the overpressures in a more or less similar manner, which is observed at gauges ps2 - ps4 and pr1 - pr4. They are located considerably distant from the charge such that the atmosphere is considered to be homogenous. In contrast to gauges ps2 - ps4 and pr1 - pr4, gauges ps0 and ps1 are still relatively near to the charge. The detonation products have not been completely burnt out. Under such circumstances, the atmosphere is a compound of the detonation products and the air. Therefore, the homogenous atmosphere assumption is not valid.

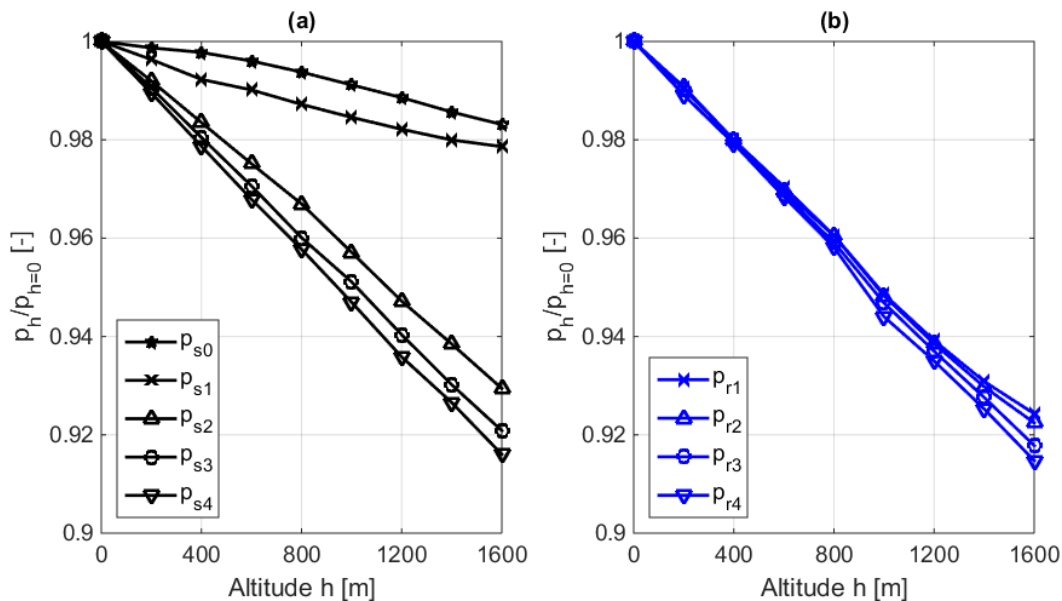


Figure 6-3: Influence of the altitude on the peak overpressures at gauges (a) ps0 - ps4; (b) pr1 - pr4

In fact, there are two opposite effects to influence the arrival of the shock wave at the gauges. The first effect is that the air density decreases with increasing altitude. From a conservation of momentum viewpoint, lower density air moves faster than higher density air if an identical

momentum is regarded. It results in an early arrival of the shock wave at the gauges. In the second effect, as observed in Figure 6-3, the overpressure decreases with increasing altitude. It is well-known that the shock velocity decreases if the associated overpressure decreases (Eq. (3-5)). This implies a late arrival of the shock wave at the gauges. Figure 6-4 compares the arrival time  $t_{a,h}$  of the shock wave at altitude  $h$  and  $t_{a,h=0}$  at mean sea level.

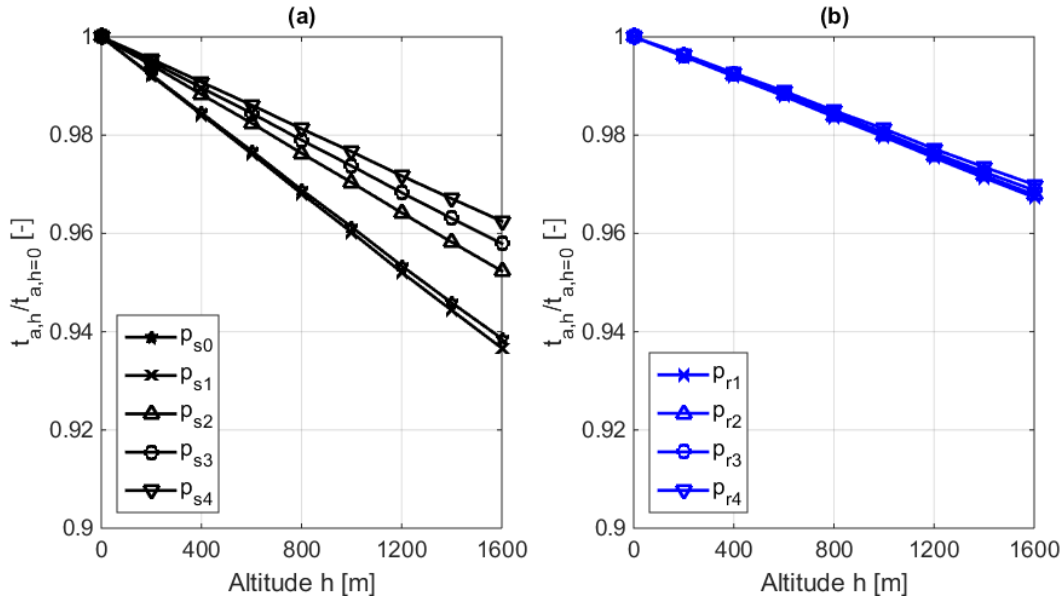


Figure 6-4: Influence of the altitude on the arrival time of the shock wave at gauges  
(a) ps0 - ps4; (b) pr1 - pr4

It is found that the arrival time of the shock wave at the gauges decreases linearly with an increase in altitude. The decrease in the arrival time is most significant at gauges ps0 and ps1 (-6.1% and -6.3%), which are near to the charge. As the distance from the gauge to the charge increases, the decrease becomes smaller, e.g. -3.0% at gauge pr4. It reveals that the aforementioned first effect prevails, which causes an early arrival of the shock wave at all gauges.

### 6.1.2 Atmospheric temperature

The influence of atmospheric temperature on the peak overpressures at respective gauges is shown in Figure 6-5. For comparison, the peak overpressures  $p_T$  at an atmospheric temperature  $T$  is scaled with the values  $p_{T=15^\circ C}$  at the standard temperature of  $15^\circ C$ . Generally speaking, the trend is that the peak overpressures slightly increase with increasing temperature, although the values fluctuate to a certain extent. Comparing the results of the temperature range from  $0^\circ C$  to  $24^\circ C$  to those of standard temperature ( $15^\circ C$ ), the differences are within  $\pm 0.5\%$  except at gauge ps1. Nevertheless, the maximum difference (-1.5%) is still considerably small.

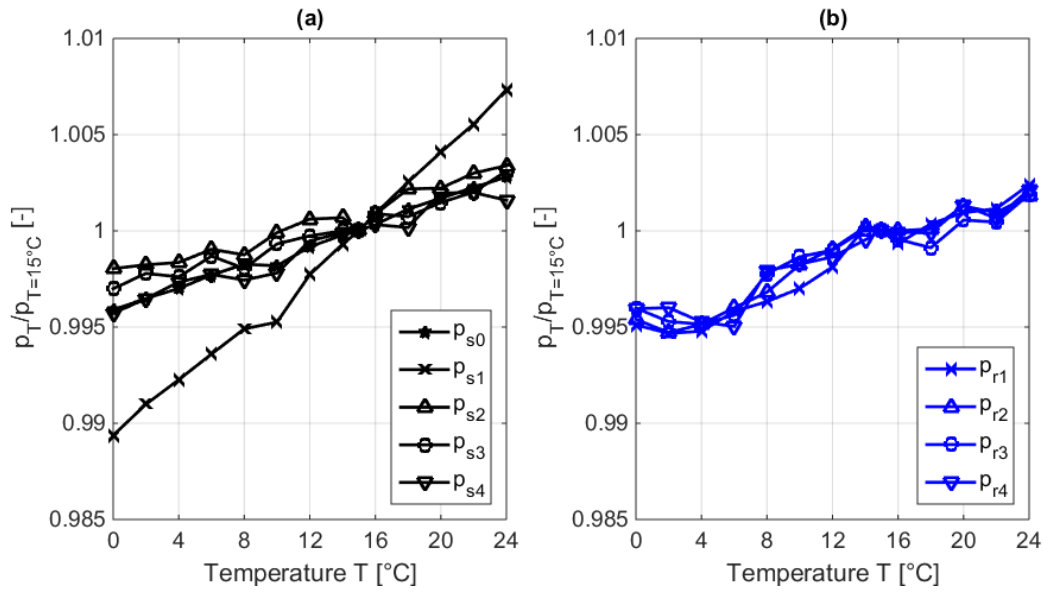


Figure 6-5: Influence of the atmospheric temperature on the peak overpressures at gauges (a) ps0 - ps4; (b) pr1 - pr4

Figure 6-6 shows the influence of atmospheric temperature  $T$  on the arrival time of the shock wave  $t_{a,T}$ , which is scaled with the arrival time  $t_{a,T=15^\circ\text{C}}$  at the standard temperature of  $15^\circ\text{C}$ . The arrival time of the shock wave at the gauges decreases as the temperature increases. This phenomenon is attributed to two effects. On the one hand, as indicated by Eq. (6-2), the air density decreases with an increasing temperature. Due to the fact that lower density air moves faster than higher density air if an identical momentum is regarded, this leads to an early arrival of the shock wave at the gauges. On the other hand, as observed in Figure 6-5, the overpressure increases with increasing temperature. This gives rise to a slightly larger shock velocity (up to 1%) and hence an early arrival of the shock wave at the gauges. For the temperature range considered in this study, the difference in the arrival time of the shock wave varies from -1.6% to +2.8%, compared to the values at the standard temperature ( $15^\circ\text{C}$ ).

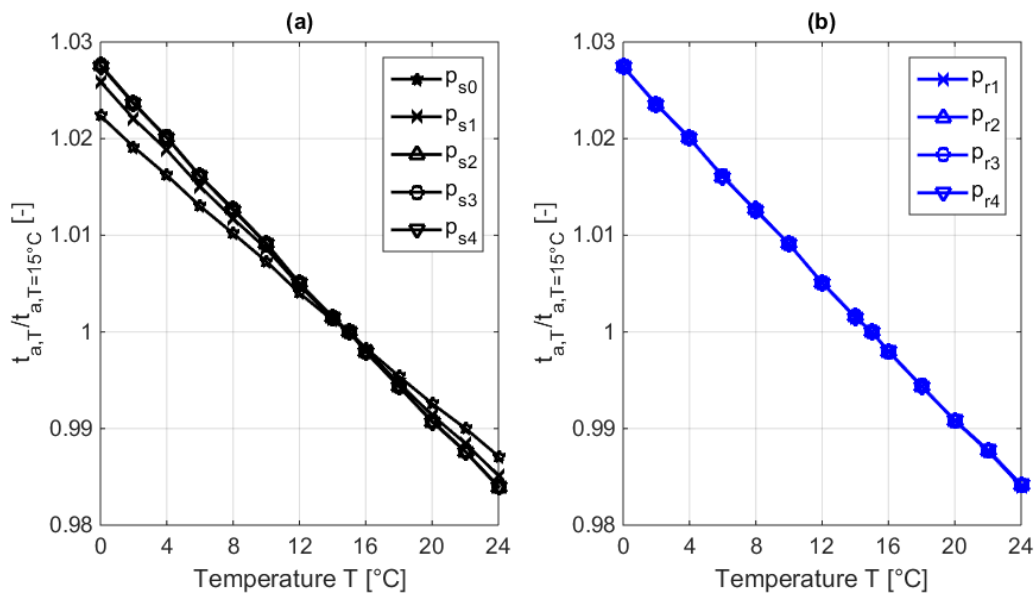


Figure 6-6: Influence of the atmospheric temperature on the arrival time of the shock wave at gauges (a) ps0 - ps4; (b) pr1 - pr4

It should be pointed out that the atmospheric pressure and ambient air density can also be affected by the air humidity to a certain degree, which is not taken into consideration in this Dissertation.

### 6.1.3 Conclusions: influence of ambient conditions on the blast loads

In summary, atmospheric temperature has only a minor effect on the blast loads behind the barriers. In contrast to temperature, altitude has a more significant influence on the blast loads. Regarding the peak overpressures at the gauges employed in the blast wall experiments, the values at an altitude of 1600m are about 2.1% - 8.5% smaller than the ones at mean sea level. Due to the change in altitude, the reduction in peak side-on overpressure at gauge ps0 is negligibly small (1.7%, Figure 6-3a). Therefore, the application of the K&B-blast loads to the ambient layer of ALE air elements is considered to be justified (Figure 6-9). These investigations confirm the statement made by *Glasstone 1980* that, at altitudes below about 1524m (5000ft), the pressure and air density in the atmosphere do not differ significantly from the values at mean sea level. Consequently, it is a reasonably good approximation to treat the atmosphere as homogenous with its properties at mean sea level.

It is worth mentioning that there are two differences in the gauge locations and elevations between the experiments of protective barriers made of steel posts and the experiments of blast walls with a canopy on top (Section 5.2.3). Firstly, gauge ps2, ps3 and ps4 were located at a horizontal distance of 5.5m, 6.5m and 7.5m from the charge, respectively (Figure 5-12b). Secondly, gauges ps1 - ps4 and pr1 were located at an elevation of 0.63m above the ground (Figure 5-12b). Conducting the same parametric studies as done in Sections 6.1.1 and 6.1.2, the same conclusion as above-mentioned can also be drawn (*Xiao et al. 2018b*).

In this Dissertation, the changes in altitude and atmospheric temperature are taken into account. The air domain involved in the numerical models described in Sections 6.3.4 and 6.4.4 is specified to the ambient conditions at the test site, which leads to:

- an atmospheric pressure of 83.68kPa and an ambient air density of 0.994 kg/m<sup>3</sup> (altitude  $h = 1585\text{m}$ , atmospheric temperature  $T = 20.2^\circ\text{C}$ ) for blast walls with a canopy on top (Section 6.3.4);
- an atmospheric pressure of 83.68kPa and an ambient air density of 1.022kg/m<sup>3</sup> (altitude  $h = 1585\text{m}$ , atmospheric temperature  $T = 12.1^\circ\text{C}$ ) for protective barriers made of steel posts (Section 6.4.4).

## 6.2 Influence of the charge height on the blast loads

If the charge is detonated on or very near to the ground surface, it is referred to as a surface burst (Section 3.8.2), in which the emerging shock wave propagates hemi-spherically. In the experiments, however, the charge was detonated at a height of 0.4m above the ground. As already explained in Section 3.8.3, a Mach stem is formed at certain ranges from the charge. To explore the influence of the Mach stem formation on the blast loads in a free field (i.e. no walls or barriers are present), the height-of-burst scenario employed in the experiments is adopted, i.e. charge mass  $W = 5\text{kg}$  TNT equivalent, charge height  $H_c = 0.4\text{m}$  (Figure 6-2). The surface

burst scenario is modelled as a hemi-spherical charge with the same charge mass (5kg TNT equivalent) on the ground. It is used here as the reference scenario for comparison. The atmospheric pressure and ambient air density derived in Section 6.1.3 are employed for the numerical simulations in this section.

Compared to the surface burst (SF) scenario, the height-of-burst (HOB) scenario has somewhat larger peak overpressures at gauges employed in the experiments of blast walls with a canopy on top (Figure 6-7) and protective barriers made of steel posts (Figure 6-8).

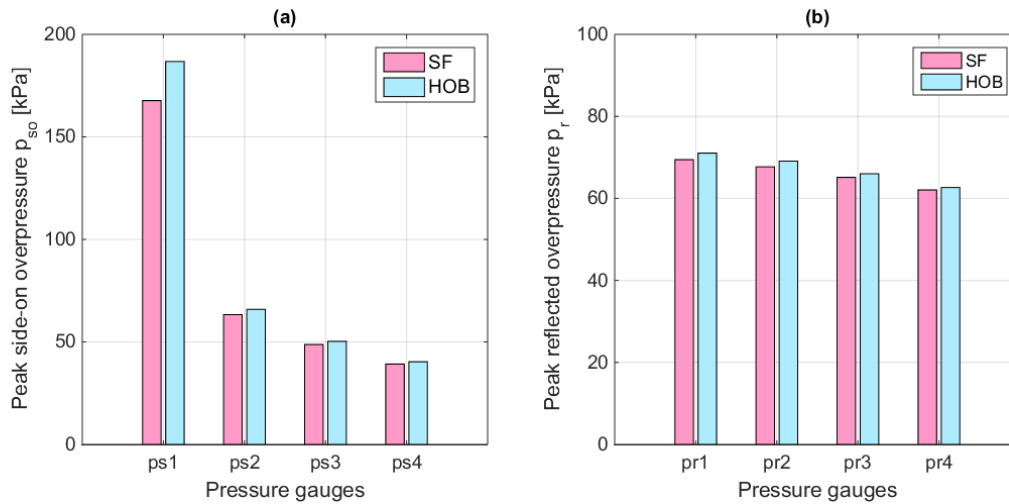


Figure 6-7: Comparison of the peak overpressures at the gauges in the experiments of blast walls with a canopy on top in case of surface burst (SF) and height-of-burst (HOB) detonations (a) gauges ps1 - ps4; (b) gauges pr1 - pr4

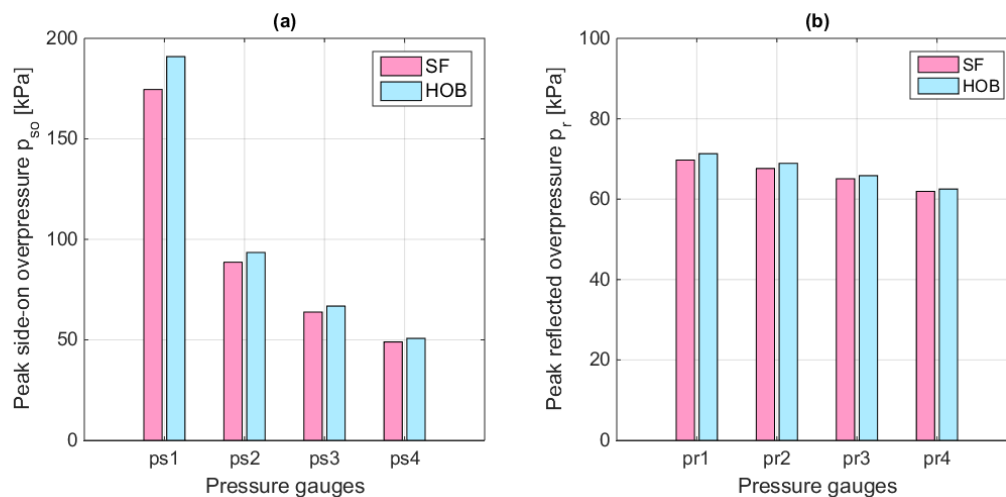


Figure 6-8: Comparison of the peak overpressures at the gauges in the experiments of protective barriers made of steel posts in case of surface burst (SF) and height-of-burst (HOB) detonations (a) gauges ps1 - ps4; (b) gauges pr1 - pr4

The Mach stem formation has a more pronounced influence at gauges ps1, i.e. 11.4% in Figure 6-7a and 9.4% in Figure 6-8a. At other gauges, i.e. ps2 - ps4 and pr1 - pr4, the peak overpressures are only slightly increased by the Mach stem formation by up to 4.1% (Figure

6-7) and 5.4% (Figure 6-8). In addition, as the distance from the charge to the observed gauge increases, the influence of the Mach stem formation on the peak overpressures diminishes.

In summary, the charge height employed in the experiments (0.4m above the ground) causes an increase of up to 11.4% in the peak side-on overpressures at gauges ps1, which are located in front of barriers. Considering the gauges employed in the experiments to evaluate the protective barrier effectiveness, i.e. ps2 - ps4 and pr1 - pr4, the influence of the charge height on the peak overpressures at these gauges can be considered as negligible since the increase in peak overpressure is only up to 5.4%. Therefore, the results derived from the numerical models in Sections 6.3.4 and 6.4.4, which neglect the Mach stem effect, can be used to compare to the experimental ones shown in Sections 5.1.4 and 5.2.4.

### 6.3 Blast walls with a canopy on top

This section presents numerical investigations of the effectiveness of various blast wall configurations providing protection against air blast. The blast walls are composed of a gabion wall with or without a canopy made of metal sheets (canopy), having different angles of inclination and mounted at the top of the wall. The influence of the flexibility of the canopy on the blast wall effectiveness is examined. The shock wave propagation and its interaction with the blast wall are performed applying the software LS-DYNA in order to calculate the blast load distribution. The peak overpressures and maximum impulses are determined by analysing the overpressure-time histories. Three experiments were conducted for each configuration (Section 5.1). Prior to the experiments, numerical models were developed in order to predict the main blast and response parameters in advance. Moreover, the experiments are used to validate the numerical models. If the numerical models are validated, they can be employed to predict the performance of other blast walls instead of conducting further experiments. In order to identify the governing parameters for the blast-resistant design of such walls, several parametric studies are carried out. These studies serve as an attempt to obtain a better understanding of the behaviour of shock waves interacting with a blast wall having a canopy.

#### 6.3.1 Numerical models of blast walls with a canopy on top

To protect a building and its occupants against air blast, a blast wall is often erected, which acts as an obstacle in the propagation path of the shock wave. The empirical approach (Section 4.2.1) of *Kingery and Bulmash 1984 (K&B)* is only valid for free field scenarios (spherical and hemi-spherical). Hence, it is not capable of describing the shock wave propagation behind a wall. Furthermore, if an interaction between the shock wave and the obstacle is concerned, it cannot be treated by this empirical approach. Under such circumstances, a numerical approach is required to simulate this complex shock wave propagation. The straightforward modelling strategy is the purely Arbitrary-Lagrangian-Eulerian (ALE) method (Section 4.2.2). However, the required larger computational time cannot be accepted in practice, since a small element size and a large air domain are needed in order to ensure the computational accuracy. As mentioned in Section 4.2.4, the combined method LBE / ALE (Section 4.2.3) is used in this Dissertation to model the shock wave propagation. Figure 6-9 illustrates a sketch of the numerical model used in Section 6.3.

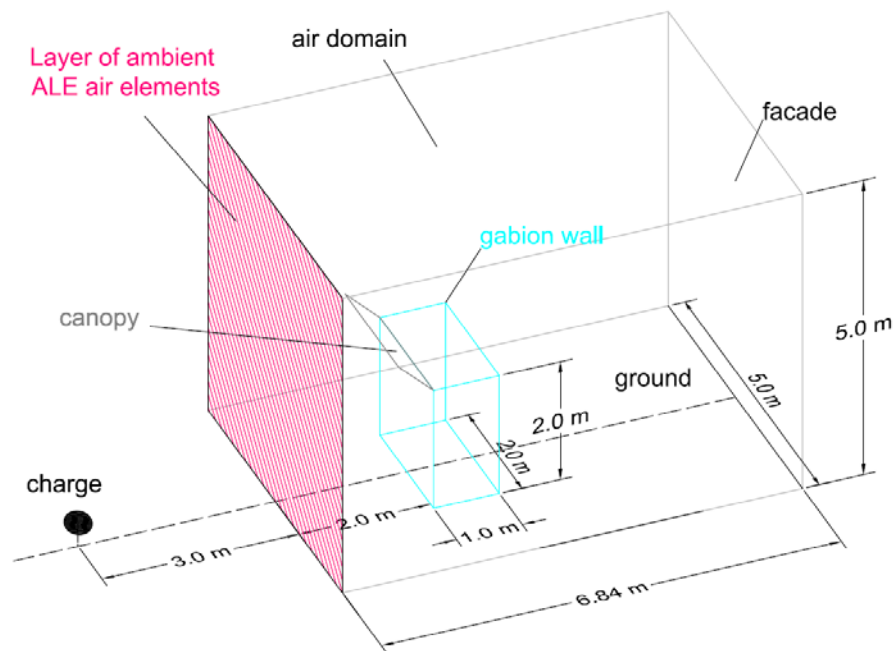


Figure 6-9: Sketch of the numerical model of the blast wall with a canopy on top  
(Xiao et al. 2018c)

The numerical simulation is subdivided into two stages. In the first stage, the empirical approach (K&B) is used to calculate the blast loads on a layer of ambient ALE air elements (Figure 6-9), which is situated at the front face of the numerical air domain facing the charge, located here 2m in front of the gabion wall. The dimensions of the air domain are 6.84m x 5m x 5m (length x width x height). On the one hand, the dimensions are chosen to cover the measurement region in the experiments (Figure 5-1b, c and d). On the other hand, the numerical models remain to be computationally efficient. In the second stage, the shock wave propagation is simulated by using the ALE formulation with a multi-material option, where the results from the first stage are used as input for the ALE air elements. This coupled approach combines the advantages of both the empirical method and the ALE method. However, the Mach stem effect (Section 3.8.3), which is caused by the charge height (0.4m above the ground) and formed in front of the blast wall, cannot be modelled using this coupled approach. The Mach stem effect is neglected in the numerical models in Section 6.3.

If a shock wave encounters an obstacle, the incident shock wave is reflected. Thus, the side-on overpressure is magnified to the reflected overpressure by a so-called reflection coefficient. *Gebbeken and Döge 2010b* conducted studies on the influence of material, structural thickness and boundary conditions of the structural system on the reflection coefficient. The authors found that, for most classical construction materials (e.g. steel, concrete and glass) and usual dimensions (thickness larger than 0.013mm), the influence of these parameters on the reflection coefficient was negligible. The reflection coefficient was almost the same as that of an ideally rigid material or structure, respectively. Therefore, it seems adequate to apply rigid boundary conditions to represent the building envelope and the blast wall if only the shock wave propagation is of interest.

As described in Section 4.1.1.1, the air is modelled via \*MAT\_NULL (*LSTC 2017*) and regarded as an ideal gas with a linear polynomial Equation of State (EoS). The front face of the air domain is specified as an ambient layer to receive the information of the empirically derived blast loads. The bottom and rear faces of the air volume represent the ground surface and the facade of a building, respectively. They are viewed as ideally reflecting surfaces, which is somewhat stronger than in the conducted experiments (*Gebbeken 2017*). Their nodes are constrained in the normal direction. Non-reflecting boundary conditions are applied to the remaining exterior surface of the air volume. The gabion wall is considered as a rigid body having flat surfaces. In lieu of explicit modelling of the wall, appropriate boundary conditions are imposed on the nodes of its exterior surfaces, i.e. the motion in the normal direction is constrained. The canopy is modelled applying two different approaches: firstly as a rigid structure (Sections 6.3.4.1 - 6.3.4.4), secondly as a flexible bending plate (Section 6.3.4.5). In the former, the same approach used to model the gabion wall is employed. In the latter, the canopy is discretized by Lagrangian shell elements modelled via \*MAT\_PLASTIC\_KINEMATIC (*LSTC 2017*), which is a rate-sensitive, elastic-plastic bilinear material with von Mises yield criterion. Strain rate effects are taken into account based on the Cowper-Symonds model. Table 4-3 summarizes the pertinent material parameters of the canopy (Section 4.1.1.3).

Using the Fluid-Structure-Interaction (FSI) (Section 4.1.5), the shock wave and the canopy are coupled in the analysis. The coupling algorithm \*CONSTRAINED\_LAGRANGE\_IN\_SOLID (*LSTC 2017*) utilizes the ALE air mesh to derive the dynamic forces on the canopy. Meanwhile, the canopy provides a dynamic constraint to the shock wave propagating through the air domain.

### 6.3.2 Mesh convergence study and model verification

For the purpose of mesh convergence and verification of the numerical models, a special configuration denoted as M0 (no wall), is modelled, in which the blast wall is not present. It is in accordance with a free field scenario. An atmospheric pressure of 101.325kPa and an ambient air density of 1.225kg/m<sup>3</sup> are used in this section, which represent the ambient conditions at mean sea level and at the standard temperature of 15°C.

To determine a reasonable mesh density for the air domain, a mesh convergence study based on configuration M0 (no wall) is conducted with the software LS-DYNA using different mesh sizes of 15cm, 10cm, 5cm, 2.5cm and 2.25cm, respectively. The numerical simulations are terminated at 30ms. A workstation including 48 processors is employed to carry out the numerical simulations. The total number of elements in the numerical model and the computational time needed to run each simulation are given in Table 6-1.

Table 6-1: Comparison of the computational time in the mesh convergence study

Mesh size [cm]	15	10	5	2.5	2.25
Number of elements [-]	59220	172500	1370000	10960000	15372000
Computational time [min]	0.7	1.3	7.4	58.6	82.0

In an attempt to examine the effect of varying the mesh density on the numerical results, the peak side-on overpressures at gauges ps1 - ps4 and the peak reflected overpressures at gauges pr1 - pr4 are selected as reference quantities for comparison. It is observed in Figure 6-10 that

the peak overpressures at all gauges converge as the mesh density increases. At certain gauges (ps1, ps2, ps3 and ps4), the peak overpressures seem to be converged already since a mesh size of 5cm is adopted and the air domain is discretized by 1370000 elements. Nevertheless, the second finest mesh (mesh size of 2.5cm) is utilized to carry out the numerical simulations in the following sections. On the one hand, a desired level of accuracy is ensured. On the other hand, the computational demand remains affordable.

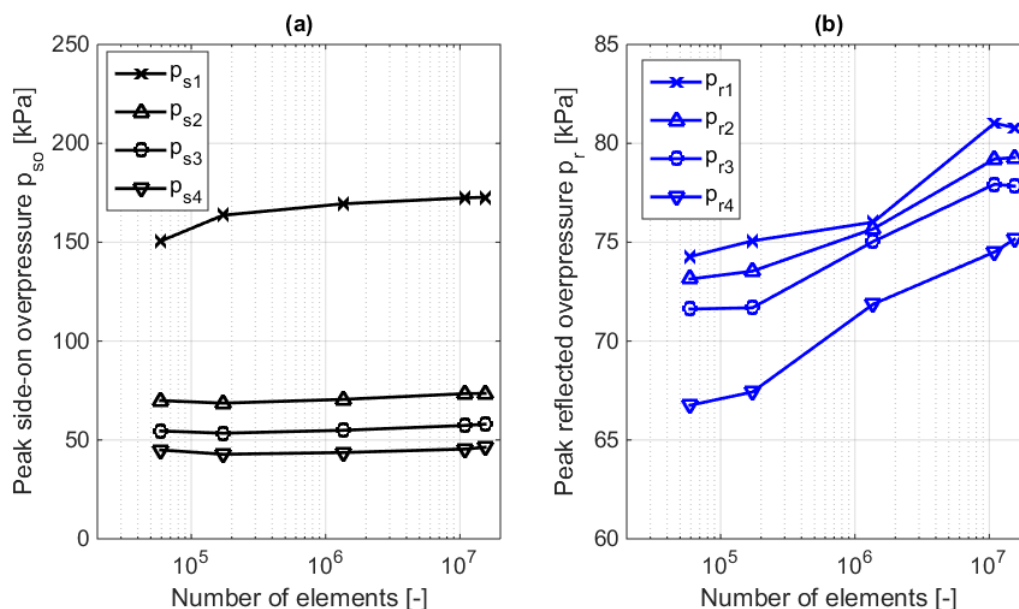


Figure 6-10: Mesh convergence study (a) side-on overpressures; (b) reflected overpressures

Based on the empirical formulae of *Kingery and Bulmash 1984*, the software ConWep (*Hyde 1988*) is able to predict the peak side-on or reflected overpressure and the arrival time of the shock front, according to the respective gauges. Thus, it is used to verify the numerical model with the special configuration M0 (no wall).

Figure 6-11 compares the peak side-on and reflected overpressures for configuration M0 (no wall) which are obtained from ConWep and LS-DYNA. It can be seen that the empirical and numerical results are in reasonable agreement with each other, except for the peak side-on overpressure at gauge ps1, where the numerical value is approximately 11.1% less than the empirical value. As observed from the experimental results, the variance at gauge ps1 is greater than that at other gauges (Table 5-2 - Table 5-5). This is most likely attributed to the influence of the cauliflower effect, in which the detonation products have not been completely burnt out. As the standoff distance increases, the influence of this effect decreases.

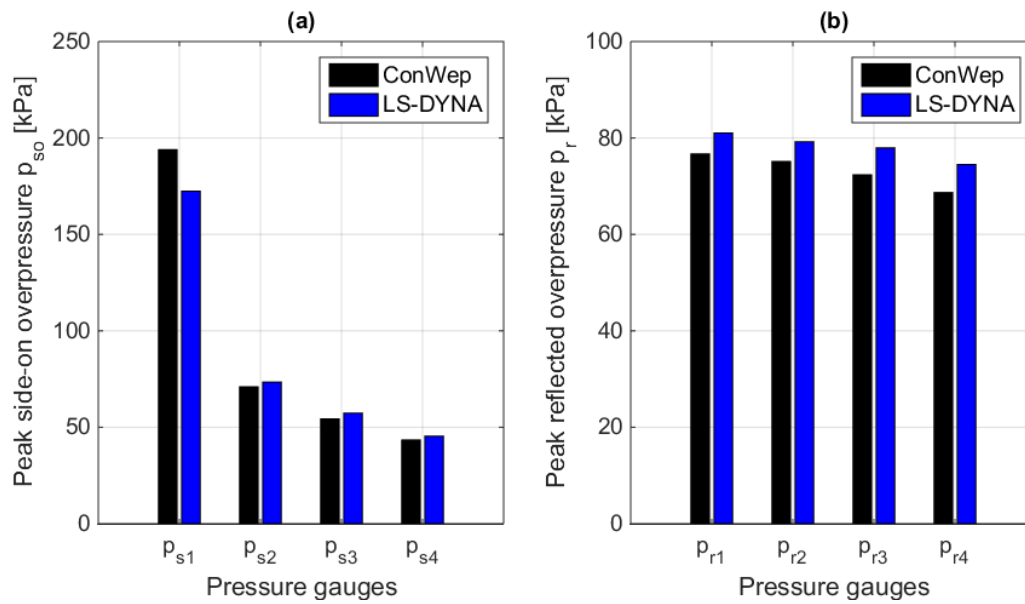


Figure 6-11: Configuration M0 (no wall) (a) peak side-on overpressures; (b) peak reflected overpressures

After verification for configuration M0 (no wall), the numerical approach can be analogously applied to configurations M1 (GWC back), M2 (GW) and M3 (GWC front) according to the individual experimental set-up.

### 6.3.3 Model validation

As described in Section 6.1, an atmospheric pressure of 83.68kPa and an ambient air density of 0.994kg/m<sup>3</sup> are used for the numerical simulations in Sections 6.3.3 and 6.3.4, which represent the ambient conditions at the test site of the Bundeswehr Technical Center for Protective and Special Technologies (WTD52) in Germany and at the average temperature (20.2°C) on 17<sup>th</sup> August 2016 between 9 and 15 o'clock.

The numerical predictions of peak side-on and reflected overpressures at gauges  $p_{s1}$  -  $p_{s4}$  and  $p_{r1}$  -  $p_{r4}$  agree reasonably with the mean values of the experimental recordings for all three configurations, especially when the standard deviations  $\sigma$  of the experimental data are taken into account. Figure 6-12 shows the experimental and numerical results for configuration M3 (GWC front). The circles denote the mean values ( $\mu$ ). The lower bound ( $\mu - \sigma$ ) and upper bound ( $\mu + \sigma$ ) are also marked in the graph, which represent the confidence interval of the experimental results.

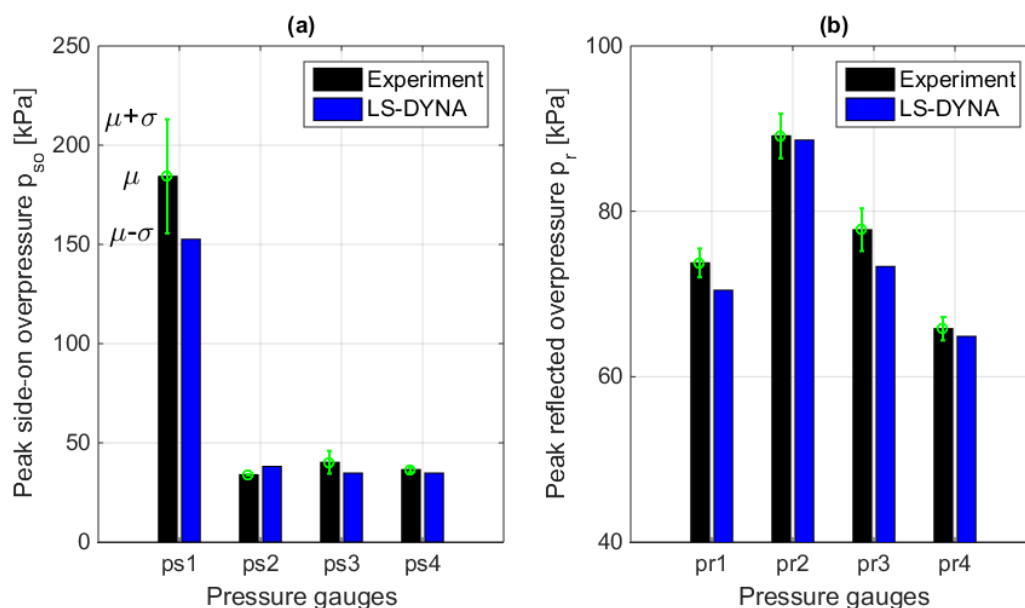


Figure 6-12: Configuration M3 - GWC front (a) peak side-on overpressures; (b) peak reflected overpressures

In general, the numerical values are less than the experimental mean values, except for gauge ps2. The underestimations of the numerical results at these gauges are attributed to the fact that this numerical simulation neglects the influence of the Mach stem formation, which reduces the overpressures at the gauges by 1.0% - 11.4% (Section 6.2). In addition, the influence of the Mach stem formation diminishes as the distance from the charge to the gauge increases. The overestimation of the numerical result at gauge ps2 is due to the simplification in the numerical model, i.e. the gabion wall is regarded as a rigid body having ideally reflecting surfaces. In the experiments, a certain amount of the blast energy is absorbed by the open porous surfaces of the gabion wall. Furthermore, gauge ps2 is located only 0.5m behind the gabion wall. The shock wave needs to flow along the rear face of the gabion wall before it reaches gauge ps2, this makes the influence of the open porous surfaces of the gabion wall more pronounced at gauge ps2 than at the other gauges.

#### 6.3.4 Numerical results

The blast wall consisting of both the gabion wall and the canopy is considered to be rigid in Subsections 6.3.4.1 - 6.3.4.4 and 6.3.4.6. The influence of the flexibility of the deformable canopy is explored in Subsection 6.3.4.5.

##### 6.3.4.1 Overpressure-time history

Using the numerical model described in Section 6.3.1, the side-on and reflected overpressure-time histories can be calculated. The experimental and numerical predictions are compared in Figure 6-13 (side-on overpressures at gauges ps1 - ps4) and Figure 6-14 (reflected overpressures at gauges pr1 - pr4) for configuration M3 (GWC front). As depicted in Figure 6-13 and Figure 6-14, the numerical approach accurately predicts the overall side-on and reflected overpressure-time histories at gauges ps1 - ps4 and pr1 - pr4, compared to the overpressure recordings captured during the experiments.

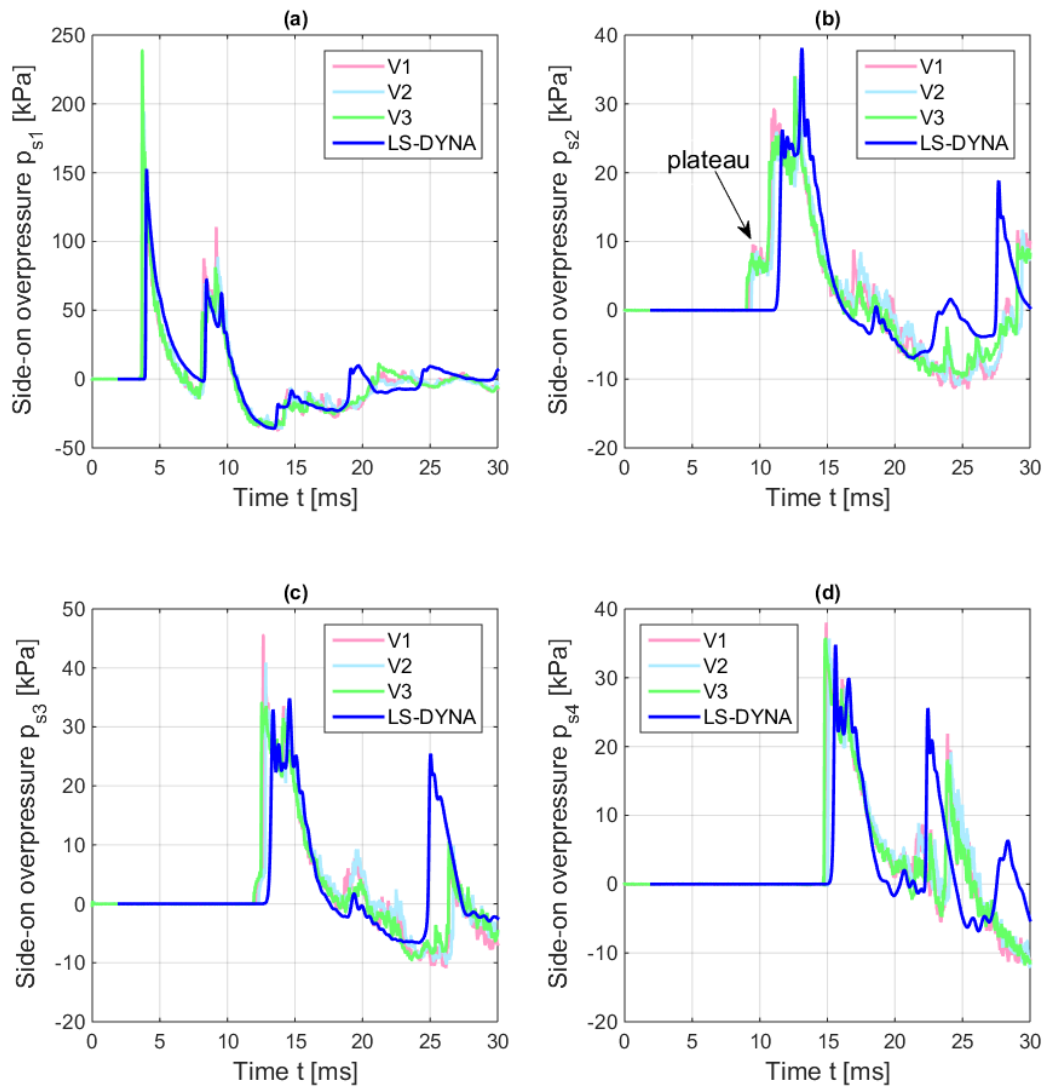


Figure 6-13: Side-on overpressure-time histories, M3 - GWC front (a) ps1; (b) ps2; (c) ps3; (d) ps4

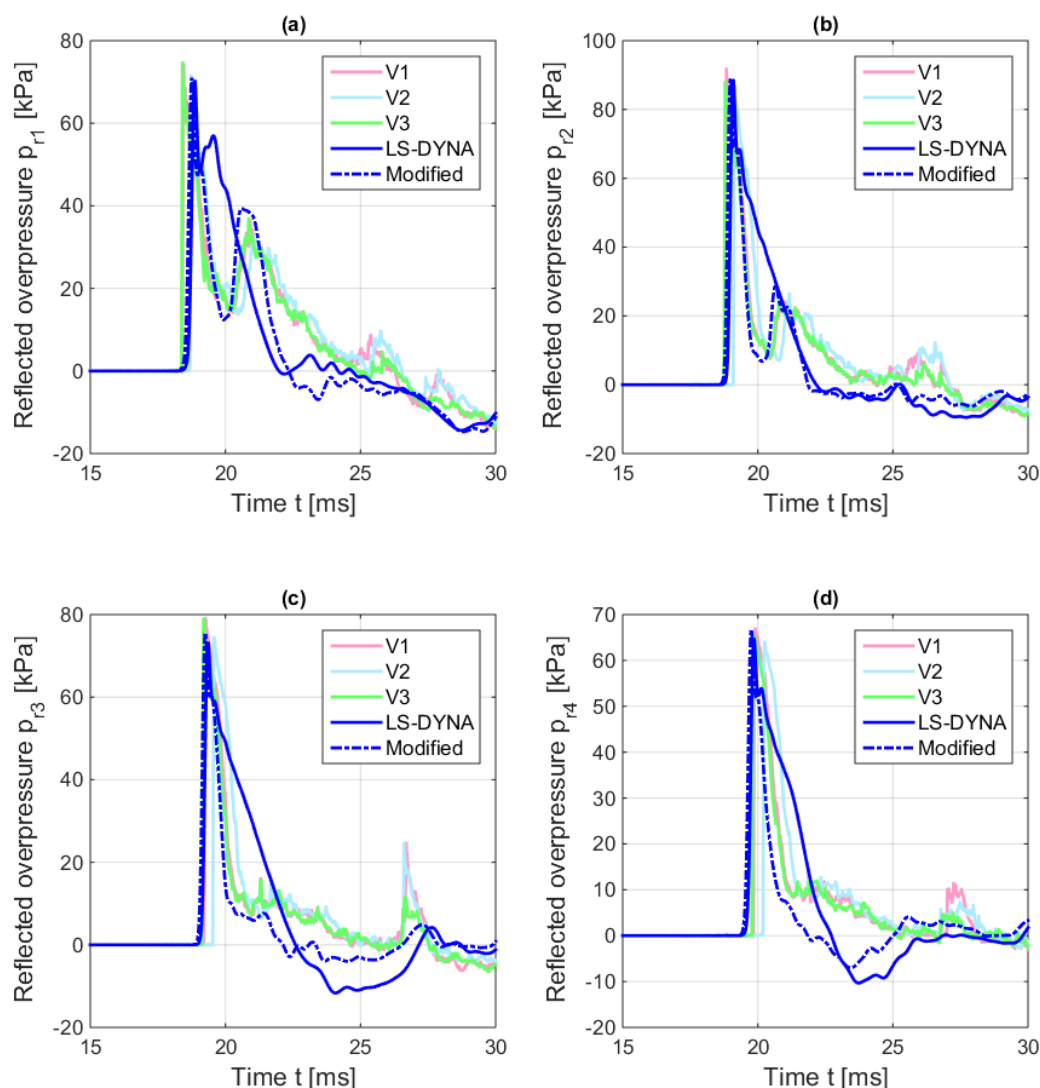


Figure 6-14: Reflected overpressure-time histories, M3 - GWC front (a) pr1; (b) pr2; (c) pr3; (d) pr4

The peak side-on overpressure and the arrival time of the shock front at gauge ps1 are accurately predicted (Figure 6-13a). The first peak in this curve is caused by the arrival of the shock wave at that gauge, whereas the second and third peaks are related to the reflection of the shock wave from the gabion wall and from the canopy. At gauge ps2 (Figure 6-13b), the first peak generated by the numerical approach, at  $t = 11.7\text{ms}$ , is associated with the arrival of the shock front, which partly flows around the sides of the wall, at that gauge. Subsequently, these parts of the waves merge with the part flowing over the top of the wall and this give rise to the peak at  $t = 13.1\text{ms}$ . These effects will be further discussed in Section 6.3.4.3.

Considering the arrival time of the shock front at gauges ps2, ps3 and ps4, the numerical result manifests a time delay of about 0.3ms compared to the experimental results (Figure 6-13b, c, d). As the shock wave travels to the facade, the difference in the arrival time of the shock front at gauges pr1 - pr4 between the numerical and experimental results decreases (Figure 6-14). The reason for the observed discrepancy in the arrival time of the shock front is caused by neglecting the Mach stem formation in the numerical simulation, which slightly reduces the overpressures at the gauges (Section 6.3.3). As observed in Figure 6-13, the first peak value in

the numerical overpressure-time history is slightly smaller than the ones in the experimental recordings. Since the shock velocity  $U$  decreases as the peak side-on overpressure  $p_{so}$  decreases (Eq. (3-5)), this underestimation in the overpressure leads to a slightly later arrival of the shock front.

As already mentioned in Section 5.1.4.1, a remarkable plateau is observed in the experimental recordings at gauge ps2 (Figure 6-13b). The reason for this plateau is most likely attributed to the presence of the small openings (slits) between the cubic gabion boxes (Figure 5-8). A small amount of the shock wave propagates directly through this slit to gauge ps2. The plateau is much less pronounced at gauge ps3 (Figure 6-13c) and is not discernible at gauges ps4 (Figure 6-13d) and pr1 - pr4 (Figure 6-14). Using the proposed numerical model (Section 6.3.1), an even and closed exterior surface is assumed for the gabion wall, hence, it is unable to capture the plateau shown in the experimental curves (Figure 6-13b). Nevertheless, the magnitude of the plateau is comparably small (only about one-third) in relation to the corresponding peak overpressure, which is of interest to derive the overpressure reduction. Beside this plateau, the numerical model accurately predicts the overall overpressure-time history at gauge ps2 (Figure 6-13b). Furthermore, no plateau appears in the overpressure-time histories at the remaining gauges. Therefore, it seems appropriate to assume that the gabion wall has an even and closed exterior surface.

### 6.3.4.2 Clearing effect of shock waves around wooden plates

In order to visualize the entire relevant reflected overpressure-time histories, the time axes in Figure 6-14 start at 15ms and extend to 30ms, which are different to the ones in Figure 6-13. As observed in Figure 6-14 (solid blue lines), the first peaks and the arrival time of the shock front at gauges pr1 - pr4 are accurately predicted by the numerical approach (Figure 6-9). However, the decay after the first peak and the subsequent peaks are not appropriately represented. It is attributed to the simplification in the numerical model (Figure 6-9) that gauges pr1 - pr4 are directly mounted on the building envelope, which represents an ideally reflecting surface and has a height of 5m. In fact, the gauges are mounted on wooden plates, which are of finite dimensions (0.4m x 0.4m) and placed 0.16m in front of the building envelope (Figure 5-4c). Moreover, the massive wall representing the building envelope has a height of 2m (Figure 5-4b). As explained in Section 5.1.3, the clearing effect will occur at gauges pr1 - pr4. Using the numerical model illustrated in Figure 6-9, the clearing effect cannot be modelled. In order to capture this effect, a modification of the numerical models needs to be made, i.e. the massive wall and the wooden plates to mount gauges pr1 - pr4 are considered. Based on the study made by *Gebbeken and Döge 2010b*, it seems adequate to apply rigid boundary conditions to represent the exterior surfaces of the massive wall and the wooden plates.

Using the modified numerical model illustrated in Figure 6-15, the overpressure-time histories at gauges pr1 - pr4 for configuration M3 (GWC front) are computed and also illustrated as dashed blue lines in Figure 6-14. It is found that the overpressures are “cleared” at all gauges, i.e. pr1 at  $t = 19.0\text{ms}$ , pr2 at  $t = 19.2\text{ms}$ , pr3 at  $t = 19.5\text{ms}$ , and pr4 at  $t = 20.0\text{ms}$ , respectively.

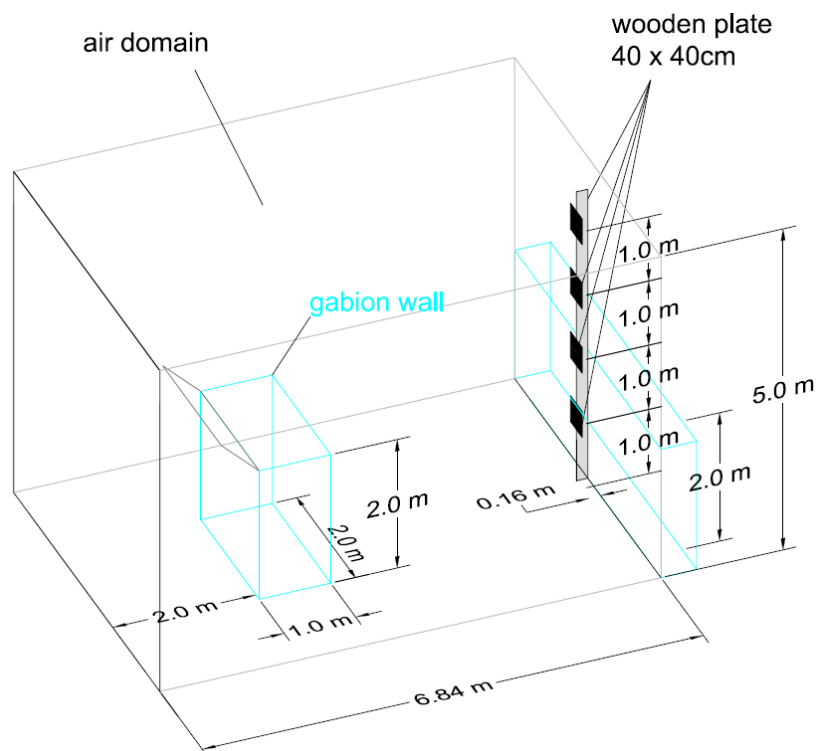


Figure 6-15: Sketch of the numerical model including wooden plates, M3 - GWC front

As the shock wave impinges on the front face of the wooden plate to mount gauge pr1, the incident shock wave is partly reflected and partly diffracted around the free edges of the wooden plate. Due to the small distance (0.16m) between the wooden plates and the massive wall (Figure 5-4c), the diffracted wave is re-reflected from the massive wall and then impinges gauge pr1 once again. This phenomenon leads to the peak overpressures of about 40kPa between  $t = 20.9\text{ms}$  and  $t = 21.1\text{ms}$  in the experimental recordings (Figure 6-14a). The modified numerical model predicts larger values than the experiments. This is most likely due to the simplification in the numerical simulation, i.e. the influence of open porous surface of the massive wall is neglected. The same phenomenon as occurred at gauge pr1 can also be observed at gauge pr2 by the peak overpressures between  $t = 20.8\text{ms}$  and  $t = 21.2\text{ms}$  (Figure 6-14b). Due to the low height of the massive wall (2m, Figure 5-4b), the reflecting surface area behind the wooden plate to mount gauge pr2 is approximately 50% of that behind the wooden plate to mount gauge pr1. Therefore, the magnitude of the peak overpressures for gauge pr2 (due to the re-reflection from the massive wall) is less than that for gauge pr1. For gauges pr3 and pr4, the diffracted waves will not be re-reflected again, i.e. they will propagate undisturbed away from the rear face of the wooden plates. Hence, the aforementioned phenomenon does not occur at gauges pr3 and pr4.

However, there is still a considerable discrepancy between the results predicted by the modified numerical model and the experimental recordings, e.g. the negative phases in the numerical results are more pronounced than in the experimental results. It is most probably related to the finite air domain size constrained by the computational resources that are currently available at the chair.

### 6.3.4.3 Shock wave propagation

In order to illustrate the shock wave propagation, Figure 6-16 presents some pressure contour plots at a horizontal plane located 1m above the ground for configuration M3 (GWC front). As aforementioned, instead of explicitly modelling the gabion wall (plotted as a white rectangular in Figure 6-16, Figure 6-17 and Figure 6-18), appropriate boundary conditions are assigned to the exterior surfaces of the wall. Based on these contour plots, the shock wave propagation in the horizontal direction can be analysed.

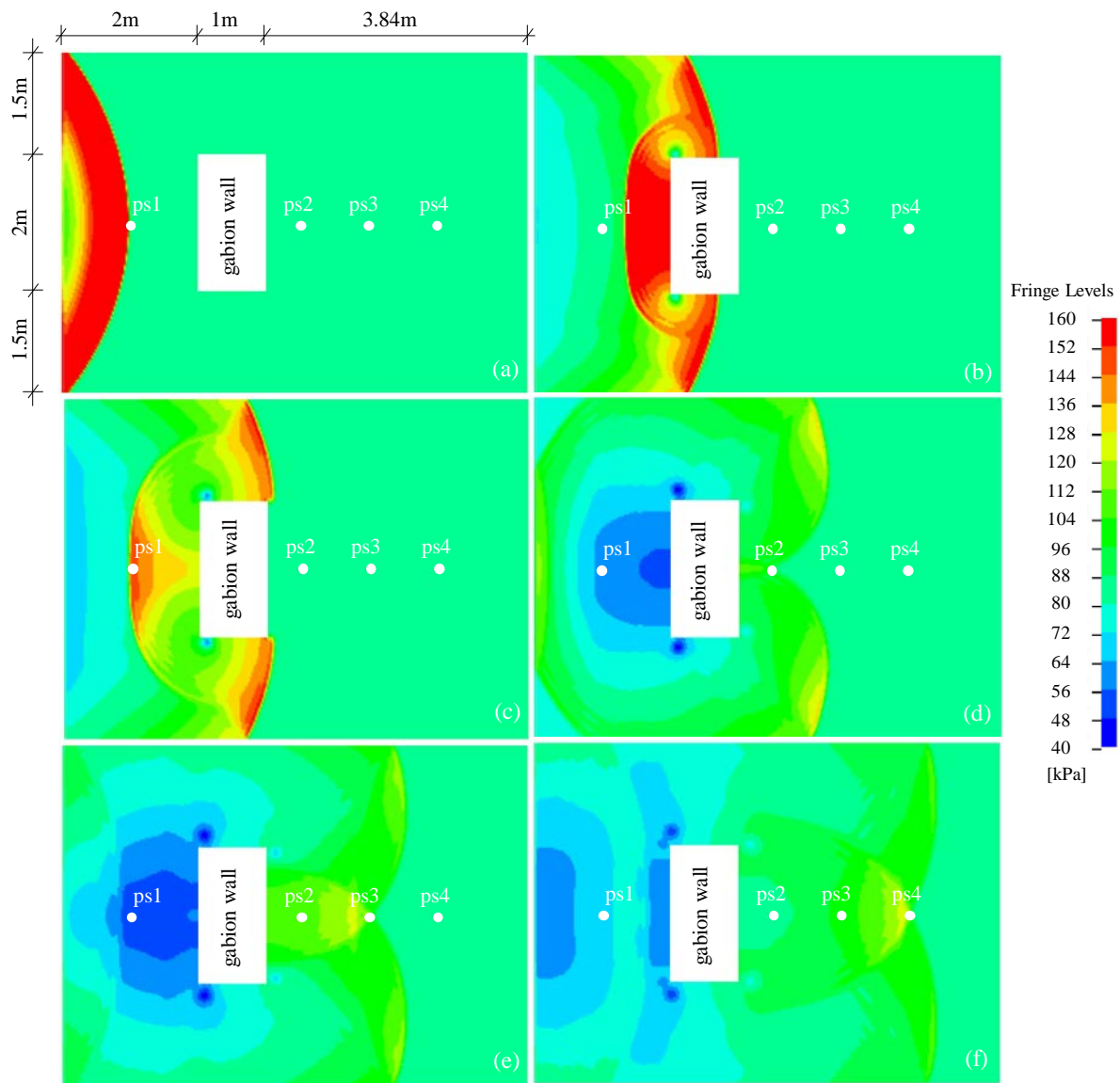


Figure 6-16: Pressure contour plots of a horizontal plane at an elevation of 1m above the ground, M3 - GWC front, plan view (a)  $t = 4.0\text{ms}$ ; (b)  $t = 7.6\text{ms}$ ; (c)  $t = 8.5\text{ms}$ ; (d)  $t = 11.7\text{ms}$ ; (e)  $t = 13.3\text{ms}$ ; (f)  $t = 15.6\text{ms}$

A layer of ambient ALE air elements, at a distance of 2m in front of the wall (Figure 6-9), is specified to receive the blast loads derived from the empirical formulae of *Kingery and Bulmash 1984* (K&B). Using the hemi-spherically derived K&B-blast loads as input for the ambient ALE air elements, the shock wave propagation in the entire air domain of the numerical model can be effectively simulated. This corresponds to the numerical approach described in Section

6.3.1. In the numerical model, the shock wave arrives at gauge ps1 at  $t = 4.0\text{ms}$  (Figure 6-16a). Once the shock wave impinges the wall, the shock wave is reflected back towards the charge. At a later time, the wave begins to travel partly around the corners and partly over the top of the wall. This affects the blast load distribution specifically due to the relatively small dimension of the wall. At  $t = 7.6\text{ms}$ , obvious vortices are generated in the corners facing the charge (Figure 6-16b). Subsequently, the wave parts travel along the sides of the gabion wall and reach the end of the edges at  $t = 8.5\text{ms}$  (Figure 6-16c), where they start to flow around the corners towards the centre of the wall's rear face. Both parts of the wave meet at the centre of the rear face and then travel towards the facade. At  $t = 11.7\text{ms}$  (Figure 6-16d), they arrive at gauge ps2. The wave parts that flow around the sides of the gabion wall arrive at gauge ps3 at  $t = 13.3\text{ms}$  (Figure 6-16e) and then arrive at gauge ps4 at  $t = 15.6\text{ms}$  (Figure 6-16f). Finally, it impinges the building envelope, from which the wave is reflected back towards the rear face of the gabion wall.

In an attempt to gain more insight into the interaction of waves flowing around the sides and over the top of the blast wall, four pressure contour plots at a horizontal plane located 2m above the ground for configuration M3 (GWC front) are illustrated in Figure 6-17.

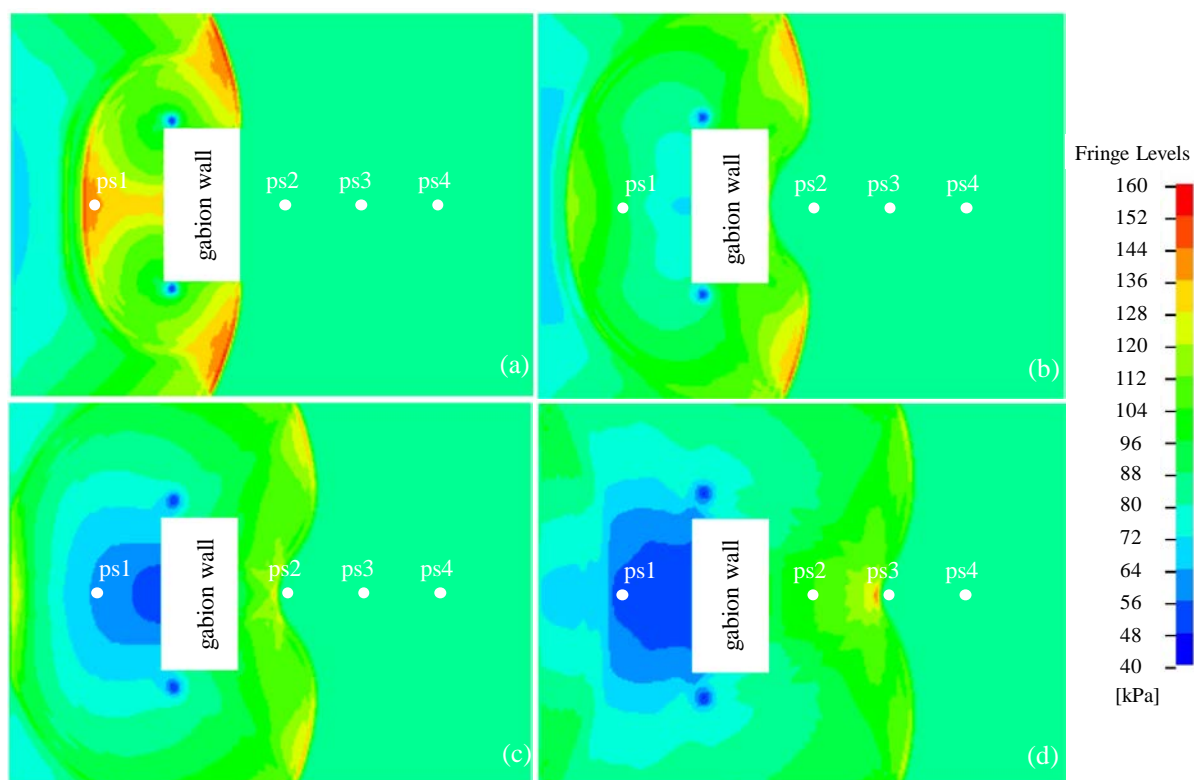


Figure 6-17: Pressure contour plots of a horizontal plane at an elevation of 2m above the ground, M3 - GWC front, plan view (a)  $t = 8.8\text{ms}$ ; (b)  $t = 10.0\text{ms}$ ; (c)  $t = 11.2\text{ms}$ ; (d)  $t = 13.3\text{ms}$

At  $t = 8.8\text{ms}$  (Figure 6-17a), the wave parts that flow around the sides of the gabion wall arrive at the right end of the wall, whereas the wave flowing over the top of the canopy arrives at this place 1.2ms later (Figure 6-18c). At  $t = 10.0\text{ms}$  (Figure 6-17b), the wave parts flowing around the sides of the wall have almost arrived at the centre point of the upper edge of the rear face.

At  $t = 11.2\text{ms}$  (Figure 6-17c) and  $t = 13.3\text{ms}$  (Figure 6-17d), an interaction between waves flowing around the sides and over the top of the blast wall can be obviously observed.

To explain the flow of the shock wave over the top of the blast wall, several pressure contour plots at a vertical plane through the centre of the blast wall are illustrated in Figure 6-18.

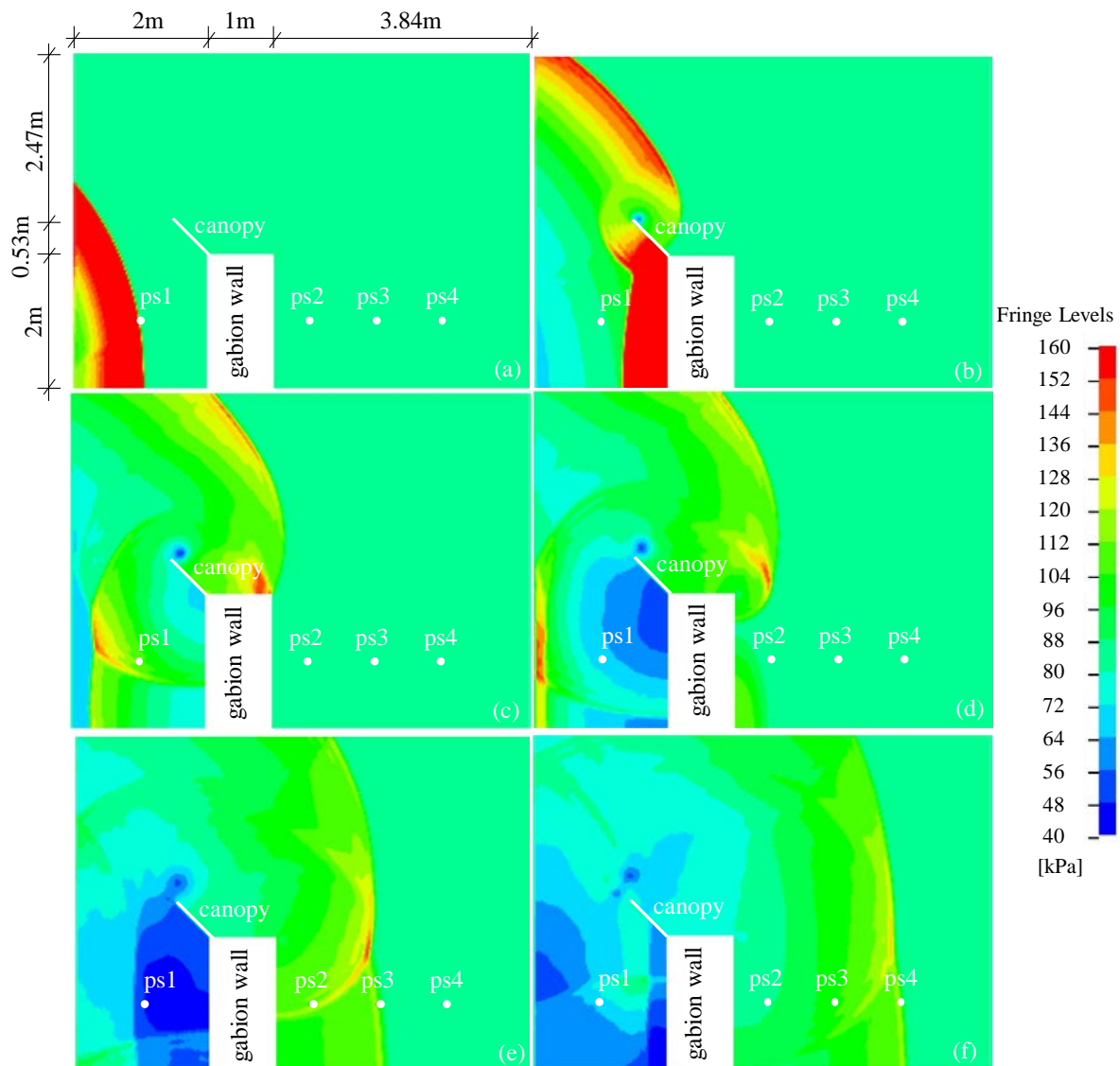


Figure 6-18: Pressure contour plots of the vertical plane through the centre of the blast wall, M3 - GWC front, side view (a)  $t = 4.0\text{ms}$ ; (b)  $t = 7.6\text{ms}$ ; (c)  $t = 10.0\text{ms}$ ; (d)  $t = 11.2\text{ms}$ ; (e)  $t = 13.3\text{ms}$ ; (f)  $t = 15.6\text{ms}$

As aforementioned, the shock wave arrives at gauge ps1 at  $t = 4.0\text{ms}$  (Figure 6-18a). At a later time  $t = 7.6\text{ms}$  (Figure 6-18b), a vortex is generated at the upper edge of the canopy for configuration M3 (GWC front). It is worth noting that if the canopy is arranged according to configuration M3 (GWC front), a special effect is observed. The incident shock wave is reflected, not only by the front face of the gabion wall but also by the canopy. This results in a superposition of both reflected waves, e.g. at  $t = 7.6\text{ms}$ . After the reflection from the blast wall, the wave partly travels upwards, in order to flow over the top of the canopy. At  $t = 10.0\text{ms}$  (Figure 6-18c), the wave part that flows over the top of the canopy arrives at the right end of

the gabion wall. At a time of 1.2ms later (Figure 6-18d), the wave parts that flow around the sides of the gabion wall have passed beyond the rear face of the gabion wall. But they have not yet interacted with the wave part flowing over the top of the canopy. Subsequently, at  $t = 13.3\text{ms}$ , the wave parts that flow around the sides of the gabion wall arrive at gauge ps3 (Figure 6-18e). It is evident that these wave parts have interacted with the wave part flowing over the top of the canopy in the region above gauge ps3. Finally, they arrive at gauge ps4 2.3ms later (Figure 6-18f).

In this section, the propagation of the shock wave interacting with blast wall configuration M3 (GWC front) is presented. Due to the limitation in the wall width (2m) of the blast wall (gabion wall and canopy), a horizontal air flow around the sides of the blast wall occurs and diminishes the shielding effect of the canopy. In practice, however, the blast walls are erected around the buildings to be protected (perimeter walls). Therefore, the aforementioned limitation in the wall width should not be an issue to affect the shielding effect of the canopy. Since the numerical models are validated, they can also be employed to investigate the shielding effect of blast walls having a significantly larger width, in which no horizontal air flow occurs. This investigation will be carried out in Section 6.3.4.6. In the next section, the results of the overpressure distribution across the facade will be presented.

#### 6.3.4.4 Overpressure distribution across the facade

In order to estimate the reduction in the peak reflected overpressures across the facade, a reference configuration M0 (no wall) is considered, in which the blast wall is not present (Section 6.3.2). Thus, the shock wave propagation is in accordance with a free field hemispherical scenario. It should be noted that the ambient conditions at the test site are used here instead of the ambient conditions at mean sea level and at the standard temperature of  $15^\circ\text{C}$  (Section 6.3.2).

Figure 6-19 (M1-rigid, M2-rigid and M3-rigid) illustrates the distribution of the peak reflected overpressure over a vertical region ranging from 0m to 4m above the ground, according to the region measured in the experiments. In order to describe the overpressure distribution across the facade in a convenient way, special axes are used in Figure 6-19. The ordinate is the elevation  $h$  of the vertical gauges, whereas the abscissa is the peak reflected overpressure  $p_r$  across the facade. The horizontal distance of the gauges is 9.84m from the charge (Figure 5-1b, c and d). If the gauge is placed below 1.2m above the ground, configuration M3 (GWC front) does not provide any reduction in the peak reflected overpressure. In the region higher than 1.2m above the ground, an increase in the peak reflected overpressure occurs. An overpressure increase was also observed in the experiments at gauges pr2 and pr3 (Figure 5-11b) for configuration M3 (GWC front). This increase is attributed to the fact that the wave parts travel around the sides of the gabion wall and then merge again behind the wall, where they are combined with the part of the wave that flows over the top of the wall in the middle region at the facade. Therefore, the peak reflected overpressures are augmented. For configurations M1 (GWC back) and M2 (GW), the peak reflected overpressures are slightly reduced in the lower range. In the middle range, an increase in the peak reflected overpressure occurs, due to the same reason as for configuration M3 (GWC front). In the upper region, an overpressure

reduction can be observed in configurations M1 (GWC back) by up to 34.9% and in M2 (GW) by up to 33.1%.

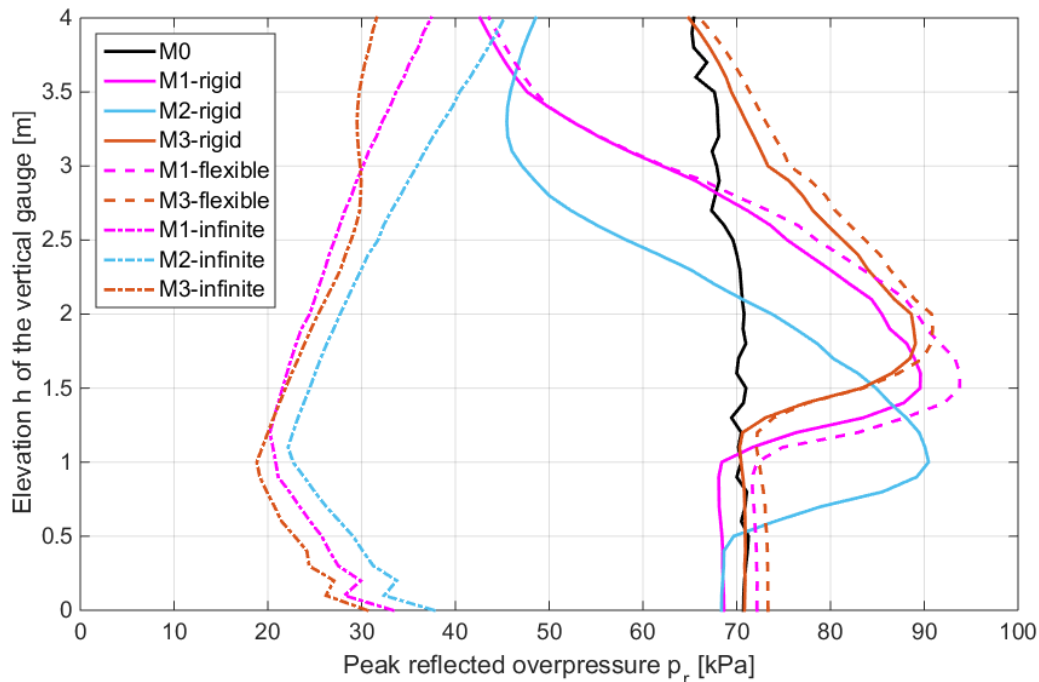


Figure 6-19: Distribution of peak reflected overpressures across the facade

As already mentioned in the previous section, the horizontal air flow around the sides of the blast wall, which is caused by the small width (2m) of the blast wall according to the experimental set-up, plays a great role in the increase of the reflected overpressure at the facade. In practice, however, the blast walls are erected around the buildings to be protected (perimeter walls). Under such circumstances, no horizontal air flow occurs around the sides of the wall. Using the validated numerical models, investigations on the blast walls having significantly larger width will be carried out in Section 6.3.4.6. In the next section, the influence of the flexibility of the deformable canopy on the blast loads behind the wall will be investigated.

#### 6.3.4.5 Flexibility of the canopy

In order to investigate the influence of the flexibility of the deformable canopy on the blast loads behind the wall, a coupled analysis is conducted, in which the interaction between the shock wave and the deformable canopy is taken into account. The results of the peak reflected overpressures are also plotted as dashed lines in Figure 6-19 (M1-flexible and M3-flexible). Due to the flexibility of the canopy, the peak reflected overpressures distributed across the facade are somewhat higher than those of rigid canopies (Section 6.3.4.4), i.e. up to 8.6% in configuration M1 (GWC back) and up to 3.5% in configuration M3 (GWC front). A postulated reason for the increase in the overpressure is that as the canopy deflects, despite quite small in amplitude, the deformable canopy reflects lesser shock wave energy back towards the charge compared to the rigid canopy assumed in Section 6.3.4.4. Thus, more blast energy is used to flow over the canopy. It results in an increase of the peak reflected overpressures at the facade. Moreover, the displacement-time histories of the canopies ( $u_{tot}$ ) are illustrated in Figure 6-20.

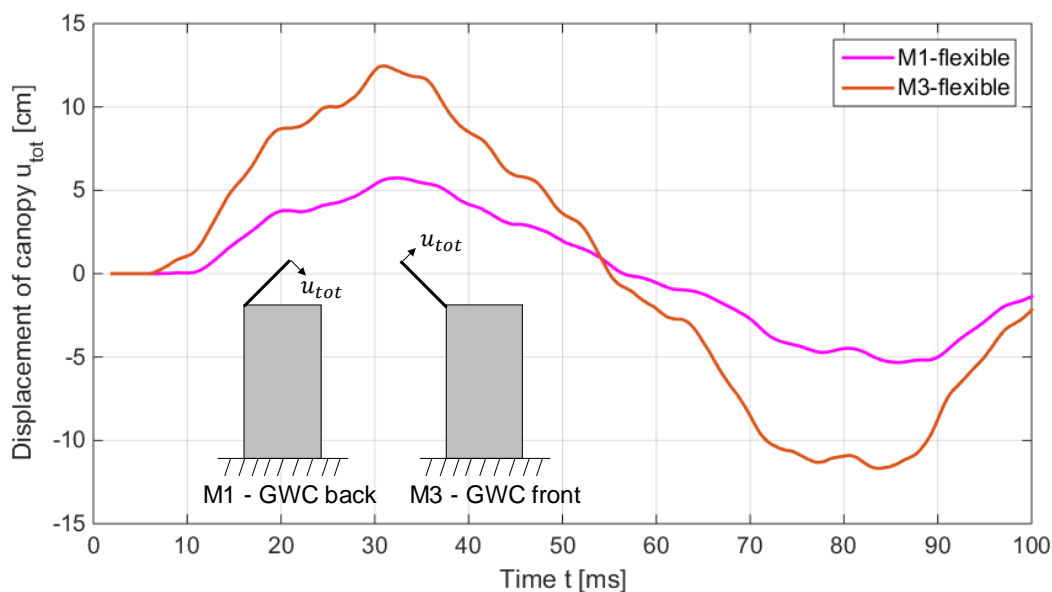


Figure 6-20: Displacement-time histories of the canopies

Similar to what can be observed from the videos, configuration M3 (GWC front,  $u_{tot} = 12.5\text{cm}$ ) has a much larger maximum displacement than M1 (GWC back,  $u_{tot} = 5.7\text{cm}$ ). It should be noted that due to different canopy arrangements, the canopy deflects downwards in configuration M1 (GWC back) and upwards in configuration M3 (GWC front). It was not precise enough to measure the displacements of the canopies using only high-speed cameras. Thus, no valid data was recorded. However, different measurement devices will be tested in forthcoming experiments. The shock front arrives at the canopy at  $t = 4.0\text{ms}$ , whereas the maximum canopy displacement for M3 (GWC front) appears at  $t = 30.9\text{ms}$ , at which the wave has already travelled around the canopy.

In summary, the numerical models accounting for the flexibility of the deformable canopy predict slightly larger overpressures across the facade than those using rigid canopy assumption. The observed maximum increase is +8.6% in configuration M1 (GWC back) and +3.5% in configuration M3 (GWC front). From an engineering viewpoint, these differences are considerably small. In addition, the canopy requires much more time to respond to the blast loads and to develop the deflection with respect to the duration of the blast load pulse. These observations confirm the validity of the rigid wall assumption used in Sections 6.3.4.1 - 6.3.4.4.

#### 6.3.4.6 Blast walls having infinite width

As already explained in Sections 6.3.4.3 and 6.3.4.4, the horizontal air flow around the sides of the gabion wall plays a significant role in the increase of blast loads at the facade behind the wall as long as the gabion wall is not adequately long to avoid these horizontal side flows of air. To explore the influence of the gabion wall width on the blast loads behind the wall, a parametric study is carried out, which is based on configuration M2 (GW, Figure 5-2b). The wall width varies from 1m to 10m with an interval of 1m. The aim is to determine the critical width of the gabion wall beyond which the air flow around the sides of the wall can be ignored. In other words, they do not affect the blast loads behind the wall any longer. Under such circumstances, the analysis might be simplified to a two-dimensional simulation using the axial

symmetry. It should be noted that the critical width of the gabion wall depends also on the charge mass  $W$ , the distance  $R_1$  from the charge to the wall and the distance  $R_2$  from the building to the wall etc.. In this study, these parameters are  $W = 5\text{kg}$  TNT equivalent,  $R_1 = 5\text{m}$  and  $R_2 = 4\text{m}$ .

Figure 6-21 illustrates the peak reflected overpressures distributed across the facade. Also included in the graph are the values obtained from configuration M0 (no wall), which represents a free field scenario. If the wall has a width of only 1m, the peak reflected overpressures are reduced by about 16 - 31%. When the wall has a width between 2m and 4m, an increase in the peak reflected overpressure occurs in the lower region of the facade between 0m and 2.1m above the ground, compared to configuration M0 (no wall). Particularly for the width of 4m, the maximum overpressure increase is 70%. If the wall is longer than 5m, the peak reflected overpressures are reduced at the entire facade. For wall widths between 7m and 10m, there is only fractional difference in the blast load distribution across the facade. Therefore, it can be concluded that for the set of parameters ( $W = 5\text{kg}$  TNT equivalent,  $R_1 = 5\text{m}$  and  $R_2 = 4\text{m}$ ) in the experiments, the width of the gabion wall should be at least 7m in order to neglect the influence of the horizontal air flow around the sides of the wall.

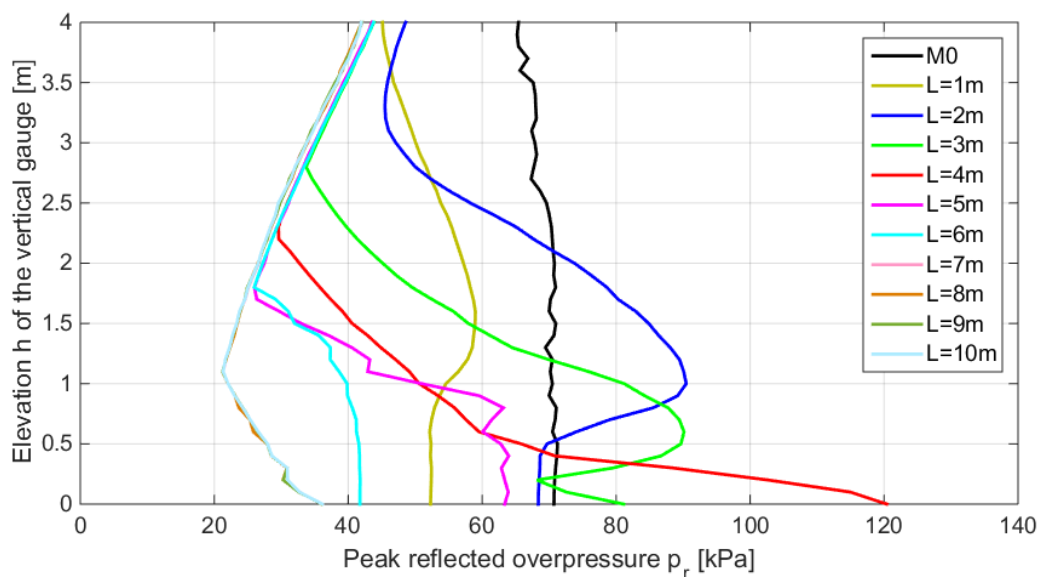


Figure 6-21: Dependence of the peak reflected overpressure distribution across the facade on the width of gabion walls

As shown in Section 6.3.4.3, two different parts of the shock wave affect the blast load distribution behind the wall. The first part flows around the sides of the wall and the second part flows over the top of the wall, which are denoted as horizontal and vertical flow, respectively. The lengths of the pertinent propagation paths at the front face of the wall are  $L/2$  (half wall width) for the horizontal flow and  $H$  (wall height) for the vertical flow. The length of the propagation path has a governing effect on the arrival time and the magnitude of the peak overpressure. If both parts of the shock wave have the same length of the propagation path, i.e.  $L/2 = H$ , these two parts will meet at the same time at the rear face of the blast wall. A superposition of these two parts of the wave occurs. Under these conditions, not only the vertical but also the horizontal flow play a role in the blast load distribution behind the wall.

Therefore, the ratio  $L/(2H)$  can be regarded as an indicator to judge whether the horizontal flow can be neglected or not. This parametric study shows that, for the experimental set-up ( $W = 5\text{kg}$  TNT equivalent,  $R_1 = 5\text{m}$  and  $R_2 = 4\text{m}$ ), the infinite wall width assumption is valid if the ratio  $L/(2H)$  is larger than 1.75.

Based on the conclusion mentioned above, the critical width of the blast wall (7m) is employed to examine the effectiveness of blast walls having an infinite wall width, in which the horizontal flow is neglected. The results of the reflected peak overpressure across the facade are also plotted as dashed lines in Figure 6-19 (M1-infinite, M2-infinite and M3-infinite). Unlike the blast wall having 2m width (Section 6.3.4.4), the shock wave is significantly attenuated, regardless of which configuration is involved. Compared to configuration M2 (GW), an additional reduction in the peak reflected overpressure is observed in configuration M1 (GWC back) and M3 (GWC front). This means that the canopies offer additional contributions to the overpressure reduction across the facade. Figure 6-22 shows the results of the overpressure and impulse reduction factors at gauges ps2 - ps4 and pr1 - pr4. The reduction factors in overpressure  $F_p$  and in impulse  $F_i$  are defined as

$$F_p = \frac{p_{no\ wall} - p_{wall}}{p_{no\ wall}} \cdot 100\%, \quad (6-3)$$

$$F_i = \frac{i_{no\ wall} - i_{wall}}{i_{no\ wall}} \cdot 100\%, \quad (6-4)$$

where  $p_{wall}$  and  $i_{wall}$  are the peak overpressure and maximum impulse at the specified gauge behind a blast wall and  $p_{no\ wall}$  and  $i_{no\ wall}$  are the peak overpressure and maximum impulse at that gauge when no blast wall is present.

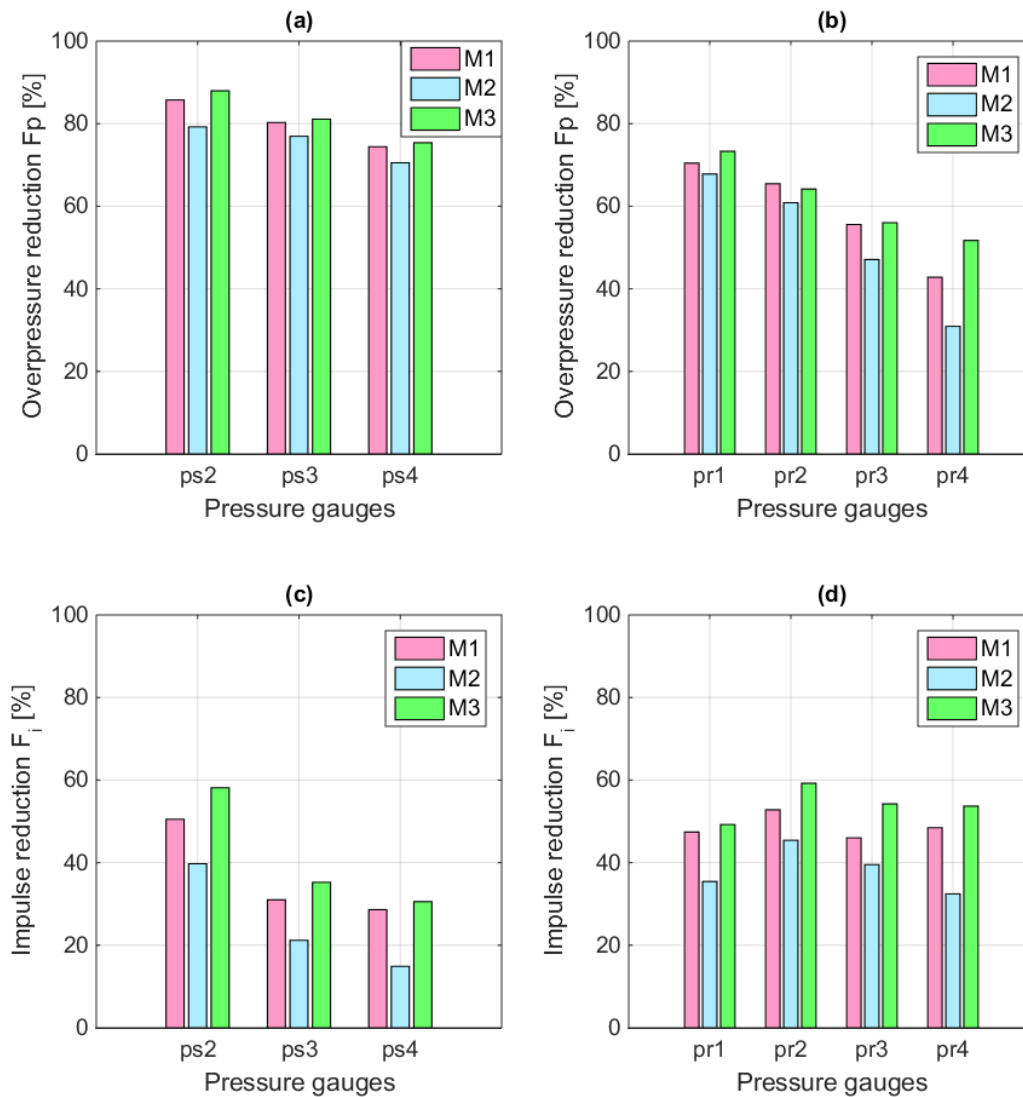


Figure 6-22: Overpressure and impulse reduction for blast walls having infinite width  
 (a)  $F_p$  at gauges ps2 - ps4; (b)  $F_p$  at gauges pr1 - pr4; (c)  $F_i$  at gauges ps2 - ps4;  
 (d)  $F_i$  at gauges pr1 - pr4

As shown in Figure 6-22, the canopies provide additional contributions to the overpressure and impulse reduction at all gauges. Configuration M3 (GWC front) shows the best performance in shock wave attenuation. Compared to a free field scenario, it offers an overpressure reduction ranging from 51.7% to 88.0% and an impulse reduction ranging from 30.5% to 59.2% at the gauges employed in the experiments.

In summary, the considered blast wall configurations are sorted in descending order of shock wave attenuation performance as follows: M3 (GWC front), M1 (GWC back) and M2 (GW).

### 6.3.5 Parametric studies

The effectiveness of blast walls in shock wave attenuation depends on a variety of parameters. In this section, the influence of two parameters on the blast wall effectiveness is explored, namely, thickness and angle of inclination of the canopy. The remaining parameters are kept the same as the experimental set-up, i.e. charge mass ( $W = 5\text{kg TNT equivalent}$ ), distance from

the charge to the wall ( $R_1 = 5\text{m}$ ), distance from the building to the wall ( $R_2 = 4.00\text{m}$ ) and locations of gauges ps1 - ps4. For the sake of simplicity, gauges pr1 - pr4 are assumed to be mounted directly on the building envelope. This means that a horizontal distance of 10m is used in the following parametric studies instead of 9.84m in the previous sections. Usually, there are not so many buildings to be protected which are located at a relatively high altitude as considered in the previous sections (1585m). In order to obtain some findings for a general use, it seems more meaningful to consider the ambient conditions at mean sea level and at the standard temperature ( $15^\circ\text{C}$ ), which result in an atmospheric pressure of 101.325kPa and an ambient air density of  $1.225\text{kg/m}^3$ . These parameters are employed in the following subsections.

**6.3.5.1 Thickness of the canopy**

In order to explore the influence of the canopy thickness on the blast loads behind the wall, a parametric study based on configuration M3 (GWC front) is carried out, in which the thicknesses  $t_c$  ranging from 1mm to 20mm are considered. The critical width (7m) of the gabion wall deduced from Section 6.3.4.6 is adopted in this study and the cantilever length  $l_c$  (Figure 5-3) of the canopy remains 0.75m. All the other parameters are kept the same as in Section 6.3.4.5.

The peak reflected overpressure distribution over the region from 0m to 4m above the ground is plotted in Figure 6-23.

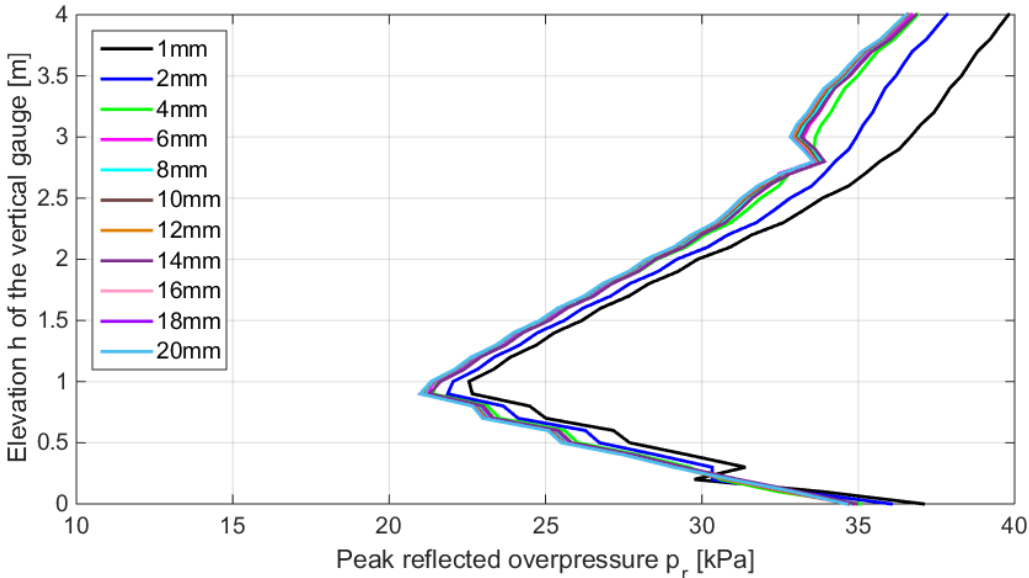


Figure 6-23: Dependence of the peak reflected overpressure distribution across the facade on the thickness of the canopy

In the lower range, i.e. 0m - 0.9m above the ground, the variation in the thickness  $t_c$  of the canopy is of less interest to the blast loads at the facade. In the upper region, the effect of the thickness of the canopy on the blast load distribution is obvious if the thickness  $t_c$  increases from 1mm to 6mm. Beyond a thickness of 6mm, a further increase in the thickness affects the peak reflected overpressure distribution across the facade only very slightly. It indicates that, for a canopy thicker than 6mm, the flexibility of the canopy has nearly no influence on the blast

load distribution behind the wall. This confirms again that the rigid assumption used in Sections 6.3.4.1 - 6.3.4.4 for the canopy (8mm) is valid. In other words, if the slenderness ratio  $l_c/t_c$ , which is defined as the ratio of the length  $l_c$  of the canopy to its thickness  $t_c$ , is larger than 125, the flexibility of the canopy should be taken into account.

Figure 6-24 illustrates the maximum displacements  $u_{tot}$  (Figure 6-20) for canopies with different thicknesses. If it has a thickness larger than 6mm, the canopy behaves elastically. Otherwise, a certain amount of plastic deformation occurs in the canopy. For example, a maximum displacement of 22.58cm occurs in the canopy having a thickness of 6mm, which corresponds to a plastic rotation of about 16.8° at the connection between the canopy and the gabion wall.

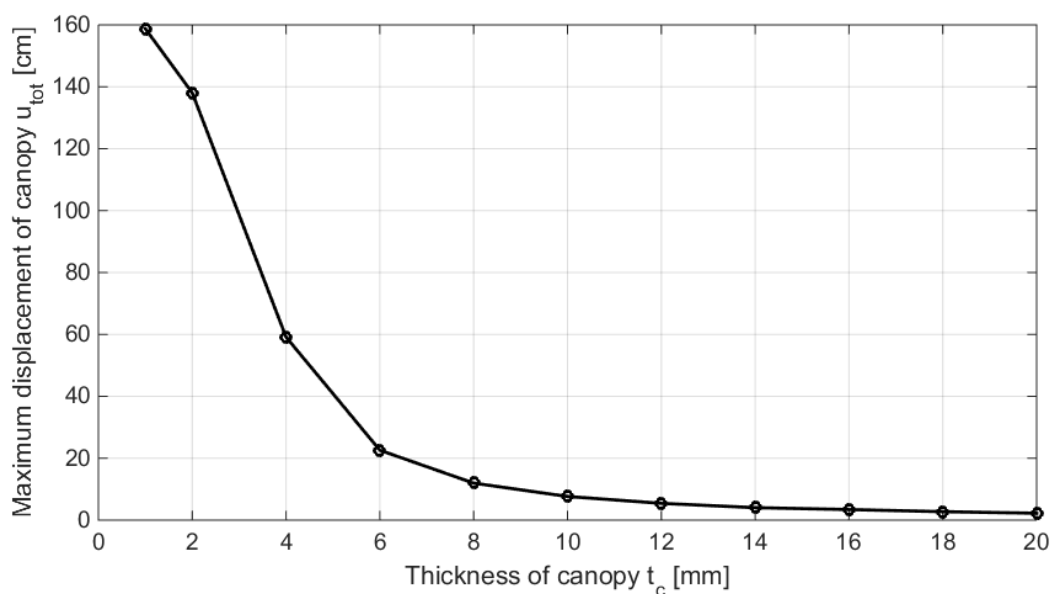


Figure 6-24: Influence of the thickness of the canopy on the displacement of the canopy

For a canopy thinner than 6mm, plastic deformation is developed at the canopy plate, especially at the connection edge between the canopy and the gabion wall. Since no erosion criterion is implemented in the strength model of the canopy (Section 4.1.1.3), the canopy with 1mm thickness can reach a maximum displacement of 158.78cm. However, in practice, before the canopy reaches this maximum displacement, it may have already sustained a certain degree of damage or even been completely destroyed, since the plastic rotation (64.7°) significantly exceeds the recommended rotation limit (12°) for structural steel plates under the protection category of preventing structural elements from collapse (*Mays and Smith 1995*).

### 6.3.5.2 Angle of inclination of the canopy

Two angles of inclination of the canopy, i.e.  $\alpha = 45^\circ$  and  $\alpha = 135^\circ$ , have already been analysed in Section 6.3.4 because they have been tested. As already mentioned in Section 6.3.4.6, the horizontal flow does not affect the blast load distribution behind the wall, if the wall width is sufficiently larger. Under such circumstances, the analysis might be simplified to a two-dimensional (2D) simulation using the axial symmetry. In order to determine the optimal angle of inclination, by which the blast wall offers the maximum overpressure and impulse reduction,

a comprehensive 2D parametric study is conducted, in which the wall width is assumed to be infinite.

The angle of inclination  $\alpha$  of the canopy is defined as illustrated in Figure 5-3. In total, 37 different angles of inclination are taken into consideration, which vary from  $0^\circ$  to  $180^\circ$  with an increment of  $5^\circ$ . The length of the canopy  $l_c$  remains 0.75m and all the other parameters are kept the same as in Section 6.3.4. Figure 6-25 illustrates the overpressure and impulse reduction factors at gauges pr1 - pr4 versus the angle of inclination  $\alpha$  of the canopy.

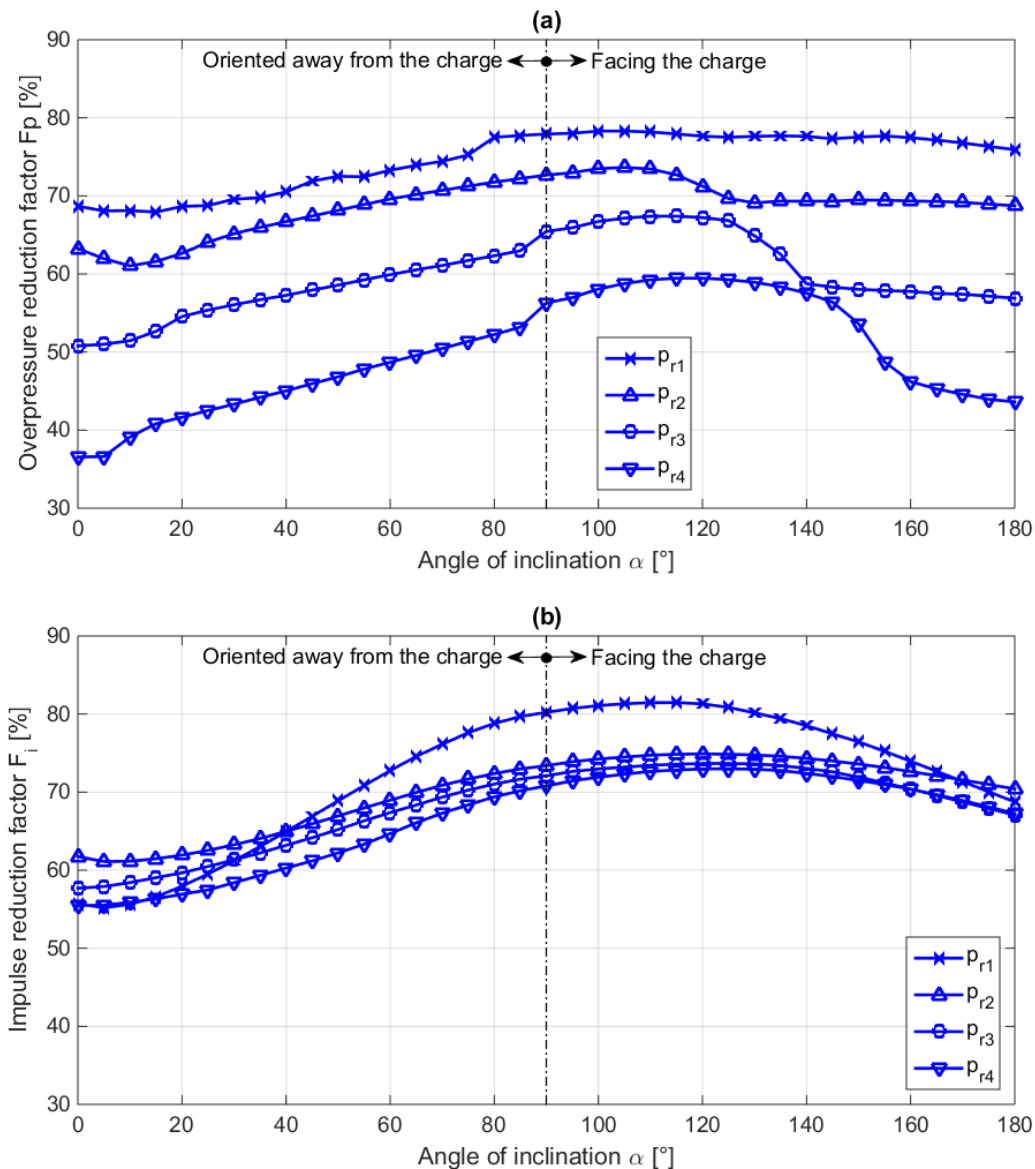


Figure 6-25: Overpressure and impulse reduction factors versus angle of inclination of canopy

If the angle of inclination with respect to the horizontal is the same, i.e.  $\alpha$  or  $180^\circ - \alpha$ , such as configuration M1 (GWC back) and M3 (GWC front), a canopy facing the charge is more efficient in shock wave attenuation than oriented away from the charge. The optimal angle of inclination, at which the canopy achieves the best performance in shock wave attenuation, lies between  $105^\circ$  and  $120^\circ$  for the overpressure reduction and lies between  $115^\circ$  and  $125^\circ$  for the impulse reduction (Figure 6-25).

It is worth mentioning that the effective height of the blast wall varies with the angle of inclination of the canopy. The effective height  $h_{eff}$  of the blast wall is defined as the height of the gabion wall ( $H = 2\text{m}$ ) plus the vertical projection of the canopy length ( $l_c \sin \alpha$ , Figure 5-3) as

$$h_{eff} = H + l_c \sin \alpha . \quad (6-5)$$

Thus, the effective height of the blast wall varies from 2m ( $\alpha = 0^\circ$ ) to 2.75m ( $\alpha = 90^\circ$ ). For illustrative purposes, the overpressure and impulse reduction factors at gauges pr1 - pr4 are plotted versus the effective height of the blast wall (Figure 6-26 and Figure 6-27).

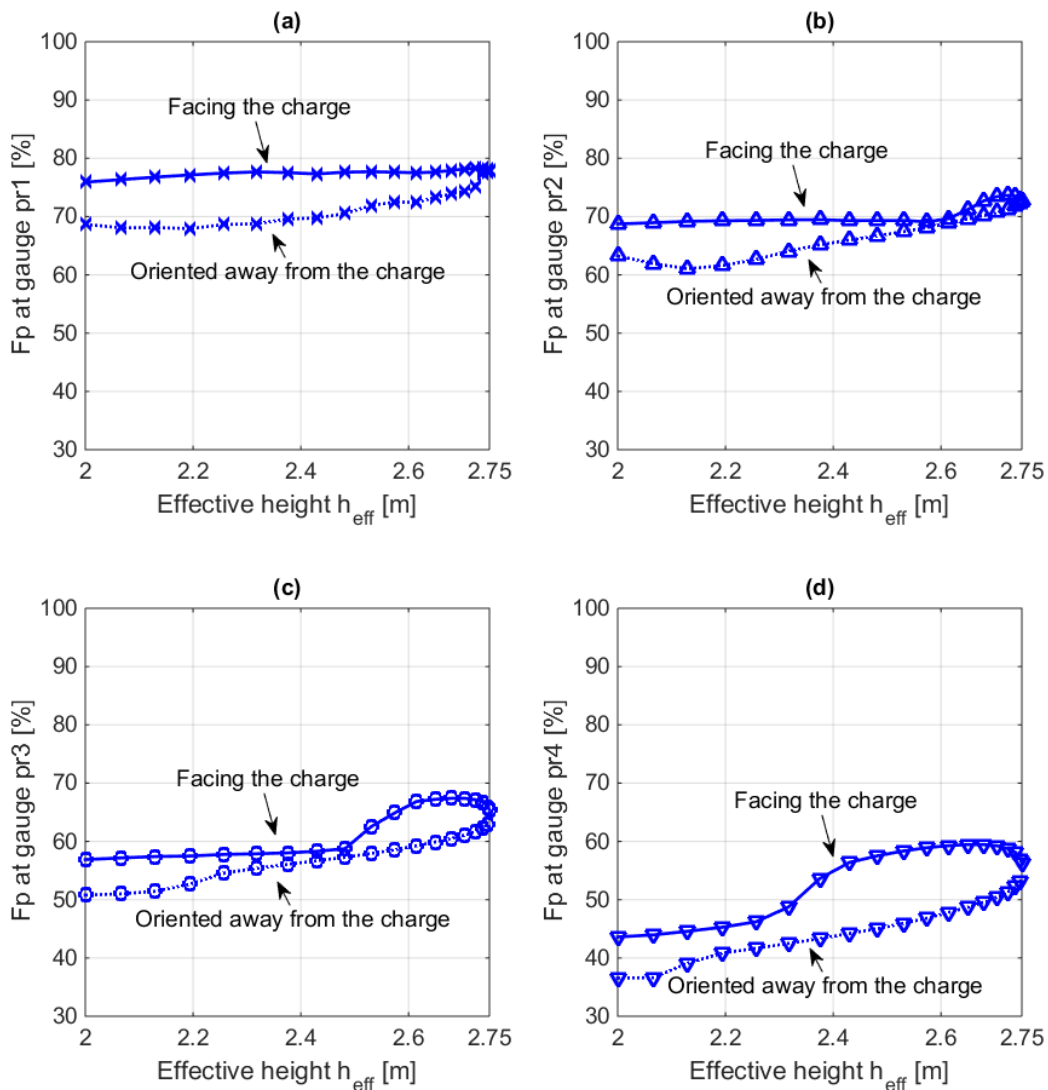


Figure 6-26: Overpressure reduction factors versus effective height of the blast wall (a) pr1; (b) pr2; (c) pr3; (d) pr4

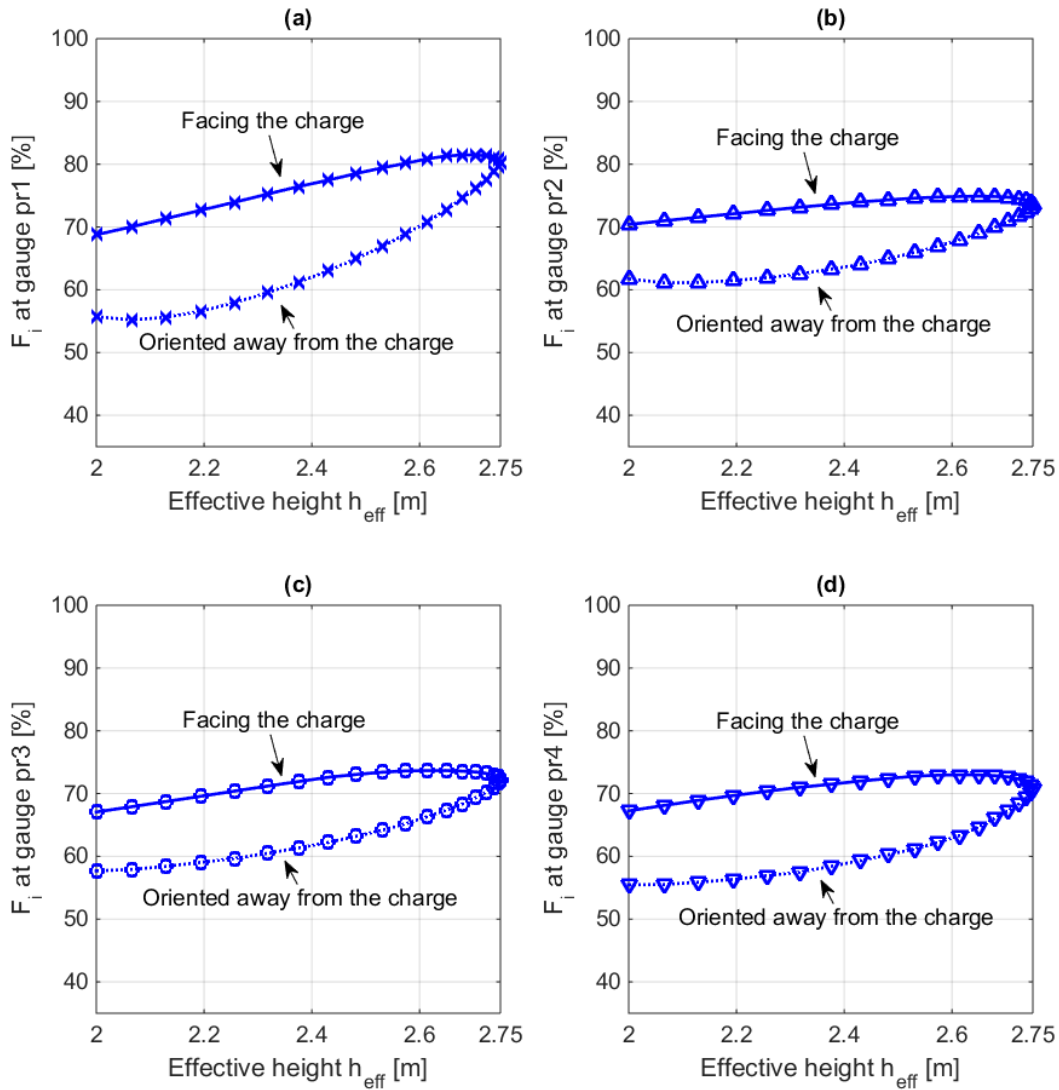


Figure 6-27: Impulse reduction factors versus effective height of the blast wall (a) pr1; (b) pr2; (c) pr3; (d) pr4

For a certain effective height (e.g. 2.19m), two angles of inclination ( $15^\circ$  and  $165^\circ$ ) of the canopy are assigned, which represent the cases oriented away from the charge and facing the charge, respectively. It is obvious that a canopy facing the charge is more efficient in shock wave attenuation than oriented away from the charge (Figure 6-26 and Figure 6-27). Regarding the canopies facing the charge, the effective height of the blast wall has almost no influence on the overpressure reduction at gauge pr1 (Figure 6-26a). A significant rise in the overpressure reduction factors at gauges pr2 - pr4 can only be found from a certain value of the effective height of the blast wall, i.e. 2.62m ( $\alpha = 125^\circ$ ) at gauge pr2 (Figure 6-26b), 2.48m ( $\alpha = 140^\circ$ ) at gauge pr3 (Figure 6-26c) and 2.26m ( $\alpha = 160^\circ$ ) at gauge pr4 (Figure 6-26d). This means that the canopy can only provide an additional contribution to the overpressure reduction, if the effective height of the blast wall exceeds a certain value (e.g. 2.62m at gauge pr2). If the canopies facing the charge are concerned, the impulse reduction increases linearly with the effective height of the blast wall until the canopy has reached the optimal angle of inclination, after then the impulse reduction decreases slightly with the effective height of the blast wall (Figure 6-27). It is worth mentioning that the maximum overpressure and impulse reduction

factors at gauges pr1 - pr4 are not achieved by an angle of inclination of  $90^\circ$ , which provides the maximum effective height of the blast wall, but achieved by the aforementioned optimal angles of inclination. In this sense, the blast walls having an inclined canopy can perform better in shock wave attenuation than the ones having a straight front face ( $\alpha = 90^\circ$ ).

In summary, regarding blast walls having infinite width, the optimal angle of inclination of the canopy lies between  $105^\circ$  and  $120^\circ$  for the overpressure reduction and lies between  $115^\circ$  and  $125^\circ$  for the impulse reduction.

### 6.3.6 Conclusions: blast walls with a canopy on top

In this section, numerical investigations were conducted to predict the blast loads behind blast walls, in which a canopy may be attached at the top of the gabion wall. The numerical models were validated against the experimental data (Section 5.1). Accounting for the flexibility of the deformable canopies, the peak overpressures at the facade are increased by up to 8.6% in configuration M1 (GWC back) and by up to 3.5% in configuration M3 (GWC front). This reveals that in these case studies the rigid canopy assumption is appropriate.

Due to the small width (2m) of the blast wall according to the experimental set-up, besides the vertical air flow over the top of the wall, the horizontal air flow around the sides of the blast wall plays a great role in the overpressure distribution behind the wall. In practice, however, the blast walls are erected around the buildings to be protected (perimeter walls). Under such circumstances, no horizontal air flow occurs around the sides of the wall. Using the validated numerical models, investigations on the blast walls having significantly larger width (denoted as infinite wall width) are carried out. For the experimental set-up (charge mass  $W = 5\text{kg}$  TNT equivalent, distance from the charge to the wall  $R_1 = 5\text{m}$  and distance from the building to the wall  $R_2 = 4\text{m}$ ), the infinite wall width assumption is valid if the ratio  $L/(2H)$  is larger than 1.75. It is indicated that configuration M3 (GWC front) shows the best performance in shock wave attenuation for all configurations studied here. It offers an overpressure reduction ranging from 51.7% to 88.0% and an impulse reduction ranging from 30.5% to 59.2% at the gauges employed in the experiments, compared to a free field scenario.

In addition, the following observations arise from the parametric studies conducted using the validated numerical models:

- It is necessary to perform a coupled FSI analysis between the shock wave and the canopy when the thickness of the canopy is relatively small, whilst if the canopy is thicker than a critical value (6mm in this paper), the canopy can be regarded as a rigid structure.
- Regarding blast walls having an infinite width, the optimal angle of inclination of the canopy lies between  $105^\circ$  and  $120^\circ$  (facing the charge) for the overpressure reduction and between  $115^\circ$  and  $125^\circ$  (facing the charge) for the impulse reduction at the gauges employed in the experiments.

## 6.4 Protective barriers made of steel posts

This section presents numerical investigations of the shock wave attenuation effect of protective barriers made of steel posts having a hollow cross-section. The shock wave propagation and its interaction with the protective barriers (steel posts and frame) are performed applying the software LS-DYNA in order to calculate the blast load distribution. The peak overpressures and maximum impulses are determined by analysing the overpressure-time histories. The numerical models are validated against the experimental data shown in Section 5.2. Furthermore, after validation, parametric studies are carried out in order to investigate the influence of further parameters on the overpressure and impulse reduction behind the barriers, i.e. the number of posts or the spacing between posts, the cross-sectional shapes of posts, and the arrangement of posts (single-layer or multi-layer, aligned or staggered). These studies serve as an attempt to obtain a better understanding of the behaviour of shock waves interacting with protective barriers made of steel posts.

### 6.4.1 Numerical models of protective barriers made of steel posts

As mentioned in Section 6.3.1, the combined method LBE / ALE (Section 4.2.3) is used in this Dissertation to model the shock wave propagation. Figure 6-28a illustrates a sketch of the numerical model used in Section 6.4. The air domain modelled in the numerical simulations has a length of 6.84m and a height of 4.5m. The width of the air domain is set to be 4m based on a parametric study. This study employs the reference configuration Mref (no posts, Figure 5-13a) to explore the influence of the width of the air domain in the numerical models on the blast loads behind the barrier. It is observed that there is no appreciable difference in the results obtained from widths between 4m and 10m. Therefore, an air domain width of 4m is employed for the studies in Section 6.4.

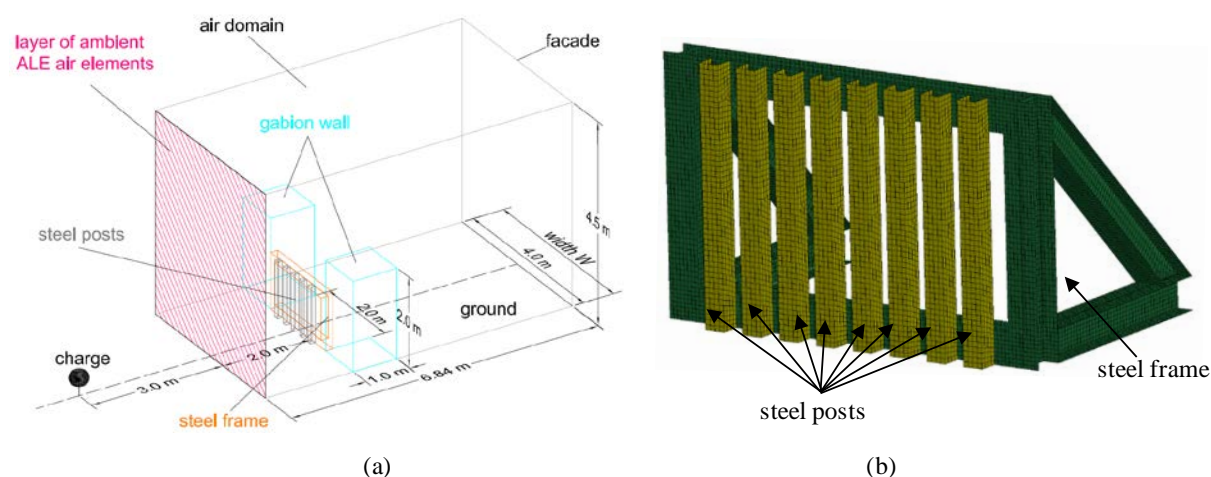


Figure 6-28: Numerical model (a) sketch of the total model; (b) FE-mesh of the steel posts and the steel frame (Xiao *et al.* 2017a and Xiao *et al.* 2018d)

As described in Section 4.1.1.1, the air is modelled via \*MAT\_NULL (LSTC 2017) and regarded as an ideal gas with a linear polynomial Equation of State (EoS). The front face of the air domain is specified as an ambient layer to receive the information of the empirically derived blast loads. The bottom and rear faces of the air volume are used to represent the ground surface

and the building envelope, respectively. They are viewed as ideally reflecting surfaces, which are somewhat stronger than in the conducted experiments (*Gebbeken 2017*). Their nodes are constrained in the normal direction. Non-reflecting boundary conditions are applied to the remaining exterior surface of the air volume. The gabion walls are regarded as rigid bodies. In lieu of explicitly modelling the walls, appropriate boundary conditions are imposed on the nodes of their exterior surfaces, i.e. the motion in the normal direction is constrained. The steel posts and the steel frame are discretized by Lagrangian shell elements (Figure 6-28b) and they are modelled with two assumptions: firstly as a rigid structure (Sections 6.4.2, 6.4.3 and 6.4.5 and Subsections 6.4.4.1 - 6.4.4.4), secondly as a flexible structure (Subsection 6.4.4.5). The influence of structural flexibility on the blast loads is explored in Subsection 6.4.4.5. In the remaining subsections, the structure is assumed to be rigid. The rigid strength model is specified via \*MAT\_RIGID (*LSTC 2017*) to the steel posts and the steel frame. The flexible material is modelled via \*MAT\_PLASTIC\_KINEMATIC (*LSTC 2017*), which is a rate-sensitive, elastic-plastic bilinear material with von Mises yield criterion. Strain rate effects are taken into consideration based on the Cowper-Symonds model. The material parameters of the steel posts and frame are assumed to be the same as those of the canopy (Table 4-3).

Using the Fluid-Structure-Interaction (Section 4.1.5), the shock wave and the barrier are coupled in the analysis. The coupling algorithm \*CONSTRAINED\_LAGRANGE\_IN\_SOLID (*LSTC 2017*) utilizes the ALE air mesh to derive the dynamic forces on the steel posts and the steel frame. Meanwhile, the steel posts and the steel frame provide a dynamic constraint to the shock wave propagating through the air domain.

### 6.4.2 Mesh convergence study and model verification

To determine a reasonable mesh density for the air domain, a mesh convergence study based on the free field scenario is conducted analogous to Section 6.3.2. In an attempt to examine the effect of varying the mesh density on the numerical results, the peak side-on overpressures at gauges ps1 - ps4 and the peak reflected overpressures at gauges pr1 - pr4 are selected as reference quantities for comparison. As already mentioned in Section 5.2.3, the gauge locations and elevations in the experiments of protective barriers made of steel posts (Figure 5-12) are somewhat different to those in the experiments of blast walls with a canopy on top (Figure 5-1). Based on the mesh convergence study and on the verification of the numerical results to the empirical results calculated by ConWep, the mesh size of 2.5cm (*Xiao et al. 2018b*) is selected to carry out the numerical simulations in the following subsections.

### 6.4.3 Model validation

As described in Section 6.1, an atmospheric pressure of 83.68kPa and an ambient air density of 1.022kg/m<sup>3</sup> are employed for the numerical simulations in Sections 6.4.3 and 6.4.4, which represent the ambient conditions at the test site of the Bundeswehr Technical Center for Protective and Special Technologies (WTD52) in Germany and at the average temperature (12.1°C) on 11<sup>th</sup> August 2016 between 9 and 15 o'clock.

For the purpose of validation of the numerical models, the reference configuration Mref (no posts, Figure 5-13a) is employed, in which the steel frame is solely present and no posts are attached to it. The side-on and reflected overpressure-time histories at respective gauges were

captured in the experiments, from which the peak side-on and reflected overpressures are evaluated. They are used to validate the numerical model with the reference configuration Mref (no posts). Figure 6-29 compares the peak side-on and reflected overpressures for the reference configuration Mref (no posts) which are obtained from experiments and from LS-DYNA. It can be seen that the experimental and numerical results are in reasonable agreement with each other, especially when the standard deviations  $\sigma$  of the experimental data are taken into account (Figure 6-29). The circles denote the mean values ( $\mu$ ). The lower bound ( $\mu - \sigma$ ) and the upper bound ( $\mu + \sigma$ ) are also marked in the graph, which represent the confidence interval of the experimental results. It is noticeable that, for the peak side-on overpressure at gauge ps1, the numerical value is 19.2% less than the mean value of experimental results. As observed from the experimental results, the coefficient of variation at gauges ps1 is rather large ( $\vartheta = 0.172$ , Table 5-6). This is most likely due to the influence of the cauliflower effect, in which the detonation products have not been completely burnt out. As the distance from the charge to the gauge increases, the influence of this effect decreases.

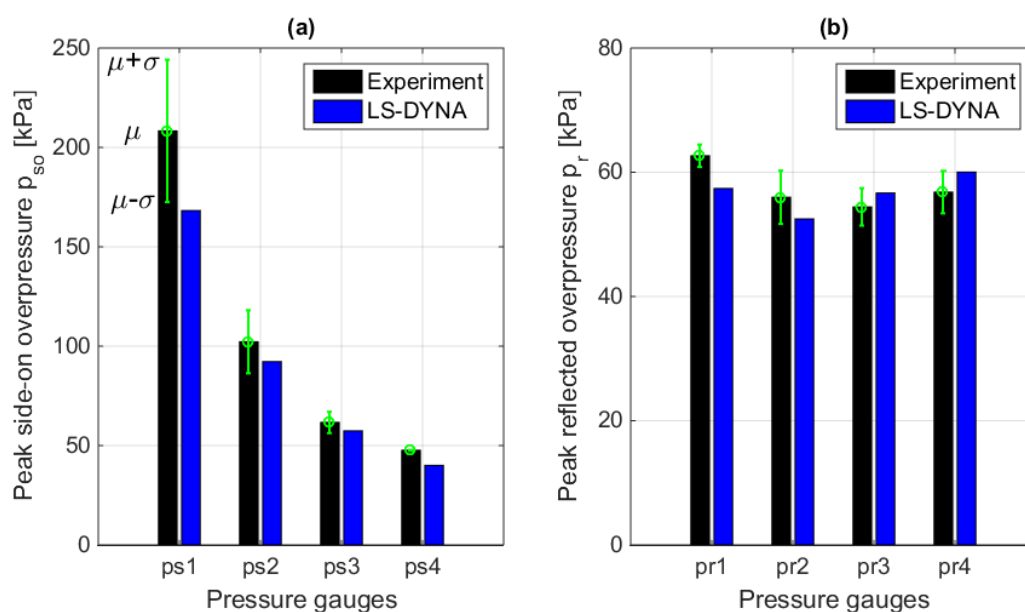


Figure 6-29: Configuration Mref (no posts) (a) peak side-on overpressures; (b) peak reflected overpressures

In general, the numerical values are less than the experimental mean values, except for gauges pr3 and pr4. The underestimations of the numerical results at gauges ps1 - ps4 and pr1 - pr2 are attributed to the fact that the proposed numerical approach neglects the influence of the Mach stem formation, which reduces the overpressures at the gauges by 0.9% - 9.4% (Section 6.2). Furthermore, the influence of the Mach stem formation diminishes as the distance from the charge to the gauge increases. The overestimations of the numerical results at gauges pr3 and pr4 are due to the simplification in the numerical model, i.e. gauges pr3 - pr4 are directly mounted on the building envelope, which represents an ideally reflecting surface and has a height of 4.5m. In the experiments, the gauges are mounted on wooden plates, which are of finite dimensions (0.4m x 0.4m) and attached to a post. This post is fixed to the massive wall at the centreline. The massive wall has a height of 2m (Figure 5-15b). In the numerical simulation, as the shock wave impinges gauge pr1, it is partly reflected. Another part of the

shock wave travels upwards along the building envelop and then successively impinges gauges pr2, pr3 and pr4. In the experiments, due to the low height of the massive wall (Figure 5-15b), a part of the shock wave has already flowed over the top of the massive wall before it impinges the gauges pr3 and pr4. Therefore, the mean values of the experimental peak reflected overpressures at gauges pr3 and pr4 are somewhat less than the numerical values.

After validation for the reference configuration Mref (no posts), this numerical approach can be analogously applied to configurations M1 ( $n_{post} = 8$ ), M2 ( $n_{post} = 5$ ) and M3 ( $n_{post} = 6$ ) for the individual experimental set-ups.

### 6.4.4 Numerical results

Using the numerical model described in Section 6.4.1, the side-on and reflected overpressure-time histories at the gauges employed in the experiments can be calculated. The steel posts and the steel frame are considered as rigid structures in Subsections 6.4.4.1 - 6.4.4.4, whereas they are modelled as flexible structures in Subsection 6.4.4.5, in which the influence of the structural flexibility on the blast loads is investigated.

#### 6.4.4.1 Overpressure reduction by the steel frame and the gabion walls

The steel frame was employed in the experiments to hold the steel posts that act as barriers. The effect of the steel frame and the gabion walls at its sides should be examined prior to investigating the configurations with steel posts. Three different models are taken into consideration in this section. The first model is in accordance with the reference configuration Mref (no posts), which consists of a steel frame construction in the middle and a gabion wall at each side (GW&SF, Figure 6-30). In the second model (GW, Figure 6-30), no steel frame but gabion walls are present. The last model (Free field, Figure 6-30) represents a free field scenario, where neither the steel frame nor the gabion walls are present. The shock wave propagation in the free field scenario is predicted using the numerical approach described in Section 6.4.1. The analysis is based on the ambient conditions at an altitude of 1585m and at an atmospheric temperature of 12.1°C.

The peak overpressures at gauges ps1 - ps4 and pr1 - pr4 are illustrated in Figure 6-30 for the three different models mentioned above. As anticipated in Section 5.2.4, there is no difference in the peak side-on overpressures at gauges ps1 between all three models. The effect due to the presence of gabion walls can be evaluated by comparing the values of the peak overpressures between the second model (GW) and the third model (Free field). No significant difference in the peak overpressures is observed at gauges ps2 and pr4 (Figure 6-30), which are closest and furthest to the rear side of the steel frame, respectively. The peak overpressures at gauges ps3 and ps4 are augmented by 1.3% and 10.5% (Figure 6-30a). This is attributed to the fact that the shock wave is disturbed to a certain extent by the presence of the gabion walls, as the shock wave flows around the sides of the gabion walls. Due to the presence of gabion walls, the peak overpressures at gauges pr1 - pr3 are reduced by 8.1 - 8.8% (Figure 6-30b).

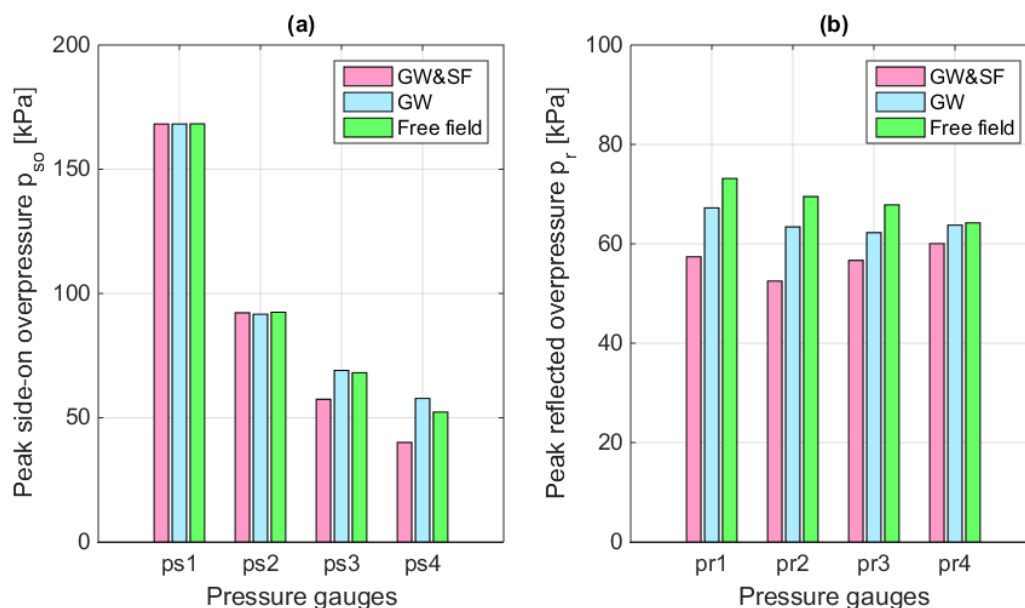


Figure 6-30: Comparison of the peak overpressures at three different numerical models, GW&SF represents the model that consists of a steel frame in the middle and a gabion wall at each side, GW represents the model that only consists of gabion walls, Free field represents a free field scenario (a) gauges ps1 - ps4; (b) gauges pr1 - pr4

The additional influence of the steel frame on the peak overpressures is explored by comparing the first model (GW&SF) to the second model (GW). Again, there is no significant difference in the peak side-on overpressures at gauges ps2. The peak overpressures at gauges ps3 and ps4 are reduced by 16.8% and 30.7% (Figure 6-30a), whilst a reduction in the peak reflected overpressure varying from 5.8% at gauge pr4 to 17.2% at gauge pr2 is observed (Figure 6-30b).

Comparing the first model (GW&SF) to the third model (Free field), the total effect of the steel frame and the gabion walls can be evaluated. No appreciable overpressure reduction is achieved at gauge ps2. The peak side-on overpressures are reduced by 15.7% at gauge ps3 and by 23.4% at gauge ps4. The reduction in the peak reflected overpressures, which varies from 6.5% at gauge pr4 to 24.5% at gauge pr2, is provided. It is worth mentioning that the overpressure reduction does not follow the trend that the overpressure reduction decreases as the distance behind the barrier increases, which can be concluded from a solid barrier (Xiao *et al.* 2017b). This is due to the fact that a part of the shock wave can directly pass the barrier through the openings containing in the steel frame (Figure 5-13a). Hence, the shielding effect behind the barrier is greatly altered compared to that behind a solid barrier.

#### 6.4.4.2 Overpressure-time history

Using the numerical model illustrated in Figure 6-28, the side-on and reflected overpressure-time histories can be calculated. The protective barriers consisting of steel posts and frame are considered to be rigid. The experimental and numerical results are compared in Figure 6-31 (side-on overpressures at gauges ps1 - ps4) and Figure 6-32 (reflected overpressures at gauges pr1 - pr4) for configuration M1 ( $n_{post} = 8$ ).

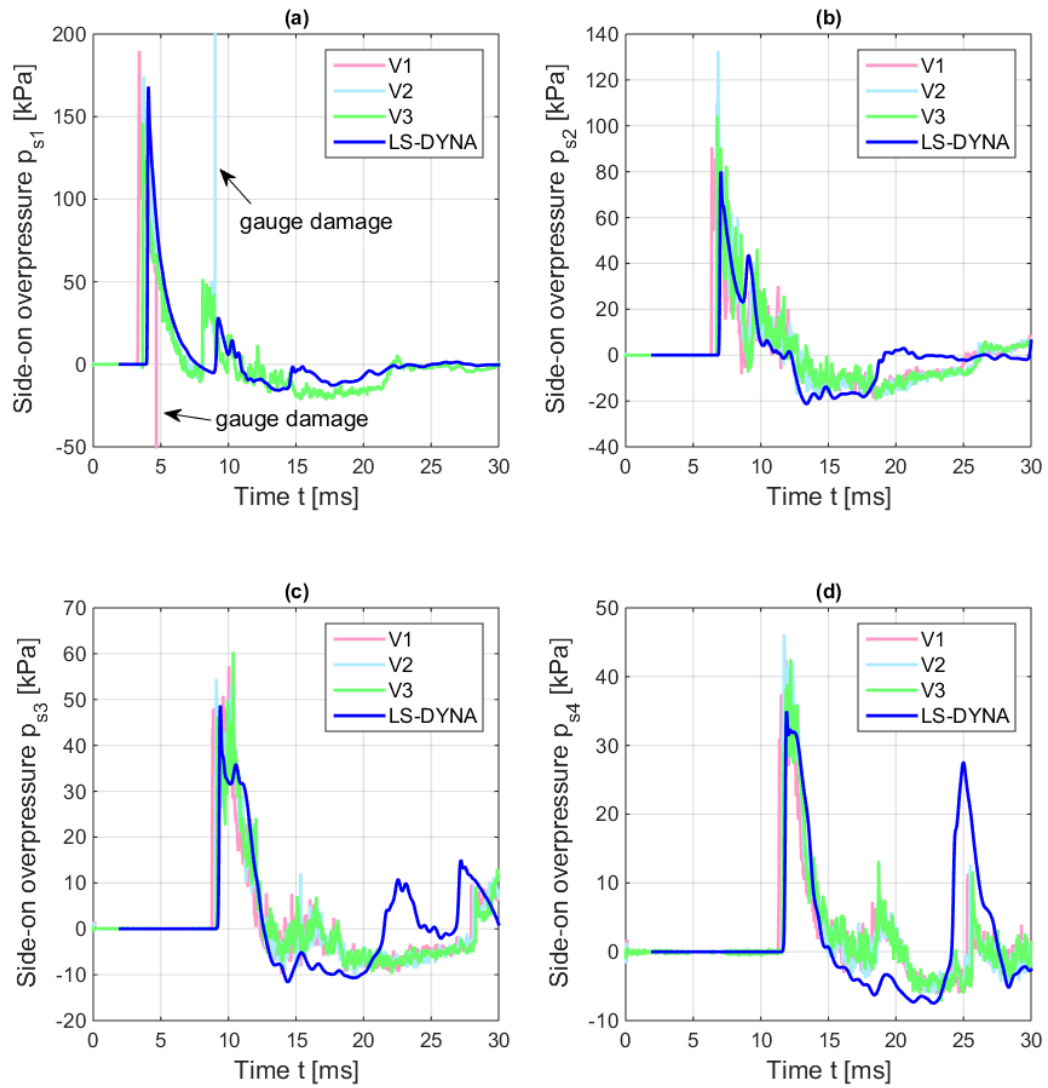


Figure 6-31: Side-on overpressure-time histories, configuration M1,  $n_{post} = 8$  (a) ps1; (b) ps2; (c) ps3; (d) ps4

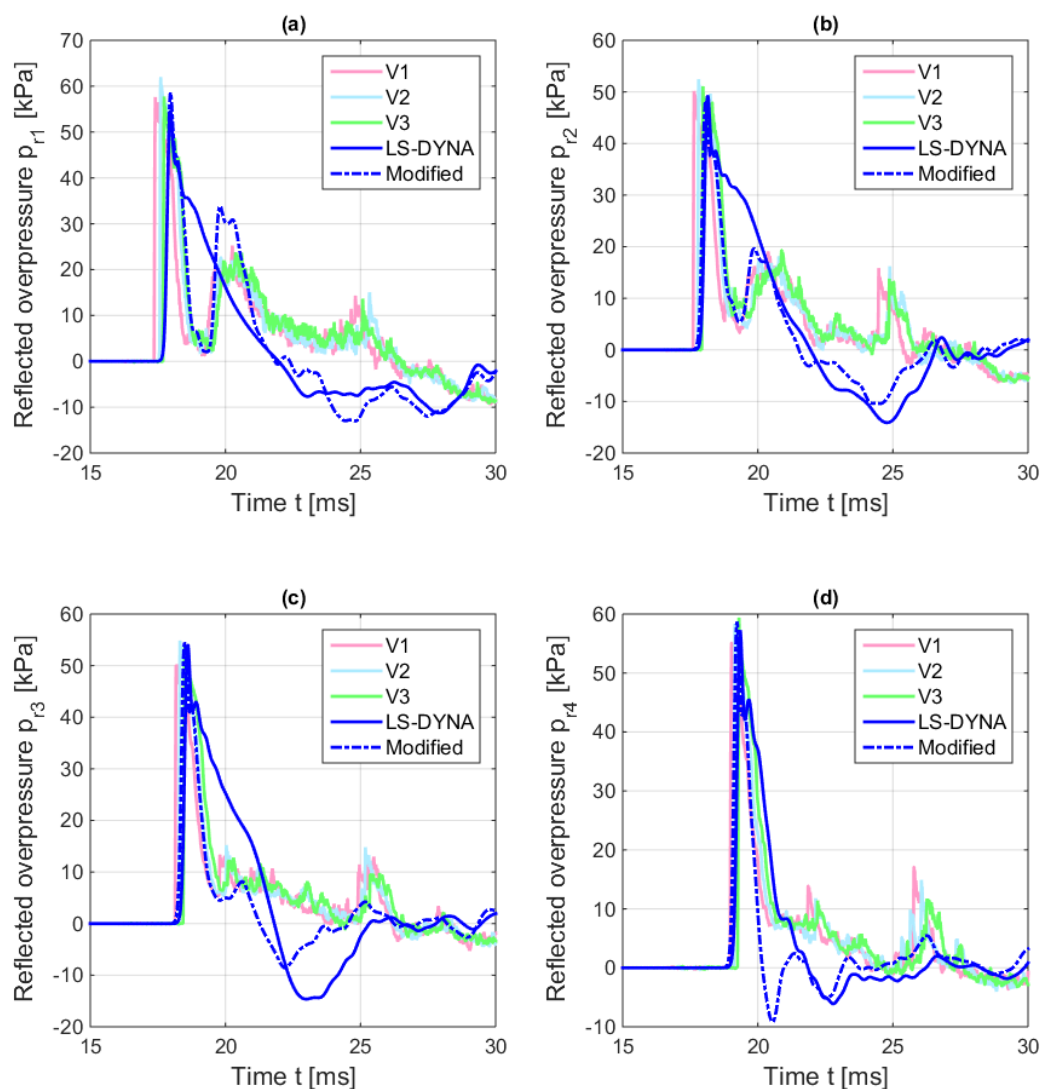


Figure 6-32: Reflected overpressure-time histories, configuration M1,  $n_{post} = 8$  (a) pr1; (b) pr2; (c) pr3; (d) pr4

The numerical model accurately predicts the overall side-on overpressure-time histories at gauges ps1 - ps4, compared to the overpressure recordings from the experiments (Figure 6-31). Due to unexpected damage to gauges, there are two abnormal histories captured at gauges ps1 during experiments V1 and V2 (Figure 6-31a). After the damage to gauges ps1, an instantaneous pressure drop and pressure rise appear in experiments V1 and V2, which are shown as vertical lines at  $t = 4.8\text{ms}$  (V1) and at  $t = 9.0\text{ms}$  (V2). For clarity, the range of the overpressures at gauges ps1 is limited between  $-50\text{kPa}$  and  $200\text{kPa}$ . As deduced from experiment V3, the incident shock wave had already arrived at this gauge at a time ( $t = 3.9\text{ms}$ ) earlier than the time when the gauges were damaged by the blast. Hence, the first peak overpressures at gauges ps1 in experiments V1 and V2 are still viewed as valid values. Together with other peak overpressures obtained from the experiments, they are used to calculate the mean value and the standard deviation of the peak overpressures at gauges ps1 (Table 5-6).

The peak side-on overpressure and the arrival time of the shock front at gauge ps1 are accurately predicted (Figure 6-31a), although the numerical approach predicts a slightly later arrival of the shock front at gauge ps1. The first peak in the numerical curve is caused by the arrival of the

shock front at that gauge, whereas the following peaks are related to the reflection of the shock wave from different posts in front of the steel frame construction. The experimental curves exhibit a somewhat more oscillatory behaviour in the reflection from posts, i.e. multiple peaks between  $t = 8.1\text{ms}$  and  $t = 8.9\text{ms}$ . For gauge ps2 (Figure 6-31b), the first peak generated by the numerical approach, i.e. at  $t = 7.1\text{ms}$ , is associated with the arrival of the shock front at that gauge, which is transmitted through the opening in the middle of the barrier (Figure 5-14). Subsequently, the transmitted wave merges with the wave flowing over the top of the barrier and gives rise to the peak at  $t = 9.2\text{ms}$ .

It is noticed that the experimental recordings at gauges ps2 - ps4 (Figure 6-31b, c and d) are much more oscillatory than the ones at gauges ps1 (Figure 6-31a). It is most likely due to the complicated flow pattern of the shock waves passing through the barrier consisting of posts (Figure 5-19). As the shock wave impinges the posts, the shock wave is partly reflected towards the charge, partly flows around the sides of posts and over the top of the barrier and the remaining part is transmitted directly through the openings between the posts. Behind the barrier, there are multiple diffracted waves around the sides of posts and multiple transmitted waves through the openings between the posts, which interact with each other. It results in a rather complicated flow pattern behind the barrier.

### 6.4.4.3 Clearing effect of shock waves around wooden plates

In order to visualize the entire relevant reflected overpressure-time histories, the time axes in Figure 6-32 start at 15ms and extend to 30ms, which are different to the ones in Figure 6-31. As observed in Figure 6-32 (solid blue lines), the first peaks and the arrival time of the shock front at gauges pr1 - pr4 are accurately predicted by the numerical model (Figure 6-28). However, the decay after the first peak and the subsequent peaks are not appropriately represented. It is attributed to the simplification in the numerical model that gauges pr1 - pr4 are directly mounted on the building envelope, which represents an ideally reflecting surface and has a height of 4.5m. In fact, the gauges are mounted on wooden plates, which are of finite dimensions (0.4m x 0.4m, Figure 5-4b) and placed 0.16m in front of the building envelope (Figure 5-4c). Moreover, the massive wall representing the building envelope has a height of 2m (Figure 5-15b). As explained in Section 5.1.3, the clearing effect will occur at gauges pr1 - pr4. Using the numerical model illustrated in Figure 6-28, however, the clearing effect cannot be modelled. In order to capture this effect, a modification of the numerical model needs to be made, i.e. the massive wall and the wooden plates to mount gauges pr1 - pr4 are considered. Based on the study made by *Gebbeken and Döge 2010b*, it seems adequate to apply rigid boundary conditions to represent the exterior surfaces of the massive wall and the wooden plates. Using the modified numerical model illustrated in Figure 6-33, the overpressure-time histories at gauges pr1 - pr4 for configuration M1 ( $n_{post} = 8$ ) are computed and also illustrated as dashed blue lines in Figure 6-32. It is found that the overpressures are “cleared” at all gauges, i.e. pr1 at  $t = 18.1\text{ms}$ , pr2 at  $t = 18.4\text{ms}$ , pr3 at  $t = 18.8\text{ms}$ , and pr4 at  $t = 19.4\text{ms}$ , respectively.

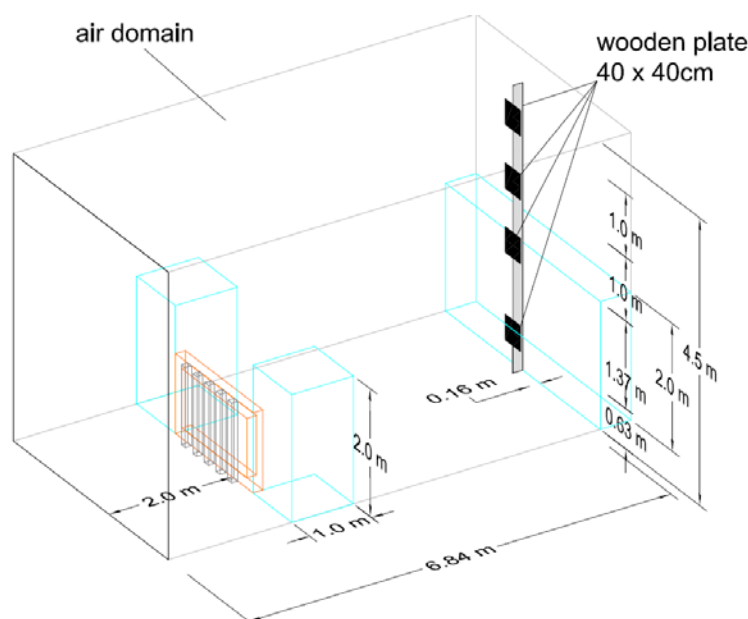


Figure 6-33: Sketch of the numerical model including wooden plates, M1 ( $n_{post} = 8$ )

As the shock wave impinges on the front face of the wooden plate to mount gauge pr1, the incident shock wave is partly reflected and partly diffracted around the free edges of the wooden plate. Due to the small distance (0.16m) between the wooden plates and the massive wall (Figure 5-4c), the diffracted wave is re-reflected from the massive wall and then impinges gauge pr1 once again. This phenomenon leads to the peak overpressures of about 20kPa between  $t = 19.6\text{ms}$  and  $t = 20.5\text{ms}$  in the experimental recordings (Figure 6-32a). The modified numerical model predicts larger values than the experiments. This is most likely due to the simplification in the numerical simulation, i.e. the influence of open porous surface of the massive wall is neglected. The same phenomenon as occurred at gauge pr1 can also be observed at gauge pr2 by the peak overpressures between  $t = 19.9\text{ms}$  and  $t = 21.0\text{ms}$  (Figure 6-32b). Due to the low height of the massive wall (2m, Figure 5-15b), the reflecting surface area behind the wooden plate to mount gauge pr2 is approximately 50% of that behind the wooden plate to mount gauge pr1. Therefore, the magnitude of the peak overpressures for gauge pr2 (due to the re-reflection from the massive wall) is somewhat less than that for gauge pr1. For gauges pr3 and pr4, the diffracted waves will not be re-reflected again, i.e. they will propagate undisturbed away from the rear face of the wooden plates. Hence, the aforementioned phenomenon does not occur at gauges pr3 and pr4.

However, there is still a considerable discrepancy between the results predicted by the modified numerical model and the experimental recordings, e.g. the negative phases in the numerical results are more pronounced than in the experimental results. It is most probably related to the finite air domain size constrained by the computational resources that are currently available at the chair.

#### 6.4.4.4 Shock wave propagation

Figure 6-34 presents some pressure contour plots at a horizontal plane located 0.63m above the ground for configuration M1 ( $n_{post} = 8$ ). As aforementioned, instead of explicitly modelling the gabion wall (plotted as large white squares in Figure 6-34), appropriate boundary conditions

are assigned to the exterior surfaces of the wall. Based on these contour plots, the shock wave propagation in the horizontal direction can be analysed.

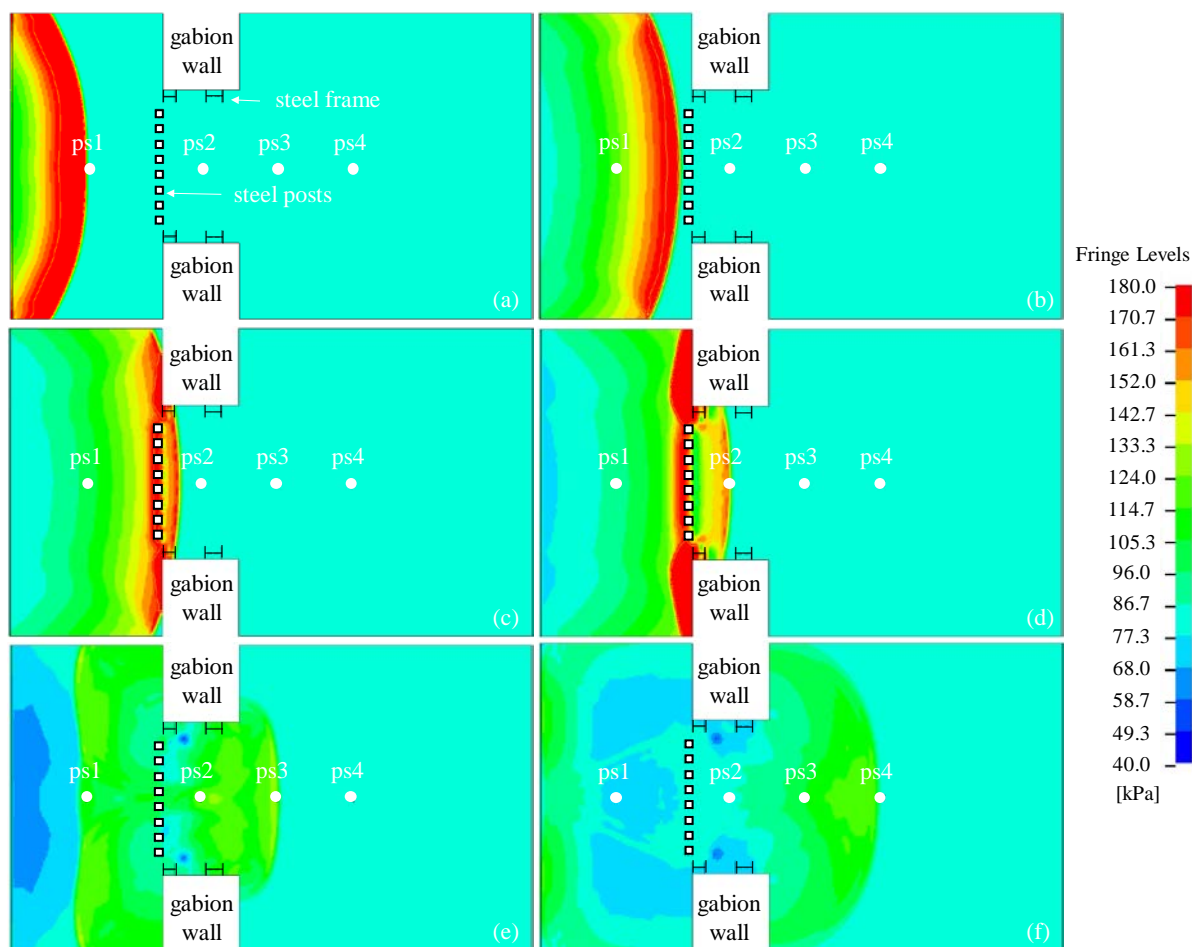


Figure 6-34: Pressure contour plots of a horizontal plane at an elevation of 0.63m above the ground, M1 ( $n_{post} = 8$ ), plan view (a)  $t = 4.0\text{ms}$ ; (b)  $t = 5.6\text{ms}$ ; (c)  $t = 6.4\text{ms}$ ; (d)  $t = 7.0\text{ms}$ ; (e)  $t = 9.4\text{ms}$ ; (f)  $t = 11.9\text{ms}$

A layer of ambient ALE air elements, at a distance of 2m from the barrier (Figure 6-28), is specified to receive the blast loads calculated by the empirical formulae of *Kingery and Bulmash 1984* (K&B). Using the hemi-spherically derived K&B-blast loads as input for the ambient ALE air elements, the shock wave propagation in the entire air domain of the numerical model can be effectively simulated. In the numerical model, the shock wave arrives at gauge ps1 at  $t = 4.0\text{ms}$  (Figure 6-34a). Once the shock wave impinges the barrier (Figure 6-34b and c), the shock wave is partly reflected back, partly transmitted through the openings between the posts and the remaining part flows around the sides of the posts and over the top of the barrier. At  $t = 6.4\text{ms}$  (Figure 6-34c), a rather complicated flow pattern is generated in the wake of the posts, where multiple waves interact, i.e. diffracted and transmitted waves from individual posts. At a later time  $t = 7.0\text{ms}$  (Figure 6-34d), the wave reaches gauge ps2, which is only 0.5m behind the rear face of the posts. Due to the interaction between multiple diffracted and transmitted waves behind the barrier, the results at that gauge are susceptible to even a very small variation in the experimental set-up, which leads to the large scatter in the experimental values of the peak overpressures ( $\vartheta = 0.196$ , Table 5-8). Subsequently, the shock wave arrives at gauges ps3

and ps4 at  $t = 9.4\text{ms}$  (Figure 6-34e) and  $t = 11.9\text{ms}$  (Figure 6-34f), respectively. Finally, it impinges the building envelope, from which the wave is reflected back towards the barrier.

#### 6.4.4.5 Structural flexibility

The protective barriers are composed of steel posts framed by a steel construction. To examine the influence of the structural flexibility on the blast load distribution behind the barriers, the numerical model using the flexible assumption is employed, in which the flexibility of the steel posts and the steel frame is accounted for in the numerical analysis. To assess the effect of the structural flexibility on the shock wave propagation, the difference in the peak overpressures based on the flexible ( $p_{flex}$ ) and rigid ( $p_{rigid}$ ) assumptions is calculated and then scaled by the values obtained from the rigid assumption as

$$\Delta = \frac{p_{flex} - p_{rigid}}{p_{rigid}} \cdot 100\% \quad (6-6)$$

Figure 6-35 illustrates the difference in the peak reflected overpressures based on the rigid and flexible assumptions for configurations M2 ( $n_{post} = 5$ ), M3 ( $n_{post} = 6$ ) and M1 ( $n_{post} = 8$ ), which are sorted in ascending order according to the number of posts. Taking into account the structural flexibility, the difference in the peak reflected overpressures is within  $\pm 5.0\%$ .

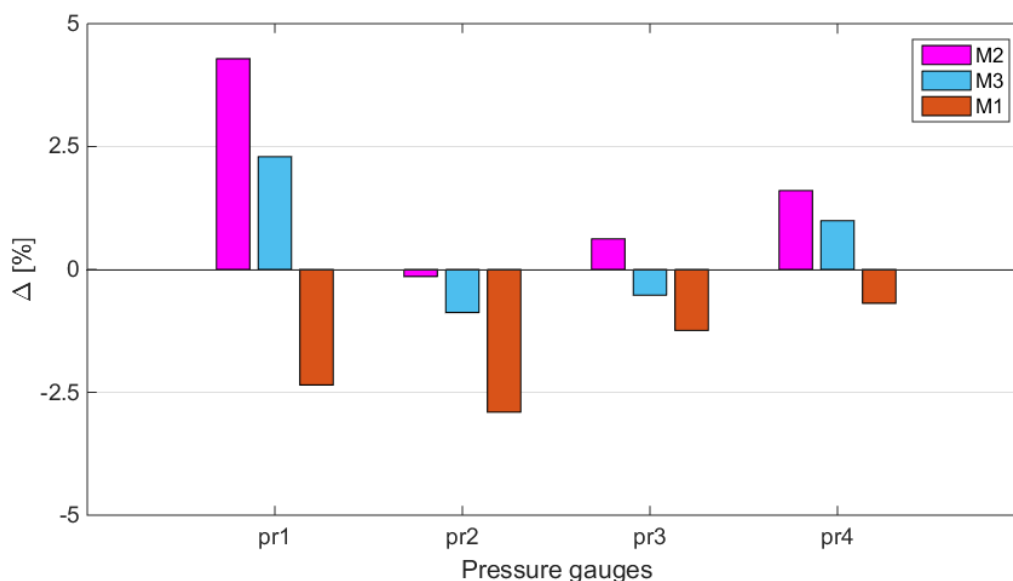


Figure 6-35: Influence of the structural flexibility on the peak reflected overpressures

In configuration M2 ( $n_{post} = 5$ ), larger values of peak overpressures are predicted by the numerical model using the flexible assumption than using the rigid assumption except at gauge pr2, where a slightly lower value of peak overpressure (-0.1%) is predicted by the numerical model using the flexible assumption than using the rigid assumption. As the number of posts increases, this effect diminishes or even an inverse effect emerges, e.g. in configuration M1 ( $n_{post} = 8$ ). The numerical model using the flexible assumption predicts slightly lower values of peak reflected overpressures than using the rigid assumption.

In summary, using the rigid and flexible assumption of barriers, the differences in the peak reflected overpressures at gauges pr1 - pr4 are less than 5.0% and are regarded as negligibly small. Therefore, it seems appropriate to apply the rigid assumption for the barriers in the numerical analyses. This assumption is adopted for the further analyses in the next sections.

#### 6.4.4.6 Overpressure and impulse reductions

Figure 6-36 shows the results of the overpressure and impulse reduction factors ( $F_p$  and  $F_i$ ) at gauges ps2 - ps4 and pr1 - pr4 for the three different steel post configurations.

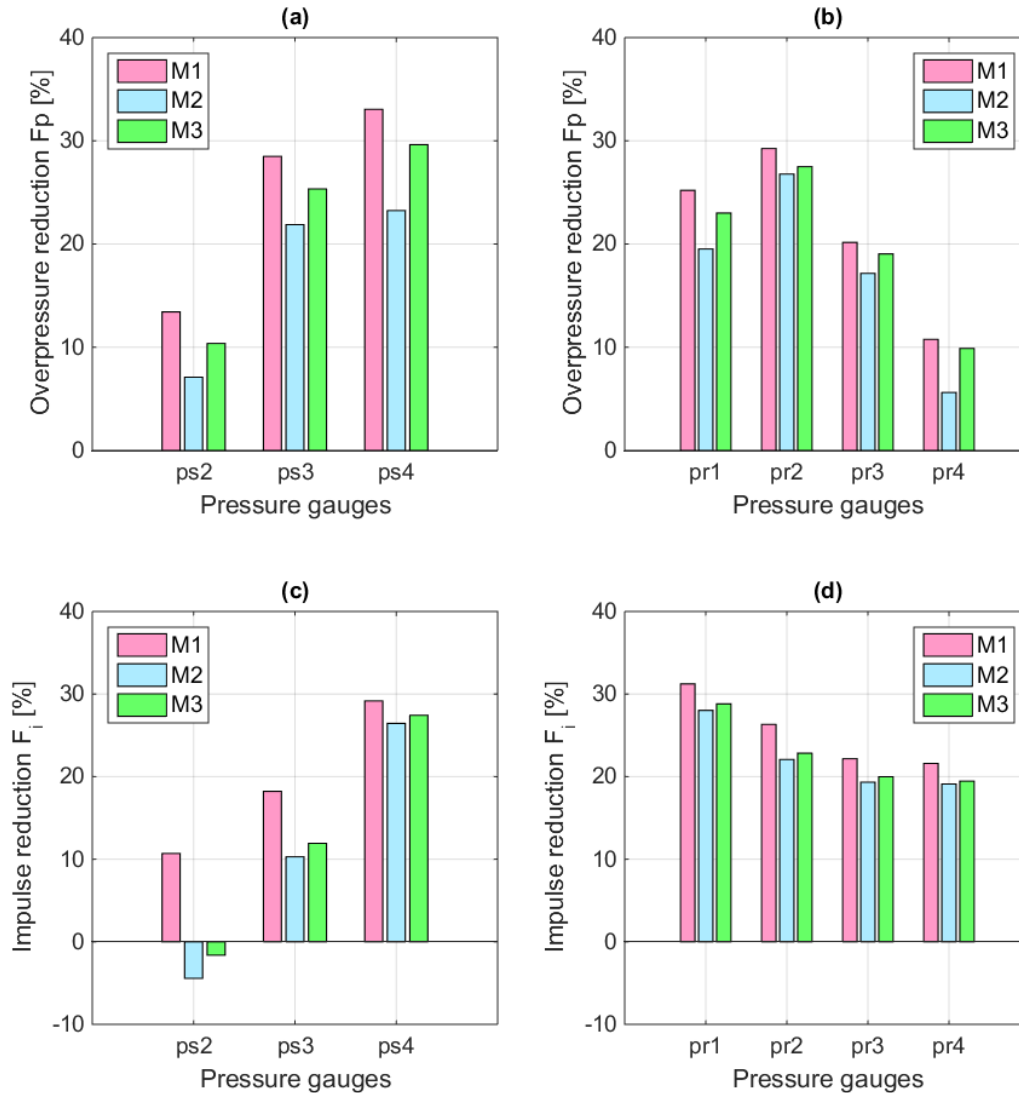


Figure 6-36: Overpressure and impulse reduction for the steel post configurations (a)  $F_p$  at gauges ps2 - ps4; (b)  $F_p$  at gauge pr1 - pr4; (c)  $F_i$  at gauges ps2 - ps4; (d)  $F_i$  at gauge pr1 - pr4

It is noticeable that the side-on impulses at gauges ps2 are slightly increased by 4.4% and 1.6% for configurations M2 ( $n_{post} = 5$ ) and M3 ( $n_{post} = 6$ ). This is most likely attributed to the superposition between the multiple diffracted waves around the sides of posts and the multiple transmitted waves through the openings between the posts. At gauges ps2, this superposition effect is more pronounced for impulse than overpressure. In addition, this superposition effect

prevails the shielding effect provided by the posts at gauges ps2 for configurations M2 ( $n_{post} = 5$ ) and M3 ( $n_{post} = 6$ ), which causes an impulse increase. The considered steel post configurations are sorted in descending order of shock wave attenuation performance as follows: M1 ( $n_{post} = 8$ ), M3 ( $n_{post} = 6$ ) and M2 ( $n_{post} = 5$ ).

In summary, configuration M1 ( $n_{post} = 8$ ) shows the best performance in shock wave attenuation. Compared to a free field scenario, it offers an overpressure reduction ranging from 10.8% to 33.0% and an impulse reduction ranging from 10.7% to 31.2% at the gauges employed in the experiments.

### 6.4.5 Parametric studies

The performance of protective barriers in attenuating the shock wave depends on various parameters, e.g. number of posts per length of the barrier, cross-sectional shapes of posts and arrangement of posts (single-layer or multi-layer, aligned or staggered). The influence of these parameters on the performance of barriers will be explored in Subsections 6.4.5.1 - 6.4.5.3. The remaining parameters are kept the same as the experimental set-up, i.e. charge mass ( $W = 5\text{kg}$  TNT equivalent), distance from the steel frame to the charge ( $R = 5\text{m}$ ) and locations of the gauges. It should be noted that the observations obtained from these parametric studies are only validated for the particular set of parameters involved in this section, i.e.  $W = 5\text{kg}$  TNT equivalent and  $R = 5\text{m}$ .

Usually, there are not so many buildings to be protected which are located at a relatively high altitude as considered in the previous sections (1585m). In order to obtain some findings for a general use, it seems more meaningful to consider the ambient conditions at mean sea level and at the standard temperature ( $15^\circ\text{C}$ ), which result in an atmospheric pressure of 101.325kPa and an ambient air density of  $1.225\text{kg/m}^3$ . These parameters are employed in the following subsections.

#### 6.4.5.1 Relative opening fraction (ROF)

In order to explore the influence of the number of posts  $n_{post}$  per length of the barrier on the shock wave attenuation behind a barrier consisting of steel posts with the same square cross-section as in the experiments (QRO 100mm x 100mm x 8mm), a parametric study based on a single-layer post arrangement is conducted. The number of posts  $n_{post}$  varies from 0 to 14, where  $n_{post} = 0$  represents the reference configuration Mref (no posts) in the experiments. As previously mentioned in Section 5.2.2, the relative opening fraction (ROF) is defined as the ratio of opening area to front face area of the barrier. A relative opening fraction of  $\text{ROF} = 100\%$  represents the reference configuration Mref (no posts) in the experiments, whilst a relative opening fraction of  $\text{ROF} = 0\%$  designates a barrier without any openings. Here, a 160mm thick reinforced concrete wall is selected for the barrier without openings. A symmetric post arrangement is assumed in this parametric study. This means that the arrangement of configurations M1 ( $n_{post} = 8$ ), M2 ( $n_{post} = 5$ ) and M3 ( $n_{post} = 6$ ) differs slightly from those in the experiments (Figure 5-14).

Figure 6-37 outlines the dependence of the overpressure and impulse reductions at gauges ps2 - ps4 and pr1 - pr4 on the relative opening fraction (ROF) of the barrier configurations. The reduction factors in overpressure  $F_p$  and impulse  $F_i$  are calculated by Eq. (6-3) and Eq. (6-4).

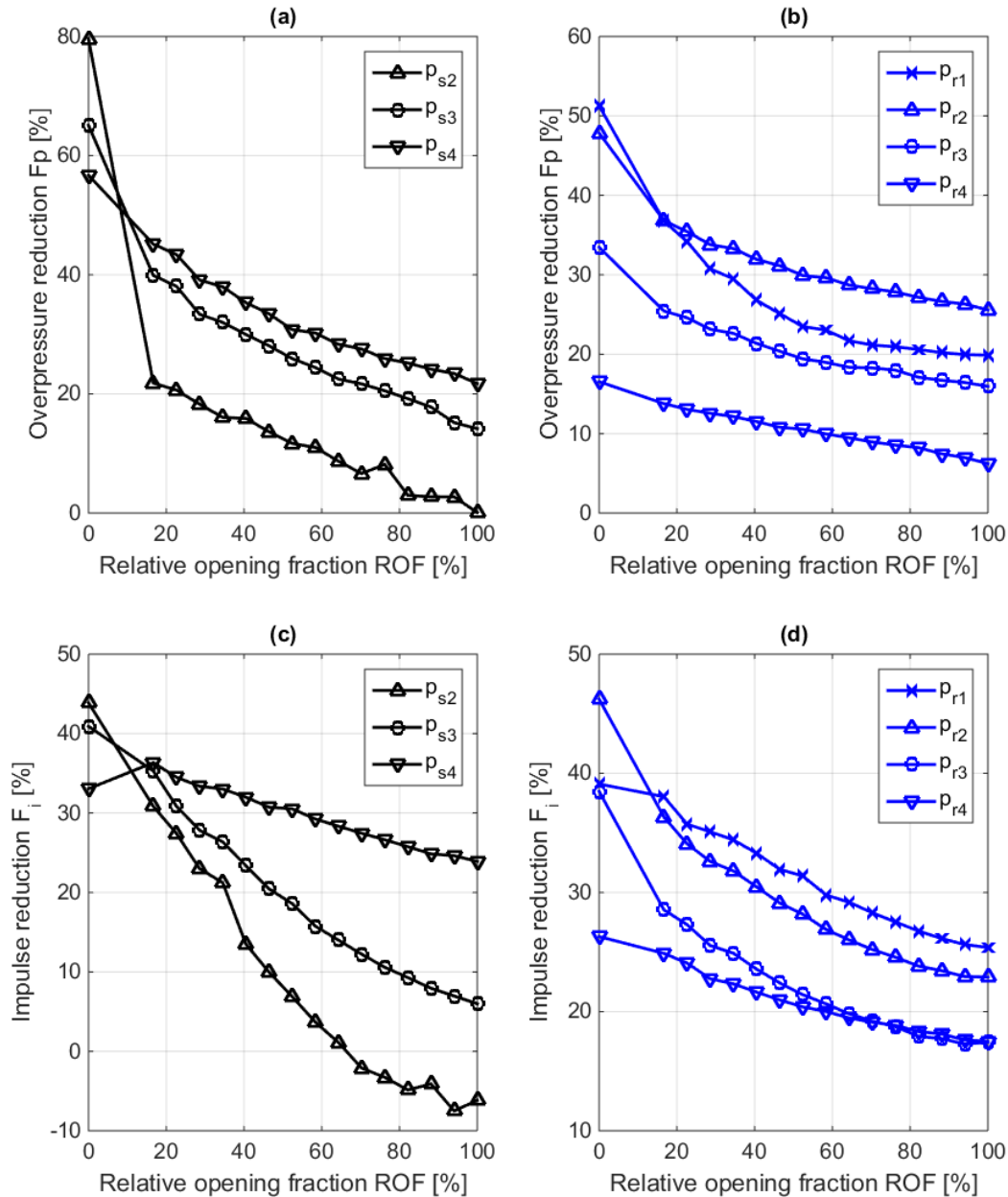


Figure 6-37: Influence of relative opening fraction on the overpressure and impulse reduction, square cross-section (a)  $F_p$  at gauges ps2 - ps4; (b)  $F_p$  at gauges pr1 - pr4; (c)  $F_i$  at gauges ps2 - ps4; (d)  $F_i$  at gauges pr1 - pr4

Generally, if the number of posts increases, which means that the relative opening fraction decreases, a larger overpressure and impulse reduction is expected. It is evident that an anomaly appears at gauge ps2 for  $F_p$  if four posts are mounted to the steel frame (ROF = 76.2%, Figure 6-37a). It is most likely due to the symmetric arrangement of the posts and the spacing between the posts (25cm in this case). As the waves flow around the sides of the two adjacent posts in the middle of the barrier and then arrive at that gauge, they cancel each other through their

interactions. This effect can also be observed if other cross-sectional shapes, e.g. circular or triangular, are used for the steel posts. In addition, this effect may be also related to the distances between the posts and the dimensions of the cross-section of the posts.

As already explained in Section 6.4.4.6, due to the fact the superposition effect of multiple waves behind the barrier prevails the shielding effect provided by the posts at gauge ps2, an impulse increase is observed if the ROF varies from 70.2% - 100% (Figure 6-37c). It is noticed that the barrier without openings (ROF = 0%) achieves a less impulse reduction at gauge ps4 than the barrier consisting of 14 steel posts (ROF = 16.7%, Figure 6-37c). This is most likely due to the fact that gauge ps4 behind the barrier without openings experiences two successive peaks in the overpressure-time history. As the wave flows over the top of the barrier, a part of it directly impinges gauge ps4, which causes the first peak. The second peak corresponds to the part of the wave reflected from the ground surface near gauge ps4. The second peak has a smaller value than the first one. However, it increases slightly the associated impulse.

In the ROF range from 16.7% to 100%, a nearly linear dependence of the overpressure and impulse reduction on the ROF is observed (Figure 6-37). In this range, adding one steel post to the arrangement causes an increase of 0.5% - 1.8% and 0.5% - 2.6% in the overpressure and impulse reduction factors. If the ROF varies from 0% to 16.7%, the overpressure and impulse reduction factors increase rapidly with a decrease in the ROF. However, such a close arrangement of the steel posts is no longer profitable from an economical viewpoint, compared to a barrier without openings.

### 6.4.5.2 Cross-sectional shape

In an attempt to explore the performance of protective barriers with different cross-sectional shapes, the square, circular, triangular I (vertex oriented away from the charge) and triangular II (vertex facing the charge) are considered (Figure 6-38). The flow direction of the shock wave is from left to right. For the sake of an easy comparison, the projected area of the non-square shapes normal to the direction of the shock wave propagation is selected to be the same as that of a square shape. Thus, the circular posts have a diameter of 100mm. The triangles are chosen to be equilateral with an edge length of 100mm.

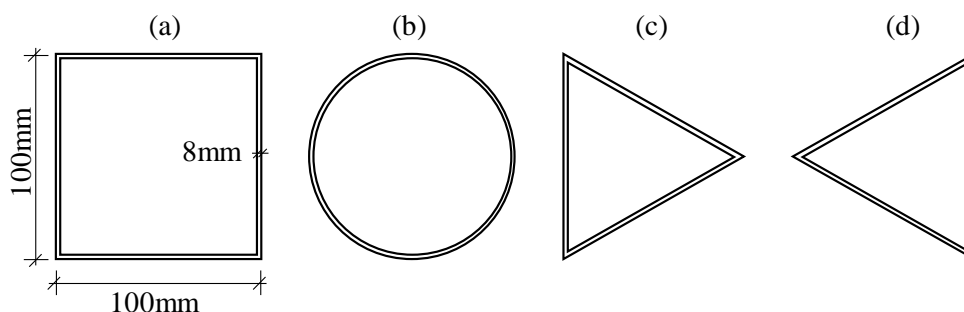


Figure 6-38: Cross-sectional shapes of the steel posts (a) square; (b) circular; (c) triangular I, vertex oriented away from the charge; (d) triangular II, vertex facing the charge

Figure 6-39 and Figure 6-40 compare the overpressure and impulse reductions at gauges ps4 (7.5m from the charge, 0.63m above the ground) and at gauges pr2 (9.84m from the charge, 2m above the ground) for the different cross-sectional shapes.

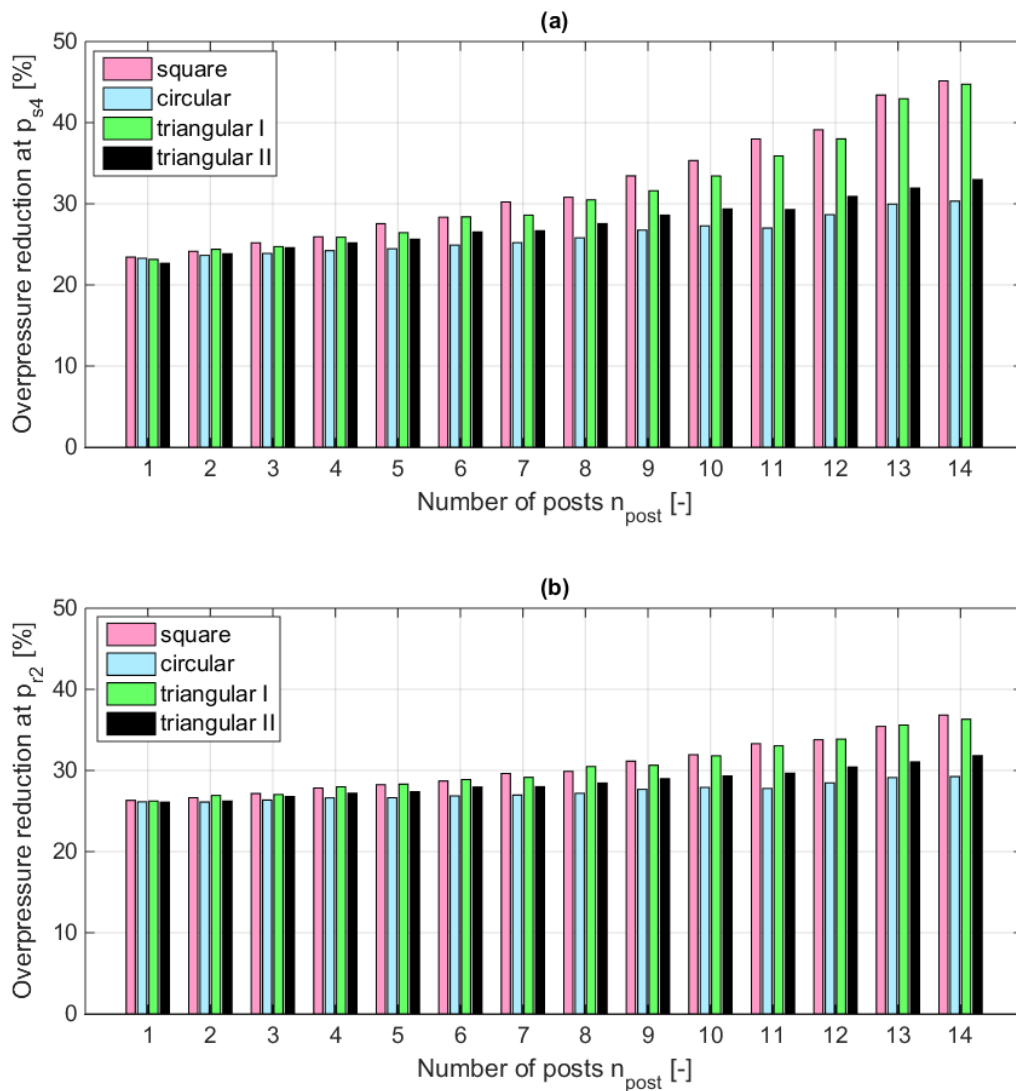


Figure 6-39: Overpressure reductions of different cross-sectional shapes, single-layer arrangement (a) gauge ps4; (b) gauge pr2

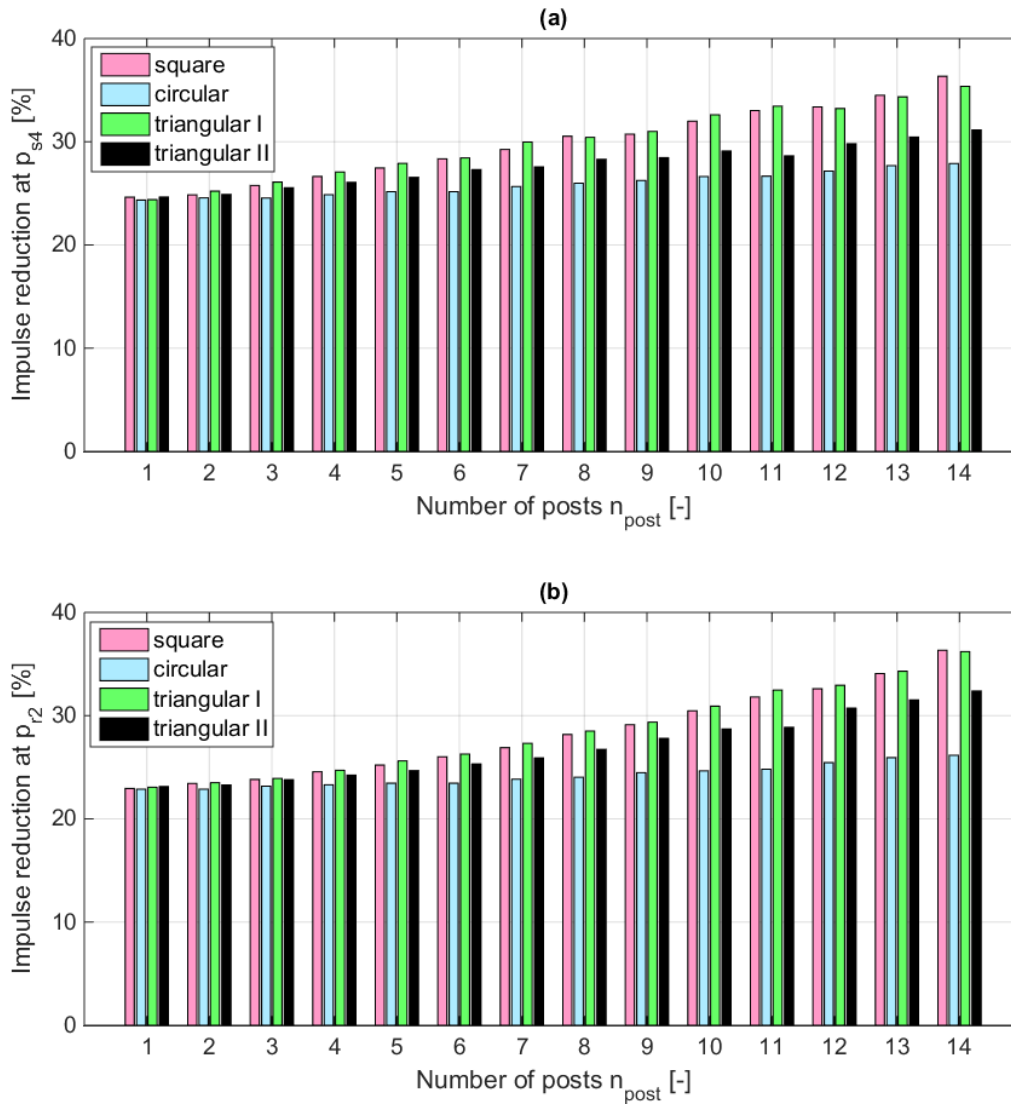


Figure 6-40: Impulse reductions of different cross-sectional shapes, single-layer arrangement (a) gauge ps4; (b) gauge pr2

The number of posts  $n_{post}$  varies from 1 to 14. In general, the square shape has the best performance in shock wave attenuation. The triangular shape I (vertex oriented away from the charge) performs almost as well as the square shape. The circular shape exhibits, as it was expected, the worst performance in shock wave attenuation. The triangular shape II (vertex facing the charge) provides a somewhat higher overpressure and impulse reduction than the circular shape. These findings can be explained by the associated drag coefficients  $C_d$  of the cross-sectional shapes (Section 3.6), which indicates the flow resistance around the barrier. The square shape and the triangular shape I (vertex oriented away from the charge) have the largest values of  $C_d = 2.0$ . As a result, such shapes achieve the best shock wave attenuation performance. The circular shape has the least value of  $C_d = 1.2$ , which leads to a worst performance in shock wave attenuation. The triangular shape II (vertex facing the charge) has a medium value of  $C_d = 1.55$ , which results in a medium performance in shock wave attenuation. It should be noted that the mentioned values of drag coefficients are only valid for long members without end effects. Experiments showed that the drag coefficient  $C_d$  is dependent on the geometry of the structure and its associated flow pattern (*Kinney and Graham*

1985). For posts with finite height, the air flows around the free edges and into the low-pressure region. It reduces the pressure drop across the post and hence the drag coefficient.

In summary, the considered cross-sectional shapes are sorted in descending order of shock wave attenuation performance as follows: square, triangular I (vertex oriented away from the charge), triangular II (vertex facing the charge) and circular.

### 6.4.5.3 Double-layer arrangement

In Sections 6.4.5.1 - 6.4.5.2, the influences of the number of posts and the cross-sectional shapes on the shock wave attenuation have already been discussed based on a single-layer arrangement of steel posts. As mentioned in Section 2.2.2, a shock wave trapping concept is recommended for a balanced design, i.e. easy entrance of the shock wave with a weak reflection followed by a strong reflection. During the balanced design process, a compromise is made between the attenuation of the shock wave and the reduction of the net blast loads on individual columns. Thus, based on the conclusion drawn in the previous section, the least effective shape (circular) should be used for the posts in the front layer, whilst the most efficient shape (square) should be used for the posts in the rear layer. For comparison, another combination of the cross-sectional shapes is also considered in this study, where both front and rear layers employ the square posts. The barrier combinations are summarized in Table 6-2, in which two categories with the different total number of posts (category I:  $n_{post} = 11$  and category II:  $n_{post} = 12$ ) are considered. For category I ( $n_{post} = 11$ ), the steel posts are staggered in the double-layer arrangement, whereas for category II ( $n_{post} = 12$ ), an aligned arrangement is adopted for the double-layer arrangement (Figure 6-41).

Table 6-2: Barrier combinations

Category	Type	Alignment	Cross-sectional shape front/rear layer	Number of posts front/rear layer	Label
I	single-layer	-	□	11	S-S11
	double-layer	staggered	□/□	5/6	D-SS56
			□/□	6/5	D-SS65
			○/□	5/6	D-CS56
			○/□	6/5	D-CS65
II	single-layer	-	□	12	S-S12
	double-layer	aligned	□/□	6/6	D-SS66
			○/□	6/6	D-CS66

To characterize the different combinations of posts, the barriers are labelled with the pertinent information of arrangements. The first letter represents the type of arrangement, i.e. single-layer (S) or double-layer (D). For a single-layer arrangement, the second letter designates the cross-sectional shape of posts, i.e. square (S) or circular (C), followed by the number of posts. For a double-layer arrangement, the second and third letters designate the cross-sectional shapes of posts in the front and rear layers. Following the letters are the numbers of posts in the front and rear layers. The distance between the front and rear layer is selected to be 100mm. Details on the arrangements of steel posts are outlined in Figure 6-41.

Category I					Category II		
S-S11	D-SS56	D-SS65	D-CS56	D-CS65	S-S12	D-SS66	D-CS66
a = 50mm	b = 100mm, c = 200mm				d = 40mm	b = 100mm, e = 180mm	
single-layer	double-layer, staggered				single-layer	double-layer, aligned	

Figure 6-41: Details of the arrangements of steel posts

Figure 6-42 and Figure 6-43 show the overpressure and impulse reductions at gauges ps2 - ps4 and pr1 - pr4 for the eight different barrier combinations. It is clear that for both categories I ( $n_{post} = 11$ ) and II ( $n_{post} = 12$ ), the single layer arrangements are most efficient among all combinations within the respective category. For category I ( $n_{post} = 11$ ), the overpressure and impulse reductions offered by the staggered arrangements D-SS56 and D-SS65 are about 4.4% - 22.3% (for  $F_p$ ) and 5.4% - 58.6% (for  $F_i$ ) lower than the single arrangement S-S11. A finding is that the staggered arrangements D-CS56 and D-CS65 can also achieve satisfactory results. The overpressure reductions at gauge pr2 are as high as 90.3% (D-CS56) and 89.8% (D-CS65) of that provided by the single arrangement S-S11. The impulse reductions at gauge pr4 are as high as 91.0% (D-CS56) and 89.8% (D-CS65) of that provided by the single arrangement S-S11. Regarding category II ( $n_{post} = 12$ ), the aligned arrangement D-SS66 is only slightly more efficient than the aligned arrangement D-CS66, which provides an overpressure and impulse reduction of up to 88.1% (at gauge pr2) and 88.9% (at gauge pr4) of that by the single arrangement S-S12. Comparing the arrangements based on the balanced consideration, e.g. the staggered arrangement D-CS56 and the aligned arrangement D-CS66, the former can provide a somewhat higher overpressure and impulse reduction than the latter arrangement, although it even has one post less. In this sense, if a double-layer arrangement is used, the staggered one can be more efficient than the aligned one.

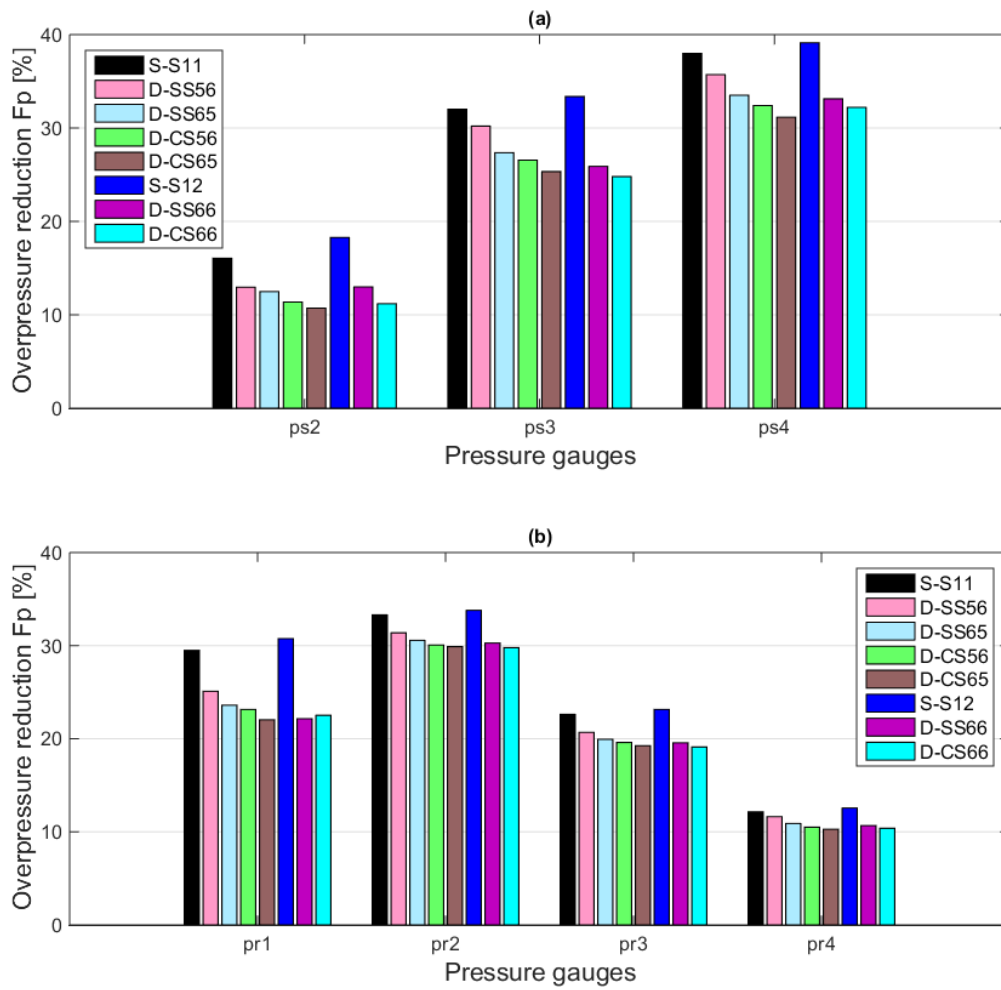


Figure 6-42: Overpressure reductions of different steel post arrangements at gauges  
 (a) ps2 - ps4; (b) pr1 - pr4

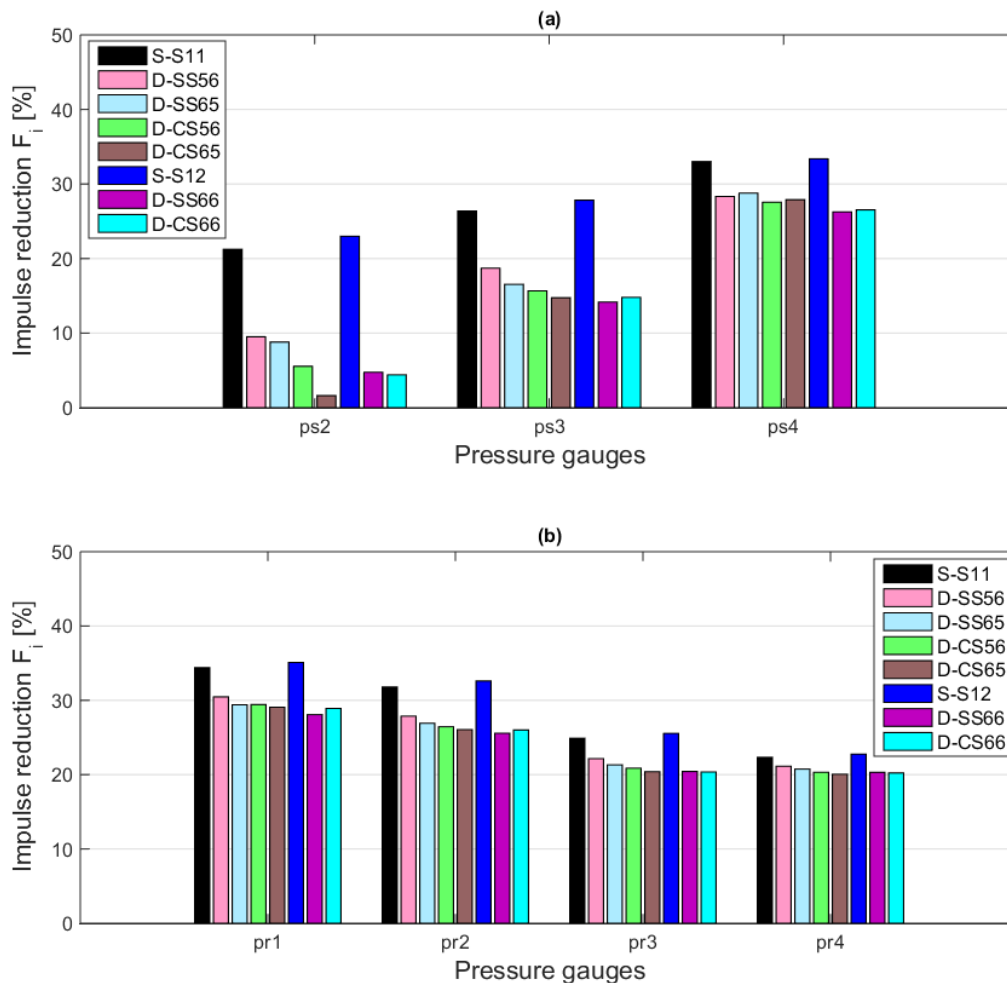


Figure 6-43: Impulse reductions of different steel post arrangements at gauges (a) ps2 - ps4; (b) pr1 - pr4

In summary, the single layer arrangements are most efficient among all combinations within the respective category. In practice, however, a balanced design concept is often recommended. If a multiple-layer arrangement is concerned, the staggered arrangement can be more efficient than the aligned one.

#### 6.4.6 Conclusions: protective barriers made of steel posts

This section presents numerical investigations of the shock wave attenuation effect provided by protective barriers with different steel post configurations. Prior to the experiments, numerical models are developed to predict the blast loads. Furthermore, the experimental data (Section 5.2) is used to validate the numerical models. The comparison of the numerical results using a rigid or flexible barrier assumption reveals that in these case studies the rigid assumption is appropriate since the differences in the blast loads are considerably small (within  $\pm 5\%$ ). The experimental and numerical results indicate that configuration M1 ( $n_{post} = 8$ ) shows the best performance in overpressure and impulse reduction in the configurations tested in the experiments. Based on the numerical results, configuration M1 ( $n_{post} = 8$ ) achieves an overpressure reduction range from 10.8% to 33.0% and an impulse reduction range from 10.7% to 31.2% at the gauges employed in the experiments, compared to the free field scenario.

Moreover, some findings arise from Section 6.4.5:

- A linear dependence of the overpressure and impulse reduction on the relative opening fraction (ROF) is observed in the ROF range from 16.7% to 100%, which indicates that adding one steel post to the arrangement reduces the peak overpressures by 0.5% - 1.8% and reduces the maximum impulse by 0.5% - 2.6%. If the ROF varies from 0% to 16.7%, the overpressure and impulse reduction factors increase rapidly with a decrease in the ROF. However, such a close arrangement of the steel posts is no longer profitable from an economical viewpoint, compared to a barrier without openings.
- Regarding the performance in shock wave attenuation, the examined cross-sectional shapes can be sorted in descending order, i.e. square, triangular I (vertex oriented away from the charge), triangular II (vertex facing the charge) and circular.
- To design the barriers in a blast-resistant manner, a balanced consideration of the maximization of the performance in shock wave attenuation and the minimization of the net blast loads on the barriers is recommended. It is demonstrated that, if a double-layer arrangement is concerned, the staggered one can be more efficient than the aligned one.

This study shows that protective barriers with openings can also provide a satisfactory level of protection. Although they may not be as effective as a barrier without openings, they can be easily constructed and used in regions where the construction of a solid barrier is not preferred. In addition, the necessary amount of material (steel in this case) and thus the construction cost can be considerably reduced.

### 6.5 Comparison of protective barriers (blast walls with a canopy on top versus protective barriers made of steel posts)

Two different types of protective barriers are numerically investigated, i.e. blast walls with a canopy on top (Section 6.3) and protective barriers made of steel posts (Section 6.4). This section compares these two types of protective barriers with respect to the following three aspects:

- Mechanism of shock wave propagation

For blast walls with a canopy on top, the combination of three distinct phenomena, i.e. reflection, absorption and diffraction, affects the blast load distribution on the building. Firstly, a part of the shock wave is reflected back by the front face of the blast wall. Secondly, a certain amount of blast energy is absorbed by the wall. Thirdly, another part of the shock wave is diffracted by the wall. For protective barriers made of steel posts, a fourth phenomenon (Transmission) occurs, namely, the shock wave is partly transmitted through the openings between the posts. Consequently, a combination of reflection, absorption, diffraction and transmission affects the blast load distribution on the building.

- Aesthetical attractiveness

The blast wall with a canopy on top can be regarded as a modified ordinary blast wall. Usually, ordinary blast walls are not readily accepted by urban society. They are usually aesthetically unattractive since they may give the occupants a prison-like feeling (living behind walls). The protective barriers made of steel posts come from the need for innovative solutions. The idea is to arrange the posts such that, on the one hand, the protection requirement against blast is reasonably met, and on the other hand, the arrangement of posts (a variety of cross-sectional shapes, single-layer or multi-layer, aligned or staggered etc.) meets the aesthetic demand to a satisfactory level. Thus, they can be integrated, for example, in an artwork during the city planning process. In this sense, they are aesthetically more attractive than blast walls with a canopy on top.

- Performance in attenuating the shock wave

In order to assess the performance of the both protective barriers in attenuating the shock wave, the most efficient configurations in respective experimental series, i.e. configuration M3 (GWC front) in the experimental series of blast walls with a canopy on top and configuration M1 ( $n_{post} = 8$ ) in the experimental series of protective barriers made of steel posts, are employed for comparison. The ambient conditions at mean sea level and at the standard temperature ( $15^{\circ}\text{C}$ ) are assumed. Furthermore, a width of 7m is chosen for the blast wall based on the conclusion drawn in Section 6.3.4.6 and the horizontal air flow around the sides of the blast walls is assumed to be negligible. The overpressure and impulse reduction factors (Eq. (6-3) and Eq. (6-4)) across the building facade are compared in Figure 6-44.

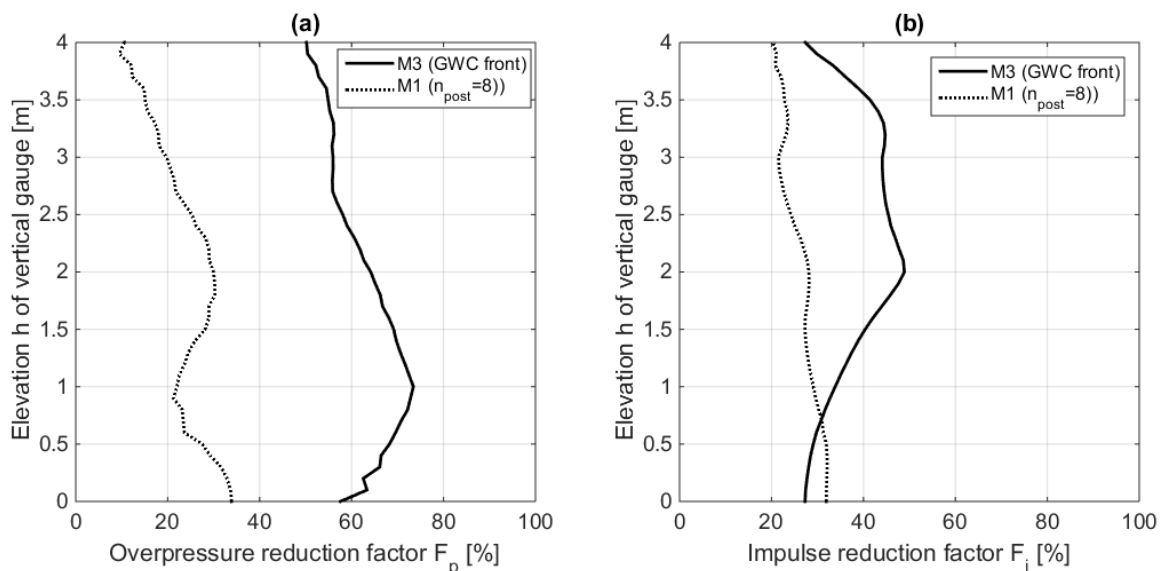


Figure 6-44: Overpressure and impulse reduction factors across the building envelope for configurations M3 (GWC front) and M1 ( $n_{post} = 8$ ) (a) overpressure reduction  $F_p$ ; (b) impulse reduction  $F_i$

Obviously, configuration M3 (GWC front) is more efficient in shock wave attenuation than configuration M1 ( $n_{post} = 8$ ) except for  $F_i$  in the lower region from 0m to 0.7m above the ground

(Figure 6-44b). Configuration M3 (GWC front) reduces the peak reflected overpressure and the maximum impulse at the building envelope by 50.2% - 73.4% and by 27.3% - 48.9%, whereas configuration M1 ( $n_{post} = 8$ ) provides only an overpressure reduction between 9.5% and 33.9% and an impulse reduction between 20.4% and 32.1%. Although the protective barriers made of steel posts may not be as effective as the blast walls with a canopy on top, it can be easily constructed and used to provide a satisfactory level of protection in regions where the construction of a solid barrier is not preferred.

### 7 Conclusions and outlook

This Dissertation contributes to the topic of effectiveness of protective barriers against air blast by combining experimental and numerical investigations. Two different types of protective barriers are involved in this Dissertation, i.e. blast walls with a canopy on top and protective barriers made of steel posts.

New experimental results of these protective barriers are provided, i.e. the overpressure-time histories at the gauges both in front of and behind the barriers. The experimental series of blast walls with a canopy on top shows that configuration M3 (GWC front), in which the canopy is oriented facing the charge (angle of inclination  $\alpha = 135^\circ$ ), achieves the best performance in overpressure and impulse reduction at gauges ps2 - ps4 (6.5m - 8.5m from the charge, 1m above the ground). The influence of the horizontal air flow around the sides of the blast wall, which is caused by the small width (2m) of the blast wall according to the experimental set-up, plays a great role in the overpressure distribution at gauges pr1 - pr4 (9.84m from the charge, 1m - 4m above the ground). Hence, no further statement can be made based on the experiments. The experimental series of protective barriers made of steel posts shows that the more posts the better shielding. Roughly speaking, configuration M1 (number of steel posts  $n_{post} = 8$ ) shows the best performance in overpressure (except at gauges ps2 and pr4) and impulse reduction (except at gauges pr1 - pr4).

Numerical simulations using the software LS-DYNA are performed to complement and / or to substitute the experiments. At first, the influence of ambient conditions (altitude and atmospheric temperature) on the blast loads is discussed. Atmospheric temperature ranging from 0°C to 24°C has only a minor effect on the blast loads behind the barriers, compared to the ones at the standard temperature of 15°C. In contrast to temperature, altitude has a more significant influence on the blast loads. Regarding the peak overpressures at the gauges employed in the blast wall experiments, the values at an altitude of 1600m (comparable to the test site at 1585m) are about 2.1% - 8.5% smaller than the ones at mean sea level. Due to the change in altitude, the reduction in peak side-on overpressure at gauge ps0 (3m from the charge) is negligibly small (1.7%). Therefore, the application of the K&B-blast loads to the ambient layer of ALE air elements is considered to be justified. The air domain involved in the numerical models of protective barriers is specified to the ambient conditions at the test site, which leads to an atmospheric pressure of 83.68kPa as well as an ambient air density of 0.994 kg/m<sup>3</sup> for blast walls with a canopy on top and 1.022kg/m<sup>3</sup> for protective barriers made of steel posts.

The influence of the charge height above the ground on the blast loads is also investigated. The charge height employed in the experiments (0.4m above the ground) causes an increase of up to 11.4% in the peak side-on overpressures at gauges ps1 (4m from the charge). Considering the gauges employed in the experiments to evaluate the protective barrier effectiveness, i.e. ps2 - ps4 and pr1 - pr4, the influence of the charge height on the peak overpressures at these gauges can be considered as negligible since the increase in peak overpressure is only up to 5.4%. Therefore, the results derived from the numerical models of protective barriers, which neglect the Mach stem effect, can be used for comparison with the experimental ones.

Furthermore, numerical investigations are performed to evaluate the shock wave attenuation effect provided by protective barriers. They successfully capture the shock wave propagation process, in which protective barriers are erected in order to reduce the blast loads on the building to be protected. The numerical models are validated by comparing them to experimental results of two barrier types, blast walls with a canopy on top and protective barriers made of steel posts.

The numerical results using a rigid or flexible barrier assumption are compared. The differences in the blast loads are considerably small, i.e. up to 9% for blast walls with a canopy on top and up to 5% for protective barriers made of steel posts. This reveals that in these case studies the rigid assumption for barriers is appropriate and is used for the further analyses in this Dissertation.

Due to the small width (2m) of the blast wall according to the experimental set-up, besides the vertical air flow over the top of the wall, the horizontal air flow around the sides of the blast wall plays a great role in the blast load distribution behind the wall. In practice, however, the blast walls are erected around the buildings to be protected (perimeter walls). Under such circumstances, there is no horizontal air flow around the sides of the wall. For the experimental set-up ( $W = 5\text{kg}$  TNT equivalent, distance from the charge to the wall  $R_1 = 5\text{m}$  and distance from the building to the wall  $R_2 = 4\text{m}$ ), the infinite wall width assumption is valid if the ratio of half wall width  $L/2$  to wall height  $H$  is larger than 1.75. Using the validated numerical models, investigations on the blast walls having infinite width are carried out. Configuration M3 (GWC front) shows the best performance in shock wave attenuation for all studied blast wall configurations. It offers an overpressure reduction ranging from 51.7% to 88.0% and an impulse reduction ranging from 30.5% to 59.2% at the gauges employed in the experiments, compared to a free field scenario.

Due to the gabion walls placed adjacent to the barrier (steel posts and frame), there is no direct air flow around the sides of the barrier of interest. Configuration M1 ( $n_{post} = 8$ ) shows the best performance in shock wave attenuation among the configurations tested in the experiments. Based on the numerical results, configuration M1 ( $n_{post} = 8$ ) achieves an overpressure reduction range from 10.8% to 33.0% and an impulse reduction range from 10.7% to 31.2% at the gauges employed in the experiments, compared to the free field scenario.

Moreover, the validated numerical models enables the evaluation of the influence of key parameters (angle of inclination of the canopy, relative opening fraction, cross-sectional shape and arrangement type of steel posts) on the effectiveness of protective barriers. Two observations arise from the parametric studies for blast walls with a canopy on top:

- It is necessary to perform a coupled FSI analysis between the shock wave and the canopy when the thickness of the canopy is thinner than a critical value (6mm in this case), whilst if the canopy is thicker than the critical value, the canopy can be regarded as a rigid structure.
- Regarding blast walls having infinite width, the optimal angle of inclination of the canopy lies between  $105^\circ$  and  $120^\circ$  (facing the charge) for the overpressure reduction

and lies between  $115^\circ$  and  $125^\circ$  (facing the charge) for the impulse reduction at the gauges employed in the experiments.

In addition, some findings arise from the parametric studies for protective barrier made of steel posts:

- A linear dependence of the overpressure and impulse reduction on the relative opening fraction (ROF) is observed in the ROF range from 16.7% to 100%, which indicates that adding one steel post to the arrangement reduces the peak overpressures by 0.5% - 1.8% and reduces the maximum impulse by 0.5% - 2.6%. If the ROF varies from 0% to 16.7%, the overpressure and impulse reduction factors increase rapidly with the decrease in the ROF. However, such a close arrangement of the steel posts is no longer profitable from an economical viewpoint, compared to a barrier without openings.
- Regarding the performance in shock wave attenuation, the examined cross-sectional shapes can be sorted in descending order, i.e. square, triangular I (vertex oriented away from the charge), triangular II (vertex facing the charge) and circular.
- To design the barriers in a blast-resistant manner, a balanced consideration of the maximization of the performance in shock wave attenuation and the minimization of the net blast loads on the barriers is recommended. It is demonstrated that, if a double-layer arrangement is concerned, the staggered one can be more efficient than the aligned one.

Lastly, comparisons are made between both types of protective barriers in three ways, i.e. mechanism of shock wave propagation, aesthetical attractiveness and performance in attenuating the shock wave. Regarding the blast walls with a canopy on top, a combination of reflection, absorption and diffraction affects the blast load distribution on the building. For protective barriers made of steel posts, a fourth phenomenon (Transmission) takes part in the mechanism of shock wave propagation. Protective barriers made of steel posts are aesthetically more attractive than blast walls with a canopy on top. Although the protective barriers made of steel posts may not be as effective as the blast walls with a canopy on top, they can be easily constructed and used to provide a satisfactory level of protection in regions where the construction of a solid barrier is not preferred. It is shown that protective barriers with openings can also provide a satisfactory level of protection. In addition, the necessary amount of material (steel in this case) and thus the construction cost can be considerably reduced.

As an outlook, the author would want to further investigate the influence of the open porous surface of gabion walls on the process of shock wave propagation. It is not possible to quantify this effect in the current work. The reflection phenomenon can be affected by the open porous surfaces, e.g. holes between the coarse-grained gravel in the gabion walls. On the one hand, the blast energy is partly absorbed by the holes between the coarse-grained gravel in the gabion walls. This leads to a certain decrease in the blast loads behind the wall. On the other hand, the shock wave is multiply reflected by the sharp edges of the coarse-grained gravel, which renders an increase in the blast loads behind the wall. Therefore, the influence of this open porous surface on the blast loads is difficult to specify. In order to gain a better understanding of this behaviour, the coarse-grained gravel of the gabion walls should be modelled. Such models

could be employed to quantify the influence of the open porous surface of gabion walls on the process of shock wave propagation.

The Mach stem effect, which is induced by the small charge height (0.4m) above the ground, is not considered in the numerical models proposed in this Dissertation. Based on a two-dimensional axisymmetric numerical simulation for a free field scenario (no barrier is present), it is observed that the Mach stem effect is negligible at gauges ps2 - ps4 and pr1 - pr4 employed to calculate the effectiveness of protective barriers, i.e. the peak overpressures are increased by up to 5.4%. However, the Mach stem effect becomes more pronounced if the observation point is close to the charge and located in the region of Mach reflection. For instance, the peak overpressure is increased by 9.4% - 11.4% at gauge ps1 (4m from the charge). Further study with a purely Arbitrary-Lagrangian-Eulerian (ALE) method, in which the charge shape and location are precisely represented, could be used to quantify the influence of the Mach stem effect on the blast loads behind the barriers.

Since this Dissertation focuses on the effectiveness of protective barriers against air blast, damage of barriers is not modelled in the numerical simulations. As already mentioned in Section 6.3.5.1, the canopy plate with a thickness less than 6mm experiences plastic deformation, especially at the connection edge between the canopy and the gabion wall. Due to the fact that no erosion criterion is implemented in the strength model of the canopy (Section 4.1.1.3), the canopy with 1mm thickness can reach a maximum displacement of 158.78cm. However, in practice, before the canopy reaches this maximum displacement, it may have already sustained a certain degree of damage or even been completely destroyed, since the plastic rotation ( $64.7^\circ$ ) significantly exceeds the recommended rotation limit ( $12^\circ$ ) for structural steel plates under the protection category of preventing structural elements from collapse (*Mays and Smith 1995*). Damage of barriers could generate secondary debris hazards. Further work with numerical models, in which erosion criterion is implemented in the strength model of barriers, could be used to evaluate the effectiveness of protective barriers against impact of debris.

## Bibliography

Abe, A. and Takayama, K. (2001), *Attenuation of shock waves propagating over arrayed spheres*, Proceedings of the SPIE, No. 4183, pp.582–589, DOI: 10.1117/12.424329.

AMCP 706-177 (1971), *Engineering Design Handbook: Explosives Series Properties of Explosives of Military Interest*, US Army.

Aquelet, N. and Souli, M. (2008), *2D to 3D ALE Mapping*, Proceedings of the 10<sup>th</sup> International LS-DYNA Conference, Detroit, USA.

Baker, W.E. (1973), *Explosions in air*, University of Texas Press, Austin, Tex.

Barakat, M.A. and Hetherington, J.G. (1998), *New Architectural Forms To Reduce The Effects Of Blast Waves And Fragments On Structures*, Transactions on the Built Environment, Vol. 32. WIT Press, UK.

Barakat, M.A. and Hetherington, J.G. (1999), *Architectural approach to reducing blast effects on structures*, Proceedings of the Institution of Civil Engineers - Structures and Buildings, Vol. 134, No. 4, pp.333–343, DOI: 10.1680/istbu.1999.31899.

Belytschko, T., Lin, J.I. and Chen-Shyh, T. (1984), *Explicit algorithms for the nonlinear dynamics of shells*, Computer Methods in Applied Mechanics and Engineering, Vol. 42, No. 2, pp.225–251, DOI: 10.1016/0045-7825(84)90026-4.

Benson, D.J. (1992), *Computational methods in Lagrangian and Eulerian hydrocodes*, Computer Methods in Applied Mechanics and Engineering, Vol. 99, 2-3, pp.235–394, DOI: 10.1016/0045-7825(92)90042-I.

Beyer, M.E. (1986), *Blast Loads Behind Vertical Walls*, in 22<sup>nd</sup> Minutes of the Explosives Safety Seminar, Anaheim, California, 26<sup>th</sup>-28<sup>th</sup> August, Defense Technical Information Center.

Biggs, J.M. (1964), *Introduction to structural dynamics*, McGraw-Hill, New York.

Bogosian, D. and Piepenburg, D. (2002), *Effectiveness of Frangible Barriers for Blast Shielding*, Proceedings of the 17<sup>th</sup> International Symposium Military Aspects of Blast and Shock (MABS), Las Vegas.

Bogosian, D., Montalva, A., Kasbeer, A. (2015), *Explosive Equivalence for Airblast Calculations*, Proceedings of the 16<sup>th</sup> International Symposium for the Interaction of the Effects of Munitions with Structures (ISIEMS), 9<sup>th</sup>-13<sup>th</sup> November, Destin, FL.

Borgers, J. and Vantomme, J. (2008), *Improving the accuracy of blast parameters using a new Friedlander curvature  $\alpha$* , DoD Explosives Safety Seminar, Palm Springs, CA.

Boutillier, J., Ehrhardt, L., Mezzo, S. de, Deck, C., Magnan, P., Naz, P. and Willinger, R. (2018), *Evaluation of the existing triple point path models with new experimental data: Proposal of an original empirical formulation*, Shock Waves, Vol. 28, No. 2, 243–252. DOI: 10.1007/s00193-017-0743-7.

Brode, H.L. (1955), *Numerical Solutions of Spherical Blast Waves*, Journal of Applied Physics, Vol. 26, No. 6, pp.766–775, DOI: 10.1063/1.1722085.

- Brode, H.L. (1956), *The Blast Wave in Air Resulting From a High Temperature, High Pressure Sphere of Air* (U), RAND Corporation, Santa Monica, CA.
- Cranz, C. (1926), *Lehrbuch der Ballistik*, 2, Berlin.
- Chapman, T.C., Rose, T.A. and Smith, P.D. (1995a), *Reflected blast wave resultants behind cantilever walls: A new prediction technique*, International Journal of Impact Engineering, Vol. 16, No. 3, pp.397–403, DOI: 10.1016/0734-743X(94)00051-W.
- Chapman, T.C., Rose, T.A. and Smith, P.D. (1995b), *Blast wave simulation using AUTODYN2D: A parametric study*, International Journal of Impact Engineering, Vol. 16, 5-6, pp.777–787, DOI: 10.1016/0734-743X(95)00012-Y.
- Chaudhuri, A., Hadjadj, A., Sadot, O. and Ben-Dor, G. (2013), *Numerical study of shock-wave mitigation through matrices of solid obstacles*, Shock Waves, Vol. 23, No. 1, pp.91–101, DOI: 10.1007/s00193-012-0362-2.
- Cheesman, R. A. R (2010), *Definition and Use of TNT Equivalencies in Assessing Loading in Confined Structures*, Proceedings of the First International Conference of Protective Structures (ICPS), Manchester.
- Cooper, P.W. (1994), *Comments on TNT equivalence*. Proceedings of the 20<sup>th</sup> International Pyrotechnics Seminar, pp. 215-226, Colorado Springs, Colorado.
- Cooper, P.W. (1996), *Explosives engineering*, Wiley-VCH, New York, NY.
- Courant, R., Friedrichs, K. and Lewy, H. (1928), *Über die partiellen Differenzengleichungen der mathematischen Physik*, Mathematische Annalen, Vol. 100, No. 1, pp.32–74, DOI: 10.1007/BF01448839 (in German).
- De Yong, L. V. and Campanella, G. (1989), *A study of blast characteristics of several primary explosives and pyrotechnic compositions*, Journal of hazardous materials, Vol. 21, No. 2, pp.125–133, DOI: 10.1016/0304-3894(89)85004-6.
- Dewey J.M. (2005), *The TNT equivalence of an optimum propane–oxygen mixture*, Journal of Physics D: Applied Physics, Vol. 38, No. 23, DOI: 10.1088/0022-3727/38/23/017.
- Dobratz, B.M. and Crawford P.C. (1985), *LLNL Explosives Handbook. Properties of Chemical Explosives and Explosive Simulants*, Lawrence Livermore National Laboratory, University of California.
- Döge, T. (2012), *Reflexion von Luftstoßwellen an nachgiebigen Materialien und Baustrukturen*, Dissertation, University of the Bundeswehr Munich (in German).
- Dusenberry, D.O. (2010), *Handbook for blast resistant design of buildings*, John Wiley & Sons, Hoboken, N.J.
- Ehrhardt, L., Boutillier, J., Magnan, P., Deck, C., De Mezzo, S., Willinger, R. and Naz, P. (2016), *Numerical simulation of the air blast interaction with simplified structures*, Proceedings of the 24<sup>th</sup> International Symposium Military Aspects of Blast and Shock (MABS), Halifax, Canada.

Eichinger, W.E. (1985), *Mach stem modeling with spherical shock waves*, Master Thesis, Faculty of the School of Engineering, The Air Force Institute of Technology Air University, Ohio.

Esparza, E.D. (1986), *Blast measurements and equivalency for spherical charges at small scaled distances*, International Journal of Impact Engineering, Vol. 4, No. 1, pp.23–40, DOI: 10.1016/0734-743X(86)90025-4.

Esteban, B. and Gebbeken, N. (2016), *A comparison of numerical modelling strategies in contact detonation scenarios with concrete targets*, International Journal of Computational Methods and Experimental Measurements, Vol. 4, No. 3, pp.231–246, DOI: 10.2495/CMEM-V4-N3-231-246.

Esteban, B. and Gebbeken, N. (2017), *A detailed comparison of two material models for concrete in the dynamic loading regime, RHT and HPG*, International Journal of Protective Structures, Vol. 8, No. 2, DOI: 10.1177/2041419617707104.

Esteban, B. (2017), *A contribution to empirical, theoretical and numerical investigations of protective structures subjected to shape charge attacks*. Dissertation, University of the Bundeswehr Munich.

Ethridge, N.H. (1965), *A Procedure for Reading and Smoothing Pressure-time Data from H. E. and Nuclear Explosions*, Army Ballistic Research Laboratories.

Formby, S.A. (1995), *Quantification of the air blast characteristics of commercial explosives*. IChemE symposium Series No. 139, 24–26 October.

Formby, S.A. and Wharton, R.K. (1996), *Blast characteristics and TNT equivalence values for some commercial explosives detonated at ground level*, Journal of hazardous materials, Vol. 50, 2-3, pp.183–198, DOI: 10.1016/0304-3894(96)01791-8.

Gebbeken, N. (2017), *Urbane Sicherheit bei Explosionen - Schutz durch Bepflanzung, Bautechnik*, Vol. 94, No. 5, pp.295–306, DOI: 10.1002/bate.201600089 (in German).

Gebbeken, N. and Döge, T. (2008), *Architectural Concepts to Reduce the Effects of Explosions*, Proceedings of the 9<sup>th</sup> International Conference on Computational Structures Technology, Athens, Greece, 2<sup>nd</sup>- 5<sup>th</sup> September, Civil-Comp Press, Stirlingshire, UK.

Gebbeken, N. and Döge, T. (2010a), *Explosion Protection - Architectural Design, Urban Planning and Landscape Planning*, International Journal of Protective Structures, Volume 1, Number 1, pp.1–21, DOI: 10.1260/2041-4196.1.1.1.

Gebbeken, N. and Döge, T. (2010b), *Determination of design loads from explosion and impact scenarios*, in: F. M. Mazzolani (Ed.), Urban Habitat Constructions Under Catastrophic Events, Proceedings of the COST C26 Action Final Conference, CRC Press, pp.119–126.

Gebbeken, N., Döge, T. and Larcher, M. (2011), *Sicherheit bei terroristischen Bedrohungen im öffentlichen Raum durch spezielle bauliche Lösungen*, Bautechnik, Vol. 88, No. 10, pp.668–676, DOI: 10.1002/bate.201101510 (in German).

Gebbeken, N., Döge, T. and Larcher, M. (2012), *Safety and Security of Urban Areas through Innovative Architectural and Structural Concepts*, in: Aschenbruck, N. (Ed.), Future security

- 2012, Proceedings of the 7<sup>th</sup> Security Research Conference, Bonn, Germany, 4<sup>th</sup>-6<sup>th</sup> September, 2012, Springer, Berlin, pp.153–164.
- Gelfand, B. (2004), *Blast effects caused by explosions*, Final Technical Report, Translation from Russian to English, European Research Office of the U.S. Army, Contract No. N62558-04-M-0004, London, England.
- Glasstone, S. (1980), *The effects of nuclear weapons*, 3rd ed., Castle House Publ, Tunbridge Wells.
- Grisaro, H.Y. and Edri, I.E. (2017), *Numerical investigation of explosive bare charge equivalent weight*, International Journal of Protective Structures, Vol. 8, No. 2, pp.199–220, DOI: 10.1177/2041419617700256.
- Hao, Y., Hao, H., Shi, Y., Wang, Z. and Zong, R. (2017), *Field Testing of Fence Type Blast Wall for Blast Load Mitigation*, International Journal of Structural Stability and Dynamics, Vol. 9, p.1750099, DOI: 10.1142/S0219455417500997.
- Held, M. (1983), *TNT - Equivalent*, Propellants, Explosives, Pyrotechnics, Vol. 8, No. 5, pp.158–167, DOI: 10.1002/prop.19830080507.
- Henrych, J. and Abrahamson, G.R. (1980), *The Dynamics of Explosion and Its Use*, Journal of Applied Mechanics, Vol. 47, No. 1, p.218, DOI: 10.1115/1.3153619.
- Hiermaier, S. (2008), *Structures Under Crash and Impact*, Springer US, Boston, MA.
- Hopkinson, B. (1915), *British Ordnance Board Minutes*, Report No. 13565, British Ordnance Office. London, UK.
- Hughes, T.J.R., Liu, W.K. and Zimmermann, T.K. (1981), *Lagrangian-Eulerian finite element formulation for incompressible viscous flows*, Computer Methods in Applied Mechanics and Engineering, Vol. 29, No. 3, pp.329–349, DOI: 10.1016/0045-7825(81)90049-9.
- Hyde, D.W. (1988), *Microcomputer Programs CONWEP and FUNPRO, Applications of TM 5-855-1, Fundamentals of Protective Design for Conventional Weapons (User's Guide)*, Defense Technical Information Center.
- IATG 01.80 (2015), *Formulae for ammunition management*, International Ammunition Technical Guideline, United Nations Office for Disarmament Affairs (UNODA).
- Ivanov, M.S., Vandromme, D., Fomin, V.M., Kudryavtsev, A.N., Hadjadj, A. and Khotyanovsky, D.V. (2001), *Transition between regular and Mach reflection of shock waves: New numerical and experimental results*, Shock Waves, Vol. 11, No. 3, pp.199–207, DOI: 10.1007/PL00004075.
- Jeremić, R. and Bajić, Z. (2006), *An approach to determining the TNT equivalent of high explosives*, Scientific-Technical Review. LVI. 58-62.
- Jones, N. (1983), *Structural aspects of ship collisions*, Chapter 11, in: Jones, N. and Wierzbicki, T. (Eds.), *Structural Crashworthiness*, Butterworth, pp.308-337.
- Jones, P.S., Vitaya-Udom, K. P. and Watt, J. M. (1987), *Design of structures to resist terrorist attack. Report 1, 1/10-scale model perimeter wall tests*, Technical report, Structures Laboratory, U.S. Army Engineer Waterways Experiment Station.

## Bibliography

---

- Kalra, A., Zhu, F., Yang, King H. and King, A.I. (2014), *Key Parameters in Blast Modeling Using 2D to 3D ALE Mapping Technique*, Proceedings of the 13<sup>th</sup> International LS-DYNA Conference, Dearborn, MI.
- Karlos, V. and Solomos, G. (2013), *Calculation of Blast Loads for Application to Structural Components*, Report No. EUR 26456 EN, European Commission, Joint Research Centre, Institute for the Protection and Security of the Citizen, Italy.
- Kingery, C.N. and Bulmash, G. (1984), *Air Blast Parameters from TNT Spherical Air Burst and Hemispherical Surface Burst*, Ballistic Research Laboratories, BRL Report No. 02555.
- Kinney, G.F. and Graham, K.J. (1985), *Explosive Shocks in Air*, Springer Berlin Heidelberg, Berlin, Heidelberg.
- Korenev, B. and Rabinovič, I.M. (1985), *Baudynamik - Konstruktionen unter speziellen Einwirkungen*, VEB Verlag für Bauwesen, Berlin (in German).
- Krauthammer, T. (2008), *Modern protective structures*, CRC Press, Boca Raton, FL.
- Krauthammer, T. (2017), *Recent observations on design and analysis of protective structures*, *Engineering Structures*, Vol. 149, pp.78–90, DOI: 10.1016/j.engstruct.2016.09.035.
- Lacher, M. (2008), *Pressure-Time Functions for the Description of Air Blast Waves*, JRC Technical Note, Report No. 46829.
- Lapoujade, V., Van Dorsselaer, N., Kevorkian, S. and Cheval, K. (2010), *A Study of Mapping Technique for Air Blast Modeling*, Proceedings of the 11<sup>th</sup> International LS-DYNA Conference. Detroit.
- Larcher, M. (2007), *Numerische Simulation des Betonverhaltens unter Stoßwellen mit Hilfe des Elementfreien Galerkin-Verfahrens*, Dissertation, Institut für Massivbau und Baustofftechnologie, Karlsruher Institut für Technologie (KIT).
- LSTC Livermore Software Technology Corp (2017), *LS-DYNA Keyword User's Manual*, Release 10.0.
- Locking, P.M. (2011), *The trouble with TNT equivalence*, Proceedings of the 26<sup>th</sup> international symposium on ballistics, 12<sup>th</sup>-16<sup>th</sup> September, Miami, FL.
- Locking P.M. (2013), *TNT equivalence - experimental comparison against prediction*, Proceedings of the 27<sup>th</sup> international symposium on ballistics, 22<sup>nd</sup>-26<sup>th</sup> April, Freiburg.
- Locking P.M. (2014), *Explosive materials characterisation by TNT equivalence*, Proceedings of the 28<sup>th</sup> international symposium on ballistics, 22<sup>nd</sup>-26<sup>th</sup> September, Atlanta, GA.
- Löhner, R. and Baum, J. D. (2010), *An assessment of architecturally appealing, semi-open shock mitigation devices*, Proceedings of the 21<sup>st</sup> International symposium on military aspects of blast and shock (MABS), Jerusalem.
- Löhner, R., Camelli F. and Stück, A. (2010), *Adjoint-based design of passive shock mitigation devices*, Proceedings of the 21<sup>st</sup> International symposium on military aspects of blast and shock (MABS), Jerusalem.

- Low, H.Y. and Hao, H. (2001), *Reliability analysis of reinforced concrete slabs under explosive loading*, Structural Safety, Vol. 23, No. 2, pp.157–178, DOI: 10.1016/S0167-4730(01)00011-X.
- Low, H.Y. and Hao, H. (2002), *Reliability analysis of direct shear and flexural failure modes of RC slabs under explosive loading*, Engineering Structures, Vol. 24, No. 2, pp.189–198, DOI: 10.1016/S0141-0296(01)00087-6.
- Mayor, R.P. and Flanders, R. (1990), *Technical Manual - Simplified computer model of air blast effects on building walls*, US Dept. of Transportation, Research and Special Programs Administration, Transportation Systems Center, Vehicle Crashworthiness Division, Safety and Security Systems Division, Kendall Square, Cambridge MA 02142, USA.
- Mayrhofer, C. (2004), *Methoden der dynamischen Grenztragfähigkeitsberechnung*, in: Thoma, K. and Gebbeken, N. and Thünemann, H. (Eds.), Workshop Bau-Protect Bauliche Strukturen unter Belastung durch Impakt und Sprengwirkung. Fraunhofer EMI, Freiburg, pp.169–184 (in German).
- Mays, G.C. and Smith, P.D. (1995), *Blast effects on buildings*, Thomas Telford Publishing.
- McKown, G.L., McIntyre, F.L., Moroney, J. and Badoeski, W. (1978), *The equivalency of composition A5*, US army armament research and development command, Large caliber weapon laboratory, Dover, New Jersey, pp. 1-60.
- Needham, C.E. (2010), *Blast Waves*, Springer Berlin Heidelberg, Berlin, Heidelberg.
- Ngo, T. D., Nguyen, N. and Mendis, P. (2004), *An investigation on the effectiveness of blast walls and blast-structure interaction*, in: Andrew Deeks und Hong Hao (Eds.), Developments in mechanics of structures and materials, Proceedings of the 18<sup>th</sup> Australasian Conference on the Mechanics of Structures and Materials, Perth, Australia, 1<sup>st</sup>-3<sup>rd</sup> December, CRC Press, pp.961–967.
- Niollet, J.E., Yuen, S.C.K. and Nurick, G.N. (2015), *A Study to Assess the Use of Cylindrical Bars as Blast Barriers*, International Journal of Protective Structures, Vol. 6, No. 2, pp.263–286, DOI: 10.1260/2041-4196.6.2.263.
- Pachman, J., Matyáš, R. and Künzel, M. (2014), *Study of TATP: Blast characteristics and TNT equivalency of small charges*, Shock Waves, Vol. 24, No. 4, DOI: 10.1007/s00193-014-0497-4.
- Philip, E.B. (1942), *The passage of blast over a wall*, Technical Report REN 556 Ministry of Works.
- Randers-Pehrson, G. and Bannister, K.A. (1997), *Airblast Loading Model for DYNA2D and DYNA3D*, Defense Technical Information Center.
- Rebelo, H. B. and Cismasiu, C. (2017), *A Comparison between Three Air Blast Simulation Techniques in LS-DYNA*, Proceedings of the 11<sup>th</sup> European LS-DYNA Conference, Salzburg, Austria.
- Rice, D., Baum, J., Tennant D. and Löhner, R. (2003), *Effect of Reinforced Concrete Column Geometry on Blast Loading and Response*, Proceedings of the 11<sup>th</sup> International Symposium on the Interaction of the Effects of Munitions with Structures (ISIEMS). Mannheim, Germany.

- Rickman, D.D. and Murrell, D.W. (2007), *Development of an Improved Methodology for Predicting Airblast Pressure Relief on a Directly Loaded Wall*, Journal of Pressure Vessel Technology, Vol. 129, No. 1, p.195, DOI: 10.1115/1.2409317.
- Rigby, S.E., Tyas, A., Bennett, T., Fay, S.D., Clarke, S.D. and Warren, J.A. (2014), *A Numerical Investigation of Blast Loading and Clearing on Small Targets*, International Journal of Protective Structures, Vol. 5, No. 3, pp.253–274, DOI: 10.1260/2041-4196.5.3.253.
- Rogg, B., Hermann, D. and Adomeit, G. (1985), *Shock-induced flow in regular arrays of cylinders and packed beds*, International Journal of Heat and Mass Transfer, Vol. 28, No. 12, pp.2285–2298, DOI: 10.1016/0017-9310(85)90047-X.
- Rose, T.A. (2001), *An Approach to the Evaluation of Blast Loads on Finite and Semi-infinite Structures*, Dissertation, Engineering Systems Department, Cranfield University.
- Rose, T.A., Mays, G. C. and Smith, P. D. (1993), *Leakage pressures behind blast walls*, Proceedings of the 6<sup>th</sup> International Symposium on Interaction of Nonnuclear Munitions with Structures, 3<sup>rd</sup>-7<sup>th</sup> May, Panama City Beach, Florida.
- Rose, T.A., Smith, P.D. and Mays, G.C. (1995), *The effectiveness of walls designed for the protection of structures against airblast from high explosives*, Proceedings of the Institution of Civil Engineers - Structures and Buildings, Vol. 110, No. 1, pp.78–85, DOI: 10.1680/istbu.1995.27306.
- Rose, T.A., Smith, P.D. and Mays, G.C. (1997), *Design charts relating to protection of structures against airblast from high explosives*, Proceedings of the Institution of Civil Engineers - Structures and Buildings, Vol. 122, No. 2, pp.186–192, DOI: 10.1680/istbu.1997.29307.
- Rose, T.A., Smith, P.D. and Mays, G.C. (1998), *Protection of structures against airburst using barriers of limited robustness*, Proceedings of the Institution of Civil Engineers - Structures and Buildings, Vol. 128, No. 2, pp.167–176, DOI: 10.1680/istbu.1998.30123.
- Rigby, S.E. and Sielicki, Piotr W. (2014), *An Investigation of TNT Equivalence of Hemispherical PE4 Charges*, Engineering Transactions, 62, 4, pp. 423–435.
- Sachs, R.G. (1944), *The Dependence of Blast on Ambient Pressure and Temperature*, Ballistic Research Laboratories, BRL report No. 466.
- Schwer, L., Teng, H. and Souli, M. (2015), *LS-DYNA Air Blast Techniques: Comparisons with Experiments for Close-in Charges*, Proceedings of the 10<sup>th</sup> European LS-DYNA Conference. Würzburg.
- Shi, Y., Hao, H. and Li, Z.-X. (2007), *Numerical simulation of blast wave interaction with structure columns*, Shock Waves, Vol. 17, 1-2, pp.113–133, DOI: 10.1007/s00193-007-0099-5.
- Shi, H.H. and Yamamura, K. (2004), *The interaction between shock waves and solid spheres arrays in a shock tube*, Acta Mechanica Sinica, Vol. 20, No. 3, pp.219–227, DOI: 10.1007/BF02486714.

- Shin, J., Whittaker, A.S. and Cormie, D. (2015), *TNT Equivalency for Overpressure and Impulse for Detonations of Spherical Charges of High Explosives*, International Journal of Protective Structures, Vol. 6, No. 3, pp.567–579, DOI: 10.1260/2041-4196.6.3.567.
- Skews, B.W., Draxl, M.A., Felthun, L. and Seitz, M.W. (1998), *Shock wave trapping*, Shock Waves, Vol. 8, No. 1, pp.23–28, DOI: 10.1007/s001930050095.
- Slavik, T.P. (2009), *A Coupling of Empirical Explosive Blast Loads to ALE Air Domains in LS-DYNA*, Proceedings of the 7<sup>th</sup> European LS-DYNA Conference, Salzburg, Austria.
- Smith, P.D. (2010), *Blast Walls for Structural Protection Against High Explosive Threats: A Review*, International Journal of Protective Structures, Volume 1, Number 1, pp.67–84.
- Smith, P.D. and Hetherington, J.G. (1994), *Blast and ballistic loading of structures*, Butterworth-Heinemann, Oxford.
- Suzuki, K., Himeki, H., Watanuki, T. and Abe, T. (2000), *Experimental Studies on Characteristics of Shock Wave Propagation through Cylinder Array*, The Institute of Space and Astronautical Science No. 676.
- Swisdak, M.M. (1975), *Explosion Effects and Properties. Part I. Explosion Effects in Air*, Defense Technical Information Center.
- Takayama, K. (1998), *Experimental investigation of shock wave / vortex interaction at the shock wave reserach center*, Proceeding of the 2<sup>nd</sup> Int. Workshop on shock wave / Vortex Interaction, pp.244–278.
- Teich, M. (2012), *Interaktionen von Explosionen mit flexiblen Strukturen*, Dissertation, University of the Bundeswehr Munich (in German).
- Teich, M. and Gebbeken, N. (2012), *Structures Subjected to Low-Level Blast Loads: Analysis of Aerodynamic Damping and Fluid-Structure Interaction*, Journal of Structural Engineering, Vol. 138, No. 5, pp.625–635, DOI: 10.1061/(ASCE)ST.1943-541X.0000493.
- Time and Date AS (2018a), *Schneizlreuth Weather History for 17. August 2016*, <https://www.timeanddate.com/weather/@6556115/historic?month=8&year=2016> (Accessed February 25, 2018.).
- Time and Date AS (2018b), *Schneizlreuth Weather History for 11. August 2016*, <https://www.timeanddate.com/weather/@6556115/historic?month=8&year=2016> (Accessed February 25, 2018.).
- UFC 3-340-01 (2002), *Design and Analysis of Hardened Structures for Conventional Weapons Effects*, USACE - Protective Design Center.
- UFC 3-340-02 (2014), *Structures to resist the effects of accidental explosions*, US Army Corps of Engineers, 2nd ed., Air Force Civil Engineer Support Agency.
- U.S. Standard Atmosphere (1976), National Oceanic and Atmospheric Administration, National Aeronautics and Space Administration and US Air Force, Defense Technical Information Center.

## Bibliography

---

van Leer, B. (1977), *Towards the ultimate conservative difference scheme. IV. A new approach to numerical convection*, Journal of Computational Physics, Vol. 23, No. 3, pp.276–299, DOI: 10.1016/0021-9991(77)90095-X.

von Neumann J. (1943), *Oblique reflection of shock waves*, Navy Dept. Bureau of Ordnance, US Dept. Comm. Off. Tech. Serv. N, Explosive Research Report No. 12, Washington DC.

Wharton, R.K., Formby, S.A. and Merrifield, R. (2000), *Airblast TNT equivalence for a range of commercial blasting explosives*, Journal of hazardous materials, Vol. 79, 1-2, pp.31–39, DOI: 10.1016/S0304-3894(00)00168-0.

Whitham, G.B. (1957), *A new approach to problems of shock dynamics, Part I: Two-dimensional problems*, Journal of Fluid Mechanics, Vol. 2, No. 02, p.145, DOI: 10.1017/S002211205700004X.

Xiao, W., Hübner, M. and Gebbeken, N. (2015), *Close-form solution of structural failure mode subjected to complex blast loadings*, in Usmani, A., Lu, Y. and Das P. (Eds.), Proceedings of the CONFAB, 2<sup>nd</sup>-4<sup>th</sup> September, Glasgow, Scotland, UK.

Xiao, W., Hübner, M. and Gebbeken, N. (2016), *Numerical derivation of the flexural transformation factors for structures subjected to blast loadings*, in: Li, Z.X., Hao, H., Du, X.L. and Wu, C. (Eds.), Proceedings of the 4<sup>th</sup> International Conference on Protective Structures (ICPS), 18<sup>th</sup>-21<sup>st</sup> October, Beijing, China.

Xiao, W., Andrae, M., and Gebbeken, N. (2017a), *Numerical prediction of the shock wave mitigation effect using protective barriers made of steel posts with a square hollow section*, Proceedings of the 17th International Symposium on the Interaction of the Effects of Munitions with Structures (ISIEMS), 16<sup>th</sup>-20<sup>th</sup> October, Bad Neuenahr, Germany.

Xiao, W., Andrae, M., Ruediger, L. and Gebbeken, N. (2017b), *Numerical prediction of blast wall effectiveness for structural protection against air blast*, Procedia Engineering, Vol. 199, pp.2519–2524, DOI: 10.1016/j.proeng.2017.09.432.

Xiao, W., Andrae, M., and Gebbeken, N. (2018a), *Numerical investigations on the Triple Point Path*, in: W. Sielicki, T. Gajewski and M. Szymczyk (Eds.), Design, Experiment and Analysis of Protective Structures, Proceedings of the 5th International Conference on Protective Structures (ICPS), 19<sup>th</sup>-23<sup>rd</sup> August, Poznan, Poland.

Xiao, W., Andrae, M. and Gebbeken, N. (2018b), *Experimental and Numerical Investigations of Shock Wave Attenuation Effects Using Protective Barriers Made of Steel Posts*, Journal of Structural Engineering, Vol. 144, No. 11, p.4018204, DOI: 10.1061/(ASCE)ST.1943-541X.0002194.

Xiao, W., Andrae, M. and Gebbeken, N. (2018c), *Experimental and Numerical Investigations on the effectiveness of blast walls with a canopy on top*, International Journal of Impact Engineering, (under review).

Xiao, W., Andrae, M., and Gebbeken, N. (2018d), *Numerical Investigations of the Shock Wave Attenuation Effects using Protective Barriers made of Steel Posts*, in: W. Sielicki, T. Gajewski and M. Szymczyk (Eds.), Design, Experiment and Analysis of Protective Structures,

Proceedings of the 5th International Conference on Protective Structures (ICPS), 19<sup>th</sup>-23<sup>rd</sup> August, Poznan, Poland.

Zhou, X.Q. and Hao, H. (2008), *Prediction of airblast loads on structures behind a protective barrier*, International Journal of Impact Engineering, Vol. 35, No. 5, pp.363–375, DOI: 10.1016/j.ijimpeng.2007.03.003.

Zong, R., Hao, H. and Shi, Y. (2017), *Development of a New Fence Type Blast Wall for Blast Protection: Numerical Analysis*, International Journal of Structural Stability and Dynamics, Vol. 17, No. 6, p.1750066, DOI: 10.1142/S0219455417500663.